UNIVERSITÀ
DEGLI STUDI
DI PADOVA

Sede Amministrativa: Università degli Studi di Padova

Dipartimento di INGEGNERIA INDUSTRIALE

SCUOLA DI DOTTORATO DI RICERCA IN: INGEGNERIA INDUSTRIALE
INDIRIZZO: INEGNERIA DELL'ENERGIA
CICLO XXVII

# EXPERIMENTAL INVESTIGATION OF FLOW BOILING IN SILICON MICROCHANNEL DEVICES FOR ELECTRONICS COOLING

**Direttore della Scuola:** Ch.mo Prof. Paolo Colombo
**Coordinatore d'indirizzo:** Ch.mo Prof. Luisa Rossetto
**Supervisore:** Ch.mo Prof. Del Col
**Co-supervisore:** Dott. Luciano Musa

**Dottorando:** Andrea Francescon

*"Whenever you find yourself on the side of the majority,*
*it is time to pause and reflect."*

Mark Twain

# Abstract

With the fast miniaturization of Very Large Scale Integration (VLSI) systems in the electronics industry, thermal management issues are becoming a serious challenge for sustaining the Moore's law trend in the next years. Flow boiling in silicon microchannel evaporators has recently arisen as one of the best solutions for the thermal management of high heat flux electronic devices. Microscale flow boiling exhibits high heat transfer rates and reduced temperature gradients optimizing electronics operation. Silicon fabrication techniques enable the development of compact and highly integrated systems. However, the lack of a complete understanding of the physics processes involved and serious technical issues are currently delaying the introduction of silicon microchannel devices in consumable products. Following the great interest of the electronics industry, silicon microchannel devices have started to be considered also for the design of future particle detectors for High Energy Physics (HEP) experiments. This work presents new insights on the two-phase fluid dynamics and flow boiling heat transfer characteristics in silicon microchannel devices. The effect of surface wall roughness is also addressed with a dedicated test section featuring tailored microfabricated structures at the channel walls. The study of interconnected silicon micro-evaporators for the efficient thermal management of future silicon particle detectors at the Large Hadron Collider (LHC) is described. The thermal performance of the device are presented and discussed. The qualification of the complete fabrication processes based on standard microfabrication techniques and the solution of important technical challenges are addressed, paving the introduction of silicon microchannel devices in the design of future detector systems. The results obtained in this study have many potential applications in all the industrial sectors where high heat fluxes need to be efficiently managed with very compact systems.

# Riassunto

Con la continua miniaturizzazione dei sistemi ad altissima integrazione nell'industria elettronica, la gestione della potenza termica dissipata da tali dispositivi sta iniziando a diventare un problema di primaria importanza per cercare di mantenere l'andamento della legge di Moore negli anni a venire. Lo scambio termico tramite evaporazione in microcanali di silico è sorto negli ultimi anni come una delle soluzioni piu promettenti per il raffreddamento di componenti elettronici ad alte dissipazioni. Gli elevati livelli di scambio termico e i ridotti gradienti termici ottimizzano il funzionamento dell'elettronica. Le tecniche di fabbricazione del silicio consentono di ottenere componenti molto precisi consentendo alti livelli di integrazione. Tuttavia, la mancanza di una conoscenza approfondita dei fenomeni fisici coinvolti e serie difficoltà tecniche stanno attualmente posticipando l'ingresso di questa tecnologia in prodotti di consumo. Seguendo il grande interesse dell'industria elettronica, i microcanali in silicio stanno iniziando ad essere considerati anche per il disegno dei futuri rivelatori di particelle per esperimenti di fisica delle alte energie. Questo lavoro presenta nuovi risultati sul deflusso bifase e lo scambio termcio per evaporazione in microcanali in silicio. L'effetto della rogosità di parete è inoltre investigato tramite lo sviluppo di una apposita sezione di test dotata di strutture micrometriche alle pareti del canale. Lo sviluppo di micro-evaporatori in silico per il raffreddamento dei futuri rivelatori di particlle in silico per il Large Hadron Collider (LHC) è presentato. Viene inoltre descritta la qualifcazione del completo processo produttivo basato su tecniche di microfabbricazione del silico e la soluzione di importanti problematiche tecniche, aprendo cosi la strada all'introduzione di sistemi di raffreddamento basati su microcanali in silicio nei futuri rivelatori di particelle.

# Contents

# List of Figures

# List of Tables

# Introduction

The restless advancements of the VLSI (Very Large Scale Integration) industry, nowadays moving towards 10 nm technology, has rapidly increased the computational power of electronic products by packing more and more transistor in integrated circuit devices according to Moore's law (Fig. 1) [1].

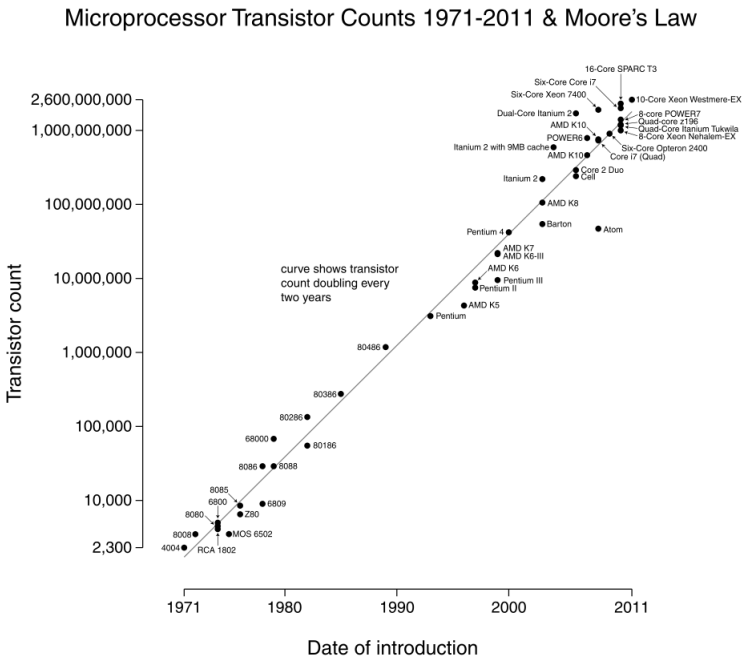


FIGURE 1: Transistor count on commercial IC chips compared with predictions of the Moore's law.

The increase of computational performance and speed and the reduction of component size have led to a rapid increase of dissipation heat fluxes on electronics components (Fig. 2). As a consequence, traditional cooling systems are becoming non-effective. New advanced cooling technologies for the thermal management of high heat flux electronics component with minimum packaging impact are required to maintain the Moore's law trend in the coming decades. After the pioneering work of Tuckerman and Pease [2], which demonstrated

the possibility to efficiently cool IC chips with microchannel arrays fabricated with standard microfabrication processes on silicon substrates, silicon microchannel cooling has rapidly become one of the most promising techniques for the thermal management of high heat flux electronics components. Microscale liquid cooling features high heat transfer rates thus minimizing the chip junction temperature for a safer operation. Flow boiling heat transfer exhibits even higher heat transfer rates and minimum temperature gradients in the fluid, but it is affected by higher pressure drop and complex fluid dynamics. Despite of the huge research conducted in the microscale fluid dynamics and heat transfer field in the past years, a complete understanding the physics of the process is still not accomplished and several topics have still to be explained. The lack of reliable design tools and the presence of unresolved technical issues are currently delaying the introduction of this technique into commercial electronic products. In Chapter 1, the main results achieved in flow boiling heat transfer research in the last years are reviewed, with emphasis on the topics of interest in this particular work. It will be shown that even if several advancements were achieved during the years, many questions need still to be solved.

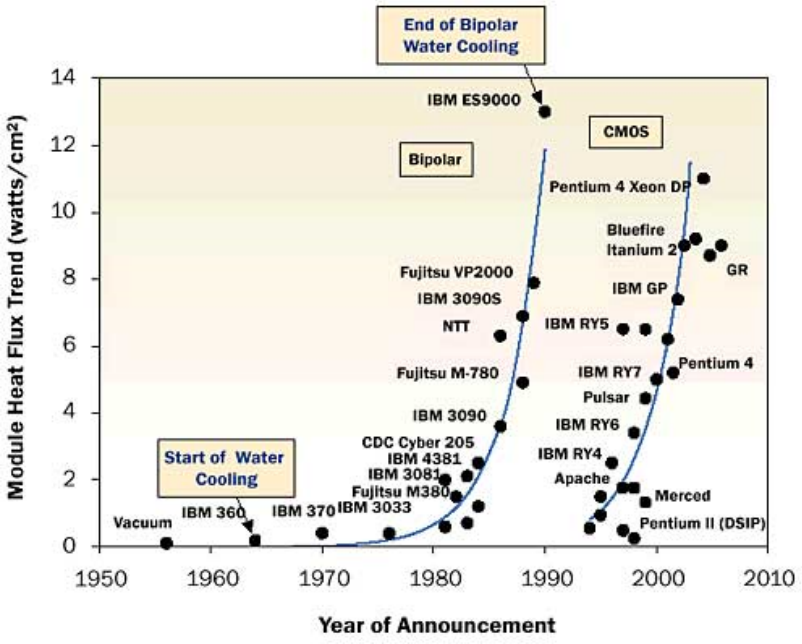


FIGURE 2: Dissipation heat flux on commercial computer CPUs over the years.

The rapid advancements of silicon microfabrication techniques driven by the electronics industry have recently enabled a wide range of new applications outside the electronics industry. The knowledge of basics microfabrication techniques is fundamental for a full comprehension of the technical choices adopted in the design and the fabrication of the

prototypes developed in this work. Chapter 2 features the description of fundamental microfabrication techniques for silicon processing. In chapter 3 the design, fabrication and assembly of a single silicon microchannel test section for flow boiling experiments is presented. The design of the device is optimize to provide reliable heat transfer data. Results of flow boiling heat transfer characteristics are presented and compared with correlations available in the literature. Another test section was then developed for addressing a major topic in two-phase fluid dynamics: the effects of channel wall roughness on two-phase flow and flow boiling heat transfer. The main results obtained are presented and discussed in this chapter. Following the great interested demonstrated by the electronics industry, silicon microchannel cooling was recently considered also for the thermal management of the on-detector electronics in silicon particle detectors for High Energy Physics (HEP) applications (Fig. 3). Silicon particle detectors for HEP application are composed by cylindrical layers of silicon microchips surrounding the interaction point of two colliding beams. By traversing these layers, particles leave electrical signals on the electronics and can thus be identified and localized. Since the main characteristics of HEP particle detectors are important for a full comprehension of the technical choices adopted in the design of the prototypes developed in this work, a brief introduction of the technology of particle detectors is presented in Chapter 4.

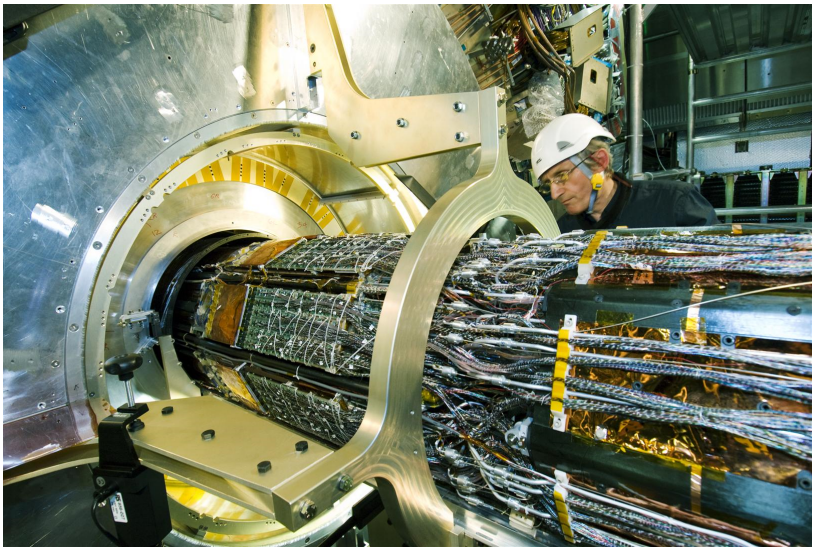

FIGURE 3: The ATLAS pixel detector during installation in the experimental hall.

The on-detector electronics generates thermal power by Joule effect: this power must be correctly remove to ensure a safe operation of the detector. Unlike the electronics for consumables, the electronics for particle detectors features lower dissipation heat fluxes, but because of the number of chips packed in the detector, can exhibit large power dissipation volume densities. In addition, the design of these systems must minimize the amount

of material included in order to reduce its interaction with the traversing particles. Silicon microchannel cooling represents an optimum solution in the design of future particle detectors for the thermal management for the on-detector electronics [3]. Silicon microfabrication techniques allow fabricating very precise components with optimized dimensions for an optimum integration into the detector layout. The development of an innovative design of silicon micro-evaporator for the thermal management of future vertex detector is presented in Chapter 5. Starting from the requirement set for the design of the system, the Chapter describes the finalization of the layout, the fabrication of the prototypes and the experimental characterization, providing hints for the optimization of the design for future developments.

# Chapter 1

# Two-phase flow and flow boiling characteristics in microchannels

Microscale flow boiling heat transfer has become in the last years a major research field for its many applications in the electronic industry. Agostini [4] compared different cooling technologies current under consideration for the thermal management of future high heat flux electronic components and concluded that flow boiling in silicon microchannels is the most promising approach for keeping the Moore' law trend in the VLSI industry. Taking advantage of the latent heat of vaporization allows for a minimization of the mass flow rate and the refrigerant charge, in favour of a greener operation. The high heat transfer rate achievable during flow boiling in microchannels promotes the removal of the power minimizing the temperature difference between the sensor and the heat sink and reducing surface temperature gradients. Silicon microfabrication technologies allow the design of miniaturized components favoring their integration into the final device. Two-phase fluid dynamics and heat transfer characteristics at the microscale are significantly different from macroscale and research in this area is still open. Many phenomena are still under investigation and a complete understanding of the processes is far. For this reason, design of microscale heat exchangers requires careful modelling and extensive testing before the device is ready for use. In the following sections, the most important results achieved in the last years in two-phase flows research are reviewed.

## 1.1 Two-phase macro-to-microscale transition

Unlike single-phase flow, where many investigations demonstrated that there is not a real macro-to microscale transition, but several scaling effects have to be taken into consideration for a detailed description of the flow at reduced characteristics lengths [5], in two-phase flow and flow boiling heat transfer there exist a transition between macro and microscale flows. This transition is confirmed by several experimental evidences [6]:

**Flow patterns:** due to the increasing importance of surface tension forces and the reducing importance of gravity effects at low characteristics scales, stratified-wavy and fully stratified regimes tend to disappear in microchannels. In general, flow pattern maps developed for standard channels work poorly when applied to microscale flow, as reported by many investigators.

**Heat Transfer:** many researchers report contradictory trends of flow boiling heat transfer coefficients versus vapor quality [7], but in general the data suggest an increase of the heat transfer coefficient with decreasing channel's size. This is another experimental evidence of macro-to-microscale transition in two-phase flows.

**Critical Heat Flux:** CHF data for microchannels show poor agreement with macroscale predictive correlations, like the widely quoted Katto-Ohno correlation [8]. Several studies proposed new correlation that better interpret the experimental data, e.g. Qu and Mudawar [9] or Ong and Thome [10].

**Void fraction:** another evidence of micro-to-microscale transition phenomena is the deviation of void fraction data from the homogeneous void fraction low reported in different studies. This deviation became more and more evident at decreasing diameters.

Pressure drop: microscale two-phase pressure drop data are much dispersed and also predictive correlations show contradictory trends. However, analysis of a vast multi-laboratory database by Ribatski, Wojtan and Thome [11] show that several quoted macroscale methods work as well as some newly developed microscale correlations. According to the authors, so far there is no evidence of macro-to- microscale transition in two-phase pressure drop.

## 1.2 Microscale two-phase pressure drop

Accurate modelling of two-phase pressure drops in microscale flow design is of fundamental importance to predict and guarantee the performance of microscale fluid systems. Precise pressure drop prediction is also very important when measuring flow boiling heat transfer coefficients in microchannels, where the local saturation temperature is often obtained from the local pressure via pressure drop correlations. The total pressure drop of a fluid under motion is sum of three different components: static pressure drop (due to variation of potential energy), momentum pressure drop (due to variation of kinetic energy) and frictional pressure drop (due to energy loss by friction) [6]:

$$\left(\frac{dp}{dz}\right)_{tot} = \left(\frac{dp}{dz}\right)_{s} + \left(\frac{dp}{dz}\right)_{m} + \left(\frac{dp}{dz}\right)_{f} \tag{1.1}$$

For the model of pressure gradients in macro-scale and micro-scale liquid-gas two-phase flows, two different approaches are possible: in the homogeneous model the two-phase mixture is assumed to behave as a single-phase fluid with pseudo-properties that are weighted relative to the liquid and gas flow fractions. In the separated flow model the phases are considered as fully segregated into two separated streams.

### 1.2.1 The homogenous model

In this model, the liquid-vapour two-phase mixture is considered as a single-phase fluid characterized by suitably averaged properties of liquid and gas. The static pressure drop for a homogeneous two-phase fluid is:

$$\left(\frac{dp}{dz}_{s}\right) = \rho_H g H \sin\theta \tag{1.2}$$

where $H$ is the vertical height, $\theta$ is the angle with respect to the horizontal and $\rho_H$ is the homogeneous density, defined as:

$$\rho_{TP} = \left(\frac{x}{\rho_G} + \frac{(1-x)}{\rho_L}\right)^{-1} \tag{1.3}$$

The momentum pressure drop can be calculated as:

$$\left(\frac{dp}{dz}_s\right) = G^2 \frac{\Delta x(\rho_L - \rho_G)}{\rho_L \rho_G} \tag{1.4}$$

The frictional pressure gradient is calculated as:

$$\left(\frac{dp}{dl}\right)_{TP} = \frac{2 f_{TP} G^2}{d_h \rho_H} \tag{1.5}$$

where the two-phase friction factor $f_{TP}$ is calculated with the proper macroscale single-phase correlation according to the actual regime defined by the two-phase Reynolds number:

$$Re_{TP} = \frac{G d_h}{\mu_{TP}} \tag{1.6}$$

Several correlations exist for the homogeneous viscosity $\mu_{TP}$ and the most used are reported below:

$$\text{Owens [12]: } \mu_{TP} = \mu_L \tag{1.7}$$

$$\text{McAdams et al. [13]: } \mu_{TP} = \left(\frac{x}{\mu_G} + \frac{(1-x)}{\mu_L}\right)^{-1} \tag{1.8}$$

$$\text{Cicchitti et al. [14]: } \mu_{TP} = x\mu_G + (1-x)\mu_L \tag{1.9}$$

$$\text{Dukler et al. [15]: } \mu_{TP} = \rho_{TP}\left[x\frac{\mu_G}{\rho_G} + (1-x)\left(\frac{\mu_L}{\rho_L}\right)\right] \tag{1.10}$$

$$\text{Beattie and Whalley [16]: } \mu_{TP} = \mu_L - 2.5\left[\frac{x\rho_L}{\rho_L - (1-x)\rho_G}\right] + \left[\frac{x\rho_L(1.5\mu_L + \mu_G)}{x\rho_L + (1-x)\rho_G}\right] \tag{1.11}$$

$$\text{Awad and Muzychka [17]: } \mu_{TP} = \mu_G \frac{2\mu_G + \mu_L - 2(\mu_G - \mu_L)(1-x)}{2\mu_G + \mu_L + (\mu_G - \mu_L)(1-x)} \tag{1.12}$$

$$\text{Lin et al. [18]: } \mu_{TP} = \frac{\mu_L \mu_G}{\mu_G + x^{1.4}(\mu_L - \mu_G)} \tag{1.13}$$

$$\text{Akers [19]: } \mu_{TP} = \frac{\mu_L}{\left[(1-x) + x\left(\frac{\rho_G}{\rho_L}\right)^{0.5}\right]} \tag{1.14}$$

### 1.2.2 Separated flow models

In the separated flow model, each phase displays different properties and it is assumed to flow at different velocities. The static pressure drop is calculated as:

$$\left(\frac{dp}{dz}_s\right) = \rho_{tp} g H \sin\theta \tag{1.15}$$

where the two-phasedensity is function of the two-phase void fraction and can be calculated as:

$$\rho_{tp} = \rho_L(1-\epsilon) + \rho_G \epsilon \tag{1.16}$$

The frictional pressure gradient in two-phase flows is usually predicted using separated flow models. In this model the two phases are assumed to travel separately at different velocities. This method, first introduced by Lockhart and Martinelli in 1949, has been continuously developed and improved since that time and it served as basis for many recent correlations also for microscale flows. Several correlations are available for the prediction of the two-phase void fraction; one of the most used is the Steiner [20] version of the drift flux model of Rouhani and Axelsson[21]:

$$\varepsilon = \frac{x}{\rho_G}\left[(1+0.12(1-x))\left(\frac{x}{\rho_G} - \frac{1-x}{\rho_L}\right) + \frac{1.18(1-x[g\sigma(\rho_L-\rho_G)]^{0.25})}{G_{total}^2 \rho_L^{0.5}}\right]^{-1} \tag{1.17}$$

The momentum pressure drop represents the change in kinetic energy of the flow and for the separated flow model can be calculated with the following equation:

$$\Delta p_{mom} = G_{total}^2 \left\{\left[\frac{(1-x)^2}{\rho_L(1-\varepsilon)} + \frac{x^2}{\rho_G \varepsilon}\right]_{out} - \left[\frac{(1-x)^2}{\rho_L(1-\varepsilon)} + \frac{x^2}{\rho_G \varepsilon}\right]_{in}\right\} \tag{1.18}$$

For the frictional pressure drop, several correlations are available but a comprehensive theory is still far. Below some of the most common correlations are reviewed starting from macroscale studies and concluding with microscale correlations.

**Lockhart-Martinelli (1949) correlation**

One of the first correlations based on the separated flow model, was developed by Lockhart-Martinelli (1949) and provides the basis for many recent methods to correlate two-phase pressure drop data. This correlation predicts two-phase frictional pressure drop from single-phase (liquid or gas) by introducing a two-phase multiplier [22]. This multiplier depends on the ratio of the pressure gradients of the liquid and vapour phases (X), also called "Lockhart-Martinelli parameter" and defined as:

$$X = \left( \frac{\left(\frac{dp}{dz}\right)_L}{\left(\frac{dp}{dz}\right)_G} \right)^{0.5} \tag{1.19}$$

Where single-phase liquid and gas pressure gradients are calculated as:

$$\Delta_{frict} = \Phi^2_{Ltt} \Delta p_L \tag{1.20}$$

$$\Delta_{frict} = \Phi^2_{Gtt} \Delta p_G \tag{1.21}$$

Their results, originally presented in graphical form were later curve fit by Chisolm [23] in the form

$$\phi_l^2 = 1 + \frac{C}{X} + \frac{1}{X^2} \tag{1.22}$$

$$\phi_g^2 = 1 + CX + X^2 \tag{1.23}$$

where the value of C, often called Chisholm parameter, depends on the regimes of the liquid and vapour.

Baroczy [24] proposed a modification of the Lockhart-Martinelli correlation accounting also for the effect of mass flux and fluid properties on the two-phase multiplier. Also in this case the results, originally presented in graphical form, were later transformed in a correlation by Chisholm and Sutherland [25].

**Gronnerrud (1972)**

This method [26], developed specifically for refrigerants, proposed an alternative expression

for the two-phase multiplier as follows:

$$\left(\frac{dp}{dz}\right)_f = \Phi_{gd}\Delta p_L \tag{1.24}$$

where:

$$\Phi_{gd} = 1 + \left(\frac{dp}{dz}\right)_{Fr}\left[\frac{\left(\frac{\rho_l}{\rho_G}\right)}{\left(\frac{\mu_L}{\mu_G}\right)^{0.25}} - 1\right] \tag{1.25}$$

where Eq. 1.25 is used for the liquid pressure gradient. The frictional pressure gradient depends on the liquid Froude number as follow:

$$\left(\frac{dp}{dz}\right)_{Fr} = f_{Fr}\left[x + 4(x^{1.8} - x^{10}f_{Fr}^{0.5})\right] \tag{1.26}$$

with

$$f_{Fr} = 1 \quad \text{for } Fr_L \geq 1 \tag{1.27}$$

$$f_{Fr} = Fr_L^{0.3} + 0.0055\left(\ln\frac{1}{Fr_L}\right)^2 \quad \text{for } Fr_L > 1 \tag{1.28}$$

**Chisholm (1973)**

Chisholm [27] proposed an alternative formulation of the two-phase multiplier, which is:

$$\Phi_{Chis}^2 = 1 + (Y^2 - 1)\left[Bx^{(2-n)/2}(1-x)^{(2-n)/2} + x^{2-n}\right] \tag{1.29}$$

where n=0.25 and Y is the ratio of the single-phase frictional pressure gradients:

$$Y^2 = \frac{(dp/dz)_G}{(dp/dz)_L} \tag{1.30}$$

The B parameter is function of the Y value and the G value and a total of 6 combinations of these two parameters were provided by Chisolm, each one with a different definition of B.

**Friedel (1979)**

The correlation proposed by Friedel [28] is one of the most quoted predictive tools for two-phase frictional pressure drops. Like the Lockhart-Martinelli correlation it introduces a two-phase multiplier to be applied to the single-phase liquid pressure drop calculated with the Blasius equation.

$$\Delta p_{fricct} = \Delta p_L \Phi_{fr}^2 \tag{1.31}$$

The Friedel two-phase multiplier is defined as:

$$\Phi_{fr}^2 = E + \frac{3.24FH}{Fr_H^{0.045} We_L^{0.035}} \tag{1.32}$$

Where the dimensionless factors are defined as:

$$Fr_H = \frac{G_{tot}^2}{g d_i \rho_H^2} \tag{1.33}$$

$$E = (1-x)^2 + x^2 \frac{\rho_L f_G}{f_L \rho_G} \tag{1.34}$$

$$F = x^{0.78}(1-x)^{0.224} \tag{1.35}$$

$$H = \left(\frac{\rho_L}{\rho_G}\right)^{0.91} \left(\frac{\mu_G}{\mu_L}\right)^{0.19} \left(1 - \frac{\mu_G}{\mu_L}\right)^{0.7} \tag{1.36}$$

$$We_L = \frac{G_{tot}^2 d_i}{\sigma \rho_H} \tag{1.37}$$

The following alternative correlation for the homogeneous density is used:

$$\rho_H = \left(\frac{x}{\rho_G} + \frac{(1-x)}{\rho_L}\right)^{-1} \tag{1.38}$$

**Muller-Steinhagen-Heck (1986)**

The authors [29] proposed a new correlation for two-phase pressure drops developed using a database of 9300 points for a variety of fluids and conditions, with a large span in the channel diameter (from 4 to 392 mm). In the proposed correlation, the two-phase pressure gradient is expressed as:

$$\left(\frac{dp}{dz}\right)_f = G(1-x)^{1/3} + Bx^3 \tag{1.39}$$

with:

$$G = A + 2(B + A)x \tag{1.40}$$

where A and B are the pressure gradient for all liquid and all vapour flows calculated with the Poisuille equation for the laminar regime and Blasius equation for the turbulent. This method can be applied with vapor qualities from 0 to 1 but it is recommended only is the ratio of liquid and vapor viscosities is less than 1000.

**Lazarek-Black (1982)**

Lazarek and Black [30] performed frictional pressure drop measurements for R-113 saturated flow boiling in a round tube with internal diameter of 0.31 cm and heated lengths of 12.3 and 24.6 cm. In their experiments they were able to isolate and separately correlate the individual pressure drops due to friction, momentum and bends. When comparing the frictional pressure drop data with the Lockhart-Martinelli correlation, they noticed that the accuracy of the prediction is considerably increased using a value of 30 for the Chisholm's parameter C, instead of the recommended value 20.

Thus, their proposed correlation for two-phase frictional pressure drop data is:

$$C = 30$$

**Moriyama-Inoue-Ohira(1992)**

Moriyama et al. [31] investigated flow pattern, pressure drop, and heat transfer for R113 boiling two-phase flow in extremely narrow channels with a thickness of 35-110 $\mu m$ between horizontal parallel plates. They proposed an analytical model based on viscous flow and took into account the effect of the capillary number on the thickness of the liquid film. They expressed the two-phase frictional multiplier ($\Phi_L^2$) as a function of liquid phase Reynolds

number ($Re_L$) and Lockhart-Martinelli parameter ($X$). Their correlation was:

$$\Phi_L^2 = 1 + \frac{K_M}{X^2} \tag{1.41}$$

$$K_M = 0.9 Re_L^{0.3} \quad \text{for } Re_L > 1.3 \tag{1.42}$$

$$K_M = 1 \quad \text{for } Re_L \leq 1.3 \tag{1.43}$$

**Mishima-Hibiki (1996)**

Mishima and Hibik [32]i, after performing an extensive experimental study with air-water two-phase flow in capillary tubes with diameter ranging from 1 to 4 mm, they noticed that in their experiments the present value of Chisholm's parameter decreases with decreasing the tube diameter. Thus, they presented an updated correlation for the C parameter including the effect of the tube diameter $d_h$:

$$C = 21(1 - e^{0.319 d_h})$$

**Yan-Lin (1998)**

Based on their experimental data [33], the authors proposed an empirical correlation of the two-phase friction factor including the equivalent Reynolds number as previously proposed by Akers et al. [19]:

$$f_{TP} = \quad 0.11 Re_{eq}^{-0.1} \tag{1.44}$$

$$Re_{eq} = \frac{GD}{\mu_L}\left[(1-x) + x\left(\frac{\rho_L}{\rho_G}\right)^{0.5}\right] \tag{1.45}$$

**Lee-Lee (2001)**

Lee and Lee [34] performed adiabatic air-water two-phase tests in horizontal rectangular channels with small depth. In their studies the gap between the upper and the lower plates of each channel ranges from 0.4 to 4 mm while the channel width being fixed to 20 mm. They report variation of the frictional pressure gradient with the superficial velocities of the liquid and the gas flows.

Based on their results they developed a new correlation for the Chisholm parameter accounting for the effect of channel height, previously introduced by Mishima-Hibiki, and also the effect of the mass flux by introducing the dimensionless parameters $\lambda$, $\Psi$ and $Re_{Lo}$

$$C = A\lambda^q \Psi^r Re_{Lo}^s \tag{1.46}$$

where the constant A and exponents $q$, $r$ and $s$ may be determined through a data regression process and the dimensionless parameters $\lambda$ and $\Psi$ are defined as:

$$\lambda = \frac{\mu_L^2}{\rho_L \sigma d_h} \tag{1.47}$$

$$\Psi = \frac{\mu_L j}{\sigma} \tag{1.48}$$

**Tran et al. (2000)**

Tran and co-workers [35] performed two-phase pressure drop measurements with three refrigerants (R-134a, R-12 and R-113) at six different pressures and in different tubes. Resulting data couldn't be satisfactorily predicted using state-of-the-art macro-scale correlations. Thus, data were used to develop a new correlation based on Chisholm B-coefficient method, defined by:

$$\phi_{f_{LO}}^2 = 1 + (\Gamma^2 - 1)\left[Bx^{0.875}(1-x)^{0.875} + x^{1.75}\right] \tag{1.49}$$

In order to account for the effect of tube dimension and fluid surface tension, Tran et al. propose a new expression for the two-phase multiplier $\phi_{f_{LO}}^2$. In developing the new correlation, the definitions of $B$ and $\Gamma^2$ were modified to better reflect the physics of flow boiling in small tubes, in particular by including a scaling factor $C$ as a multiplier on $\Gamma^2$ and using the Confinement number $Co$ proposed by Kew and Cornwell [36] to replace $B$. The new proposed correlation is:

$$\phi_{f_{LO}}^2 = 1 + (C\Gamma^2 - 1)\left[Cox^{0.875}(1-x)^{0.875} + x^{1.75}\right] \tag{1.50}$$

**Zhang-Webb (2001)**

Zhang and Webb [37]performed single-phase and two-phase frictional pressure drop measurements with three refrigerants (R-134a, R-22 and R-404a) in small diameter tubes with hydraulic diameters ranging from 2.13 to 6.20 mm. Their single-phase pressure drop data are in well agreement with the Blasius equation showing a mean deviation less than 10%. On the contrary, the Friedel correlation over predicts most of the two-phase pressure drop data and the over prediction was shown to increase when reducing the hydraulic diameter and when increasing the saturation temperature. A new revised expression of the two-phase multiplier, based on the Friedel correlation, is then presented by the authors. In developing the new correlation, they decided not to simply adjust the coefficients and exponent of the Friedel correlation, but to consider different property groups. Thus, the reduced pressure p r was used to replace the non-dimensional groups of density and viscosity ratios in the associated terms in the Friedel correlation, and We and Fr terms were discarded from the expression. With these considerations and a regression analysis of their two-phase pressure drop data, the following equation was obtained:

$$\phi_{LO}^2 = (1-x)^2 + 2.87x^2 \left(\frac{P}{P_C}\right)^{-1} + 1.68x^{0.8}(1-x)^{0.25} \left(\frac{P}{P_C}\right)^{-1.64} \tag{1.51}$$

Comparison of the new proposed correlation with their experimental data shows that 85% of the data are within 20% and the mean deviation is 11.5%.

The proposed correlation has a mean deviation of 12.8% in predicting the frictional pressure two-phase drop data of data set presented in their study.

**Kawahara-Chung-Kawaji (2002)**

Two-phase pressure drop experimental data were obtained in this study [38] for a 100 $\mu$m diameter fused silica circular tube using a water/nitrogen mixture. Compared with the homogeneous model predictions using different viscosity models, the agreement with the data set is generally poor. Better predictions were achieved with a separated flow approach using the Lockhart-Martinelli correlation using a modified parameter

$$C = 0.24$$

Instead of $C = 5$ as suggested by the original correlation. Good agreement (within $\pm 10\%$) was also obtained using the Lee-Lee correlation.

**Yu et al. (2002)**

Experimental two-phase pressure drop tests were performed in a small horizontal tube of 2.898 mm inner diameter with water [39]. The two-phase frictional pressure gradient data were compared with the predictions of the Chisholm correlation and a consistent over prediction of the data was reported. After noticing that from the three terms in the Chisholm correlation, the $1/X^2$ term is dominant in their data set, the authors proposed a modification of the two-phase frictional multiplier better representing the experimental points:

$$\Phi_{Fl}^2 = X^{-1.9} \tag{1.52}$$

**Warrier-Dhir-Momoda (2002)**

In this study[40], experiments have been performed in small rectangular channel with $D_h = 0.75$ mm and FC-84 as test fluid. The test section consists of five parallel channels 307 mm long. Over the range of mass flux tested, the flow regimes of the liquid flowing alone and the vapour flowing alone are laminar and turbulent respectively. Therefore, for the particular flow conditions the Lockhart-Martinelli parameter is:

$$X = 18.65 \left(\frac{\rho_G}{\rho_L}\right)^{0.5} \left(\frac{1-x}{x}\right) \frac{Re_g^{0.1}}{Re_L^{0.5}} \tag{1.53}$$

For the prediction of the current data set, the Martinelli correlation was adopted but, differently from the original formulation, the C parameter was taken to be 38, irrespective of the liquid and vapour flow regimes:

$$C = 38$$

**Qu-Mudawar (2003)**

Based on their experiments of two-phase pressure drop in a water-cooled micro-channel heat sink, the authors [41] proposed a new version of the C parameter of the Lockhart-Martinelli

correlation incorporating the effect of both channel size (after Mishima-Hibiki's study) and the mass velocity.

The new expression of the C parameter is:

$$C = 21\left[1 - e^{-0.319 d_h}\right](0.00418G + 0.0613) \tag{1.54}$$

**Lee-Mudawar (2005)**

Using a mechanistic approach to address fluid dynamics of two-phase flow, the authors [42] assume that the two-phase fluid flow is the net result of interaction between liquid inertia, liquid viscous force and surface tension. The effect of these forces is taken into account adopting two dimensionless numbers as the Reynolds and Weber numbers based on the liquid properties:

$$Re_{LO} = \frac{G d_h}{\mu_L} \qquad We_{LO} = \frac{u_L G^2 d_h}{\sigma} \tag{1.55}$$

The C parameter in the two-phase pressure drop multiplier is modified as follows:

$$C = c_1 Re_{LO}^{c_2} We_{LO}^{c_3} \tag{1.56}$$

where the constants c1, c2 and c3 depend on the flow condition. The following two correlations were then derived based on the flow states of liquid and vapour:

$$C_{vv} = 2.16 Re_{LO}^{0.047} We_{LO}^{0.6} \qquad \text{(laminar liquid-laminar vapour)} \tag{1.57}$$

$$C_{vt} = 1.45 Re_{LO}^{0.25} We_{LO}^{0.23} \qquad \text{(laminar liquid-turbulent vapour)} \tag{1.58}$$

**Hwang-Kim (2006)**

From their tests on pressure drop characteristics in Microscale using R-134a as a test fluid, the authors [43] report increase of the two-phase pressure drop with increasing quality, increasing mass flux and decreasing tube diameter. Existing correlations failed to accurately predict the data set, so a new correlation was developed in the form of the Lockhart-Martinelli correlation where they try to include all the parameters related to the two-phase

flow. The surface tension effect is included through the confinement number, which was first defined by Kew and Cornwell. From their data points they also observed variation of the C-coefficient with respect to the variation of the liquid only Reynolds number and the Martinelli parameter: these two parameters are therefore included in the proposed correlation.

$$C = C_0 Re_{LO}^{C_1} X^{C_2} N_{conf}^{C_3} \tag{1.59}$$

where the constants $C_0$, $C_1$ ,$C_2$ and $C_3$ were obtained applying the least square method to their experimental data.

**Sun-Mishima (2009)**

In this study [44] the authors collected a large database of 2092 points of two-phase pressure drops from 18 previous works with several working fluids (R123, R134a, R22, R236ea, R245fa, R404a, R407C, R410a, R507, Co2, water and air), hydraulics diameter ranging from 0.506 to 12 mm and $Re_L$ from 10 to 37000 and $Re_G$ from 3 to 400000. From the analysis of the database they observed that in the laminar flow region ($Re_L < 2000$ and $Re_G < 2000$) the Chisholm parameter is significantly affected not only by the Laplace number (as previously observed by Zhang, by also by $Re_L$. For this reason the proposed the following correlation for the laminar region:

$$C = 26\left(1 + \frac{Re_L}{1000}\right)\left[1 - \exp\left(\frac{-0.153}{0.27La + 0.8}\right)\right] \tag{1.60}$$

They also observed the $C$ parameter changing with Re and $C/X$ strongly depending on ($Re_G/Re_L$ ) in the turbulent region ($Re_L$ or $Re_G > 2000$) and so they proposed the following correlation:

$$\Phi_L^2 = 1 + \frac{C\left(\frac{Re_G}{Re_L}, \frac{1-x}{x}\right)}{X^n} + \frac{1}{X^2} \tag{1.61}$$

where n=1.19 and $C = 1.79(Re_G/Re_L)^{0.4}((1-x)/x)^{0.5}$.

**Zhang-Hibiki-Mishima (2010)**

In the attempt to modify the Mishima-Hibiki correlation for the C-parameter in the Lockhart-Martinelli correlation, the authors [45] make use of the Artificial Neural Network technique

in order to identify the dominant parameters to correlate the two-phase friction multiplier. It is found that in mini-channels the non-dimensional Laplace constant, defined as

$$Lo = \left[\frac{\sigma}{(\rho_l - \rho_G)}\right]^{0.5} / d_h \tag{1.62}$$

is a main parameter to correlate the Chisholm parameter as well as the distribution parameter. In this way they are also able to make dimensionless the $C$ parameter that in the Hibiki-Mishima correlation have a dimension. The proposed correlation expresses the Chisholm parameter as follow:

$$C = 21\left[1 - e^{-\left(\frac{0.358}{Lo}\right)}\right] \tag{1.63}$$

The applicable ranges of this correlation are the following: $0.014 \leq d_h \leq 6.25$ mm and $Re_L$ ¡=2000 and $Re_G$ ¡=2000. For liquid-gas two-phase flow the equation may work better if the constant of -0.358 is replaced with -0.674, while for liquid-vapor two-phase flow the constant of -0.142 is suggested. The new correlation was then tested with experimental data from 13 data sets and showed a slight improve of the Mishima-Hibiki correlation exhibiting a mean deviation of 12.7% instead of 12.9.

**Li-Wu (2010)**

Li and Wu [46] collected database of 769 data points covering 12 fluids and a wide range of operational conditions and channel dimensions and compared the data set against eleven existing correlations for macro and microscale two–phase flows. From the comparison it results that the Cicchitti et al. correlation is the best homogeneous model, while the Muller-Steinhagen-Heck is the best separated correlation. Trying to improve the prediction accuracy for two-phase pressure drop in Microscale, they select the Bond and the Reynolds number for the description of the fluid dynamics. They observed three different trends of the Chisolm parameter against the Bond number and developed a specific correlation for each of these trends. For $Bo \leq 1.5$ the flow is dominated by surface tension:

$$C = 11.9Bo^{0.45} \tag{1.64}$$

| **Liquid** | **Vapor (Gas)** | $C$ |
|---|---|---|
| Turbulent | Turbulent | $0.39Re_{fo}^{0.003}Su_{go}^{0.10}\left(\frac{\rho_l}{\rho_g}\right)^{0.35}$ |
| Turbulent | Laminar | $8.7\times10^{-4}Re_{fo}^{0.17}Su_{go}^{0.50}\left(\frac{\rho_l}{\rho_g}\right)^{0.14}$ |
| Laminar | Turbulent | $0.0015Re_{fo}^{0.59}Su_{go}^{0.19}\left(\frac{\rho_l}{\rho_g}\right)^{0.36}$ |
| Laminar | Laminar | $3.5\times10^{-5}Re_{fo}^{0.44}Su_{go}^{0.50}\left(\frac{\rho_l}{\rho_g}\right)^{0.48}$ |

TABLE 1.1: Values of the C parameter for different flow conditions.

For $1.5 < Bo \leq 11$ surface tension, inertia and viscous forces are all important

$$C = 109.4(BoRe_L^{0.5})^{-0.56} \tag{1.65}$$

For $Bo > 11$ the effect of surface tension becomes negligible and no simple correlation could be developed so Beattie and Whalley correlation is used. They also support the previously proposed macro-to-micro scale transition threshold as

$$BoRe_L^{0.5} = 200 \tag{1.66}$$

**Kim-Mudawar (2012)**

In the attempt of developing a universal predictive approach for two-phase frictional pressure gradients representing many different fluids with different thermophysical properties and very broad ranges of all geometrical and flow parameter of practical interest, a new database of 7115 frictional pressure gradient data points for both adiabatic and condensing microscale flows was collected. The proposed approach [47] utilizes the original formulation of Lockhart and Martinelli, where the $C$ parameter is modified with new dimensionless groups that account for small channel hydraulic diameter. The $C$ parameter depends on the flow condition of the liquid and vapour phase and the values it assumes are resumed in the table below Where the Suratman number is defined as:

$$Su = \frac{Re^2}{We} = \frac{\rho\sigma D_h}{\mu^2} \tag{1.67}$$

According to the authors, this new correlation provides excellent predictive capability against the entire collected database, with an overall MAE of 23.3% and fairly uniform accuracy over broad ranges of all relevant parameter.

**Lee-Garimella (2008)**

Two-phase pressure drop data with flow boiling of water in a silicon test section with different channels inner diameter were obtained in this study [48]. Experimental fata points were compared with previous correlations with poor agreement. With regression analysis techniques on the experimental data set, a new correlation for the C parameter in the Lockhart-Martinelli correlation is proposed:

$$C = 2566 \cdot G^{0.5466} D_h^{0.8819} (1 - e^{-0.319 D_h}) \tag{1.68}$$

This correlation is able to represent the influence of the mass flux and an improved representation of the channel size effect thank to the introduction of an additional correction term.

**Choi et al. (2009)**

Choi et al.[49] measured pressure drop during two-phase flow of propane in minichannels with inner diameter of 1.5 and 3 mm. Their results show that pressure drop is a function of mass flux, inner tube diameter, surface tension, density and viscosity. The data were correlated by a modified version of the Lockhart-Martinelli correlation, where the C parameter is formulated based on the two-phase Reynolds number and the two-phase Weber number as follows:

$$C = \left( \Phi_f^2 - 1 - \frac{1}{X^2} \right) X = 1732.953 Re_{tp}^{-0.323} We_{tp}^{-0.24} \tag{1.69}$$

**Cioncolini (2009)**

Cioncolini et al.[50] investigated the prediction of gas-liquid two-phase pressure drop gradients in the macro-to-microscale range focusing on the annular flow pattern. By comparing twenty-four empirical correlations against an experimental data set containing 3908 points for eight different gas-liquid combinations and 22 different tube diameters, they found that the correlations of Lombardi, Friedel and Baroczy-Chisholm give the best predictions on

macroscale data, while the correlations of Lombardi, Muller-Steinhagen-Heck and the homogeneous model with the Cicchitti viscosity give the best predictions of the microscale data set. Trying to better capture the physics of the annular two-phase flow, they performed dimensional analysis of the problem. It results that the Weber number of the droplet laden gas core is the main dimensionless parameter, since including intrinsically the effect of the gas core velocity, the entrained liquid fraction and the average liquid film thickness. It is defined as follows:

$$We_c = \frac{\rho_c \nu_c^2 d_c}{\sigma} \tag{1.70}$$

Based on this analysis, the proposed a new correlation of the two-phase Fanning friction factor based only on the core Weber number as follows:

$$f_{tp} = 0.172 We_c^{-0.372} \tag{1.71}$$

For the use of the correlation in microscale applications they suggested the following modified version, including the liquid film Reynolds number:

$$f_{tp-\mu} = 0.019 We_c^{0.372} Re_l^{0.318} \tag{1.72}$$

With

$$Re_l = (1-e)(1-x)\frac{Gd}{\mu_l} \tag{1.73}$$

The new correlation gives the best results when predicting macroscale two-phase pressure drops and good results are also obtained at the microscale.

**Cavallini (2009)**

In this paper [51], the authors present a modified version of the Friedel correlation for the prediction of two-phase pressure drops during condensation or adiabatic liquid gas flows in minichannels with different surface roughness. The model is expressed by the following

equations:

$$\left(\frac{dp}{dz}\right)_f = \Phi_{LO}^2 \left(\frac{dp}{dz}\right)_{f,LO} = \Phi_{LO}^2 2 f_{f,LO}^* \frac{G^2}{D_h \rho_L} \tag{1.74}$$

$$f_{LO}^* = 0.046 Re_{LO}^{-0.2} = 0.046 \left(\frac{G D_h}{\mu_L}\right)^{-0.2} \quad \text{for any } ReLO \tag{1.75}$$

$$\Phi_{LO}^2 = +3.595 F H (1-E)^W \tag{1.76}$$

$$W = 1.398 p_R \tag{1.77}$$

$$Z = (1-x)^2 + x^2 \frac{\rho_L}{\rho_G} \left(\frac{\mu_G}{\mu_L}\right)^{0.2} \tag{1.78}$$

$$F = x^{0.9525}(1-x)^{0.414} H = \left(\frac{\rho_L}{\rho_G}\right)^{1.132} \left(\frac{\mu_G}{\mu_L}\right)^{0.44} \left(1 - \frac{\mu_G}{\mu_L}\right)^{3.542} \tag{1.79}$$

This model, developed for shear stress dominated flows (J¡2.5), could be extended to greater gas velocities and lower vapor qualities by modifying the liquid friction factor as follows:

$$\left(\frac{dp}{dz}\right)_{f,LO} = 2 f_{LO} \frac{G^2}{D_h \rho_L} \tag{1.80}$$

$$f_{LO} = 0.046 \left(\frac{G D_h}{\mu_L}\right)^{-0.2} \quad \text{for } Re_{LO} > 2000 \tag{1.81}$$

$$f_{LO} = \frac{C}{\left(\frac{G D_h}{\mu_L}\right)} \quad \text{for } Re_{LO} < 2000 \tag{1.82}$$

with C=16 for circular section and C=14.3 for square section. The model was further expanded to include the effect of surface roughness by modifying the liquid friction factor equation as shown below:

$$f_{LO}^* = 0.046 Re_{LO}^{-0.2} + 0.7 \frac{2Ra}{D_h} \quad \text{for } \frac{2Ra}{D_h} < 0.0027 \tag{1.83}$$

**Del Col (2013)**

Del Col et al. [52] performed adiabatic two-phase pressure drop tests with different fluids (R134a, R1234yf, R32, R245fa) inside circular, square and irregular shape channels with hydraulic diameters ranging from 0.96 mm to 2 mm and relative roughness ranging from 0.0017 to 0.003. The data set obtained was compared with the Cavallini et al. pressure drop model and revealed, beside a relatively low average deviation, a certain overestimation at

low liquid-only Reynolds number, while working well at high $\mathrm{Re}_{LO}$. This was explained by the authors by the fact that in the Cavallini correlation the effect of the tube internal surface roughness is independent on the flow characteristics, while one would expect the effect of surface roughness on the frictional pressure losses depending on fluid properties and mass flux, being smaller at lower mass velocities and higher liquid-phase viscosities, and thus lower liquid-only Reynold number $\mathrm{Re}_{LO}$ . This is clear in single-phase flow, where in the laminar region the friction factor is accurately described by the Hagen-Pouiseuille equation, which does not include surface roughness effects. In the turbulent region instead, Blasius equation for smooth tube tends to underestimate f, while the Colebrook and Churchill equations provide better predictions by computing the friction factors as a function of both Re and RR. In order to relate the pressure drop effect of the RR to the fluid operating condition, the authors propose a modification of the liquid only friction factor contained in the Cavallini equation as follows:

$$f_{LO} = 0.046(Re_{LO})^{-0.2} + 0.7RR \cdot X \tag{1.84}$$

where

$$X = \begin{cases} 0 & \text{if } Re_{LO} \leq Re^{+}_{LO} \\ 1 & \text{if } Re_{LO} \geq 3500 \\ 1 + \frac{A - 0.046 Re_{LO}^{-0.2}}{0.7RR} & \text{if } Re^{+}_{LO} < Re_{LO} < 3500 \end{cases} \tag{1.85}$$

and $A = 0.046(3500^{-0.2}) = 8.9938 \cdot 10^{-3}$. This new equation interpolates the equation for rough channels and the equation for smooth channels ($RR = 0$) introducing a transition between the two curves from $Re^{+}_{LO}$ and $Re_{LO} = 3500$.

$Re_{LO}$ is defined as the liquid only Reynolds number at which the smooth tube friction factor is equal to the one for rough tubes evaluated at $Re_{LO} = 3500$.

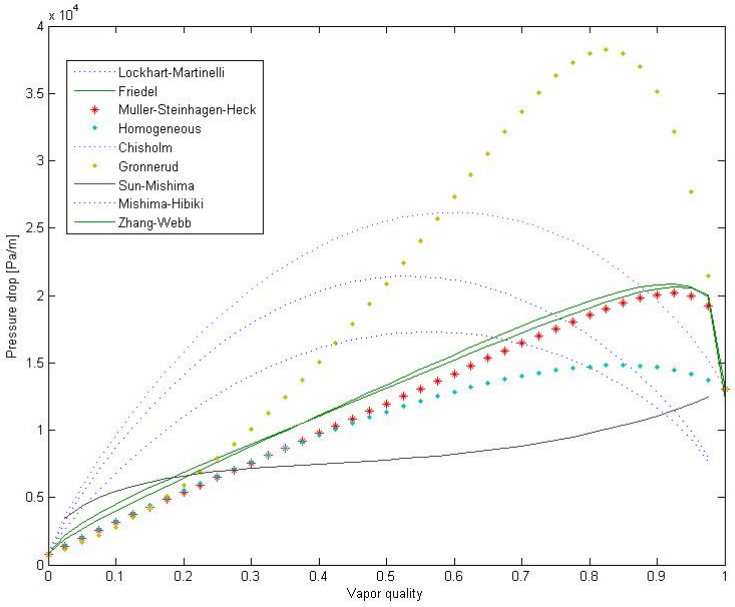


FIGURE 1.1: Comparison of different predictive methods for two-phase frictional pressure drop R134a Dh=4 mm G=500 $kgm^{-2}s^{-1}$ $T_{sat}$=30 C q=15000 $Wm^{-2}$.

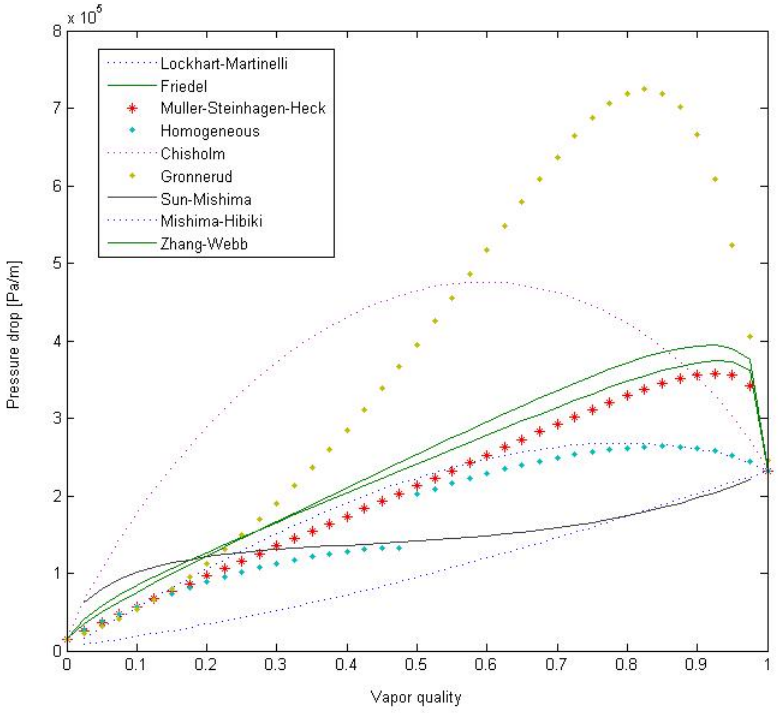


FIGURE 1.2: Comparison of different predictive methods for two-phase frictional pressure drop R134a Dh=0.4 mm G=500 $kgm^{-2}s^{-1}$ $T_{sat}$=30 C q=15000 $Wm^{-2}$.

## 1.3 Flow boiling heat transfer

In a growing number of applications, silicon microchannels are developed for thermal management and heat transfer applications. In these cases, the prediction of the heat transfer coefficient is very important. As will be shown in this paragraph, the knowledge of heat transfer mechanism during microscale flow boiling is still far from clear. As shown by Agostini et al. [53], trends reported in experimental data for flow boiling heat transfer coefficients are often in contrast with each other. This complicates the development of predictive cor8887relations, which are often obtained from the experimental data sets. In this section, the most widely quoted correlations for the prediction of flow boiling heat transfer are described and some of them are compared in the condition of interest for this study.

**Chen (1996)**

One of the first correlations for flow boiling heat transfer in convective flow is the one of Chen [54]: he assumed the local two-phase heat transfer coefficient h tp to be the sum of the nucleate boiling contribution $h_{nb}$ and the convective contribution $h_{cb}$, as originally suggested by Bergles-Rohsenow [55]:

$$h_{tp} = h_{nb} + h_{cb} \tag{1.86}$$

The nucleate pool boiling correlation of Forster-Zuber[56] is used for h nb while the Dittus-Boelter[57] correlation is used for the convective component $h_{cb}$. Chen also introduced a suppression factor S to the nucleate boiling component for accounting for the steeper temperature gradient near the tube wall under convection, condition that could partially suppress nucleation sites and thus reducing the nucleate component.

$$S = \frac{1}{1 + 0.00000253 Re_{tp}^{1.17}} \quad Re_{tp} = Re_L F^{1.25} \tag{1.87}$$

On the other hand, an enhancement factor is included in the convective component for accounting for the increased convective heat transfer because by the vapour motion during

the evaporation process:

$$F = \left(\frac{1}{X_{tt}} + 0.213\right)^{0.736} \tag{1.88}$$

**Shah (1982)**

Shah [58] proposed that the boiling heat transfer coefficient h is the largest of that given by the following equations:

$$h_{tp} = 230 Bo_{LO}^{0.5} \tag{1.89}$$

$$h_{tp} = 1.8 \left[Co \left(0.38 Fr_{LO}^{-0.3}\right)^n\right]^{-0.8} h_{LO} \tag{1.90}$$

$$h_{tp} = F \exp\left\{2.7 \left[Co (0.38 Fr_{LO}^{-0.3})^n\right]^{-0.15}\right\} h_{LO} \tag{1.91}$$

$$h_{tp} = F \exp\left\{2.47 \left[Co (0.38 Fr_{LO}^{-0.3})^n\right]^{-0.1}\right\} h_{LO} \tag{1.92}$$

where $h_{LO}$ is calculated with the Gnielinski correlation and the parameter $F$ and $n$ are calculated as:

$$F = \begin{cases} 14.7 Bo^{0.5} & \text{if } Bo \geq 0.0011 \\ 15.4 Bo^{0.5} & \text{if } Bo < 0.0011 \end{cases} \tag{1.93}$$

$$n = \begin{cases} 0 & \text{if horizontal with } Fr_{LO} \geq 0.04 \text{ or vertical} \\ 1 & \text{if horizontal with } Fr_{LO} < 0.04 \end{cases} \tag{1.94}$$

**Gungor-Winterton (1986-7)**

A modified version of the Chen correlation was proposed by Gungor and Winterton [59] based on a large database of over 3600 data points from the literature for water, refrigerants (R-11, R-12, R-22, R-113, R-114) and ethylene glycol. By employing the additive concept previously adopted by Chen, they represented the flow boiling heat transfer coefficient as the sum of a nucleate boiling component and a convective term:

$$h_{tp} = h_{nb} + h_{cb} \tag{1.95}$$

The single-phase liquid heat transfer coefficient is calculated with the Dittus-Boelter correlation using the local liquid fraction of the flow $G(1-x)$, while differently from the Chen's

approach, the Cooper [60] correlation is used for the nucleate pool boiling heat transfer coefficient. The convection enhancement factor F is here not only dependent from the Martinelli parameter $X_{tt}$ but also from the heat flux via the Boiling number:

$$E = 1 + 24000Bo^{1.16} + 1.37\left(\frac{1}{X_{tt}}\right)^{0.86} \tag{1.96}$$

The boiling suppression factor S is slightly updated as:

$$S = \frac{1}{1 + 0.00000115E^2Re_l^{1.17}} \tag{1.97}$$

with $Re_l$ based on the liquid fraction $G(1-x)$. Gungor and Winterton [61] later presented a simplified version of their correlation based only on the convective boiling mechanism:

$$\alpha_{tp} = E\alpha_l \tag{1.98}$$

where the new two-phase convection multiplier E is:

$$E = 1 + 3000Bo^{0.86} + 1.12\left(\frac{x}{1-x}\right)^{0.75}\left(\frac{\rho_l}{\rho_g}\right)^{0.41} \tag{1.99}$$

The single-phase liquid heat transfer coefficient is again calculated using Dittus-Boelter correlation using the local liquid fraction of the flow $G(1-x)$.

**Kenning-Cooper (1989)**

The authors [62] performed saturated flow boiling experiments with water in vertical tubes. From the analysis of their data they concluded that saturated convective coefficient depends primarily on the local parameters in the annular flow. For the prediction of the data they proposed a new correlation based on the Chen equation, but with the main difference that here convective and nucleate boiling contributions are not additive. The equation is the following:

$$h_{tp} = (1 + 1.8X_{tt}^{-0.87})h_l \tag{1.100}$$

where $X_{tt}$ is the turbulent-turbulent Lockhart-Martinelli parameter and the single-phase liquid heat transfer coefficient is calculated with the Dittus-Boelter correlation:

$$h_l = 0.023 Re_l^{0.8} Pr_l^{0.4} \left( \frac{k_l}{D_h} \right) \tag{1.101}$$

**Kandlikar (1990)**

Based on a large data set of 5246 data points collected by the author from 24 different experimental investigations with ten fluids, Kandlikar [63] proposed an improved version of its previously developed correlation [64] using the additive mechanism adopted by Chen for accounting for the nucleate boiling and convection mechanism in two-phase convective flows using the convection number $Co$ for the convective term and the boiling number $Bo$ for the nucleation term in the following form:

$$\frac{h_{tp}}{h_L} = C_1 Co^{C_2} + C_3 Bo^{C_4} F_{fl} \tag{1.102}$$

where the single-phase liquid heat transfer coefficient is calculated with the Dittus-Boelter correlation. In a subsequent paper Kandlikar [65] recommended the use of the Petukhov-Popov [66] and the Gnielinski [67] correlations. The deficiency of the previous equations in predicting the pool boiling term is overcome by introducing a fluid dependent correction factor F fl obtained from a regression analysis based on the data set of each single fluid. The influence of stratification at low flow rates in horizontal tubes was taken into account by introducing the liquid all Froude number in the convective boiling terms as follows:

$$\frac{h_{tp}}{h_L} = C_1 Co^{C_2} (25 Fr_{lo})^{C_5} + C_3 Bo^{C_4} F_{fl} \tag{1.103}$$

The values of the constants $C_1 - C_5$ are obtained from a regression analysis on the available data set for the convective boiling region ($Co < 0.65$) and the nucleate boiling region ($Co > 0.65$). In conclusion, the correlation assumes the following form:

$$h_{tp} = \max \left( h_{tp,NBD}, h_{tp,CBD} \right) \tag{1.104}$$

here:

$$h_{tp,NBD} = 0.6683 Co^{-0.2}(1-x)^{0.8} f_2(Fr_{LO}) h_{LO} + 1058.0 Bo^{0.7}(1-x)^{0.8} F_{fl} h_{LO} \quad (1.105)$$

$$h_{tp,NBD} = 1.136 Co^{-0.9}(1-x)^{0.8} f_2(Fr_{LO}) h_{LO} + 667.2 Bo^{0.7}(1-x)^{0.8} F_{fl} h_{LO} \quad (1.106)$$

Ffl is a fluid dependent parameter accounting for nucleation characteristics of the liquid on a given surface. In a subsequent paper, Kandlikar [68] successfully extended this methodology to augmented tubes and compact evaporators. Kandlikar and Steinke[69][70] extended the correlation to laminar and transitional regimes using the right correlation for the all-liquid flow single-phase heat transfer coefficient reflecting the actual flow regime as follows: For

| | |
|---|---|
| $Re_{LO} \geq 3000$ | Gnielinski correlation |
| $1600 \leq Re_{LO} < 3000$ | Linear interpolation |
| $Re_{LO} < 1600$ | Laminar flow eqaution |

the application to small diameter tubes, the authors observed that decreasing the diameter, orientation effects start to become negligible and the Froude number effect is neglected in their correlation by setting $f_2(Fr_{LO}) = 1$.

**Liu-Winterton (1991)**

Liu and Winterton [71] proposed the following correlation:

$$h_{tp} = \left[(Sh_{nb})^2 + (Fh_L)^2\right]^{0.5} \quad (1.107)$$

where $h_L$is calculates with the Dittus-Boelter equation and h nb is calculated with the Cooper correlation. The S and F factors are calculated as:

$$F = \left[1 + xPr_L\left(\frac{\rho_L}{\rho_G - 1}\right)\right]^{0.35}, \quad S = \frac{1}{(1 + 0.055 F^{0.1} Re_L^{0.16})} \quad (1.108)$$

**Wattelet et al. (1994)**

The authors of this paper [72] proposed a correlation based on their own experimental data of R12, R134a and a mixture in a 7.04 mm tube. The proposed correlation is:

$$h_{tp} = \left[h_{nb}^{2.5} + (FR_L)^{2.5}\right]^{1/2.5} \quad (1.109)$$

where $h_L$ is calculates with the Dittus-Boelter equation and h nb is calculated with the Cooper correlation. The factors R and F are defined as:

$$R = \begin{cases} 1.32 Fr_L^{0.2} & \text{if } Fr_L < 0.25 \\ 1 & \text{if } Fr_L \geq 0.25 \end{cases} \qquad F = 1 + 1.925 X^{-0.83} \tag{1.110}$$

where X is the Lockhart-Martinelli parameter.

**Lazarek-Black (1982)**

Lazarek and Black [73] proposed one of the first correlations for flow boiling heat transfer in microscale channels, based on their database of saturated flow boiling of R113 in a 3.15 mm inner diameter tube.

$$h_{tp} = 30 Re_{LO}^{0.857} Bo^{0.714} \frac{\lambda_L}{D_h} \tag{1.111}$$

$$Re_L = \frac{G D_h}{\mu_L} \qquad Bo = \frac{q}{G h_{fg}} \tag{1.112}$$

**Kew-Cornwell (1992)**

Kew and Cornwell [74] proposed a modification of the Lazarek-Black equation in order to account an observed increase in the heat transfer coefficient with the vapour quality in larger tubes, by including the vapour quality x. Their equation is the following:

$$h_{tp} = 30 Re_{LO}^{0.857} Bo^{0.714} (1-x)^{-0.143} \frac{\lambda_L}{D_h} \tag{1.113}$$

**Tran et al. (1996)**

The authors of this study [75] performed boiling heat transfer measurements with R12 in a small circular channel (D h =2.46 mm) and a small rectangular channel (Dh=2.40 mm). The authors reported heat transfer coefficient measurements almost independent of vapour quality and mass flux with a strong heat flux dependence, concluding that the heat transfer mechanism is nucleate boiling dominated. Only at very low wall superheats (¡2.75 K) a convection-dominant region was detected, with a sharp and clear transition between the two regions. The authors correlated the data in the nucleation-dominated region with a

modified Stephan-Abdelsalam [76] equation as:

$$h = (8.4 \cdot 10^{-5})(Bo^2 We_L)^{0.3} \left(\frac{\rho_L}{\rho_G}\right)^{-0.4} \tag{1.114}$$

**Yan-Lin (1998)**

Based on their data of flow boiling heat transfer coefficient of R-134a in a 2mm diameter pipe, Yan and Lin [77] proposed the following equation based on the Kandlikar correlation:

$$h_{tp} = (C_1 Co^{C_2} + C_3 Bo^{C_4} Fr_{LO})(1-x)^{0.8} h_l \tag{1.115}$$

The empirical constants $C_1, C_2, C_3$ and C 4 are assumed to be function of the liquid only Reynolds number $Re_{LO}$ and reduced temperature TR. They are obtained through a best fitting approach based on this data set.

**Yu et al. (2002)**

Based on their water flow boiling tests in 2.98 mm diameter horizontal tube, Yu et al. [78] proposed an updated version of the correlation previously presented by Tran et al. as follows:

$$h_{tp} = 640000(Bo^2 We_L)^{0.27}(\rho_L/\rho_G)^{-0.2} \tag{1.116}$$

**Zhang-Hibiki-Mishima (2004)**

Based on the analysis of experimental investigations on flow boiling, Zhang et al. [79] proposed a new version of the Chen's correlation adapted for other conditions than liquid turbulent/ gas turbulent for which the correlation was originally developed. They assumed the nucleate boiling mechanism to be dominant in a microchannel and therefore they keep the Forster-Zuber correlation for predicting the nucleate boiling heat transfer coefficient $h_{nb}$ and they also assume the suppression factor S to be applicable in other conditions. For what concern the convective boiling term, the enhancement factor F (originally introduced for accounting for the increase in convective turbulence due to the presence of the vapour

phase) is related to the two-phase friction multiplier $\Phi^2_{f,tt}$

$$F = MAX(F', 1) \tag{1.117}$$

$$F' = 0.64\Phi_{f,tt} \qquad \Phi_{f,tt} = 1 + \frac{C}{X} + \frac{1}{X^2} \tag{1.118}$$

Where $X$ is the Martinelli parameter defined as $X = \left[ \left(\frac{dp}{dz}\right)_l / \left(\frac{dp}{dz}\right)_g \right]^{0.5} = \left(\frac{f_l}{f_g}\right)^{0.5} \left(\frac{1-x}{x}\right) \left(\frac{\rho_g}{\rho_l}\right)^{0.5}$ where the single-phase friction factor is calculated with the proper equation according to the fluid condition determined by the single-phase Reynolds number. For the single phase heat transfer coefficient, the Dittus-Boelter correlation (valid only in turbulent condition) is replaced by a set of equation in order to fit the actual flow condition). Two sets of correlations are selected in terms of flow orientation due to the difference in the effect of gravity.

**Wharrier-Dhir-Momoda (1998)**

Based on a limited data set of flow boiling tests of FC-84 inside 0.75mm ID channels, Warrier et al. [80] developed a new correlation only dependent on the Boiling number Bo and the vapour quality x:

$$\frac{h_{tp}}{h_{sp}} = 1 + 6.0Bo^{1/16} + f_2 x^{0.65} \tag{1.119}$$

$$f_2 = f(Bo) = -5.3[1 - 855Bo] \tag{1.120}$$

**Kandlikar-Balsubramanian (2004)**

The original correlation by Kandlikar on flow boiling heat transfer is here [81] extended to minichannels and microchannels by suitably taking into account the low Reynolds number encountered in these geometries. Thus, the actual liquid flow condition (laminar or turbulent) is considered when calculating the liquid all heat transfer coefficient. Since stratified flow is usually not observed at the microscale, the Froude number was removed by the correlation whilst the effect of the fluid/material combination is again considered through the coefficient $F_{sf}$. New correlations for predicting the nucleate boiling heat transfer coefficient

h nb and the convective boiling heat transfer coefficient $h_{cb}$ were presented as follows:

$$\frac{h_{nb}}{h_l} = 0.6683 \left[ \left( \frac{\rho_g}{\rho_l} \right)^{0.5} \left( \frac{1-x}{x} \right)^{0.8} \right]^{-0.2} (1-x)^{0.8} + 1058.0 Bo^{0.7} (1-x)^{0.8} F_{sf} \quad (1.121)$$

$$\frac{h_{cb}}{h_l} = 1.136 \left[ \left( \frac{\rho_g}{\rho_l} \right)^{0.5} \left( \frac{1-x}{x} \right)^{0.8} \right]^{-0.9} (1-x)^{0.8} + 667.2 Bo^{0.7} (1-x)^{0.8} F_{sf} \quad (1.122)$$

As in the previous version of the method, the larger of the two coefficients is selected as $h_{tp}$. For the calculation of the single-phase liquid heat transfer coefficient, first the liquid Reynolds number $Re_l$ is calculated. For $Re_l > 3000$ they recommend using either the Gnielinski (1976) correlation or the Petukhov (1970) correlation. For $Re_l < 1600$ they suggest using the appropriate laminar flow heat transfer correlation while for $1600 < Rel < 3000$ they propose using an interpolation between the previous cases. Finally, for deep laminar flows ($Re_l < 100$) they suggest using the nucleate boiling heat transfer coefficient as the value of $h_{tp}$.

**Saitoh-Daiguji-Hihara (2007)**

Saitoh and colleagues [82] proposed a Chen-type correlation including the effect of the tube diameter. This is expressed by the Weber number of the gas phase $We_g = G_g^2 D/\sigma\rho_g$ that is included in the enhancement factor F together with the Martinelli parameter $X$, and thus:

$$F = f(X, We_g) = 1 + \frac{\left(\frac{1}{X}\right)^l}{1 + We_g^m} \quad (1.123)$$

While the suppression factor S is still function of the two-phase Reynolds number Re tp defined as $Re_{tp} = Re_l F^{1.25}$:

$$S = \frac{1}{1 + a(Re_{tp} \cdot 10^{-4})^n} \quad (1.124)$$

The parameters a,l,m and n were determined with a regression analysis on experimental data and the resulting values are $a = 0.4$, $l = 1.05$, $m = -0.4$ and $n = 1.4$. For the prediction of the nucleate boiling heat transfer coefficient $h_{nb}$ the Stephan-Abdelsalam's correlation is selected:

$$h_{nb} = 207 \frac{k_l}{d_b} \left( \frac{q d_b}{k_l T_l} \right)^{0.75} \left( \frac{\rho_g}{\rho_l} \right)^{0.581} Pr_l^{0.533} \quad (1.125)$$

where db is the bubble departure diameter of nucleate boiling defined as

$$d_b = 0.51 \left[ \frac{2\sigma}{g(\rho_l - \rho_g)} \right]^{0.5} \tag{1.126}$$

**Sun-Mishima (2009)**

Sun and Mishima [83] proposed a new improved correlation that includes the liquid Reynolds number $Re_{lo}$ and the boiling number introduced by Lazarek-Black, and also the liquid Weber number and the liquid and gas density ratio following the work of Tran et al. and Yu et al. Using a regression method on a new database of 2505 data points for 11 fluids covering diameters from 0.21 to 6.05 mm, the following equation was obtained:

$$h_{tp} = \frac{6 Re_{LO}^{1.05} Bo^{0.54}}{We_l^{0.191} (\rho_l/\rho_g)^{0.12}} \frac{\lambda_l}{D_h} \tag{1.127}$$

**Bertsch-Groll-Garimella (2009)**

Starting from a database of 3899 data points from 14 experimental studies in the literature covering 12 different fluids and hydraulic diameters ranging from 0.16 to 2.92 mm, the authors [84] developed an improved semi-empirical correlation based on the formulation proposed by Chen characterized by the superposition approach. The flow boiling heat transfer coefficient is described as the sum of the nucleate boiling component and the convective boiling component with appropriate correction factors:

$$h_{tp} = S h_{nb} + F h_{cb} \tag{1.128}$$

For the nucleate heat boiling transfer coefficient the Cooper correlation, developed for pool boiling, was selected since it has been shown to provide good predictions of experimental heat transfer coefficients in microchannels:

$$h_{nb} = 55 P_r^{0.12 - 0.2 \log_{10} R_p} (-\log_{10} P_r)^{-0.55} M^{-0.5} (q'')^{0.67} \tag{1.129}$$

Where $P_r$ is the reduced pressure, M [kgkmol$^{-1}$ ] is the molecular mass of the fluid and $R_p4$ is the surface roughness (to be set equal to 1 if unknown). The convective heat transfer

coefficient is calculated as the average of the convective heat transfer coefficient for pure liquid and pure vapour, with a linear dependence on the vapour quality $x$:

$$h_{cb} = h_{cb,l}(1-x) + h_{cb,g}x \tag{1.130}$$

For the single-phase convective heat transfer, the Hausen correlation for developing laminar flows is chosen due to the low Reynolds number and the relatively short length usually encountered in microchannels:

$$h_{cb,k} = \left( 3.66 + \frac{0.0668 \frac{D_h}{L} Re_k Pr_k}{1 + 0.04 \left[ \frac{D_h}{L} Re_k Pr_k \right]^{\frac{2}{3}}} \right) \frac{k_k}{D_h} \qquad k = l, g \tag{1.131}$$

The suppression factor is assumed to be:

$$S = 1 - x \tag{1.132}$$

which is simple and still recovers physically correct values for extreme values of the vapour quality. The enhancement factor F, since influenced by the confinement of bubbles in small channels, includes the confinement number Co. It also must reduce to 1 for pure liquid and pure vapour, and be greater than 1 within the two-phase regime. The following formulation was therefore adopted:

$$F = 1 + f(Co, x) = 1 + ae^{-bCo}(x^2 - x^6) \tag{1.133}$$

where the value of the two parameters a and b, determined from the experimental database, are $a = 80$ and $b = 0.6$. The final equation is then:

$$h_{tp} = h_{nb}(1-x) + h_{cb}\left[1 + 80(x^2 - x^6)e^{-0.6Co}\right] \tag{1.134}$$

**Kaew-On-Wongwises (2009)**

Kaew-On and Wongwises [85] performed experimental tests on heat transfer coefficients of R-410a in a rectangular multiport minichannel with 3.48 hydraulic diameter. From the

analysis of the data, a new correlation is proposed in the form of the Lee-Lee correlation:

$$h_{tp} = Sh_{sp} \quad \text{with } h_{sp} = 0.023 Re_l^{0.8} Pr_l^{0.4} \frac{k_l}{D_h} \tag{1.135}$$

where S is a two-phase correction factor defined as:

$$S = 1.737 + 0.97(\beta\Phi_l)^{0.523} \tag{1.136}$$

where $\beta$ is the aspect ratio and $\Phi_l$ l is the two-phase multiplier based on the Lockhart-Martinelli parameter:

$$\Phi_l^2 = 1 + \frac{C}{X} + \frac{1}{X^2} \qquad X = \left[ \frac{\left(\frac{dp}{dz}\right)_l}{\left(\frac{dp}{dz}\right)_g} \right]^{0.5} \tag{1.137}$$

The parameter C is assumed to be function of the aspect ratio, friction factor and hydraulic diameter:

$$C = -3.356 + 41.863e^A + B \tag{1.138}$$

with

$$A = -69.475\beta f_l D_h \qquad B = 498\beta f_l D_h \tag{1.139}$$

where f l is the single-phase liquid friction factor proposed by Haaland [86]:

$$4f_l = \left[ \frac{1}{-1.8 \log\left[ \frac{6.9}{Re_l} + \left( \frac{\varepsilon/D_h}{3.7} \right) \right]^{1.11}} \right]^2 \qquad Re_l = \frac{GD_h(1-x)}{\mu_l} \tag{1.140}$$

**Kaew-On et al. (2011)**

In this study, the authors [87] investigated the flow boiling heat transfer characteristics of R134a in a multiport minichannel heat exchanger with a counter flow tube-in-tube design. They obtained average heat transfer coefficients over the entire length of the test section, which is 220 mm long. The experiments were performed at varying heat fluxes while the saturation pressure, mass flux, and inlet quality of each condition were kept constant. According to their boiling curves, the flow boiling regime is dominated by nucleate boiling, and

this is confirmed by the fact that heat transfer coefficients increase with increasing heat flux while are independent of mass flux. They present a new correlation based on the previous correlation proposed by Kaew-On and Wongwises (2009). This equation is based on the Boiling and the liquid Weber number as follows:

$$h_{tp} = SBo^{0.185} We_l^{0.0013} h_l \tag{1.141}$$

Where the liquid single-phase heat transfer coefficient is calculated with the Dittus-Boelter equation and the S factor is calculated as:

$$S = 1.737 + 0.97(\beta^{0.5}\Phi_l^2)^{0.523} \tag{1.142}$$

With the two-phase multiplier calculated as in the previous correlation.

**Jacobi-Thome (2002)**

Jacobi and Thome [88] proposed a new model for evaporation in the elongated-bubble regime in microchannels. This model, differently form most previous methods, assumes that evaporation of the thin film surrounding the vapor slug is the dominant heat transfer mechanism. The main block of this model is the pair composed by a vapor plug followed by a liquid slug. For this reason, the method is also called the "two-zones mode". When the liquid plug passes, it leaves a uniform liquid film of initial thickness $\delta_O$. When the vapor slug arrives, the liquid thickness reduces as the evaporation take place. The period of pair generation is obtained using the conduction-limited model of Plesset and Zwick [89] in a uniformly heated liquid and gives:

$$\tau = \left(\frac{R\rho_V \tau}{\rho_L c_{pL} \Delta T_{eff}}\right)^2 \frac{\pi}{12\alpha_L} \tag{1.143}$$

where $\Delta T_{eff}$ is the effective nucleation superheat. After pair formation, several properties such as void fraction $\varepsilon(t)$, velocity $U(t)$, and vapor quality $x(t)$ can be calculated using basic fluid dynamics concepts. The minimum film thickness is obtained at the trailing edge of the

vapor bubble. This can be modelled as:

$$\delta_{min} = \delta_O - \frac{q}{\lambda \rho_L} \frac{L_p(t)}{U(t)} \tag{1.144}$$

At this stage, averaging over the period and the length of the pair, the heat transfer coefficient is obtained from an average film thickness. Local heat transfer coefficient is:

$$h(s,t) = k_L \left( \delta_O - \frac{q L_p(t)}{4 \lambda \rho_L U(t)} \right)^{-1} \tag{1.145}$$

The local heat transfer coefficient can be determined as the flow equations are solved for local quality, void fraction and location. This requires a numerical solution of a nonlinear algebraic-differential-equation set. The model requires the knowledge of two parameters that are not easy to determine: the effective nucleation superheat $\Delta_{eff}$ and the initial film thickness $\delta_O$ . The authors suggest techniques for estimating these two parameters, but their efficacy is only qualitative. The model is able to capture the trends reported by some researchers, in particular Bao et al [90]. In particular, the model predicts the heat transfer coefficient to increase with heat flux; this effect is higher at higher heat fluxes. The model also predicts the heat transfer coefficient to be insensitive to mass flux and vapor quality.

**Thome-Dupont-Jacobi (2004)**

Thome-Dupont-Jacobi (2004) In this paper [91] the authors expand the previous two-zone model including a third dry-out zone at the trailing edge of the vapor slug when the liquid film thickness reduces to zero before a new liquid plug arrives. The heat transfer coefficient is thus obtained as a time-averaged local heat transfer coefficient during the cyclic passage of the three-zones. Like in the previous paper, first the bubble formation frequency is obtained assuming that the bubble grow according to the Zwick-Plesset model and detach when the bubble radius reaches the channel's radius. However, as remarked by the authors, in reality the bubble will be detached earlier by the shear exerted by the flow, thus reducing the generation frequency. For the initial film thickness the Moriyama-Inoue [92] correlation is adopted. The two correlations for the two conditions (viscous boundary layer controlled and surface tension controlled) are joined by an asymptotic method. The final correlation

is:

$$\frac{\delta_O}{d} = C_{\delta_O}\left(3\sqrt{\frac{\nu_L}{U_p d}}\right)^{0.84}\left[(0.07Bo^{0.41})^{-8} + 0.1^{-8}\right]^{1/8} \tag{1.146}$$

where $C_{\delta_O}$ is a correction factor to be determined from a best fit to experimental data and the Bond number is defined as:

$$Bo = \frac{\rho_L d}{\sigma} U_p^2 \tag{1.147}$$

The variation of the liquid film thickness is obtained assuming that all the energy entering the channel is used to vaporize the liquid. This allows the calculation of the maximum duration of the film at position $z$ as:

$$t_{dry-film} = \frac{\rho_L \Delta h_{LV}}{q}\left[\delta_O(z) - \delta_{min}\right] \tag{1.148}$$

If this time is smaller than the time for the arrival of the vapor slug, no dry-out will occur and the model reduces to two zones. Otherwise, dry-out will occur at the trailing edge of the vapor slug and the dry-out time can be calculated. At this stage, heat transfer coefficient in each zone is calculated and then the time-averaged heat transfer coefficient h is calculated in one period $\tau$. The local heat transfer coefficient in the evaporating film, assuming stagnant liquid film, is controlled by one-dimensional conduction across the film, thus modelled as:

$$h_{film}(z) = \frac{\lambda_L}{\delta_O - \delta_{end}} \ln\left(\frac{\delta_O}{\delta_{end}}\right) \tag{1.149}$$

For the liquid and vapor slugs, heat transfer coefficients are obtained from the respective local Nusselt number at the actual flow regime assuming hydrodynamically and thermally developing flow. For the laminar regime, the Shah-London equation is used while for the transition and turbulent regions the Gnielinski correlation is adopted. The local, time-averaged heat transfer coefficient at the location z is then defined as:

$$h(z) = \frac{t_L}{\tau} h_L(z) + \frac{t_{film}}{\tau} t_{film}(z) + \frac{t_{dry}}{\tau} h_\nu(z) \tag{1.150}$$

As pointed out before, the model has three adjustable parameters, which are difficult to predict: the minimum thickness of the liquid film at dryout $\delta$ min, the correction factor $C_{\delta O}$

and the bubble departure frequency $f$.

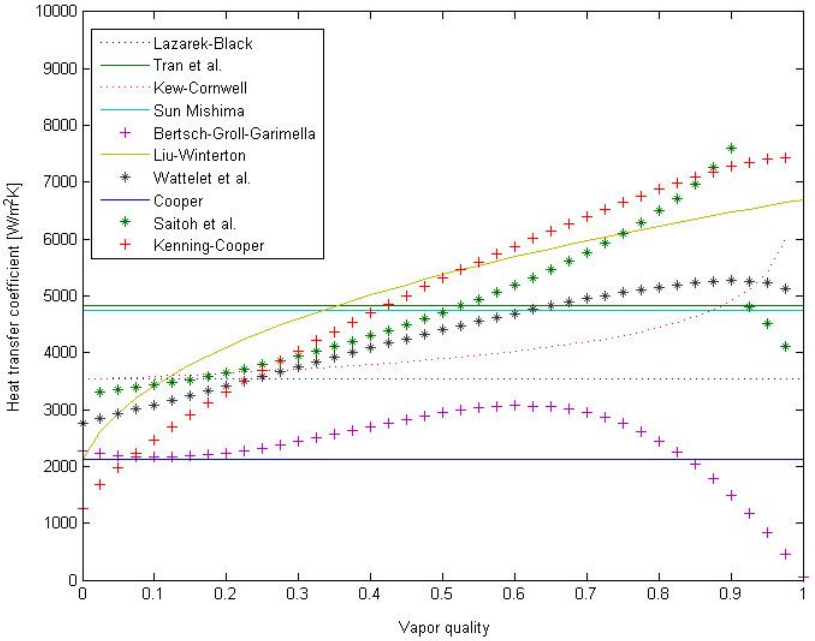


FIGURE 1.3: Comparison of different predictive methods for flow boiling heat transfer coefficient R134a Dh=4 mm Tsat=30 C q=15000 $Wm^{-2}$.

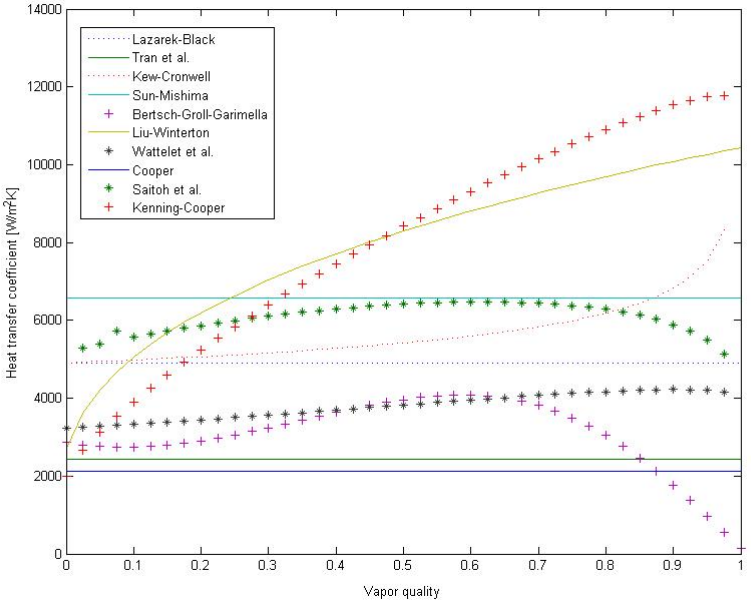


FIGURE 1.4: Comparison of different predictive methods for flow boiling heat transfer coefficient R134a Dh=0.4 mm G=500 kg/m2K q=15000 $Wm^{-2}$.

## 1.4 Onset of nucleate boiling

The Onset of Nucleate Boiling (ONB) represents the condition at which the channel wall temperature rises sufficiently above the local saturation temperature so that pre-existing vapor in wall sites can nucleate and grow. The flow abruptly moves from single phase to two-phase conditions with dramatic changes: pressure drop increases because of interfacial stresses between the two phases and heat transfer coefficient increases significantly because of the improved heat transfer mechanism. If heat flux is constant at the channel wall, the ONB marks a rapid decrease of the wall temperature. The prediction of the Onset of Nucleate Boiling (ONB) is of fundamental importance in the design of microscale evaporators for thermal management applications. Several studies have been performed in this field after the work of Hsu (1962) who first introduced a criterion for the prediction of ONB. It is now recognized that nucleation starts in nucleation sites, which are small cavities in the wall of the channel resulting from the roughness of the surface. This cavities trap vapor or gases and this heterogeneous phase in the liquid bulk is the starting point of the nucleation. If the temperature of the wall exceeds the saturation temperature, the bubble inside the cavity grows and appears at its mouth. The difference between the pressure inside the bubble and the pressure of the surrounding liquid is balanced by the surface tension forces. This can be expressed in terms of the Young-Laplace equation for a spherical bubble as:

$$p_V - p_L = \frac{2\sigma}{r_b} \tag{1.151}$$

**Hsu (1962)**

Hsu postulated that the bubble nucleus would grow only if the minimum temperature surrounding the bubble (the temperature at the tip of the bubble) is higher than the saturation temperature corresponding to the pressure inside the bubble; this is known as the minimum superheat criterion for boiling inception.

The temperature of the liquid bulk at the channel length z can be obtained with an energy balance assuming constant liquid properties, uniform heat flux and steady conditions:

$$T_{B,z} = T_{B,i} + (q'' p_z)/(\mathrm{m} c_p) \tag{1.152}$$

The wall temperature at the channel length z is related to the local bulk fluid temperature through the local heat transfer coefficient h z , that can be calculated with single-phase heat transfer correlations according to the local condition of the flow.

$$T_{W,z} = T_{B,z} + q''/h_z \tag{1.153}$$

The local temperature around the bubble is obtained assuming a linear temperature gradient in a layer of thickness $\delta_t$ from the temperature at the wall to the temperature in the bulk liquid. The thickness $\delta_t$ of the thermal layer can be obtained equating the heat transfer rates by conduction and single-phase convection:

$$h(T_W - T_B) = \frac{k_L}{\delta_t}(T_W - T_B) \tag{1.154}$$

$$\delta_t = k_L/h \tag{1.155}$$

At a given location $z$, the temperature in the liquid at the tip of the bubble $y_b$ is obtained from the assumption of the linear temperature gradient as:

$$T_{L,yb} = T_W - (y_b/\delta_t)(T_W - T_B) \tag{1.156}$$

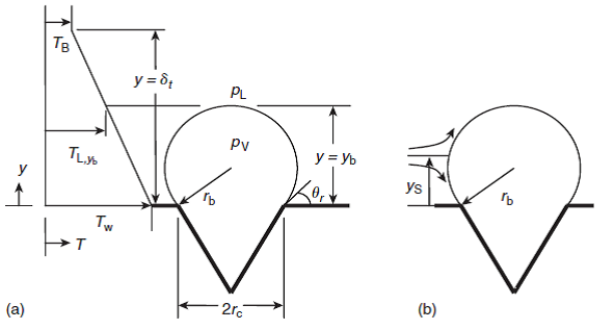


FIGURE 1.5: Geometrical characteristics of a growing bubble in a conical cavity.

where $T_{L,yb}$: liquid temperature at $y = y_b$, $T_B$ local temperature of the fluid and $T_W$: local wall temperature. Introducing the Clausius-Clapeyron equation ($dp/dT = h_{LV}/[T_{sat}(v_V - v_L)]$) to relate the pressure difference to the corresponding difference in saturation temperature, and neglecting the effect of interface curvature on the change in saturation temperature, the excess of temperature needed to sustain the vapor bubble can be written as

$$(p_V - p_L) = \frac{[T_{L,sat}(p_V) - T_{sat}]h_{LV}}{T_{sat}(v_V - v_L)} \tag{1.157}$$

where

- $T_{L,sat}(pV)$: saturation temperature in K corresponding to the pressure $p_V$;
- $T_{sat}$: saturation temperature in K corresponding to the system pressure pL;
- $h_{LV}$: latent heat of vaporization at $p_L$;
- $v_V$ and $v_L$: vapor and liquid specific volumes.

Combining Eqs. 1.151 and 1.157, and assuming $v_V >> v_L$, we get:

$$T_{L,sat}(p_V) = T_{sat} + \frac{2\sigma}{r_b}\frac{T_{sat}}{\rho_V h_{LV}} \tag{1.158}$$

which represents the minimum temperature required at any point on the liquid-vapor interface to sustain the vapor bubble. The condition for nucleation is therefore:

$$T_{L,y_b} \geq T_{L,sat}(p_V) \tag{1.159}$$

Combining Eqs. 1.156 and 1.158 yields the condition for nucleating cavities of specific radii:

$$(y_b/\delta_t)(T_W - T_B) - (T_W - T_{sat}) + \frac{2\sigma}{r_b}\frac{T_{sat}}{\rho_V h_{LV}} = 0 \tag{1.160}$$

The bubble radius rb and height yb are related to the cavity mouth radius through the receding contact angle $\theta_r$:

$$r_b = r_c/\sin\theta_r, \qquad y_b = r_b(1 + \cos\theta_r)/\sin\theta_r \tag{1.161}$$

Introducing these relations into Eq. 1.160, a quadratic equation is obtained which gives the range of nucleating cavities for a given wall superheat:

$$\{r_{c,min}, r_{c,max}\} = \frac{\delta_t(\sin\theta_r)}{2(1+\cos\theta_r)} \frac{\Delta T_W}{\Delta T_W + \Delta T_{sub}} \left[1 \mp \sqrt{1 - \frac{8\sigma T_{sat}(p_L)(\Delta T_W + \Delta T_{sub})}{\rho_V h_{LV} \delta_t (\Delta T_W)^2}}\right] \tag{1.162}$$

The wall heat flux at the incipience of nucleat boiling results to be:

$$q''_{ONB} = \frac{k_L h_{fg} \rho_G (T_W - T_{sat})^2}{12.8\sigma T_{sat}} \tag{1.163}$$

**Sato-Matsumura (1963)**

Sato and Matsumura (1963), independently from Hsu, developed a similar correlation but assumed a hemispherical bubble nucleus ($\theta = 90$) and obtained the following correlation:

$$q''_{ONB} = \frac{k_l h_{fg} \rho_G (T_W - T_{sat})^2}{8\sigma T_{sat}} \tag{1.164}$$

**Bergles-Rosenhow (1964)**

ergles and Rosenhow (1964) performed pool experiments with water on stainless steel and nickel surfaces with pressure ranging from 15 to 2000 psia. They proposed an empirical expression for the heat flux at ONB as function of the system pressure:

$$q''_{ONB} = 1082 p^{1.156} \left[1.8(T_W - T_{sat})\right]^{2.16/p^{0.0234}} \tag{1.165}$$

where $q''_{ONB}$ is in W/m$^2$, $p$ is in bar and Cis in °C.

**Jens-Lotte (1965)**

Jens and Lottes (1965) proposed the following empirical correlation for the determination of the heat flux at ONB:

$$q''_{ONB} = \left(\frac{T_W - T_{sat}}{25 \exp\left(-\frac{p}{62}\right)}\right)^4 \tag{1.166}$$

with $p$ in bar, $T$ in K and $q''$ in MW/m$^2$.

**Thom (1965)**

Thom (1965) later proposed a modified version of the Jens-Lotte correlation as:

$$q''_{ONB} = \left( \frac{T_W - T_{sat}}{22.65 \exp\left(-\frac{p}{87}\right)} \right)^2 \tag{1.167}$$

**Davis-Anderson (1966)**

Davis and Anderson (1966) extended the analytical analysis of Hsu by including the effect of the contact angle:

$$q''_{ONB} = \frac{k_L h_{fg} \rho_G (T_W - T_{sat})^2}{8(1 + \cos\theta)\sigma T_{sat}} \tag{1.168}$$

**Yin et al. (1963)**

Yin et al. (1993) proposed the following correlation:

$$q''_{ONB} = \frac{T_W - T_{sat}}{7.195 p^{1.82} \gamma^{-0.072}} \tag{1.169}$$

with $p$ in bar, $T$ in K and q in W/m$^2$.

**Kandlikar et al. (1997)**

Kandlikar et al. (1997) numerically solved the flow field around the bubble nucleus and identified a stagnation point at $1.1 r_b$ . Their proposed correlation is therefore:

$$q''_{ONB} = \frac{k_L h_{fg} \rho_G (T_W - T_{sat})^2}{8.8\sigma T_{sat}} \tag{1.170}$$

**Celata et al. (1997)**

Celata et al. (1997) performed experimental evaluation of the onset of nucleate boiling in water forced convective flow at high liquid velocity and subcooling. They proposed the following correlation for the heat flux at the onset of the nucleate boiling:

$$q''_{ONB} = 0.00195 (T_W - T_{sat})^2 \exp 0.023p \tag{1.171}$$

**Basu et al. (2002)**

Basu et al. (2002) performed subcooled flow boiling experiments on a flat copper plate and a nine-rod zircalloy-4 bundle. The data show that the heat flux and wall superheat at the ONB are dependent on the flow rate, liquid subcooling and contact angle. Based on their data, the authors proposed the following correlation:

$$q''_{ONB} = h_{sp}(T_W - T_{sat}) + h_{sp}(T_{sat} - T_f) \tag{1.172}$$

$$(T_W - T_{sat}) = \frac{4\sigma T_{sat}}{D_c h_{fg}\rho_V} \qquad D_c = F\left[\frac{8\sigma T_{sat}k_L}{h_{fg}\rho_V q''_W}\right]^{1/2} \tag{1.173}$$

$$F = 1 - \exp\left[\left(\frac{\pi\theta}{180}\right)^3 - 0.5\left(\frac{\pi\theta}{180}\right)\right] \tag{1.174}$$

**Ghiasiaan-Chedester (2002)**

Ghiaasiaan and Chedester (2002) proposed a semi-empirical method for the calculation of the heat flux at ONB in microtubes. This method is based on the hypothesis that in microchannels the thermocapillary force tends to suppress the microbubbles generating on wall cavities. Their expression is the following:

$$q''_{ONB} = \frac{k_L h_{fg}\rho_V (T_W - T_{sat})^2}{C\sigma T_{sat}} \tag{1.175}$$

$$C = 22\xi^{0.765} \qquad \xi = \frac{\sigma_f - \sigma_w}{\rho_f u_o R^*} \tag{1.176}$$

$$R^* = \left[\frac{2\sigma T_S k_L}{q''_{ONB}\rho_V h_{fg}}\right]^{1/2} \tag{1.177}$$

**Qu-Mudawar (2002)**

The authors performed experiments measuring ONB in a multiple microchannels heat sink using deionized water at different test conditions. From visual observation of the process they observed some differences with respect to macroscale results. Based on their experiments, they developed a new mechanistic model for the predition of ONB based on an iterative process. First the velocity field at the microchannel exit is determined from the analytical solution for fully developed laminar flow. Then the bubble departure radius rb

is calculated solving proposed correlations. The dimensionless temperature field $T$ is determined across the heat sink unit cell. At this point, a small value is assigned to $q''$ and the mean exit temperature Tout is determined from an energy balance. The liquid temperature field T is determined by substituting $q''$ and Tout in the dimensionless temperature field $T$ and the lowest temperature along the bubble interface is calculated for each active site long the microchannel. Then the value of heat flux $q''$ is increased by steps until a bubble satisfies the superheat criterion, with the lowest temperature along its interface just exceeding the saturation temperature.

**Liu-Lee-Garimella (2005)**

The authors experimentally investigated ONB in the flow of water thorough a microchannel heat sink by high–speed imaging under various flow conditions. Based on the experimental data an analytical model was developed to predict the heat flux and the bubble size at ONB. The model accounts for ONB heat flux dependence on fluid inlet velocity and subcooling, contaxt angle, microchannel dimensions and fluid exit pressure. The condition for the Onset of Nucleate Boiling is:

$$\sqrt{T_W} - \sqrt{T_S} \geq \sqrt{\frac{2\sigma C q''_W}{\rho_V h_{fg} k_L}} \tag{1.178}$$

where $C = 1 + \cos\theta$ is the form factor.

## 1.5 Microscale surface roughness effects

At the decrease of the channel diameter, wall roughness starts to have a significant impact on the fluid dynamics and heat transfer characteristics. For the effect of wall roughness on the friction factor Kandlikar [107] considered the effect of the cross-sectional area reduction due to the protruding roughness elements and introduced a constricted diameter defined as $D_{cf}$=D-2e for the calculation of the friction factor. Mala and Li [108] performed water flow tests in microtubes with diameters ranging from 50 to 254 $\mu$m, reporting significant deviations from classical theories at decreasing diameters and increasing Reynolds numbers. For accounting for these effects they proposed a modified viscosity model based on Merkle's work [109]. In this model, surface effects of the surface roughness on microscale laminar

flow are included in a roughness-viscosity function. The additional momentum transfer due to the surface roughness is included in a roughness-viscosity term $\mu_R$. This parameter is expected have a higher value near the wall and gradually diminish toward the centre of the channel and is also expected to be proportional to Re. Experimental data theories. Sabry [110] adopted a different approach assuming that the liquid flow is partially separated from the wall by a thin gas film trapped inside irregularities at the wall, thus modifying the friction factor, the critical Reynolds number and the Nusselt number. This model could explain the dependency of the friction factor and Nusselt number on the Reynolds number in the laminar regime observed by several researchers. Kuo and Kleinstreuer [111] proposed the modelling of the roughness region as an equivalent porous medium layer adjacent to the core fluid. This method is called Rough-Layer Model (RLM). The equivalent porous layer is characterized by a porosity a (or permeability k) and height h. Croce e D'Agaro [112] performed numerical studies of roughness effects on single-phase fluid flow. In their work, surface roughness is modelled through a set of randomly generated peaks with different shapes and distributions. They reported a significant increase in the Poiseuille number for all the configurations considered but a limited effect on the Nusselt number and highly dependent on the peak shape. In a subsequent work [113], Croce e D'Agaro compared their numerical results with the Modified Viscosity (MV) model developed by Mala and Li and the Porous Medium Layer (PML) model developed by Kuo and Kleinstreuer. According to their comparison, the PML approach is able to catch some details of the velocity profiles and the effect of the roughness height, while the MV model is too much dependent on the specific application for a good comparison. The authors further extended their investigations to three-dimensional roughness effects [114]. In this work, roughness is modelled as a set of three-dimensional conical peaks distributed on the ideal plain surface of the microchannel. The result shows that surface roughness significantly increase the Poiseuille number, while the effect on the Nusselt number is much smaller. This confirms their previous results with 2D numerical simulations. The authors proposed corrective terms based on the geometrical characteristics of the modelled roughness to account for the roughness effects on Poiseuille

and Nusselt number:

$$fRe = (fRe)_0(1 + 20\lambda\varepsilon \cdot \exp -\gamma) \tag{1.179}$$

$$Nu = (Nu)_0(1 + 20\lambda\varepsilon \cdot \exp -\gamma) \tag{1.180}$$

With a similar approach, Zhang et al. [115] modelled the rough surface with triangular, rectangular and semicircular roughness elements. They found that unlike smooth microchannels, Poiseuille number and Nusselt number are no longer constant with Reynolds number and are larger than the classical values. For what concern the peaks geometry, while the flow over semicircular and triangular elements induces strong recirculation and flow separation which increase the heat transfer and the pressure drop, the effect of rectangular elements is significantly weaker. Kosar and co-workers [116] performed water flow boiling experiments in microchannels with Dh=227 $\mu$m and 7.5 $\mu$m wide re-entrant cavities on the sidewalls over a wide range of heat fluxes and mass fluxes. They identified two distinct boiling regions, a nucleate boiling dominated region and a convective boiling dominated region depending on mass velocity and heat flux values. They proposed a method for predicting the transition between these two regions based on Re and Bo. The authors didn't attempt to draw quantitative conclusion on the performance of the re-entrant cavities because of lack of experimental data in the same test section without cavities. Pate et al. [117] performed flow boiling experiments in a silicon array of 19 microchannels containing six pyramidal shaped re-entrant cavities evenly spaced along the bottom wall of the channel to promote controlled nucleation activity. Each cavity has a 20 $\mu$m mouth size. The experimental results show a decreasing value of the temperature overshoot at ONB with increasing mass flux. The expected reduction of the heat flux at ONB provided by the cavities is much reduced by the use of a highly-wetting fluid (FC-72) which caused flooding of the cavities. Kuo et al. [118] investigated flow boiling characteristics of de-ionized water in 227 $\mu$m hydraulic diameter channels with re-entrant cavities. They measured active nucleation site density, bubble frequency and departure diameter and flow patterns at different operating conditions. They observed flow patterns similar to those encountered in macrochannels. Unlike large-scale channels, they observed that wall superheat temperatures do not seem to affect

the nucleation site density. The activation of nucleation site is much different compared to macrochannels: they attribute this deviation to the increasing bubble-departure-diameter to channel-hydraulic-diameter ratio in microchannels. Lu and Pan [119] studied the flow boiling of water in parallel diverging microchannels with mean Dh=120 $\mu$m with artificial nucleation sites. The artificial nucleation sites are laser-etched pits on the bottom wall with a mouth diameter around 20-22 $\mu$m. They investigated three different channels: one without cavities, one with cavities only on the downstream half of the channel and one with cavities distributed along the full channel. The results show that the heat transfer mechanism is dominated by convective boiling. The heat transfer coefficient increases with increasing mass flux. Heat transfer coefficient in the channel with artificial nucleation sites is higher than the smooth channel and it increases with the number of sites. This is also confirmed by flow visualization which reports a larger boiling activity in the channel with cavities for the full length. On the other side, two-phase pressure drop also increase with the number of artificial nucleation sites. Kandlikar et al. [120] studied the effect of fabricated nucleation sites in the flow boiling of water in microchannel of Dh=332 $\mu$m. Nucleation sites were created at regular intervals on the bottom surface of the channel by a laser engraving process. The sites have a mouth ranging from 5 to 30 $\mu$m and are spaced at a regular interval of 762 $\mu$m along the full channel. The results show that the addition of nucleation sites improves the thermal performance of the microchannels but cased also a significant increase in the flow instability with large pressure drop fluctuations and important backflow phenomena. For this reason, they suggest the use of inlet restrictors to improve the stability of the flow boiling process. Jones and Garimella [121] experimentally investigated the effect of the wall surface roughness on water flow boiling in microchannels using an array of ten microchannels produced by saw-cutting with nominal dimensions of 500x500 $\mu m^2$. Three different samples were tested: one with original roughness from the saw-cutting process (Ra=1.4 $\mu$m) and two channel with surface roughness increased by Electrical Discharge Machining (Ra=3.9 $\mu$m and Ra=6.7 $\mu$m). The experiments indicate that the surface roughness tested has negligible impact on the boiling incipience wall temperature and Critical Heat Flux. The effect of the surface roughness on the saturated boiling heat transfer start to be important at wall heat fluxes higher than 700 $kWm^{-2}$ and for q=1500 $kWm^{-2}$ an increase of 20

# Chapter 2

# Microfabrication technologies

Silicon microfabrication techniques have seen an incredible development in the last decades under the push of the electronics industry. The increase of computational power in consumable products is strictly connected with the development of innovative techniques for the improvement of Very large Scale Integrated systems. In recent years Micro-ElectroMechanical Systems (MEMS) have re-used, adapted or even extended microfabrication methods introducing in some cases new ways to fabricate at the micro and nano scale. The realization of the prototypes investigated in this project involves several microtechnology processes and different silicon microfabrication techniques. The fabrication of the devices has been performed at the class 100 clean room of the Centre for MicroNanotechnology at EPFL (École Polytechnique Fèdèrale de Lausanne). The knowledge of microtechnology and microfabrication process basics is required for a full understanding of some technical choices made in the design of the devices and the definition of the fabrication process flow. For this reason, in this chapter some basics of microtechnology are reported. A general description of standard microfabrication techniques is presented with more emphasis on the processes used in this work. The core part of this description is based on two reference books, "Fundamentals of microfabrication and nanotechnology" by M. Madou [93] and "Introduction to microfabrication" by S. Franssila [94].

## 2.1 Wafer preparation and cleaning

A very important step before any wafer processing is surface preparation and cleaning. Contaminants on the wafer surface include solvent stains, dust and smoke particles. They could affect the process in many ways, thus great care must be taken in order to ensure proper surface conditions. Several processes have been developed for removing wafer contaminants and the most used are presented here.

**RCA cleaning** The RCA cleaning is a process, developed by Kern in 1965 [95] while at RCA Corp., which consists of three main steps [96]: in the first step (RCA1) organic contaminants and particles are removed from the surface of the wafer in a base-peroxide mixture. This step produces a thin silicon dioxide layer (about 10 A) along with a metallic contamination to be removed in the subsequent steps. The second step (HF dip) is a short immersion in a 1:100 or 1:50 solution of HF + $H_2O$ at 25 °C for about fifteen seconds, in order to remove the thin native oxide layer and some fraction of ionic contaminants. It has to be performed with ultra-high purity materials to avoid recontamination of the highly reactive bare silicon surface. The last step (RCA2) removes the remaining traces of metallic (ionic) contaminants in a solution of 6 parts of deionized water, 1 part of aqueous HCl, 1 part of aqueous $H_2O_2$ at 75 or 80 °C, typically for 10 minutes. This step leaves a thin passivating layer on the wafer surface, which protects the surface from subsequent contamination.

**Piranha Recirculation Tank** Piranha is a trade name for a chemical mixture consisting of sulphuric acid ($H_2SO_4$) and hydrogen peroxide ($H_2O_2$) mixed in concentration ratios of around 4:1 $H_2SO_4$:$H_2O_2$. There are two main applications for piranha in wafer fabrication: 1) it is used to remove organic contaminants from thesurface of the wafer during cleaning sequences; and 2) it is used to strip photoresist from the surface of the wafer. Piranha tanks feature a filtered recirculation loop to ensure that fresh solution is continuously delivered to the wafer surface. This feature is especially important when removing photoresist films. Piranha solutions are typically operated at high temperatures of $120 - 140$ °C, necessitating the use of quartz tanks and precise temperature control. At these temperatures, the $H_2O_2$ decomposes very quickly, and *spiking* or injection of fresh $H_2O_2$ is usually performed.

**Ozone-water** The ozone-water method is a Piranha alternative. In this process, water of 25-90 °C (depending on the application) is sprayed onto the substrate as it is rotated. At the same time, dry ozone gas is injected into the reaction chamber. The ozone diffuses through the thin boundary layer of water to react with the organics on the substrate.

## 2.2 Photolithography

Photolithography is a microfabrication technique that allows transferring a pattern from a suitable mask to the substrate wafer. Photolithography for pattern transfer is a complex task and includes several process steps (Fig 2.1) that will be described in details in this section. Photolithography is the most expensive step in microelectronics technology, representing up to 35% of the wafer manufacturing cost, thus great care is reserved to the optimization of this process.

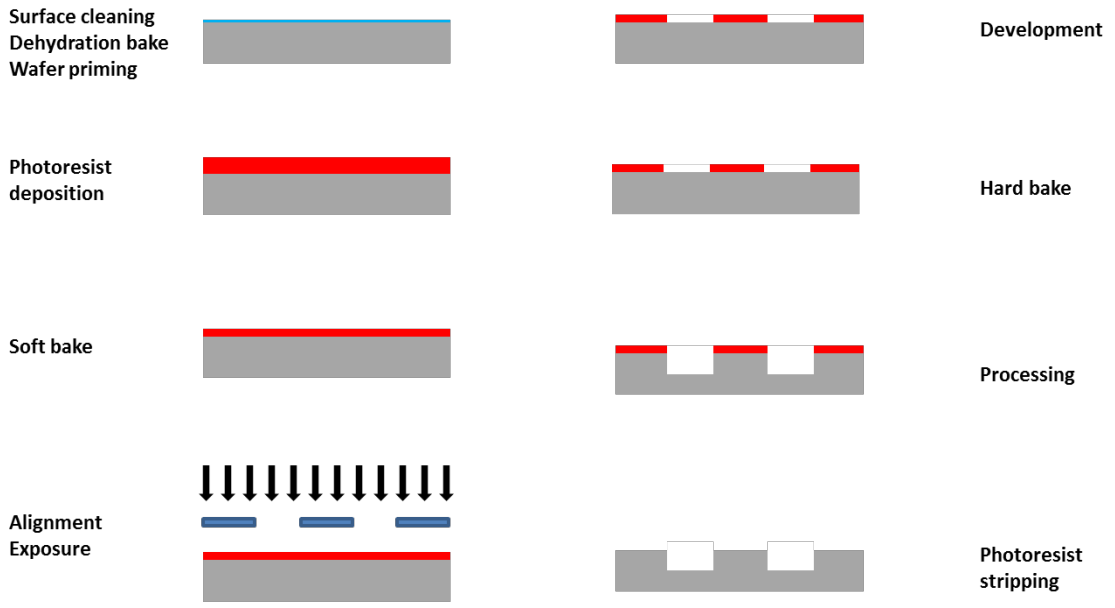


FIGURE 2.1: Typical process flow of a photolitographic step

Various lithographic techniques are available to transfer an image onto a silicon substrate. Amongst them, the most common are optical lithography, also called photolithography, which is the industry standard thanks to its high throughput, and electron beam lithography, mainly used for its high resolution capabilities [97]. Photolithography relies on the image

projection of patterns represented on a mask, generally a transparent quartz plate with opaque chromium features, into a photosensitive polymer film. The original image to be transferred, etched onto the photomask, is aligned to the photoresist-coated wafer, and exposed by UV radiation. Exposure changes photoresist solubility, which enables selective removal of resist in the subsequent development step. Photoresist is an organic polymer sensitive to UV radiation. Resists have three main components:

- Base resin, which determines the mechanical and thermal properties of the fluid;
- Photoactive compound (PAC), which determines sensitivity to radiation;
- Solvent, which controls viscosity, allowing precise deposition onto the substrate.

Two resist categories are available: positive tone resists, for which the exposed areas are dissolved in the developer, leading to resist patterns similar to the image of the mask, and negative tone resists, for which exposed areas become insoluble in the developer and give resist patterns that are the complementary image of the opaque chromium patterns on the mask. In positive photoresists the photochemical reaction during exposure weakens the polymer by rupture or scission of the polymer chains, and the exposed resist become more soluble in developing solutions. In a negative tone photoresist the chemical reaction strengthen the polymer by random cross-linkage of polymer chains, becoming less soluble to developers. The lithographic process starts with a surface preparation: first the surface is cleaned, with the processes described in the previous section since contaminants and particles on the wafer's surface could seriously compromise the photolithography output. Then, moisture is removed, since water on the wafer's surface can affect the resist deposition process. Moisture removal is performed by evaporation for 15 minutes at 80-90°C in a convection oven. The native $SiO_2$ on a Si wafer forms long-range hydrogen bonds with water adsorbed from the air: when resist is deposited on the substrate, it adheres to the water molecules rather than to the surface, resulting in poor adhesion. To avoid this problem, a substrate pre-treatment is performed in order to enhance the adhesion of the resist: Hexamethyl-disilazane vapour (HMDS, (H3C)3–Si–NH–Si–(CH3)3) is applied at reduced pressure to form a monomolecular layer on the wafer surface, making the wafer hydrophobic, which prevents moisture

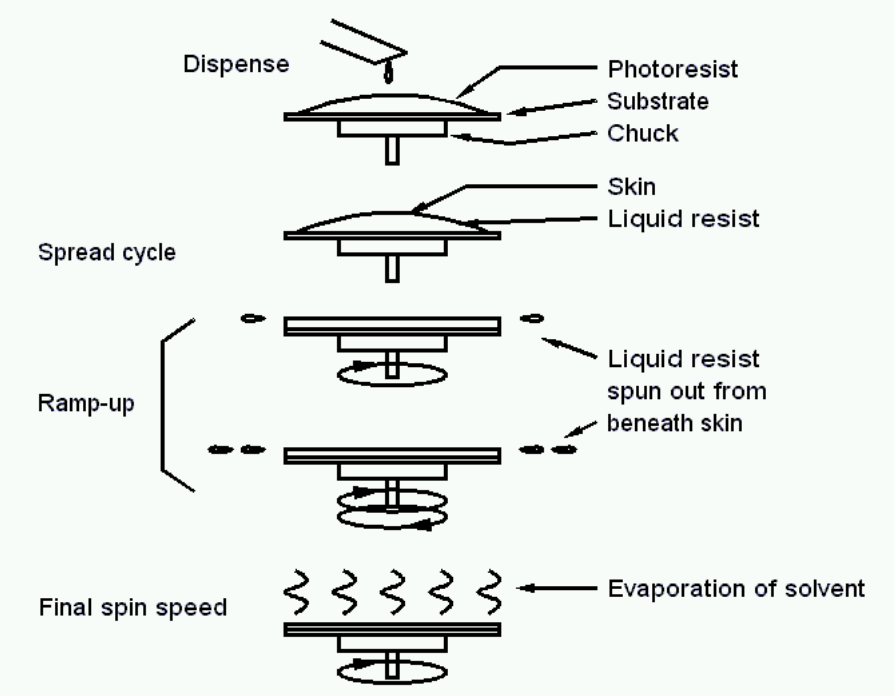


FIGURE 2.2: Spin-coating of photoresist over a wafer.

condensation. This is especially important for materials like metals, polysilicon and PSG, because resist adhesion to these materials is generally poor. Adhesion promotion is also a guarantee against cleanroom humidity variations and an equalizer for wafers with different storage times. At this stage, the resist is deposited on the substrate as thin film of some micrometres: thin resists are preferred for better resolution, but thinner resists are prone to particle defects, and pinhole density rapidly increases when resist thickness is limited. The most important resist deposition technique is spin-coating (Fig **??**). In this technique, the wafer is held on a spinner chuck by vacuum and a small amount of resist is deposed on the wafer slowly rotating (500 RPM), enabling the spread of the fluid over the substrate. After the dispense step the rotating velocity is increased with high acceleration up to relatively high velocities (1500-6000 RPM depending on the desired result) to thin the fluid to near its final thickness. At these speeds, centrifugal force causes the resist to flow to the edges, where it builds up until expelled when surface tension is exceeded. Final film thickness and other properties will depend on the nature of the fluid material (viscosity, drying rate, percent solids, surface tension, etc.) and the parameters chosen for the spin process. Factors such as final rotation speed, acceleration, and fume exhaust affect the properties

of the coated films. One of the most important factors in spin coating is repeatability, as subtle variations in the parameters that define a spin-coating process can result in drastic variations in the coated film[98]. Spin processing over severe topography is difficult: liquid-like film will fill grooves and crevasses, and a highly non-uniform resist thickness results. This is a problem for deep-etched MEMS structures. For this tasks, different coating techniques exists, like spray coating, meniscus coating, electrophoretic deposition, dip coating, extrusion coating etc. After coating, the resist still contains up to 15% solvent and may contain built-in stresses. To completely evaporate the solvent and release the stresses, the wafer undergoes a soft bake (or pre-exposure bake) at $90 - 100\,^{\circ}\mathrm{C}$ for about 20 minutes in a convection oven or at $75 - 85\,^{\circ}\mathrm{C}$ for 1-3 minutes with a vacuum hot plate. After this, the wafer is ready for the pattern transfer: this is done exposing the photosensitive resist to a UV light through a mask with the desired pattern to be transferred to the substrate. The mask is a quartz plate where the pattern in reported in a thin chromium film. The pattern is transfer ontothe mask by writing a photoresist layer with a high precision laser and then etching the exposed chromium in an etchant bath. During exposure to UV light, the solubility of the photoresist changes enabling selective removal of resist in the following development step. The incident light intensity ($\mathrm{W/cm^2}$) multiplied by the exposure time (in seconds) give the energy dose ($\mathrm{J/cm^2}$) received by the resist. The choice of the exposure wavelength depends on the light source in line with the critical dimensions to be achieved. Discharge mercury lamps have been used for years, choosing successively the g-line (436 nm) and i-line (365 nm) wavelengths. Then excimer laser have been selected as deep UV sources, i.e. KrF (248 nm) and ArF (193 nm) lasers, as they were much more powerful than mercury lamps. During the development phase, the unpolymerized exposed resist is selectively dissolved into the developer. Development by solvents can be based on at least three types of exposure-induced changes: variation in molecular weight of the polymer (by cross-linking or by chain scission), reactivity change and polarity change. Development can be performed by immersion and spray developers. During batch immersion development, wafers are batch-immersed for a timed period in a in a developer bath and agitated at a specific temperature while during batch spray development fan-type sprayers direct fresh developing solution across wafer surfaces. After development the wafer undergoes a mild

oxygen plasma treatment (so-called descumming) that removes unwanted resist traces left behind after development and a post-bake (or hard bake) that removes residual coating solvent and developer and anneals the film to promote interfacial adhesion of the resist that has been weakened either by developer penetration along the resist/substrate interface or by swelling of the resist. Hard baking also improves the hardness of the film and avoids solvent bursts during vacuum processing. At this point the patterned wafer is ready for process with additive and subtractive techniques: these techniques will be discussed in detail in the next sections. Once the wafer has been processed and the photolithography needs to be removed in order to continue with the fabrication steps, resist stripping is necessary, which is organic polymer etching. Two methods are available for resist stripping: wet and dry etching. In wet stripping, wafers are batch-immersed in a suitable liquid remover which chemically alters the resist so that it no longer adheres to the substrate. Besides commercial removers, available both for negative and positive tone resists, other strippers include Piranha, RCA clean, acetone, strong acids and more. Recently dry stripping techniques started to be preferred for resist stripping as they poses fewer disposal problems of toxicity, flammability and chemical contamination. Also, dry stripping is more performant with high removal rate and throughput. The most used dry stripping technique is oxygen plasma stripper, which converts the organic photoresist in a gaseous product that is pumped away. Other techniques include gaseous chemical reactants (e.g. ozone) and radiation (UV).
Other techniques include gaseous chemical reactants (e.g. ozone) and radiation (UV). Pho-

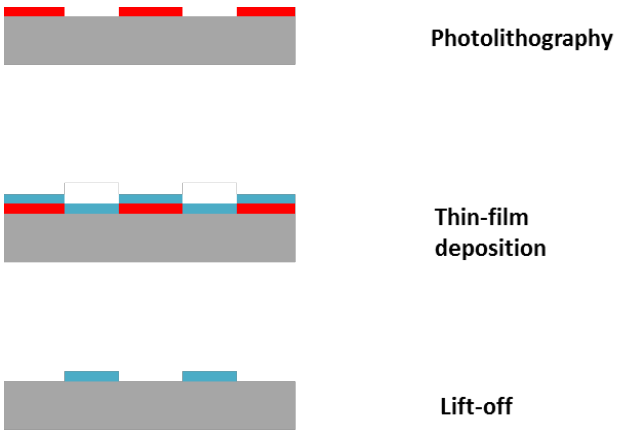


FIGURE 2.3: Basic lift-off process flow

tolithography technique is fundamental for another microfabrication process called lift-off.

This process is very useful for patterning catalytic metals such as Platinum that are not easily patterned with etching techniques. The basic process flow for lift-off is shown in Fig 2.3. First, a photolithography with the negative of the pattern to be transferred onto the substrate is performed. Then the thin-film layer is deposited with techniques which will be described in the next section. At this point the wafer is immersed in a solvent bath: the solvent dissolves the photoresist underneath the deposited material starting from the edges of the unexposed photoresist and lifts off the unwanted material leaving only the desired thin film pattern. Selection of the suitable photoresist technology and the proper thin-film deposition technique is fundamental for the optimization of the lift-off process.

## 2.3 Thin films

Deposition of thin films over substrates is a very important feature in many microfabrication processes. Thin films could play the role as permanent parts of finished devices, but they are also used temporarily during wafer processing as protective films, sacrificial layers and etch and diffusion masks. Two main deposition techniques are available nowadays: Physical Vapor Deposition PVD (direct line-of sight impingement deposition techniques) and Chemical Vapor Deposition CVD (diffusive-convective mass transfer deposition techniques).

### 2.3.1 Physical Vapor Deposition (PVD)

The general idea of PVD is material ejection from a solid target material and transport in vacuum to the substrate surface. There exist several different PVD techniques:

- Thermal evaporation (mainly by resistive heating, RF induction heating and e-beam assisted heating)
- Sputtering (mainly by DC and RF plasmas and Magnetrons)
- Ion plating and cluster deposition
- Laser ablation deposition

- Aerosol deposition

The basic PVD process consists of the following elementary steps, performed in a vacuum chamber:

1. Synthesis of the coating vapor from the source material;
2. Transport of the vapor to the substrate in vacuum;
3. Condensation of vapours onto the surface of the substrate.

In evaporative PVD, the target material (mostly pure metal) is first deposited in a suitable container (e.g. a tungsten crucible) and transformed into vapor (sublimated) by heating: heated metals have high vapor pressures and in high vacuum, the evaporated atoms will be transported to the substrate surface. Atoms arrive at thermal speeds, which results in basically room-temperature deposition. There are very few parameters in evaporation that can be used to tailor film properties. There is no bombardment in addition to thermalized atoms themselves, which bring very little energy to the surface. Substrate heating is possible, but because of high vacuum requirement, is difficult to provide heat avoiding outgassing of impurities from heated system parts. Shutter blades can be used to prevent deposition on the wafers during unstable flux (e.g., at the start of the deposition or during parameter ramping). Shutter blades enable very accurate and abrupt interfaces to be made, almost at the atomic thickness limit. The simplest way to evaporate materials for PVD is resistive heating. In this method, a high current is injected through the high refractory material forming the crucible where the material is placed. The crucible heats up by joule effect reaching the evaporation temperature of the material. Since the process is performed in high vacuum, the temperature required for vaporization is significantly lower than the temperature required at atmospheric pressure, and the absence of air prevents oxidation of the source material. One drawback of this technique is the possible contamination of the deposited film with metal from the crucible. Alternative methods for evaporating the source material include electron beam (e-beam) and radio-frequency (RF) induction evaporation. In the electron beam mode of operation a high intensity e-beam gun (3-20 KeV) is focussed on the

target material that is placed in a water-cooled copper crucible. In this way the source melts locally, reducing contamination with the materials composing the crucible. In RF induction heating, a water-cooled RF coupling coil surrounds a crucible with the material to be evaporated. Since two-thirds of the RF energy is absorbed within one skin depth ofthe surface, the frequency of the RF supply must decrease as the size of the evaporant charge increase. A different technique of Physical Vapor Deposition is sputtering. Sputtering is sometime preferred over evaporation because of a wider availability of materials to work with, better step coverage and better adhesion to substrate. While evaporation is generally limited to metals, sputtering can be applied to nearly any material also non-metallic materials, alloys, ceramics and polymers. In the basic sputtering process (Fig 2.4), the target plate at high negative potential (or cathode) is bombarded with energetic Argon ions (Ar+) generated in a glow discharge plasma, situated in front of the target. The bombardment process causes the ejection of target material mainly as neutral atoms by momentum transfer. Atoms are then transported to the substrate wafers in vacuum and condense on the surface as a thin film. Secondary electrons are also emitted from the target surface as a result of the ion bombardment, and these electrons play an important role in maintaining the plasma. In contrast to evaporation, the energy flux to the substrate surface can be substantial. From one side this has beneficial effects, improving adhesion and making the film denser. On the other side too high energies can cause damage to the film, the substrate and underlying structures (thin oxide breakdown because of high voltages). Sputtering requires operation at higher pressure (1 to 10 mTorr) than evaporation pressure (three to five orders of magnitude) in order to sustain the DC plasma with the production of ionizing collisions between secondary electrons released from the cathode and the gas in the chamber. Because of the higher operation pressure, sputtered atoms will experience multiple collisions in the path between the cathode and the anode. Thanks to these collisions, sputtered atoms arrive at the substrate with random incident angles thus improving step coverage compared to evaporation. However, if the pressure is too high, a significant number of metal atoms are not able to pass through the sputtering gas being reflected back to the cathode, thus decreasing the deposition rate. On the other side, sputtering at low pressure improves film adhesion because of the higher energy of incident particles and reduces contamination of the film by

trapped gas molecules, resulting in higher density and purity films. The basic sputtering

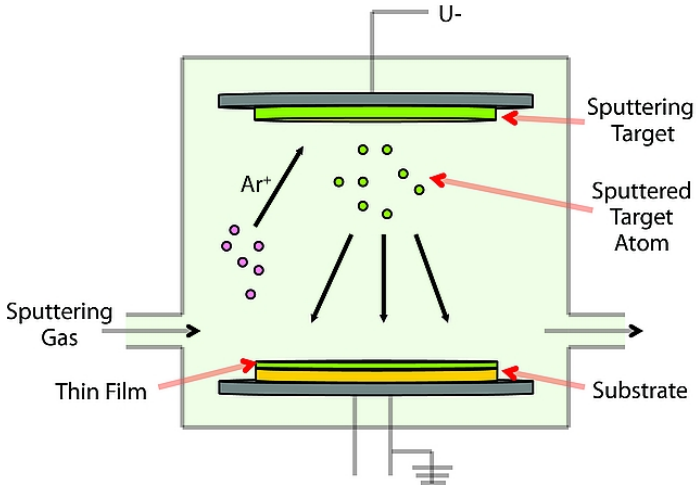


FIGURE 2.4: Layout of a Sputtering chamber for PVD deposition.

process is limited by low deposition rates, low ionisation efficiencies in the plasma, and high substrate heating effects. These limitations have been overcome by the development of magnetron sputtering and, more recently, unbalanced magnetron sputtering. Magnetron sputtering features a magnetic field which optimize the plasma density in front of the target thus increasing ion bombardment of the target leading to higher dissipation rates while working at lower operating pressures (typically, 10$\sim$ 3 mbar, compared to 10$\sim$ 2 mbar) and lower voltages (typically, 500V, compared to 2 to 3 kV). Furthermore, secondary electrons emitted by the cathode as a result of ion bombardment are bent by the crossed fields and are collected by ground shields. This eliminates the secondary electrons bombardment of the substrate, which is one of the main sources of substrate overheating [99] [100]. Ion plating combines evaporation of the source material with ionization of the atom flux by an electron filament or plasma. In a standard setup the substrate is placed in the upper part of the chamber acting as cathode, while the source material (anode) is placed below. Argon ions plasma is activated in the vacuum of the chamber: this results in ion bombardment of the substrate which creates a very clean surface. At this point the source material is heated until sublimation with the same methods used in vacuum evaporation (resistance heating, e-beam bombardment,...). Sputtering continues during deposition: thus, the ion bombardment of the substrate consists not only of the original argon ions but also of source material ions energized by the plasma. This process results in films with uniform thickness

and excellent adhesion to the substrate. From the standpoint of adhesion, the principal benefits obtained from the ion plating process are: (1) ability to sputter clean the surface and maintain it clean until the film deposition start; (2) provide a high energy flux to the substrate surface, giving a high surface temperature, thus enhancing diffusion and chemical reaction without necessitating bulk heating; (3) alter the surface and interfacial structure by introducing high defect concentrations, physically mixing the film and substrate material, and influencing the nucleation and growth of the depositing film [101].

### 2.3.2 Chemical Vapour Deposition (CVD)

In Chemical Vapor Deposition (CVD), chemical reactions are at the base of the thin film deposition onto the substrate's surface. In CVD, the source material at vapor phase, often diluted with an inert carrier gas, reacts at a target hot surface to depose a solid thin film. In this technique, the diffusive-convective transport to the hot substrate surface involves many intermolecular collisions, and mass and heat transfer modelling of deposition rates is much more complex compared to PVD deposition techniques. The control of the CVD reaction is performed through the thermodynamics of the reaction, the kinetics of the reaction and the mass transport of reactants and byproducts. The available parameters to control the process are thus temperature, pressure and chemical activity. Chemical vapor deposition has a number of key advantages compared to other thin film deposition techniques. These advantages include the ability to coat a surface with complex topography with a layer of uniform thickness, the ability to deposit a coating on one surface, and not on another, and low deposition temperatures (which can be a primary concern for thermally sensitive substrates). However, CVD of metals is not widely adopted mainly because the film properties are often not adequate or the deposition process cannot be predictably controlled to achieve a reproducible and reliable process. The main steps in a CVD thin film deposition process include:

1. Mass transport of reactants and diluent gases (if present) in the bulk gas flow region from the reactor inlet to the deposition zone;

2. Gas-phase reactions (homogeneous) leading to the formation of film precursors and byproducts;

3. Mass transport of film precursors and reactants to the target surface;

4. Adsorption of film precursors and reactants on the target surface;

5. Surface migration of the film formers to the growth sites;

6. Surface reactions (heterogeneous) of adatoms occurring selectively on the surface, and incorporation of film constituents into the growing film by nucleation;

7. Desorption of byproducts of the surface reaction;

8. Mass transport of byproducts in the bulk gas flow region away from the deposition zone toward the reactor exit.

Decomposition of the source gases is induced either by temperature (thermally driven CVD) or by plasma (Plasma Enhanced CVD or PECVD) or other energy sources (a radio-frequency plasma, photoradiation or laser radiation). In case of thermally driven CVD reactions, a temperature gradient is imposed on the reactor: the gas-phase species form in the hot region and then diffuse towards the target surface. Thermal CVD processes take place in the range 300 to 900 ∘C (very much source gas dependent), and PECVD processes at ca. 100 to 400 $^{\circ}C$, typically at 300 $^{\circ}C$. CVD reaction rates obey Arrhenius behaviour, that is, exponentially temperature dependent. Two temperature regimes can be found for most CVD reactions (Fig 2.5): when the temperature is low, the surface reaction rate is low, and there is an overabundance of reactants. The reaction is then in the surface reaction–limited regime. This is compensated by the fact that deposition takes place on up to 100 wafers simultaneously. When the temperature increases, the surface reaction rate increases exponentially, and above a certain temperature, all source gas molecules react at the surface. The reaction is then in the mass transport–limited regime because the rate is dependent on the supply of a new species to the surface. The fluid dynamics of the reactor then plays a major role in deposition uniformity and rate. In the case of mass transport limited reaction, the deposition process can be enhanced in low-pressure CVD reactors (¡10

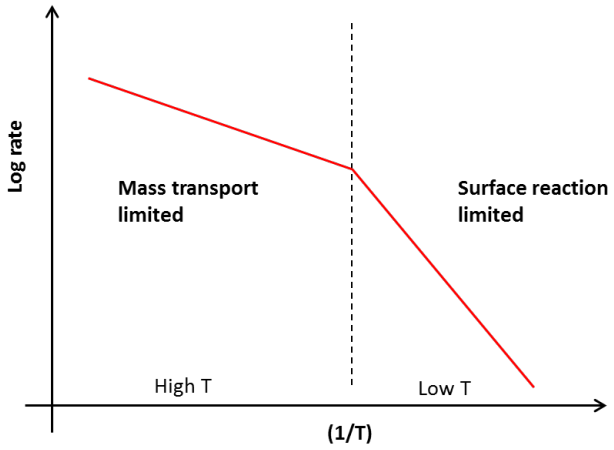


FIGURE 2.5: Kinetics of CVD reactions

Pa). Thanks to the reduced pressure, the diffusivity of the gas species is increased by a factor 1000. This allows vertical stacking of wafers at very close spacings since the rate of arrival of reactants is less important. LPCVD reactors provide excellent film uniformities (better than 5%). Although these reactors have lower deposition rates, in industrial applications this is compensated by the much larger wafer capacity.

### 2.3.3 Thermal oxidation

Silicon oxide is a very important feature in silicon microfabrication technology being used in many different steps like insulation in electrical stacks, hard mask for etching, surface treatment, protective layer and many others. Silicon at ambient conditions exhibits a native oxide of nanometre thickness on the silicon surface. This oxide is limited in thickness and not stoichiometric. Thermal oxidation of silicon is achieved by heating the substrate to temperatures typically in the range of $900 - 1200\,^{\circ}\mathrm{C}$. The atmosphere in the furnace where oxidation takes place can either contain pure oxygen (dry oxidation) or water vapor (wet oxidation). Both of these molecules diffuse easily through the growing $SiO_2$ layer at these high temperatures. Oxygen arriving at the silicon surface can then combine with silicon to form silicon dioxide.

$$\text{Dry oxidation: } \mathrm{Si(s)} + \mathrm{O_2} \rightarrow \mathrm{SiO_2(s)} \tag{2.1}$$

$$\text{Wet oxidation: } \mathrm{Si(s)} + \mathrm{2H2O} \rightarrow \mathrm{SiO_2(s)} + \mathrm{2H2(g)} \tag{2.2}$$

Thermal oxidation is a slow process: dry oxidation at 900 °C for 1 h produces ca. 20 nm thick oxide and wet oxidation for 1 h produces ca. 170 nm. Exact values are dependent on silicon crystal orientation: oxidation rate of ¡111¿ is somewhat higher than that of ¡100¿ silicon; highly dopedsilicon oxidizes faster than lightly doped material, and the higher the oxygen pressure, the higher the rate. The rate of oxide growth is usually predicted by the Deal-Grove model [102]. What is important to know is that the growth of the oxide layers proceeds at the interface both towards the outside but also within the silicon bulk. For every unit thickness of silicon consumed, 2.17 unit thicknesses of oxide will appear. Conversely, if a bare silicon surface is oxidized, 44% of the oxide thickness will lie below the original surface, and 56% above it.

## 2.4 Etching

In microfabrication technology, etching consists in selective removal of substrate material according to the patterned transferred by the photolithography process. Etching is divided into two main technologies: wet etching and plasma (or dry) etching. Etch rates are typically 100-1000 nm/min for both wet and plasma processes, except for silicon, where special techniques enable rates up to 20 $\mu$m/min. Some materials cannot be wet etched, for example SiC, GaN, TiC and diamond: these materials can, however, be plasma etched. Some materials cannot be etched even with plasmas, because no suitable source gas/volatile product combination exists: for these materials Ion Beam Etching (IBE), a purely physical etching, can be used.

A typical etching process usually consists of three main steps:

1. Transport of etchants to surface;
2. Surface reaction;
3. Removal of product species.

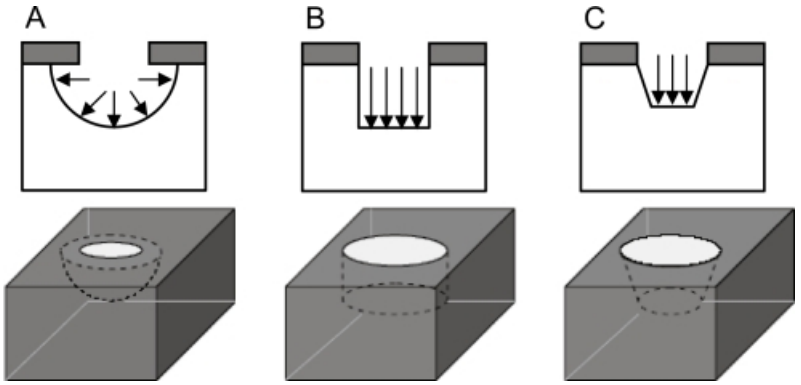


FIGURE 2.6: Isotropic etching (A), anisotropic etching with vertical walls (B) and anisotropic wet etching (C).

Resulting etching profiles can be subdivided in two main categories: *isotropic etching*: it is the most commonly encountered etch profile (Fig 2.6(A)). Most wet etchants result in an isotropic profile, and it is also encountered in plasma and dry etching. Dry etching of silicon with $XeF_2$ gas, without plasma, results in isotropic profiles. Similarly, HF-vapour etching of oxide is isotropic dry etching. In plasma etching, the degree of isotropy can be controlled by the etching parameters, from fully isotropic to fully anisotropic.

*anisotropic etching*: in contrast to isotropic etching means different etch rates in different directions in the material. The classic example of anisotropic etching is the Bosch process for the etching of deep vertical trenches with Dry etching techniques (Fig 2.6 (B)). Another example of anisotropic etching is the $< 111 >$ crystal plane sidewalls that appear when etching a hole in a $< 100 >$ silicon wafer in a chemical such as potassium hydroxide (KOH) (Fig 2.6 (C)). The result is a pyramid shaped hole instead of a hole with rounded sidewalls with isotropic etchant.

### 2.4.1 Wet etching

Wet etching is a material removal process that uses liquid chemicals or etchants to remove materials from a wafer. Wet etching mechanisms fall into two major categories:

$$\text{Metal etching by electron transfer:} \qquad \mathrm{Me(s)} \rightarrow \mathrm{Men} + (\mathrm{aq}) + \mathrm{ne}^- \tag{2.3}$$

$$\text{Insulator etching: by acid-base reaction:} \qquad \mathrm{SiO_2} + 6\mathrm{HF} \rightarrow \mathrm{H_2SiOF_6} + 2\mathrm{H_2O} \tag{2.4}$$

The rate limiting steps in etching are similar to those encountered in CVD:

1. The surface reaction is slow, and it determines the rate.
2. The surface reaction is fast, and rate is determined by etchant availability (transport of reactant by diffusion and convection).

Wet chemical etching of silicon usually provides a higher degree of selectivity than dry etching techniques. Wet etching is usually also faster: a few microns to tens of microns per minute for isotropic etchants and about 1 um/min for anisotropic wet etchants versus 0.1 um/min in typical dry etching (not considering high-density plasmas that recently reached up to 6 um/min etch rate).

Isotropic etching of silicon is accomplished by dipping the wafers in aggressive acetic etchants that produce rounded isotropic patterns. The most common isotropic etchant for silicon is a HF-$HNO_3$-$H_2O$ mixture because it produces smooth surfaces and has a fast etch rate [103]. Acid etching in $HNO_3$ 1 HF mixture is reported to proceed with following global reactions [104]:

$$\mathrm{Si} + 4\mathrm{HNO_3} \rightarrow \quad \mathrm{SiO_2} + 4\mathrm{NO_2} + 2\mathrm{H_2O} \tag{2.5}$$

$$\mathrm{SiO_2} + 6\mathrm{HF} \rightarrow \qquad \mathrm{H2SiF6} + 2\mathrm{H_2O} \tag{2.6}$$

Oxidants other than $HNO_3$ can also be used. Fluoric acid is used also for wet etching of silicon oxide and silicon nitride. The addition of ammonium fluoride creates a buffered HF solution (BHF) also called buffered oxide etch (BOE). The addition of $NH_4$ F to HF controls the pH value and replenishes the depletion of the fluoride ions, thus maintaining stable etch rates. It also reduces the etch rates for a better process control and reduction of peels photoresist used in lithographic patterning. Some oxides produce insoluble products in HF solutions. A common buffered oxide etch solutioncomprises a 6:1 volume ratio of 40% $NH_4F$ in water to 49% HF in water. This solution will etch thermally grown oxide at approximately 2 nanometres per second at 25 degrees Celsius. The process is based on the

above equation:

$$SiO_2 + 6HF = H_2SiF_6 + 2H_2O \tag{2.7}$$

In anisotropic wet etching of monocrystalline silicon in alkaline solutions, the etch rate depends on the crystallographic orientation of the etched surface and the type and concentration of the solution used. All anisotropic wet etchants are aqueous alkaline solution, where the main component can be either organic or inorganic. Most used liquid etchants for anisotropic etching of silicon comprises:

1. KOH (Potassium Hydroxyde)
2. EDP (Ethylenediamine pyrocatechol)
3. TMAH (Tetramethyl ammonium hydroxide)
4. $N_2H_2$

In anisotropic etching, the etch rate is much higher in one direction than in another, exposing the slowest etching crystal planes. For KOH etching, the values of the relative etch rates for the three planes of interests can be as high as: $< 111 > =1$, $< 100 >= 400$, and $< 110 >= 600$ [**?** ]. Depending on the crystal orientation chose, the $< 111 >$ planes are either at $54.74^\circ$ with respect to the wafer's surface (for $< 100 >$ silicon) or perpendicular to it (for $< 110 >$ silicon). These differences in the etch rates in the different planes enables the development of many different structures. For a $< 100 >$ wafer, rectangular structures with concave corners are easily done with four sidewalls (111) and the plane (100) at the bottom. If the lateral planes meet, etching is self-limiting and resulting shape is an inverted pyramid. In $< 110 >$ wafers the etching starts vertically along the (111) planes then self-limiting shapes like U-grooves or V-grooves, develop when the slower etching (110) plane appears. It would be possible in this case to etch perfectly vertical walls if the mask is perfectly aligned. The most common anisotropic liquid etchant is potassium hydroxide (KOH). It is safer to use than an EDP (ethylenediamine, pyrocatechol, and water) solution which is another anisotropic etchant for silicon. KOH etch, in near saturated solutions (1:1 in water by weight) at $80\,^\circ C$ produces a uniform and bright surface with 1.3-1.4 um/min etch

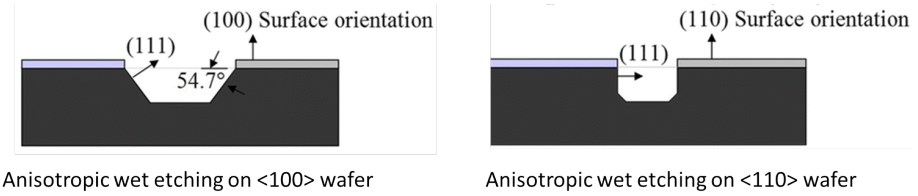


FIGURE 2.7: Anisotropic wet etching profiles for $< 100 >$ and $< 110 >$ wafers.

rates. The addition of Isopropanol into KOH changes the relative etch rates of crystal planes and depending on the exact conditions, either of the (100) or the (110) planes will exhibit the maximum etch rate. Etching non-uniformity is aggravated at higher temperatures and abundance of bubbles is seen emerging from the silicon surface during KOH etching. The etching selectivity with $SiO_2$ is quite low in KOH etching.

### 2.4.2 Dry etching

In dry etching techniques, the substrate is etched by gaseous species. Dry etching always requires the formation of plasma in a vacuum chamber. The glow-discharge plasma is used to dissociate a suitable stable feed gas (e.g. $SF_6$ for Si etching) generating the gas-phase etching environment, which consists of positive and negative ions, electrons, radicals and neutral [134]. All these species are important in the etching process and they are generated in the plasma by three main mechanisms:

$$\text{Ionization:} \quad e^- + Ar^- \rightarrow Ar^+ + 2e^- \tag{2.8}$$

$$\text{Excitation:} \quad e^- + O_2^- \rightarrow O_2^+ + 2e^- \tag{2.9}$$

$$\text{Dissociation:} \quad e^- + SF_6 \rightarrow e^- SF_5^* + F^+ \tag{2.10}$$

Exited molecules like $CF_4^*$ are very reactive and etch the substrate by chemical processes while ionic species like $CF_3^+$ are accelerated by the RF field and impart energy to the surface by momentum transfer. If the reaction is thermodynamically favoured, no ion bombardment is needed for etching and the role of the ion bombardment is simply to induce directionality.

The basic hardware for dry etching consists of opposed parallel plate electrodes contained in the vacuum chamber maintained at low pressure (0.01-1 Torr). When a RF voltage is applied

between the electrodes (typically at 13.56 Mhz), current flows forming a plasma, which emits a characteristic glow. Ions and reactive species are generated by particle collisions in the plasma. When the plasma starts, the electrons that are more mobile that ions, charge up the capacitively inducted electrode. Since no charge can be transferred over the capacitor the electrode retains a negative DC bias, also called self-bias V DC since induced by the plasma itself. The self-bias voltage is about half the peak-to-peak applied RF voltage [105]. The radiofrequency voltage applied between the two electrodes promotes the oscillation of the free electrons and their collision with gas molecules, producing self-sustained plasma. During oscillation in the RF field, electrons pick up enough energy to cause ionization, thus sustaining the plasma at lower pressure than in DC plasmas. Positive ions generated in the plasma are accelerated by the large field at the cathode and hit the substrate at near-normal incidence, with energy ranging from a few to several hundred electronvolts, depending on the plasma conditions and the chamber design. One of the main parameter determining plasmacondition is the total reactor pressure. As the reactor pressure decreases, the energy of the particles sharply increases because both the self-biased voltage and the mean free path of the ions increase. Dry etching techniques are usually divided in the following categories,

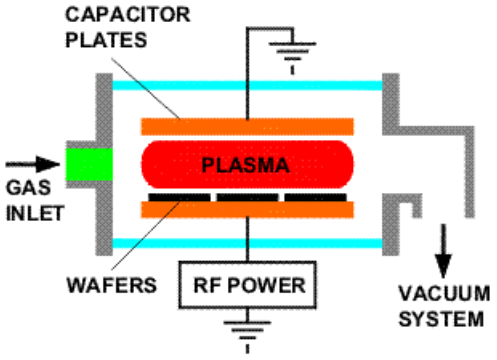


FIGURE 2.8: Basic setup of a RF plasma etcher.

based on the process driving the etching:

1. Purely physical dry etching or Ion Beam Etching (IBE);
2. Purely chemical dry etching or Chemical Plasma etching (CPE);
3. Synergetic Reactive Ion Etching (RIE).

In Ion beam etching, energetic argon ions $Ar^+$ are accelerated by the plasma towards the substrate and the resulting etching is a consequence of purely physical effects, the momentum transfer between the energetic inert ions and the substrate that causes bond breakage and material ejection. No chemical reactions occur at the surface of the target. Redeposition of ejected material is minimized by etching at low pressure (¡1 mTorr). Since it is difficult to ignite the plasma in such low pressure, it is generated in a remote high pressure chamber and then ions are extracted with electrostatically controlled grids and directed to the substrate. This method is relatively slow compared to other dry etching techniques, with etch rates limited to several hundreds of angstroms per minute. For some materials for which there are no chemical etchants for plasma processing, IBE is the only available technique for dry etching. In Chemical Plasma Etching, reactive neutral species such as chlorine and fluorine atoms and molecular species generated in the plasma diffuse to the substrate where they react with the surface to form volatile products. In this technique, the only role of plasma is to supply gaseous, reactant species to the surface. The diffusion of the neutrals has not a preferential path, so isotropic, rounded features are obtained. In the basic setup, a neutral feed gas such as $CF_4$ is injected in a glow discharge. By impact with energetic particles in the plasma, reactive species are formed, such as $CF_3^+$ , CF3 an F. After diffusing towards the wafer, reactive species are adsorbed into the substrate and react with the material forming reaction products that leave the surface by desorption and diffusion. Synergetic Reactive Ion Etching takes advantage of both etching mechanisms overcoming the limitation of each technique alone. In this process, the inert ions activate the surface of the substrate enhancing the reactivity of the neutral species [106]. Thanks to the strong directionality ofthe ions, a certain isotropy is reached, since the enhancing effect produced by the ion species is active only in one direction. Chemical reactions between the radicals and neutrals (fluorine, CF3, CF2 and so forth) and the substrate material occur at the surface and produce either volatile species such as SiF4 or their precursors such as SiF, SiF2 or SiF3. At the same time positive ions such as CF3+ are accelerated across the plasma sheath and remove material by sputtering. The combination of the chemical activity of reactive species and sputtering can result in much higher material erosion rates in the vertical than in the lateral direction, which creates anisotropic profiles. The realization of high aspect ratio structures usually

required in MEMS applications with dry etchingtechniques was initially prevented by three major problems related with dry etching technology:

1. Low etch rates: the low rates of silicon etching (1 um/min) made not practical the etching of deep structures in industrial applications;
2. Aspect ratio: because of the characteristics of dry etching it was difficult to maintain high aspect ratios in deep etches with a proper control;
3. Selectivity: masking materials could not sustain the deterioration during a long etch.

The development of High-density plasma sources enabled Deep Reactive-Ion Etching (DRIE) which represents one of the main reasons for the success of MEMS. The most important high density plasma source is Inductively Coupled Plasma (ICP). The main novelties on these rather new ICP-RIE systems are the following:

- Separation of the main plasma from the wafer
- A higher plasma density
- Improved Radio Frequency RF-power supply
- Improved performance for pumping and mass-flow systems
- Pulsed Low Frequency LF substrate biasing
- New chemistry and new process (Bosch and cryogenic)

These hardware and process novelties led to improved performances, for instance:

- Higher selectivity for deep etching (DRIE)
- Higher aspect ratio (AR)
- Higher etching rate, either for anisotropic or isotropic etching
- Reduction of parasitic effects: notching, aspect ratio dependent Etching (ARDE), etc...

In standard RF plasma etchers, it is not possible to obtain high plasma densities with low self-bias required for optimum etch characteristics and minimum substrate damage [136]. This because at low pressure, high RF voltages are required to maintain proper plasma densities and thus high self-bias voltages are generated. Higher plasma densities can be achieved in Inductively Coupled Plasma (ICP) reactors. In these reactors, a copper coil is wrapped around the RIE chamber. The coil, operating in RF mode at the standard 13.56 Mhz, creates a time varying magnetic field around the chamber, which produces an azimuthal electric field in the chamber leading to the formation of the plasma. This field also confines the plasma electrons thus increasing the density. The plasma then diffuses from the source into the chamber. This setup enables decoupling the plasma density, controlled by the coil in the upper chamber, and the ion bombardment energy determined by the RF bias in the lower chamber. With this technology, silicon etch rates up to 6 um/min, with uniformity better than 5% and selectivity to silicon oxide higher than 150:1 were achieved by differentresearchers. In order to increase anisotropy, the wafer chuck is cooled at cryogenic temperatures (77 K) using helium gas flow during the etching. The cryogenic cooling of the chuck results promotes condensation of reactant gases and protects the sidewalls from etching. This technique may introduce important stresses on the wafer. A good alternative for high aspect ratio deep silicon etching is the Bosch process, patented by Robert Bosch GmbH in 1994 [107]. The Bosch deep etching process is carried out in ICP high density-plasma systems [108]. This process consists of a sequential alternation of chemical isotropic etching with $SF_6$ at low pressure (to produce vertical etch) and sidewall passivation with $C_4F_8$ at higher pressure to enhance sidewall passivation. At the beginning of the process (a) $SF_6$ is introduced in the chamber for 7-8 s at low pressure etching quasi-isotropically the exposed substrate surface (b). In the following step, $C_4F_8$ is introduced in the chamber at higher pressure for 2-3 s. $C_4F_8$ creates a uniform protecting layer on the exposed surfaces (c). In the following step, when $SF_6$ is reintroduced, it first attacks the protection layer. The layer is completely removed from the bottom surface thanks to the sputtering effect of accelerated ions. In the remaining time, SF 6 proceeds with a further isotropic etching on the exposed bottom surface (d). The sidewall protection layer is slightly attacked by the chemical species, so it prevents the walls from etching during the whole step. This sequence

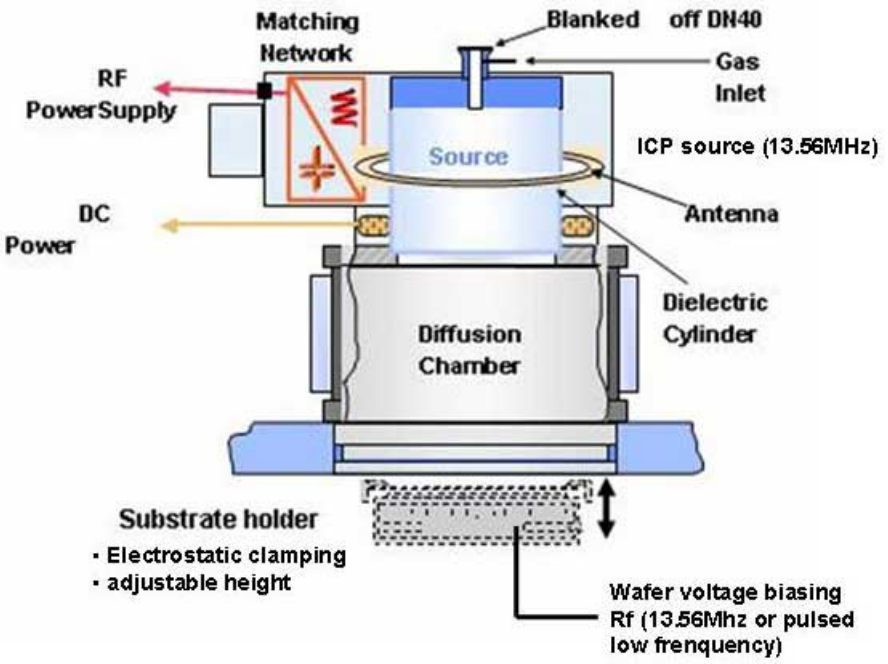


FIGURE 2.9: Setup of a ICP etcher.

is repeated until the desired depth is achieved. This pulsed operation produces undulating sidewalls also called scallops, as it is possible to see in Fig 2.10.

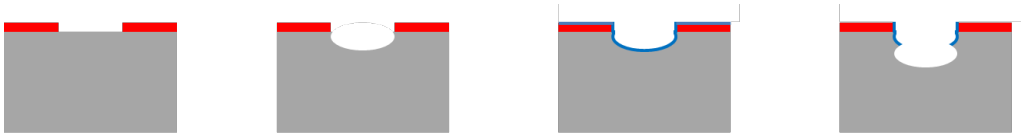


FIGURE 2.10: The Bosch process for Deep Reactive Ion Etching (DRIE)

## 2.5 Bonding

Bonding is a packaging technology at wafer-level for joining two wafers together. In microchannel fabrication, bonding created seals channels by closing the trenches etched in one wafer with another cover wafer. For a successful wafer bonding the main requirements are smoothness, flatness and cleanliness of the two surfaces to be bonded. Smoothness is of paramount importance for wafer bonding. If the micro roughness exceeds a critical value

the wafers are not bondable [109]. This critical value is usually around 0.5 nm for silicon/silicon direct bonding, while is much higher for other bonding techniques. Surface flatness is another important prerequisite: two sufficiently smooth wafers will spontaneously bond at room temperature despite a flatness variation of a few micrometres. However, if the flatness variations are too large, unbonded areas will result. Cleanliness is also very important since particles at the bond interface will prevent bonding locally because the wafers cannot conform abruptly to particles. Only below a critical particle size the wafers can conform to the contamination and the resulting void is identical to the particle size. This critical size is given by:

$$h_{\text{crit}} = 5(t\gamma(1-\nu^2)/E)^{0.5} \tag{2.11}$$

where $t$ is the wafer thickness, $\gamma$ is the surface energy, $\nu$ is the Poisson ratio and $E$ is the Young's modulus. The quality of the bonding is determined by the fraction of the interfacial area being in intimate contact and the strength of the bond interaction. For the detection of unbonded areas, both destructives and non-destructives techniques are available. In general, the non-destructive detection of voids is not a difficult task, unlike the quantitative evaluation of the strength of adhesion. Non-destructive techniques for voids detections are based on optical transmission, scanning acoustic microscopy and X-ray diffraction topography but alternative solutions are also available. There are three main classes of bonding techniques [110]:

- Direct bonding
- Anodic bonding
- Intermediate layer bonding

**Direct bonding** Direct bonding relies on forces that attract smooth and flat surfaces together when they are at intimate contact, like intermolecular forces and van der Waals forces. Depending on the surface species involved, hydrogen bonds may also develop at the interface, but neither van der Waals forces nor hydrogen bonds are strong enough to join the two surfaces irreversibly. The bonding strength is then enhanced by annealing at elevate

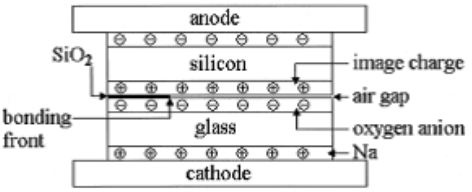


Fig. 3. A cross-sectional view of the Si-glass bonding pair demonstrating the charge distribution during the bonding process.

FIGURE 2.11: Typical setup for a Si-glass anodic bonding.

temperature, where chemical reactions take place between the surface species of opposing wafer sides which usually yield strong covalent bonds. Direct bonding is very demanding in term of surface quality: it has been experimentally observed that a roughness no greater than 10 A and a bow lower than 5 $\mu$m (on a 4" wafer) are required for a proper direct bond.

**Anodic bonding** Anodic bonding of silicon to glass (also called Field-assisted thermal bonding) has many features that make it easy to perform and thus desirable in many applications:

1. t has less stringent requirements in term of surface quality, since the glass conform at $400 - 500\,^{\circ}\mathrm{C}$ sealing structures and irregularities up to 50 nm hermetically;

2. Native oxides or deposited oxides do not prevent bonding;

3. Bonding quality can be visually inspected from the glass side.

The standard setup for anodic bonding includes a hot plate or a heating chamber, a DC power supplyconnected to suitable electrodes and a probe for the application of the load (Fig 2.11). When glass is heated at $350\,^{\circ}\mathrm{C}$, sodium oxide (NaO2) decomposes into sodium and oxygen ions. By applying a -1000 V voltage difference at the bonding wafers, sodium ions (Na+) move towards the glass top surface and oxygen ions towards the silicon surface (O2-). This process creates a depletion region and electrostatic forces pull the glass and the silicon wafer together. Oxygen ions react at the glass/silicon interface according to the reaction:

$$\mathrm{Si} + 2\mathrm{O}^2 \rightarrow \mathrm{SiO}_2 + 4\mathrm{e}^- \tag{2.12}$$

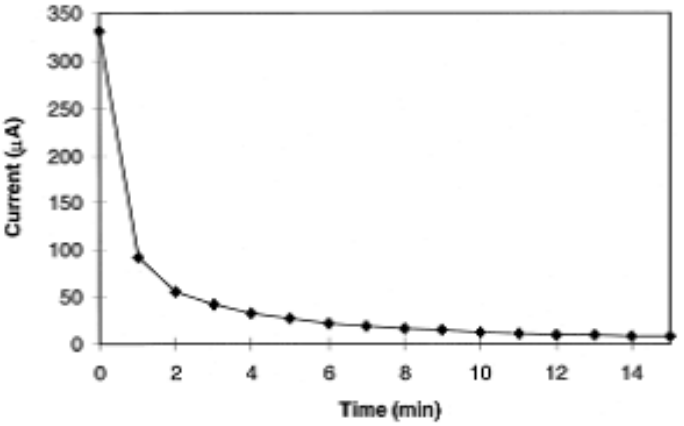


Fig. 4. Plot of current as a function of time plot during the bonding process for p-type Si and Corning 7740. Both surfaces were pre-cleaned with acetone and a voltage of 450 V was applied.

FIGURE 2.12: Typical current vs. time plot for Si-glass anodic bonding.

while sodium ions are neutralized at the cathode. The bonding of the two surfaces is incepted by applying pressure at the centre of the wafer. At this point the current rapidly increase because the contact area increases. Once the current reaches the maximum value it starts decreasing exponentially as oxygen ions react at the interface to form SiO2 (Fig 2.12). Usually when the current reaches 10% of its peak value the process is considered concluded [111]. **Intermediate layer bonding** This bonding technique makes use of an intermediate layer for joining the two wafers. Most used materials include:

- Au thin films for eutectic bonding;
- Solder (using thin-film deposited solders or preforms)
- Polymers
- Low melting temperature glasses (including glass frits)
- Soft metal thin films for thermocompression bonding

Bonding with intermediate layers is sometimes preferred over direct bonding techniques because of lower processing temperatures, high tolerance to particle contamination, possibility to bond structured wafers, low costs and high outputs.

# Chapter 3

# Experimental investigation of flow boiling heat transfer in a single microchannel

Microscale flow boiling heat transfer is currently a major research field. The high number of applications arising from the industry demand for predictive tools to help the design of efficient microscale thermal management solutions but a complete knowledge of the physical processes involved in flow boiling at reduced characteristics length is still missing. The aim of this study is to enhance the current knowledge of the microscale flow boiling heat transfer processes with a dedicated experimental investigation. A single silicon microchannel test section was designed and fabricated to perform microscale flow boiling experiments. This chapter describes the main results obtained with these tests. First, the design of the test section is presented. A single microchannel test section was selected to avoid sources of uncertainties deriving from the fluid distribution to multiple parallel channels. This choice introduces concerns related to the uniformity of the heat flux at the channel walls and the minimization of heat losses to the environment. To solve the first issue numerical simulations were performed in order to optimize the design of the test section achieving a good

uniformity of the heat flux at the channel walls and optimizing the deduction of the channel internal wall temperature from the heater temperature measurements. Then, special attention was devoted to the insulation of the test section minimizing heat losses to the surrounding. Every design aspect had to be studied to assure compatibility with the production process. The test section was fabricated at the class 100 clean room of the Centre of MicroNanoTechnology (CMi) at EPFL (École Polytechnique Fédérale de Lausanne) using standard microfabrication techniques. A dedicated process flow was developed for the fabrication of the device and every step of the process had to be validated to guarantee the expected performance. For the assembly of the test section, special techniques were developed to interface the silicon microchannel with the external piping system and to provide reliable measurements of the parameters of interest. Preliminary validation tests, performed to assess the capabilities of the measuring section, validated the design of the test section. Flow boiling tests were conducted at different operating conditions allowing obtaining several characteristic data like conditions at the Onset of Nucleate boiling, characterization of the boiling curves and measurement of the heat transfer coefficients. The results obtained are then compared with predictive tools available in the literature. This work addresses another fundamental aspect of flow boiling heat transfer: the effect of surface roughness on flow boiling characteristics. For this study, another test section was realized featuring tailored surface roughness elements. The results obtained with this configuration are presented in the last section and compared with the data obtained with the plain microchannel.

## 3.1 Design of the test section

The test section is a single microchannel made of silicon with a Borofloat®glass cover allowing visualization of the two-phase flow patterns. The channel is 0.4 mm high and 0.4 mm wide. These dimensions were selected as a compromise between size reduction and maximum pressure drop tolerated by the testing setup. This is also one of the dimensions envisaged for the design of the distribution lines in the interconnected frame microchannel devices presented in Chapter 5. The length of the channel was set to 51 mm both to control maximum pressure drop in all expected operating conditions and to fit the device

in a standard 4" silicon wafer used for the fabrication. The width and the thickness of the test section were optimized to provide uniform heat flux and constant temperature at the three silicon walls of the channel. The fourth side is obtained by closing the channel with the glass cover and it is assumed to be adiabatic. Based on the thickness of commercially available wafers and the capability of microfabrication processing, two possible geometries were identified: a 0.5x0.5 mm2 square channel in a 1 mm thick wafer, and a 0.4x0.4 $mm^2$ square channel in a 0.5 mm thick wafer. In order to select the best configuration, a steady-state thermal conduction numerical analysis was performed on a cross section of the devices using Fluent. The glass cover wafer, initially neglected, was introduced later to simplify the analysis. The domain of the simulation is shown in Fig. 3.1. Heat flux is applied on the heating section below the channel and heat transfer coefficient is applied at the three side of channel according to analytical correlations from the literature. After calculating the vapour quality expected at 4 different locations along the channel (L=0.02 m, L=0.03 m, L=0.04 m, L=0.05 m), experimental heat transfer coefficient data from [112] were selected and imposed at the three walls of the channel.

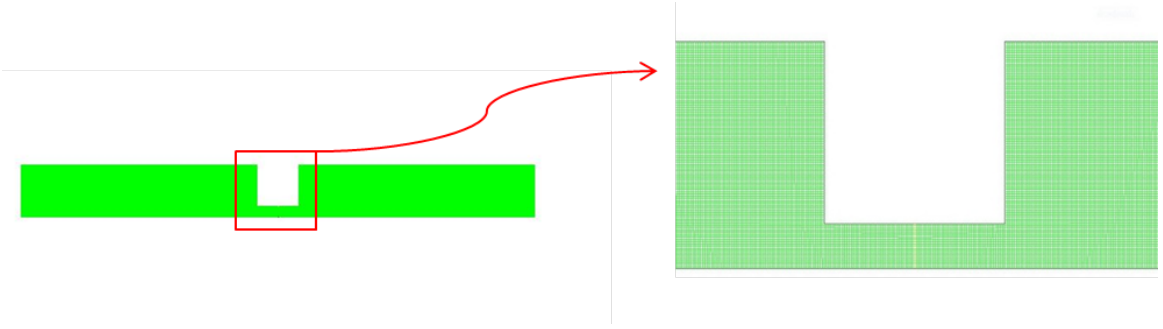

FIGURE 3.1: Domain of the numerical simulation (left) and detailed of the fine mesh adopted (right).

Numerical results (Fig. 3.2) show that 0.5 mm thickness provides a more uniform heat flux distribution at the channel's walls in all test cases: a maximum temperature variation within 0.2 °C is obtained for a heat flux of 240 $kWm^{-2}$ at the channel walls.

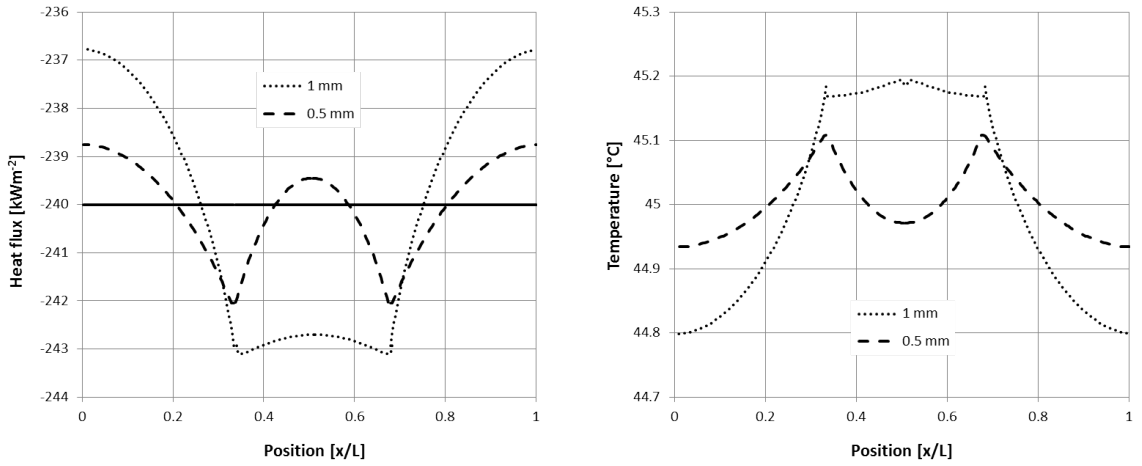


FIGURE 3.2: Comparison of the numerical results for the two configurations tested for a wall heat flux of q=240000 $Wm^{-2}$

The width of the heater providing thermal power to the microchannels was also optimized with numerical simulations to improve heat flux uniformity at the channel walls. Several heater widths were compared (1.4, 1.6, 1.8 and 2 mm) for the same heat flux on the channel walls at different heat flux values. The results for the wall heat flux q=240 $kWm^{-2}$ are reported in Fig. 3.3 and in Fig. 3.4

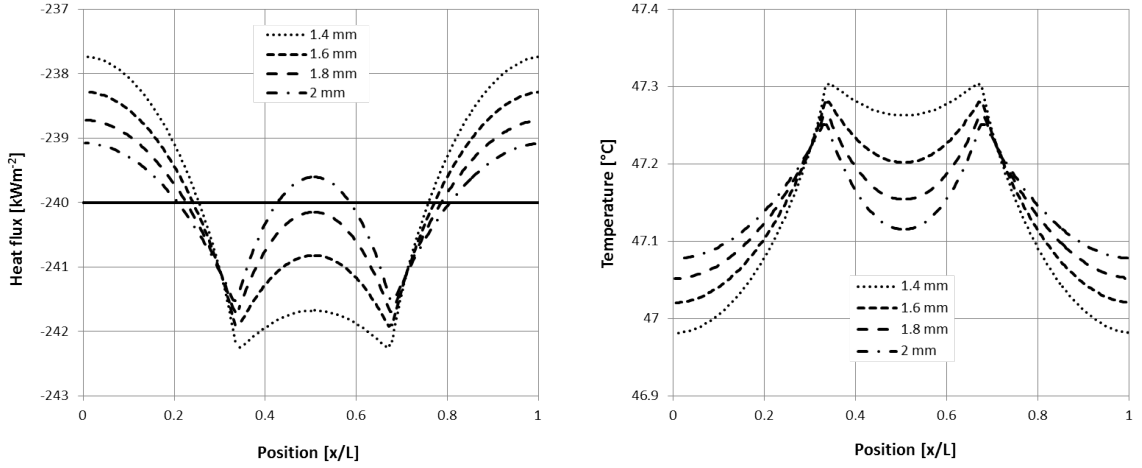


FIGURE 3.3: Numerical results of wall heat flux and temperature uniformity for different widths of the heater for a heat flux at the wall q=240000 $Wm^{-2}$.

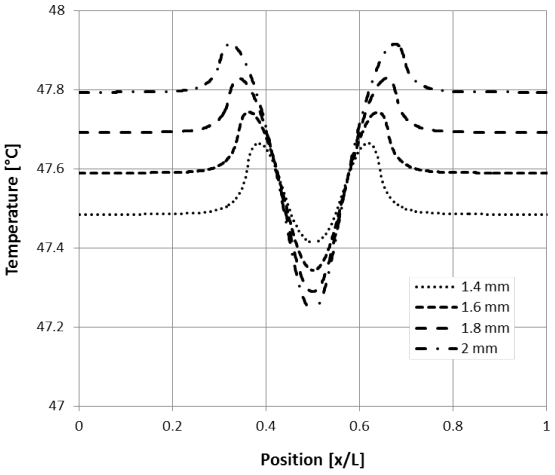


FIGURE 3.4: Numerical results of the heater temperature uniformity for different widths of the heater for a heat flux at the wall q=240000 $Wm^{-2}$.

It is possible to see that the uniformity of the heat flux and the temperature at the channel walls increases at increasing heater widths while the uniformity of the heater temperature lowers when reducing the thickness of the heater. However, it is also possible to notice that while the influence of the first two parameters is quite reduced for all the thicknesses tested, the variation on the heater temperature is quite important. It is also worth reminding that the heater surface temperature is a fundamental parameter, since this value is used to obtain the channel wall temperature used for the calculation of the heat transfer coefficient. For this reason, the lowest heater width of 1.4 mm was selected for the design of the test section. In this configuration, the maximum variation of the heater wall temperature is within 0.2 °C. At this point, the influence of the top glass cover was introduced. A standard 0.525 mm thick borosilicate wafer was chosen, since it is available at the fabrication site. For this simulation, experimental data from Del Col. et al. [113] were used for the silicon walls of the microchannels while analytical data from Sun-Mishima [88] were used for the glass side where the heat flux is much lower and no experimental data are available. Since the heat flux at the glass wall is not known a priori, an iterative process was used to associate the right heat transfer coefficient to the actual heat flux. First, a certain heat flux is assumed at the glass wall and the relative heat transfer coefficient is calculated with the Sun-Mishima correlation. The heat flux obtained from the simulation is then compared with the value assumed and corrected accordingly until convergence. The independence of this method

from the initial value has been checked selecting different initial heat flux values. Two test cases were considered, and the values are reported in Tab 3.1:

| **Case** | **Wall Heat Flux** [**kWm**−2] | **HTC** [**kWm**−2$K$**-1**] | **G** [**kg m**−2$s$**-1**] | **x** [–] |
|---|---|---|---|---|
| 1 | 70 | 18.5 | 500 | 0.3 |
| 2 | 110 | 24 | 500 | 0.55 |

TABLE 3.1: Test cases used in the numerical simulations

For the first case, the total power dissipated through the glass side is 5.4 In the end, the influence of the total width of the test sample was investigated (Fig.3.5 and Fig. 3.6) . Two different widths were considered: 5 mm and 8 mm. The same test cases reported in Tab 1 were considered.

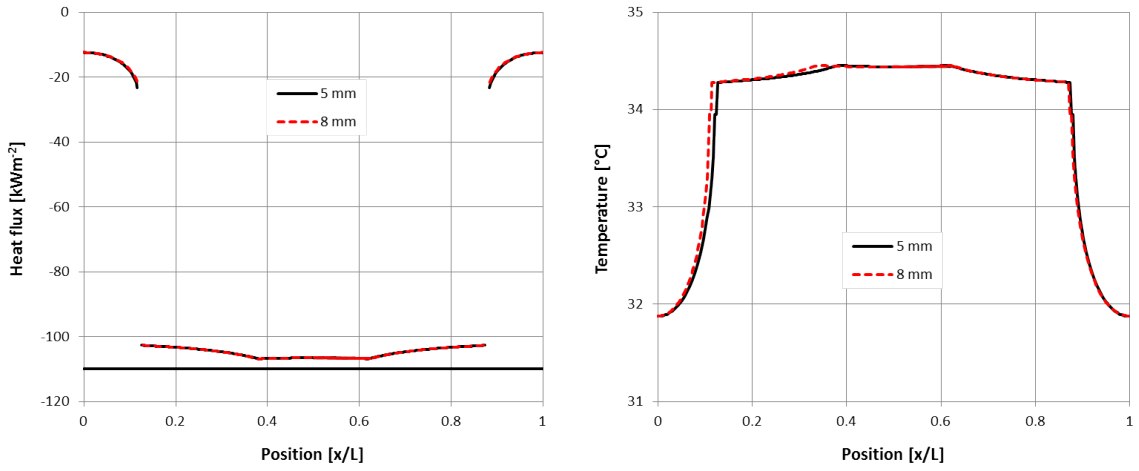


FIGURE 3.5: Numerical results of wall heat flux and temperature uniformity for two different widths of the sample for test case 2.

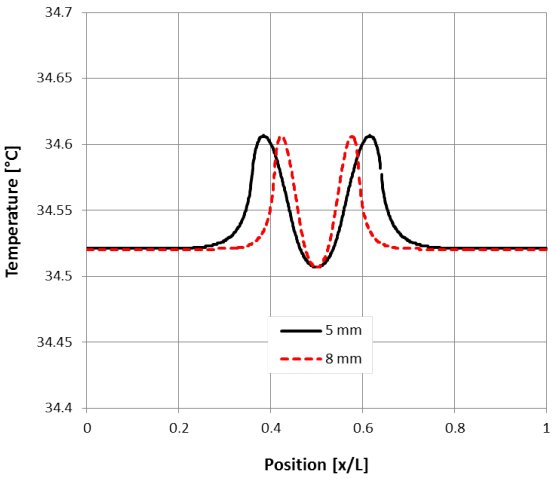


FIGURE 3.6: Numerical results of the heater temperature uniformity for two different widths of the sample for test case 2

Results show that for both cases the influence of the sample width is negligible. Based on this result, a width of 8 mm was selected to simplify the assembly procedure and in particular the soldering of the electrodes to the Platinum heater and the soldering of the fluid ducts on the glass side. To reduce thermal losses and axial conduction the inlet and outlet ducts are installed on the glass side. The connection to the microchannel is provided by two holes obtained on the glass cover in correspondance of the two ends of the channel.

## 3.2 Fabrication of the test section

For the fabrication of the test section, a dedicated process flow (Fig. 3.7) was developed to integrate all the features selected for the design with available microfabrication techniques. The process flow starts with a 525 $\mu$m thick silicon wafer single side polished. Since the process makes use of both side of the substrate, the first step performs thinning of the wafer and polishing of the second face with a Chemical-Mechanical Polishing (CMP) process to a final thickness of 500 $\mu$m. After a RCA cleaning, a 2 um oxide layer is grown on the wafer with a thermal oxidation process. This oxide layer is used both as hard mask for processing and for protection of the silicon face during the various steps of the process. With a photolithography on the frontside of the wafer, the pattern of the microchannels

is transferred to the wafer. The pattern is etched on the oxide layer with a dry etching process with a $He/C_4F_8$ plasma. The photolithography resist is then removed with an oxygen plasma and a liquid stripper. At this point, the oxide hard mask is used to etch the microchannel into the silicon substrate with a Deep Reactive Ion Etching (DRIE) process. Once the nominal depth of the microchannel is reached, the oxide hard mask is removed and the wafer surface prepared for the anodic bonding that seals the microchannels with the Borofloat®glass wafer. First the oxide is removed with $He/C_4F_8$ plasma, leaving only some tens of nanometres of oxide. Then, the last layer is removed in a Buffered Oxide Etching (BOE) bath which provides a much smoother surface thus improving the results of the anodic bonding. Inlet and outlet holes are obtained in the glass wafer by drilling with a diamond drill. Surface preparation for both silicon and glass wafers is performed in a Piranha bath. At this point the two wafers are first aligned with each other and then bonded with an anodic process at 380°C ensuring perfect sealing of the individual microchannels. The alignment between the two wafers is performed at the microscope providing a very good accuracy. The process continues with the processing of the backside of the wafer, where the metal heating elements are envisaged. First the protection oxide layer is removed with a plasma etching. Then a photolithography transfers the layout of the heaters on the silicon substrate. At this point a uniform metal film of 200 nm of Platinum is deposited by sputtering on the wafer's backside. A 20 nm Ti layer is also deposited to enhance the adhesion force of the platinum layer to the silicon substrate. With a lift-off process, the photolithography resist is removed, thus removing the metal layer where it was not foresee, leaving the platinum heaters precisely position at the bottom of each microchannel. In order to allow soldering of the inlet and outlet ducts directly on the glass surface, a metal layer is deposited by sputtering around the inlet and outlet holes drilled on the cover wafer. In order not to cover the microchannels with metal thus avoiding optical inspection, a hard mask is used to localize the deposition around the holes. The metal stack definition was optimized with several tests to obtain a good substrate for soldering. The final deposit includes 50 nm Ti, 350 nm Cu, and 100 nm Au. Cu is the main soldering substrate, Ti provides adhesion enhancement on the surface and the Au layer acts as the flux for soldering. The same stack is then deposited on the back side to obtain soldering pads on the platinum heater

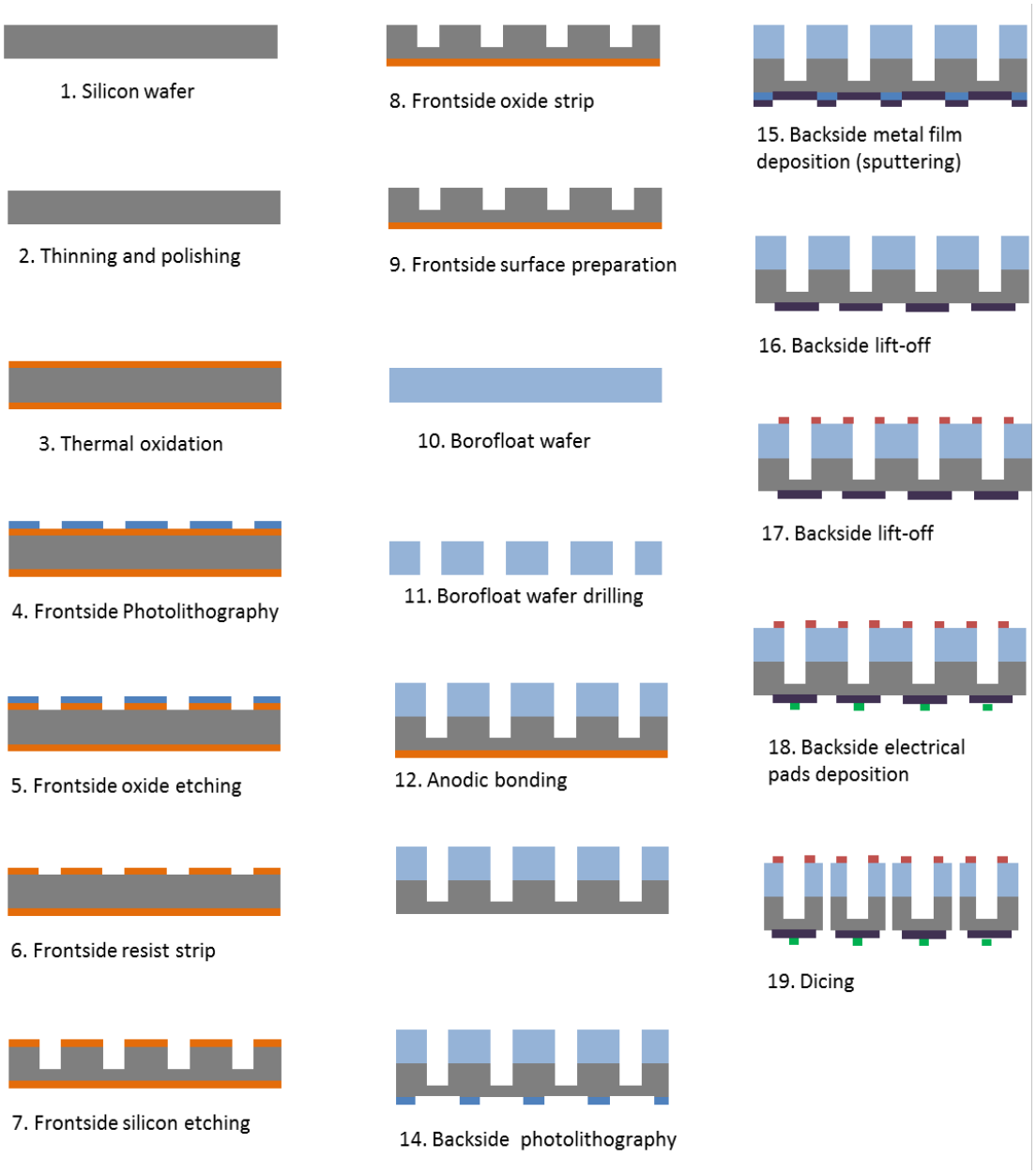


FIGURE 3.7: Process flow for the fabrication of the silicon single microchannel test section.

for connecting the electrodes. Also in this case a protective mask precisely aligned with the heater is used to localise the deposit. At this point, the individual microchannels in the wafer are diced out with an automatic dicing saw (Fig. 3.8).

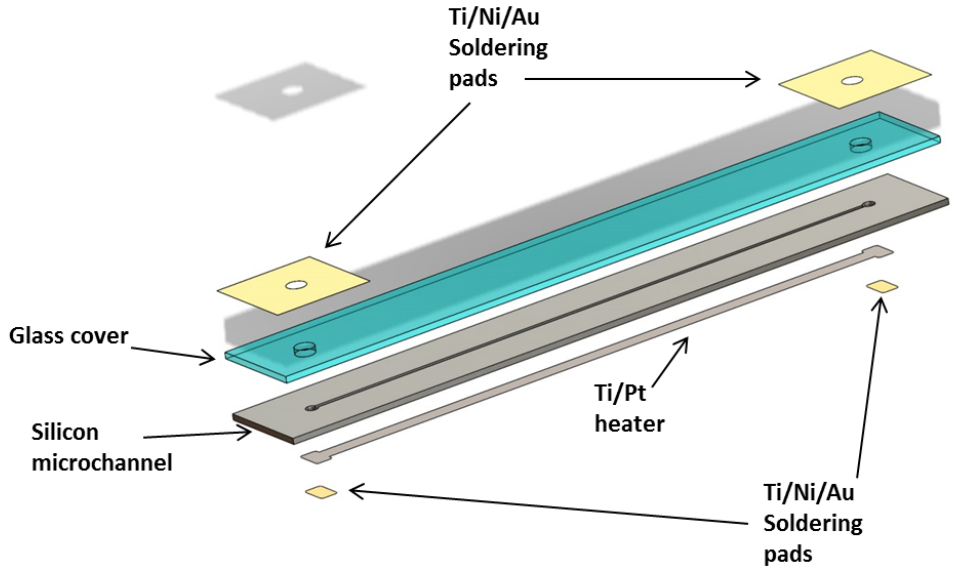


FIGURE 3.8: Schematic of the different components of the microchannel test section at the end of the fabrication process.

## 3.3 Assembly of the test section

Once the fabrication process flow is concluded, the single microchannel device is assembled into the final test section. This process includes all the steps envisaged to equip the sample with the required instrumentation for the experimental characterization and the installation of the microchannel in its final testing configuration. First, the test section is equipped with thermocouples, glued on the surface of the platinum heater. Two thermocouples were installed, both calibrated before installation. The first thermocouple is installed at 18 mm from the entrance of the channel and the following at 36 mm. Then, electrodes are soldered to the metal pads at the ends of the platinum heater. The electrodes are tin soldered with standard electronic soldering techniques. The inlet and outlet ducts are 1/16" stainless steel tubes soldered to the plate. An innovative technique is used to provide self-centring of the tubes and precise control of the fraction of the tube inserted in the hole. This technique is based on standard Swagelok®olives. Front and back olives are fixed at one end of the tube, providing a stable foot print for the tube. The front olive is in stainless steel, providing a

leak tight connection with the tube, while the back ferrule is in brass, allowing tin soldering on the metal film. In this way it is possible to tailor the fraction of the tube entering the hole. In this case it is less than 0.5 mm to avoid interference with the microchannel cross section. In order to avoid contamination of the microchannel during the soldering process, this step is performed with a low pressure counter current nitrogen flow. The inlet-outlet ducts have a 90° bend to allow the positioning of the instrumentation on the same support housing the test section. Just after the bend, a stainless steel T-junction provides connection to a differential pressure transducer for the measurement of the pressure drop. The inlet is also connected to an absolute pressure transducer for the measurement of the inlet pressure. After the exit of the T-junction (Fig. 3.9) the tube diameter is increased to 6 mm in order to reduce the pressure drop. This choice also allows the measurement of the fluid's temperature inside the 6 mm tube in direct contact with the fluid.

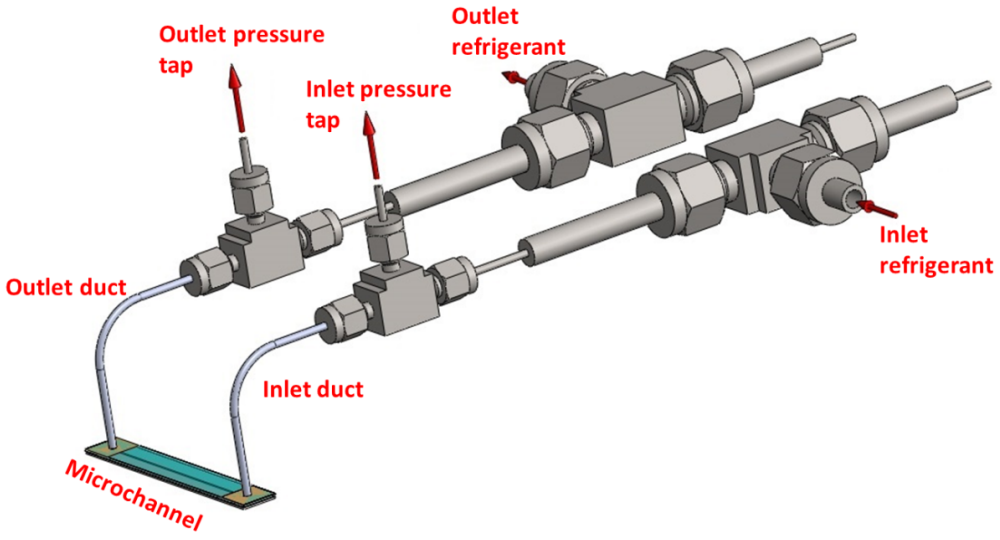


FIGURE 3.9: Schematic of the different components of the microchannel test section at the end of the fabrication process.

## 3.4 Experimental test facility

Experimental tests have been conducted in the Laboratory of Two-phase Heat Transfer of the Industrial Engineering Department at the University of Padova using R134a as refrigerants. The test rig used for the experimental tests is depicted in Fig. 3.10. It consists of the primary (refrigerant) loop and of two auxiliary loops: the cold water loop to control the subcooling at the inlet of the measuring section and the brine loop to control the refrigerant condensation after the test section. The subcooled refrigerant from the condenser passes through a filter drier and then enters in a variable speed gear pump, which allows setting the mass flow measured by a Coriolis-effect mass flow meter. Before entering the test section, the working refrigerant can be further subcooled. The subcooler is a tube-in-tube heat exchanger in which the primary fluid is cooled using brine flowing in the auxiliary loop. The refrigerant is finally sent to the test section. During the test runs, the refrigerant enters the pre-section as subcooled liquid. The thermodynamic state of the refrigerant at the inlet of the pre-section is determined from temperature and pressure measurements. The pre-section is a counter-flow heat exchanger in which flow rate and inlet temperature of distilled water are set to have the desired subcooling degree of the refrigerant at the inlet of the measuring section. The mass flow rate of the distilled water is measured by a Coriolis-effect mass flow meter. The water outlet temperature in the pre-section is measured by a T-type thermocouple and the water temperature difference between inlet and outlet is measured by a copper constantan triple-junction thermopile. Static mixers have been positioned upstream of the water temperature sensors and therefore the measured temperatures can be considered as the mean effective water temperature. The enthalpy of the refrigerant at the measuring section inlet is obtained from the temperature and pressure measurements at the section inlet. The pressure is gauged through three digital pressure transducers, connected to manometric taps to measure the fluid pressure at the inlet of the pre-section and upstream and downstream of the silicon microchannels frame.

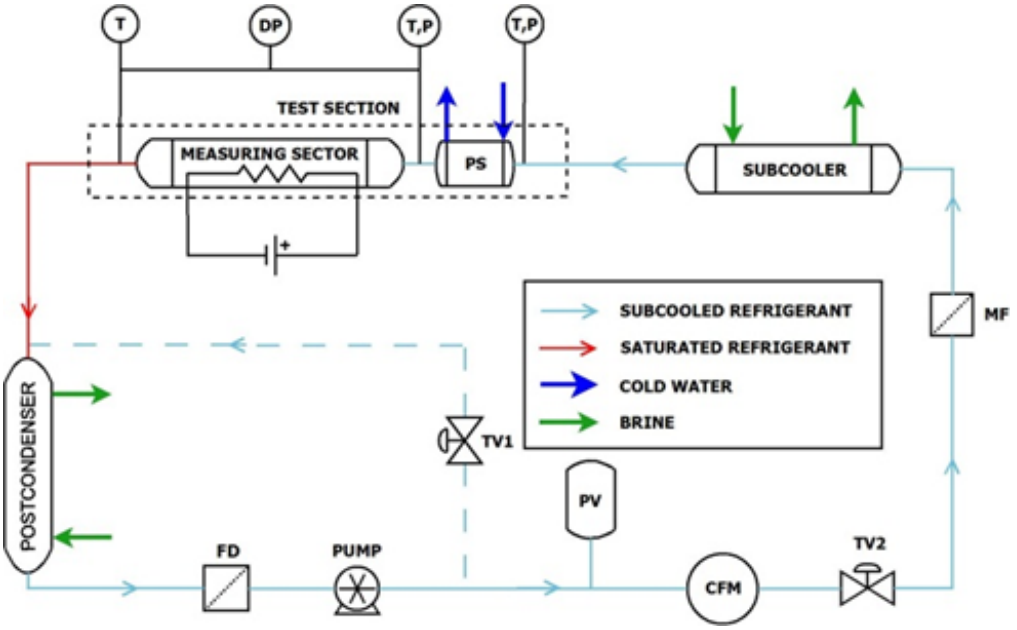


FIGURE 3.10: Experimental setup installed in the Two-phase Heat Transfer Lab in Padova used for the tests presented here (FD=filter drier, PV=pressure vessel, CFM=Coriolis-effect mass flow meter, TV=throttling valve, MF=mechanical filter, PS=pre-section, P=pressure transducer, T=temperature transducer, DP=differential pressure transducer).

Two refrigerated thermal baths are used: one provides the distilled water used as secondary fluid for the heat transfer in the pre-section, the other serves brine at 5°C to the subcooler and to the auxiliary loop of the condenser, in which the working refrigerant is condensed after exiting the measuring section. In every test run, when the apparatus is working in steady state conditions, measurements of thermo-fluid-dynamic parameters are recorded for 50 s with a step time of 1 s.

## 3.5 Thermal losses assessment

Before starting the experimental characterization, thermal losses from the test section to the environment have been accurately assessed. Thermal losses consist of two main components: heat exchange with the silicon plate of the microchannels $P_{AMB}$ and heat exchange from the fluid to the surrounding along the inlet and outlet ducts $P_{IN-OUT}$ (Fig. 3.11).

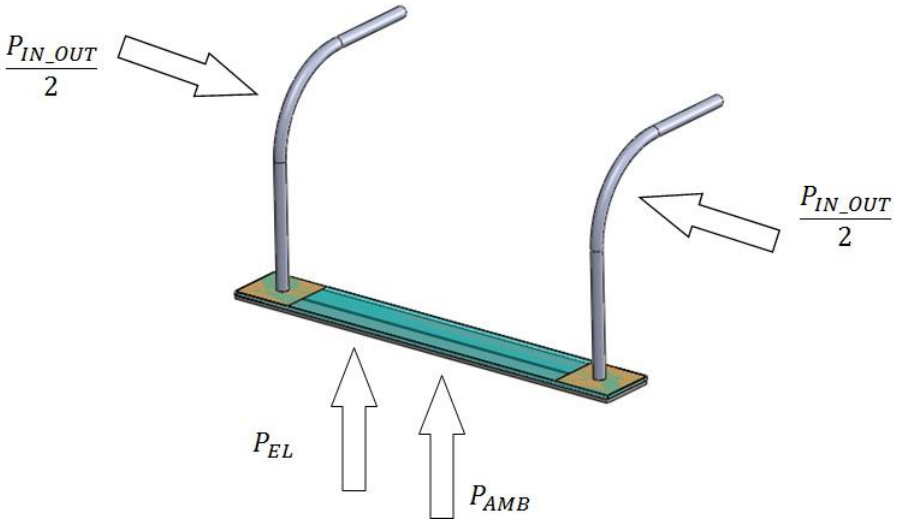


FIGURE 3.11: Schematic of the power sources to the test section.

The first term is measured experimentally by creating vacuum condition inside the test section in order to avoid convective heat exchange inside the duct. Power is then applied on the platinum heater $P_{EL}$. This power is entirely dissipated to the surrounding resulting:

$$P_{EL} = P_{AMB} \tag{3.1}$$

In this way it is possible to correlate heat losses from the silicon plate to the environment for different surface temperature. Results are reported in Fig. 3.12.

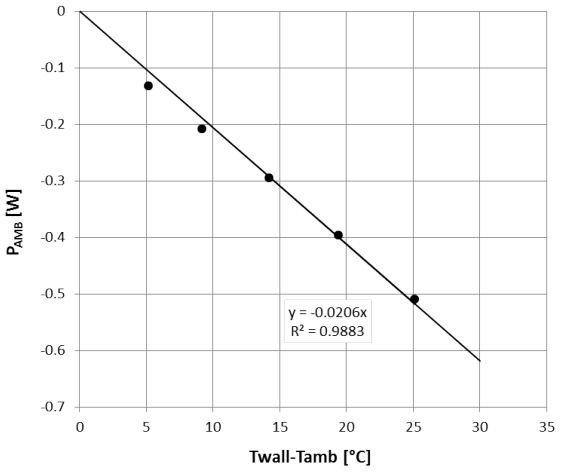


FIGURE 3.12: Experimental measurements of the heat loss component $P_{AMB}$.

For the evaluation of the second heat loss component $P_{IN-OUT}$, single-phase fluid flow is established in the test section. Three different mass fluxes were tested ranging from 1000 to 2300 kg $m^{-2}s^{-1}$. For each mass flux the inlet temperature is varied acting on the secondary fluid in the presection. No electrical power is provided to the platinum heater. In these conditions, the power absorbed by the fluid is the sum of the power exchanged through the silicon plate $P_{AMB}$ and the power exchanged along the inlet and outlet ducts $P_{IN-OUT}$:

$$P = P_{amb} + P_{IN-OUT} \tag{3.2}$$

The total power absorbed by the fluid P is obtained with a thermal balance on the fluid:

$$P = mc_p(T_{out} - T_{in}) \tag{3.3}$$

while the power exchanged though the silicon plate can be evaluate with the techniques shown before based on the plate surface temperature. Results of the power exchanged though the inlet and outlet ducts is presented in Fig. 3.13.

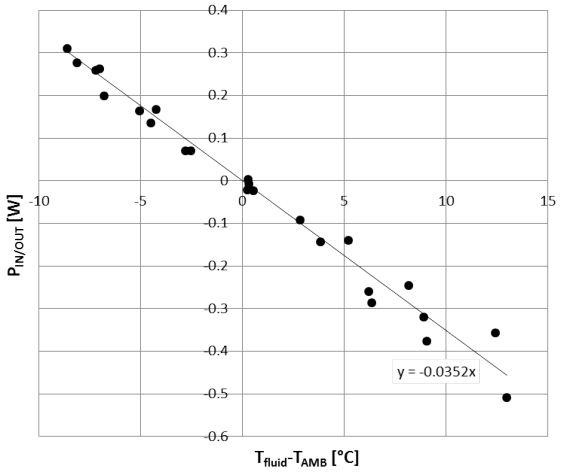


FIGURE 3.13: Experimental measurements of the heat loss component $P_{IN-OUT}$.

The verification of the experimental procedure adopted for the characterization of the individual heat loss components has been performed with another test with single-phase flow

with mass flux ranging from 900 a 5500 kg $m^{-2}s^{-1}$. Electrical power is provided to the platinum heater in the range 1.5 – 12 W. Global thermal balance is checked considering all the heat source contributions identified and resumed in Fig. 3.9: supply electrical power$P_{EL}$, power exchanged through the silicon plate $P_{AMB}$ and power exchanged along the inlet and outlet ducts $P_{IN-OUT}$. The sum of all these contributions should give the power absorbed by the fluid P, and quantified through an energy balance:

$$P = P_{EL} + P_{amb} + P_{IN-OUT} \tag{3.4}$$

The results of this test are shown in Fig. 3.14. As it is possible to see, the accuracy of the global thermal balance is very good, meaning that the single contributions have been estimated correctly.

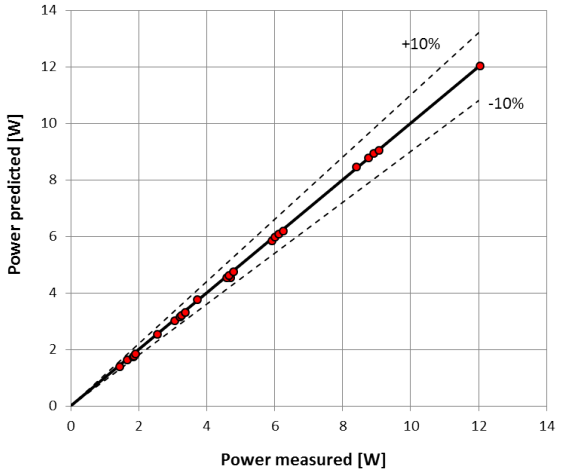


FIGURE 3.14: Experimental verification of the thermal balance on the fluid.

## 3.6 Single-phase characterization

Single-phase characterization is a fundamental step before any flow boiling experiment. The aim of this step is to perform single-phase tests at different operating conditions measuring fundamental parameters like the channel pressure drop and the heat transfer characteristics.

The experimental data obtained are compared with common correlations in term of friction factor and heat transfer coefficient.

### 3.6.1 Single-phase pressure drops

Single-phase pressure drop tests were performed in adiabatic conditions. The fluid enters the test section with a temperature close to the ambient temperature to minimize heat exchange with the ambient. No electrical power is provided to the platinum heater. Experiments were performed at mass fluxes ranging from G=250 $kgm^{-2}s^{-1}$ to G=4000 $kgm^{-2}s^{-1}$ in the Reynolds number range of Re=500-8000. The friction factor is obtained from the pressure drop in the channel as:

$$f_{exp} = \frac{Dp_{chann}\rho D_h}{2G^2 L} \tag{3.5}$$

The pressure drop in the channel is obtained from the pressure drop measured by the differential pressure transducer at the extremities of the test section by considering the local pressure drops present from the pressure tap to the beginning of the channel both for the inlet and the outlet. Three main contribution of local pressure drops were identified: pressure drop in the 90° bend in the stainless steel inlet and outlet connection ducts, sharp 90° bend from the stainless steel ducts to the silicon substrate and area variation from the inlet hole to the channel cross section. These contributions, calculated according to correlations proposed by Idelchik [3], are subtracted from the total pressure drop measured by the transducer to obtain the pressure drop in the channel. Results for the experimental friction factor as function of the Reynolds number are presented in Fig. 3.15. As it is possible to see in Fig. 3.14-3.18, experimental data show an early departure from laminar conditions around Re=1000. This could be caused by the sharp variation of the fluid direction and the variation of the cross section from the inlet duct to the microchannel introducing sources of turbulence to the flow.

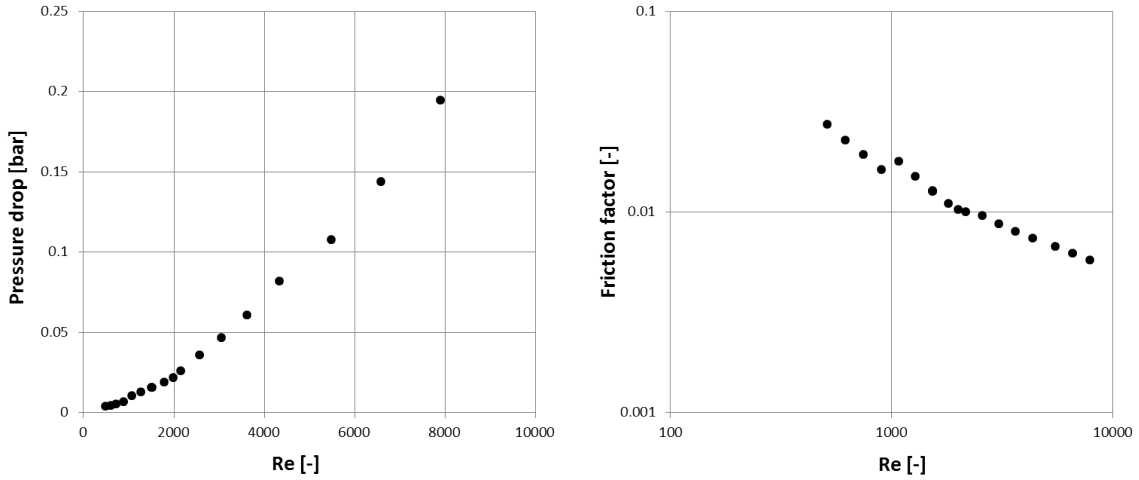


FIGURE 3.15: Experimental pressure drop and friction factor as function of the Reynolds number.

Comparisons of the friction factor data with available correlations for single-phase flow are reported in the following plots.

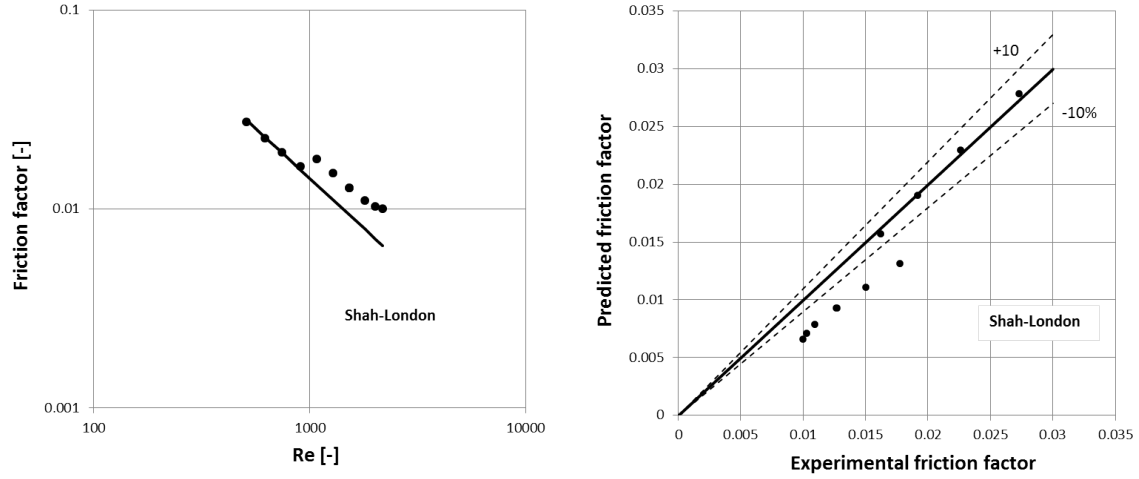


FIGURE 3.16: Comparison of the experimental friction factor data with the Shah-London correlation.

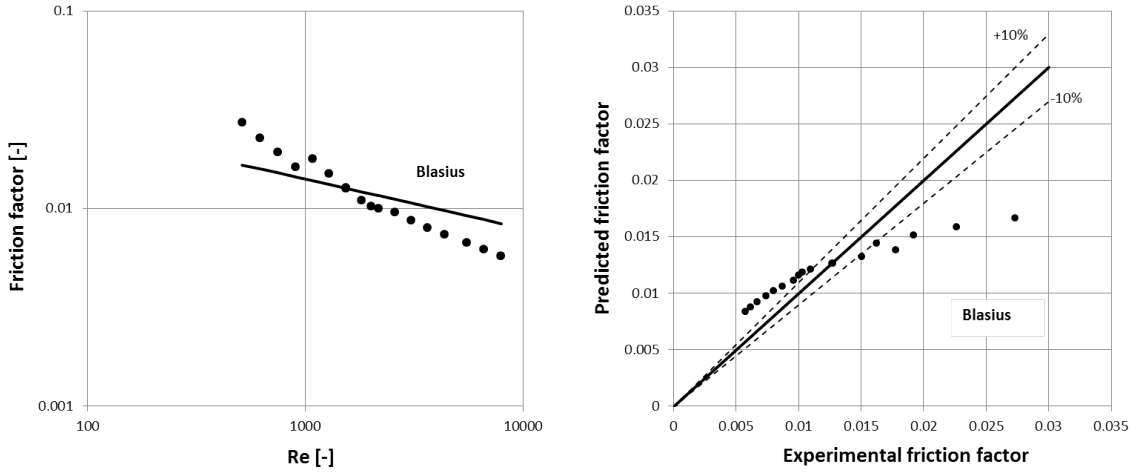


FIGURE 3.17: Comparison of the experimental friction factor data with the Blasius correlation.

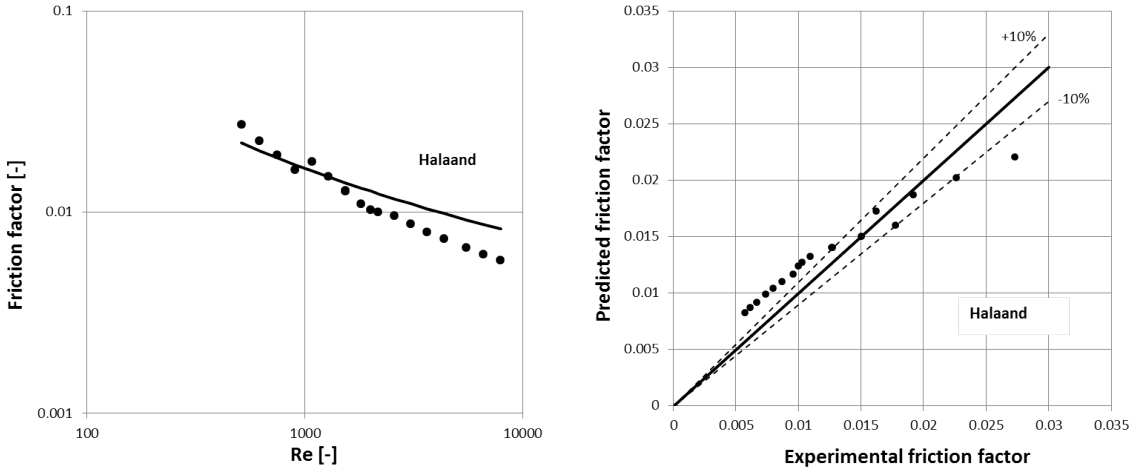


FIGURE 3.18: Comparison of the experimental friction factor data with the Haaland correlation.

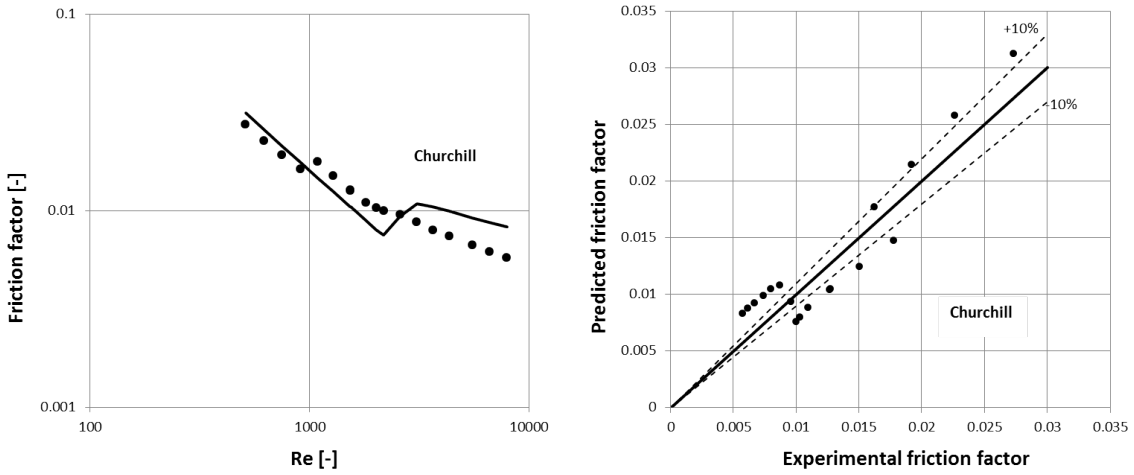


FIGURE 3.19: Comparison of the experimental friction factor data with the Churchill correlation.

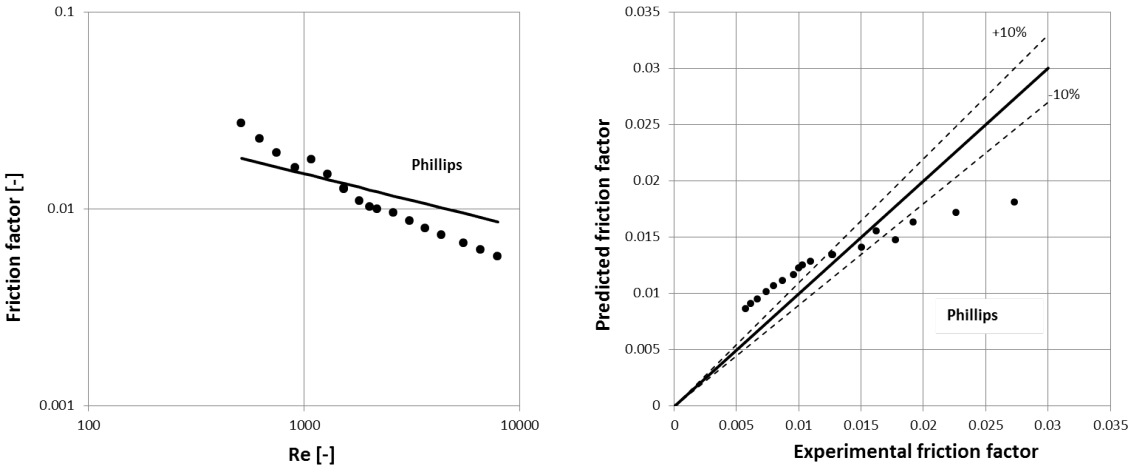


FIGURE 3.20: Comparison of the experimental friction factor data with the Phillips correlation.

The comparison of the friction factor experimental data with appropriate e correlations shows that the Shah-London correlation is able to predict very well the four points before the departure from the laminar characteristics. After this point, turbulent correlations show a MAE around 22% in the prediction of the experimental data, also considering correlations for all Reynolds number like Churchill or the correlation of Phillips which includes the effect of the developing region.

| Correlation | MAE% | Comments |
|---|---|---|
| ShahLondon | 1.84 | four points |
| Blasius | 22.24 | full data set |
| Haaland | 20.5 | full data set |
| Churchill | 22.14 | full data set |
| Phillips | 23.9 | full data set |

TABLE 3.2: Resume of the comparison of friction factor data with predictive correlations

### 3.6.2 Single-phase heat transfer

Single-phase liquid flow heat transfer tests are performed at a constant refrigerant flow rate and constant fluid parameters. Increasing power is applied on the platinum heater. Mass fluxes tested ranges from G=260 to 5500 kg m−2s−1 with Reynolds numbers ranging from 600 to 11000. The heat flux at the walls of the channel ranges from 24.5 to 195 kWm−2. The heat transfer coefficient is calculated as the ratio of the heat flux at the channel walls and the temperature difference between the average surface temperature measured on the heater and the average fluid temperature between inlet and outlet:

$$h = \frac{Dp_{chann}\rho D_h}{2G^2 L} \tag{3.6}$$

The real power P is obtained from the electric input power $P_{EL}$ by taking into account heat losses. The heat exchange area is represented by the three silicon side of the channel, while the fourth glass side is considered adiabatic. The Nusselt number is obtained from the heat transfer coefficient as:

$$Nu = \frac{h_{exp} D_h}{k_f} \tag{3.7}$$

where $k_f$ is calculated at the average temperature and pressure in the channel. The single-phase heat transfer coefficients and Nusselt number obtained during the tests are presented in Fig. 3.21 as a function of the Reynolds number.

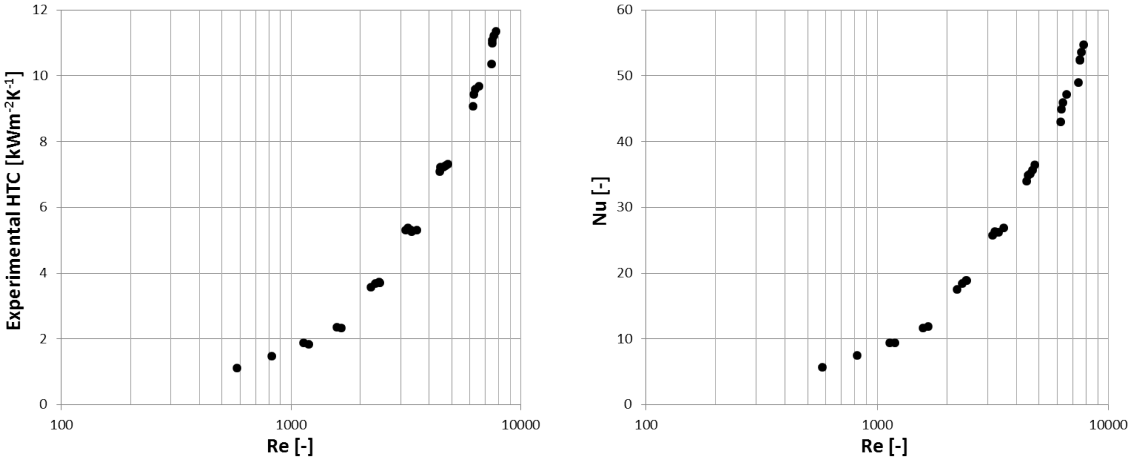


FIGURE 3.21: Experimental single-phase heat transfer coefficient and Nusselt number data.

The comparison of the experimental data with standard correlations for single-phase heat transfer coefficient is presented in Fig. 3.22-3.28. As for the single-phase flow tests, an early departure from laminar characteristics is observed. While laminar correlations like Shah-London and Hausen are able to predict only one point at the lowest Re, correlations for the turbulent regime are able to predict the full data set with acceptable accuracy.

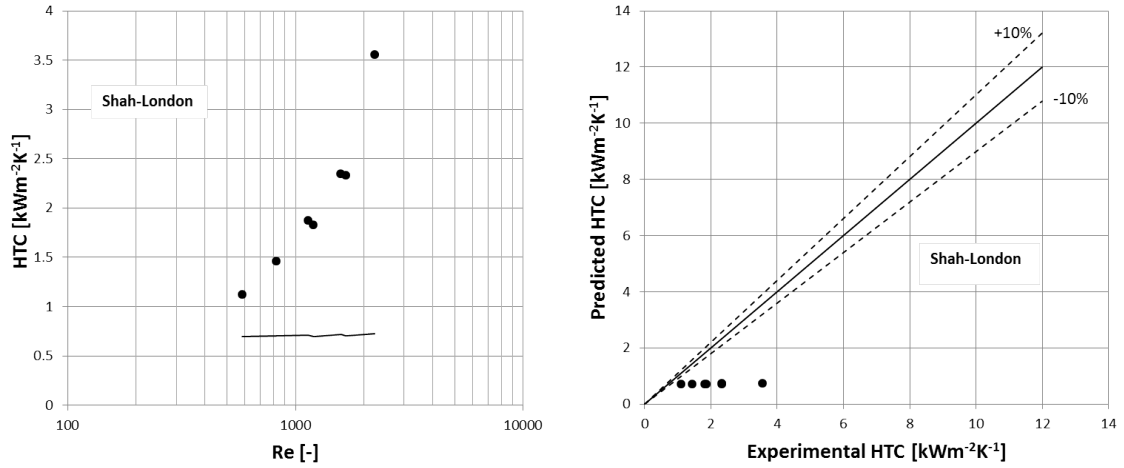


FIGURE 3.22: Comparison of the experimental heat trasfer coefficient data with the Shah-London correlation

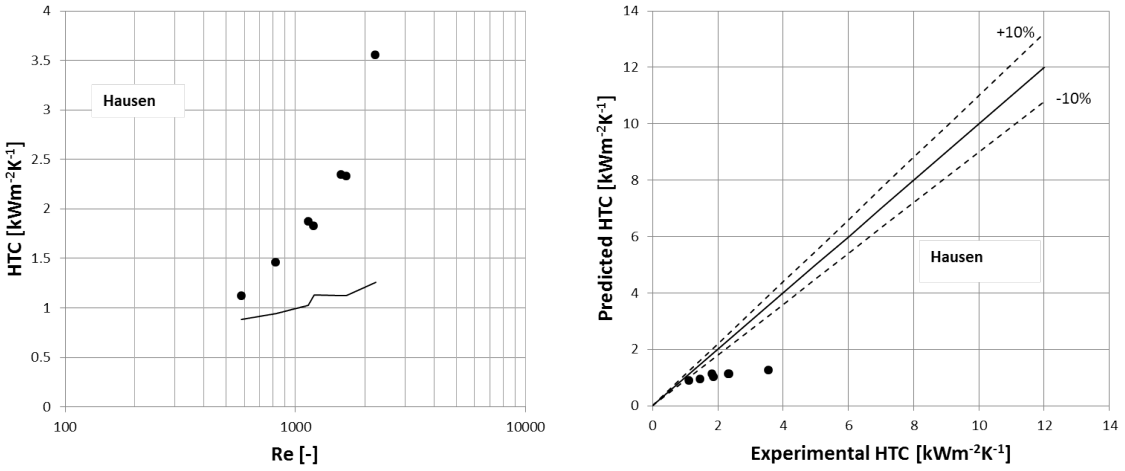


FIGURE 3.23: Comparison of the experimental heat trasfer coefficient data with the Hausen correlation

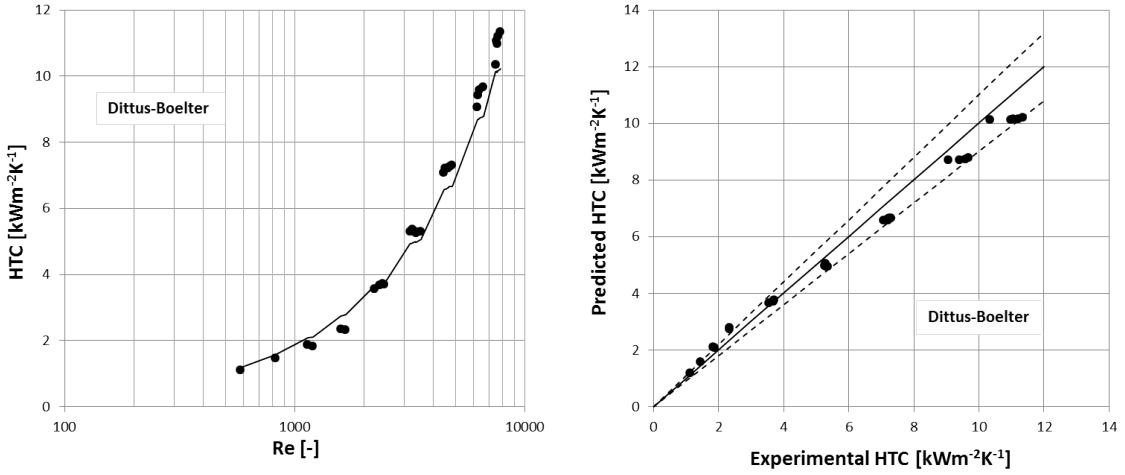


FIGURE 3.24: Comparison of the experimental heat trasfer coefficient data with the Dittus-Boelter correlation

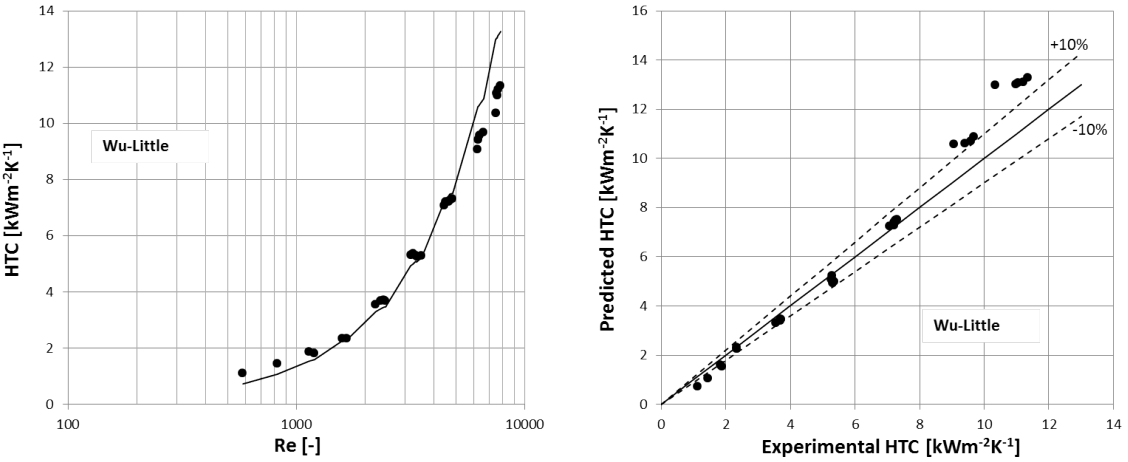


FIGURE 3.25: Comparison of the experimental heat trasfer coefficient data with the Wu-Little correlation

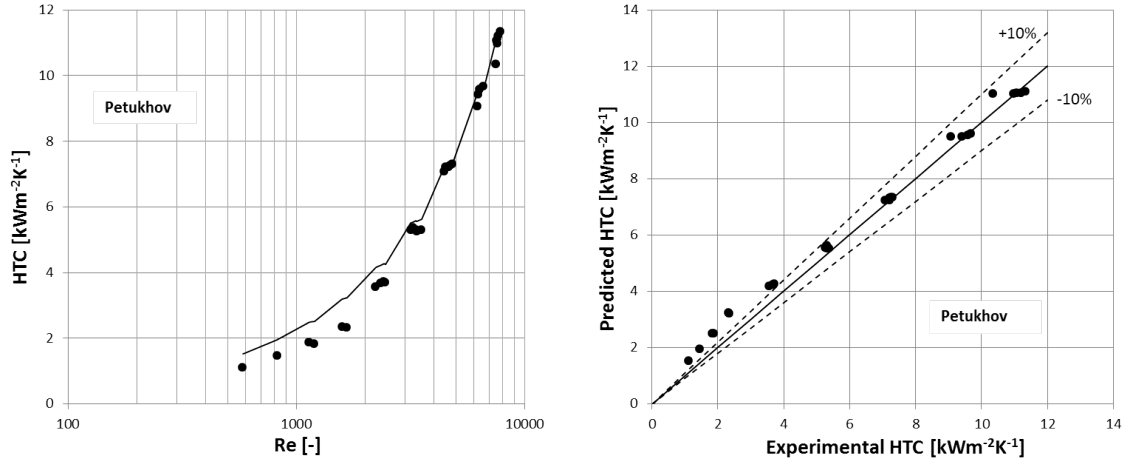


FIGURE 3.26: Comparison of the experimental heat trasfer coefficient data with the Petukhov correlation

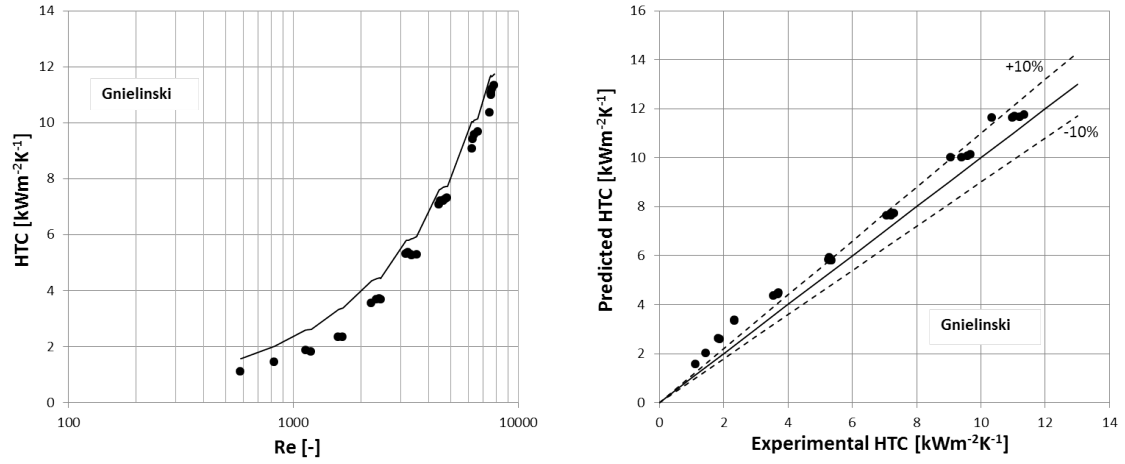


FIGURE 3.27: Comparison of the experimental heat trasfer coefficient data with the Gnielinski correlation

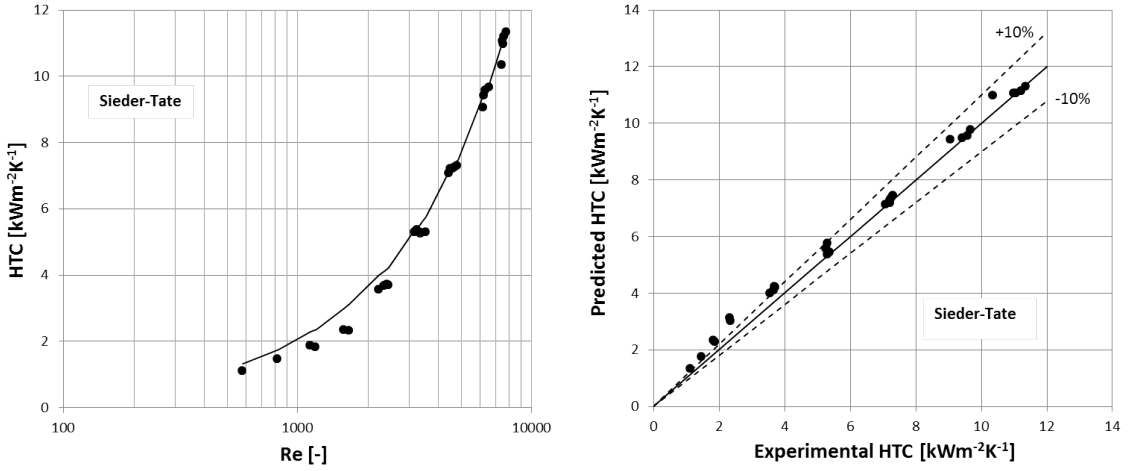


FIGURE 3.28: Comparison of the experimental heat trasfer coefficient data with the Sieder-Tate correlation

From Tab. 3.3 it is possible to see that laminar correlations are not able to represent the experimental heat transfer coefficient data even in a reduced set at the lowest Reynolds numbers. On the other side, correlations for the turbulent regime are able to represent the full data set with MAE around 10%. The best result is obtained by the Dittus-Boelter correlation which is able to represent the full data set with MAE=7.6%.

| **Correlation** | **MAE%** | **Comments** |
|---|---|---|
| ShahLondon | 61.8 | seven points |
| Hausen | 44.1 | seven points |
| Dittus-Boelter | 7.6 | full data set |
| Wu-Little | 10.6 | full data set |
| Petukhov | 11.2 | full data set |
| Gnielinski | 16.3 | full data set |
| SiederTate | 10.2 | full data set |

TABLE 3.3: Resume of the comparison of heat transfer coefficient data with predictive correlations

## 3.7 Onset of Nucleate boiling and boiling curves

Flow boiling tests are performed at constant saturation pressure $T_{sa}t$=30°C and constant mass flux. Four different mass fluxes were tested G: 400, 800, 1200 e 1600 kgm−2s−1. For each test case the fluid enters the test section with 5°C of subcooling. The power applied the platinum heater is increased at step of 0.25 W until the onset of nucleate boiling (ONB) occurs. ONB is clearly detected by the sudden increase of the pressure drop and the fall of the surface temperature as it is possible to see in Fig.3.29.

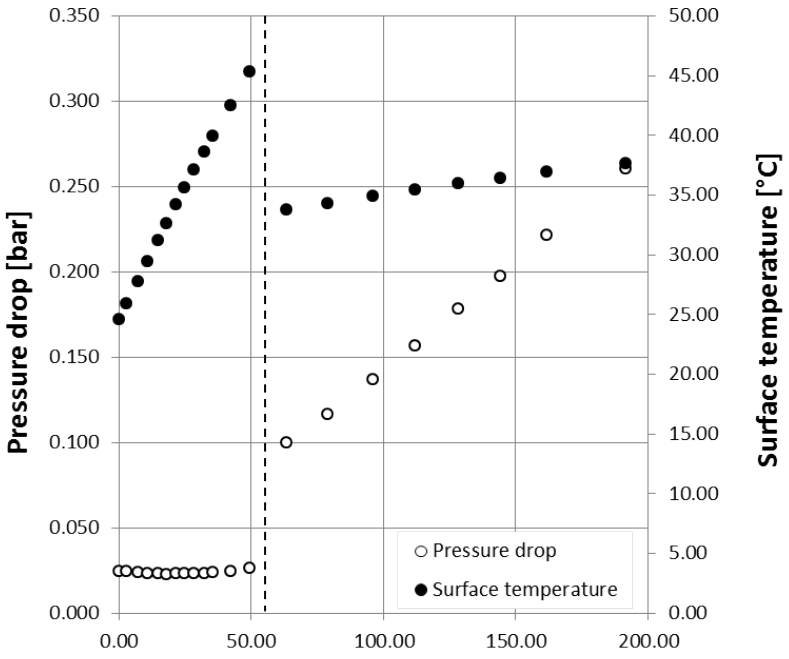


FIGURE 3.29: Surface temperature and pressure drop trends before and after ONB.

The Onset of Nucleate Boiling (ONB) is the point when first vapor bubbles are generated inside the liquid marking the transition from single–phase liquid flow to a two-phase flow regime. This transition is accompanied by a sudden increase of pressure drop because two-phase interfacial stresses and a significant enhancement of the heat transfer rate. Experimental results of the heat flux at the Onset on Nucleate Boiling are presented in Fig. 3.30 compared with predictive correlations.

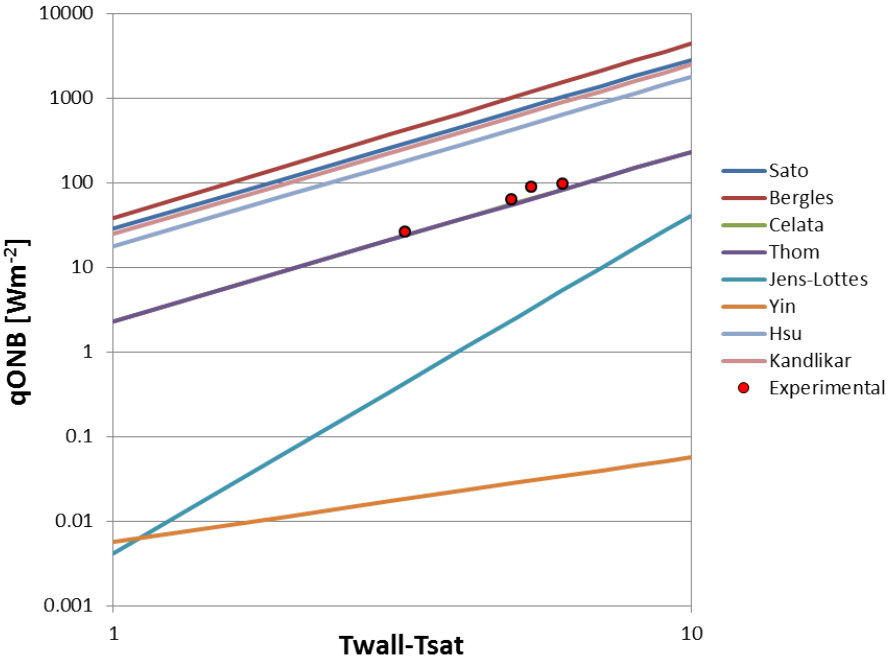


FIGURE 3.30: Comparison of the experimental data of the heat flux at the Onset of Nucleate boiling with predictive correlations.

The best predictive correlation for the representation of the qONB data obtained in this study are the correlations of Celata et al. [114] and Thom et al. [115] with a MAE around 15%. After the ONB occurrence, the power provided to the heater is kept increasing so the full boiling curve is obtained for each muss flux. The boiling curve is obtained both at increasing power and decreasing power to investigate any possible hysteresis effects. Boiling curves obtained for each mass flux testes are presented in Fig. 3.31-3.34.

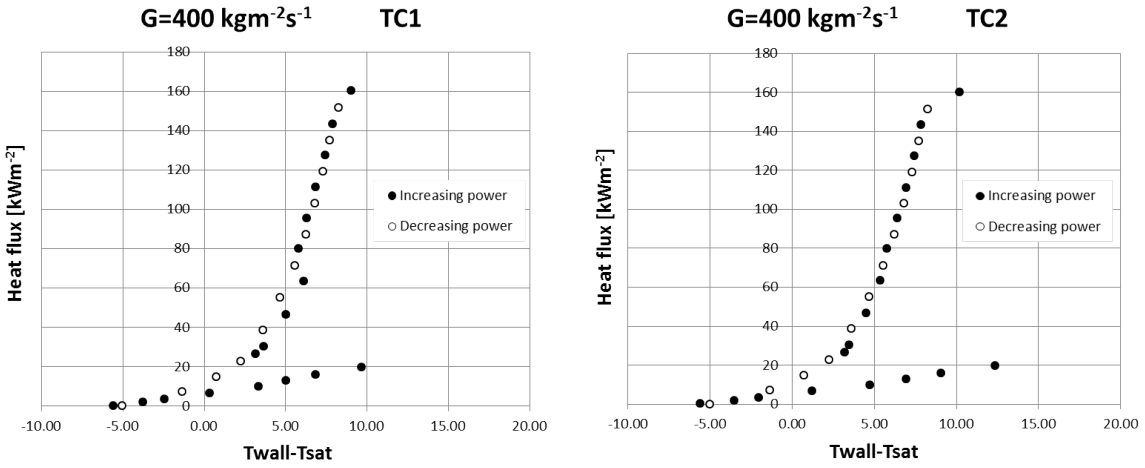


FIGURE 3.31: Comparison of the experimental data of the heat flux at the Onset of Nucleate boiling with predictive correlations.

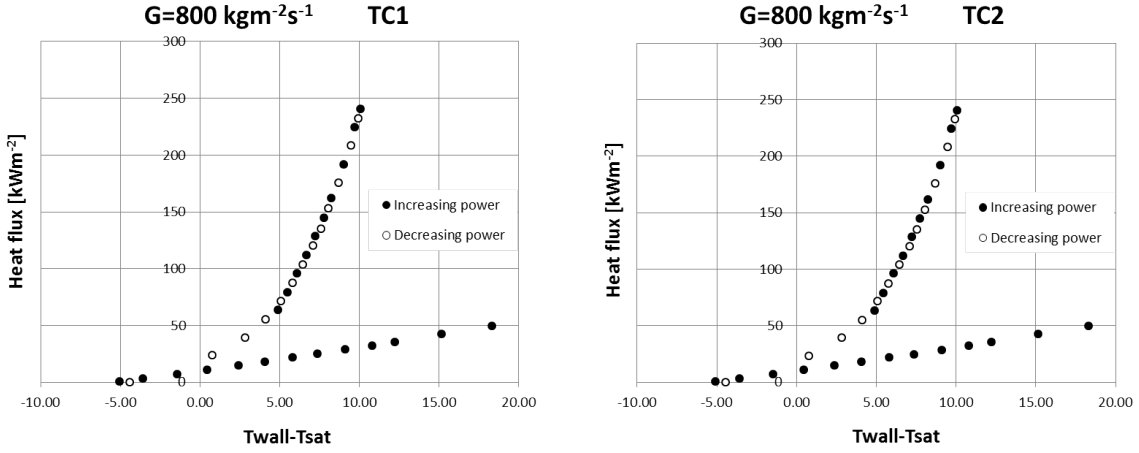


FIGURE 3.32: Comparison of the experimental data of the heat flux at the Onset of Nucleate boiling with predictive correlations.

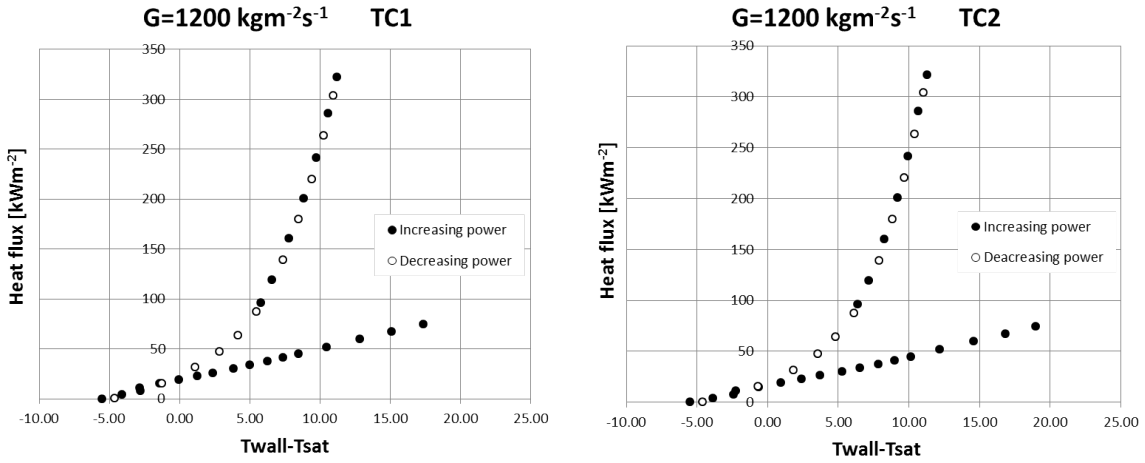


FIGURE 3.33: Comparison of the experimental data of the heat flux at the Onset of Nucleate boiling with predictive correlations.

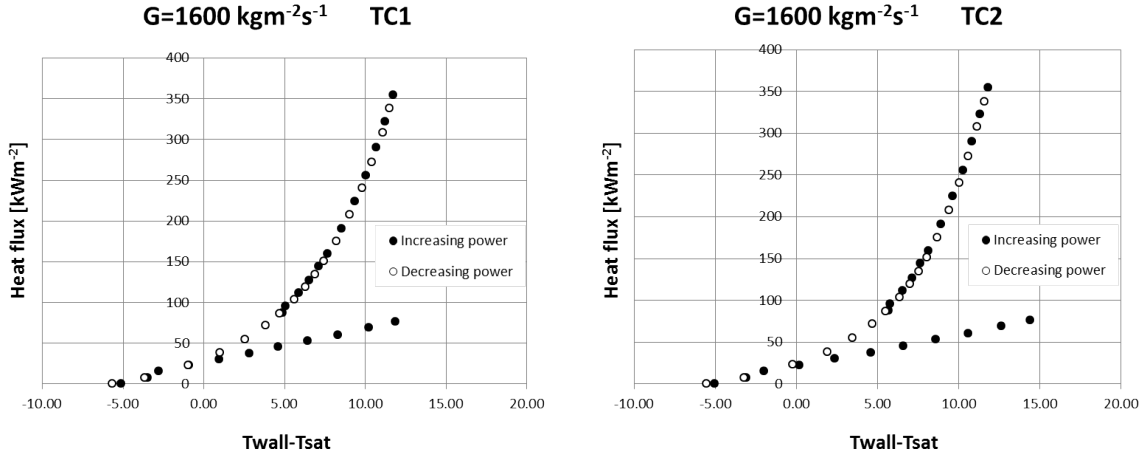


FIGURE 3.34: Comparison of the experimental data of the heat flux at the Onset of Nucleate boiling with predictive correlations.

From the previous figures it is possible to see that during single-phase flow at low heat fluxes the surface temperature increases until the temperature difference between the surface of the channel walls and the fluid saturation temperature is high enough to activate the first nucleation sites marking the onset of nucleate boiling. From this point on, the power is increased at lower temperature differences because of the higher heat transfer rate. Once reached the maximum set heat flux (Critical Heat Flux was not investigated in this study) the power is decreased step by step and the boiling curve at decreasing power is obtained. As it is possible to see from the previous pictures, no hysteresis was observed between the

boiling curves at increasing and decreasing power. By comparing all the boiling curves obtained in the same position along the channel is possible to evaluate the effect of the mass flux on the boiling curve (Fig. 3.35). The effect of the mass flux is visible during single-phase flow, as expected, but it is negligible once the boiling process starts.

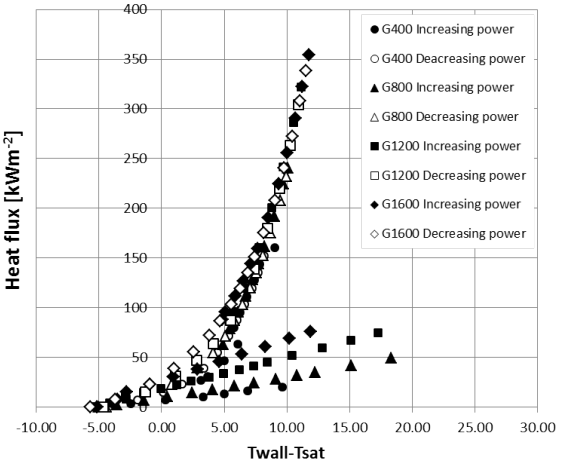


FIGURE 3.35: Comparison of boiling curves at different mass fluxes.

It's worth noting from Fig. 3.33 that except for the lowest mass flux value (G=400 kgm−2s−1) the temperature overshoot at ONB decreases at increasing mass fluxes, as previously reported by [117].

## 3.8 Flow boiling heat transfer coefficient

The flow boiling heat transfer coefficient is calculated as:

$$h = \frac{P/A}{(T_{wall} - T_{sat})} = \frac{q}{(T_{wall} - T_{sat})} \tag{3.8}$$

The temperature of the channel wall $T_{wall}$ is obtained from the local measurement of the thermocouple considering the conductive thermal resistance of the silicon substrate. The local saturation temperature $T_{sat}$ along the channel is obtained from the local saturation pressure. The local pressure is calculated assuming a linear pressure profile from the inlet

to the outlet of the channel. The pressure drop in the channel is obtained from the total pressure drop measured by the differential pressure transmitter by considering the local pressure drop components described for the single-phase pressure drop tests. The same correlations are adopted for the calculations of the local pressure drops but in this case, for the components at the outlet of the channel, where the fluid is in two-phase conditions, the properties of the fluid are calculated assuming the homogeneous description of two-phase flows. The vapor quality at the local position is obtained assuming a linear profile from the inlet vapor quality $x_{in}$ and the outlet vapor quality $x_{out}$. At the inlet, where the fluid is in single-phase conditions, the vapor quality is calculated based on the local pressure and temperature as:

$$x_{in} = \frac{h_{in} - h_L}{h_V - h_L} \tag{3.9}$$

The exit vapor quality is based on the energy balance of the fluid as:

$$h_{out} = h_{in} + \frac{P}{\dot{m}} \tag{3.10}$$

Experimental results of the heat transfer coefficient as a function of the local vapor quality are presented in Fig. 3.34 for the different mass fluxes tested.

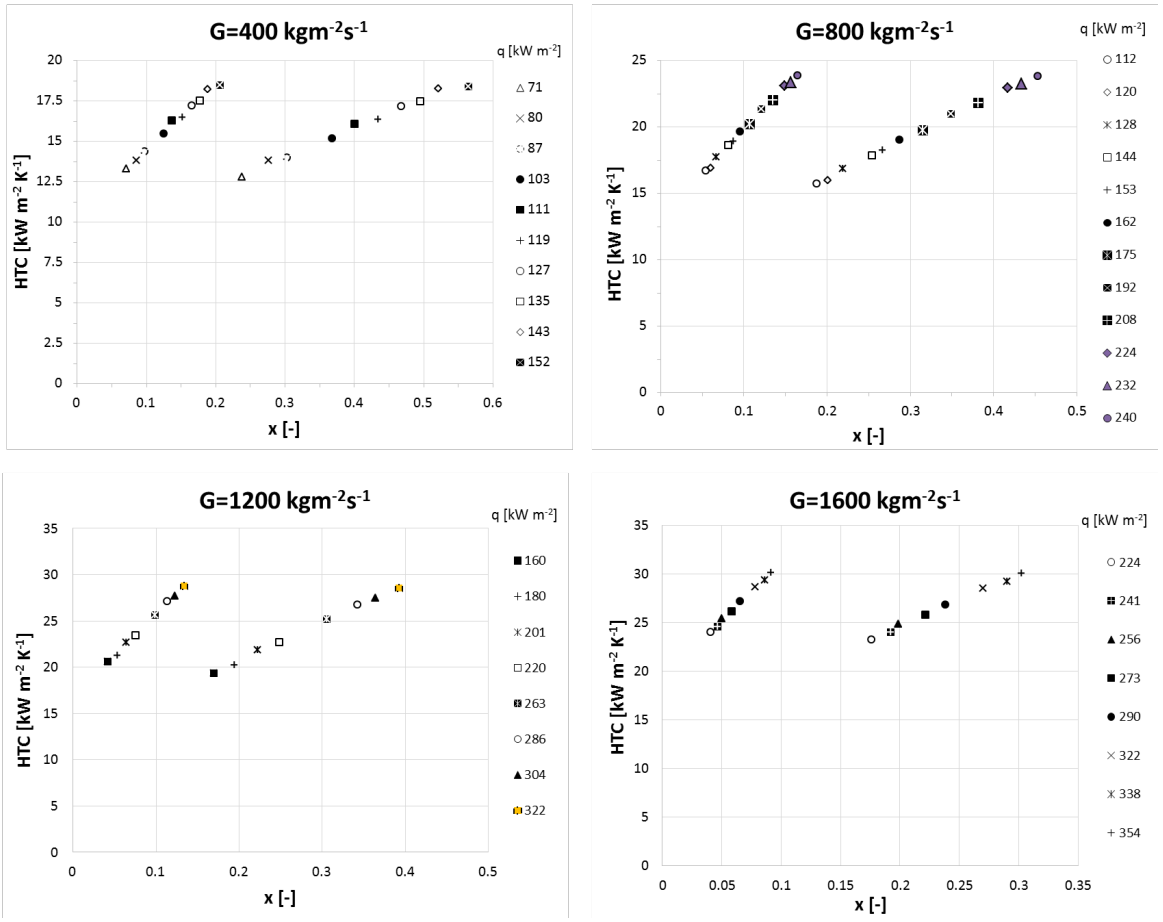


FIGURE 3.36: Heat transfer coefficient as a function of the local vapor quality for the four mass fluxes tested.

The trend of the heat transfer coefficient versus the local vapor quality x is shown in Fig. 3.37. As it can be seen, for the conditions tested in this work, the heat transfer coefficient is not significantly affected by the vapor quality.

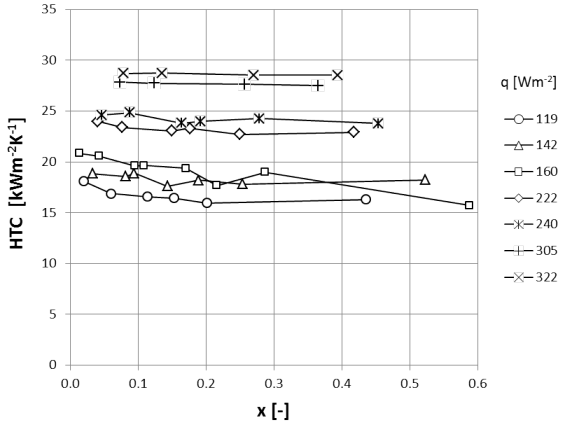


FIGURE 3.37: Heat transfer coefficient as a function of the local vapor quality for the four mass fluxes tested.

Experimental heat transfer coefficient data were compared with predictive correlations available in the literature. The results of the comparison are shown in the following figures.

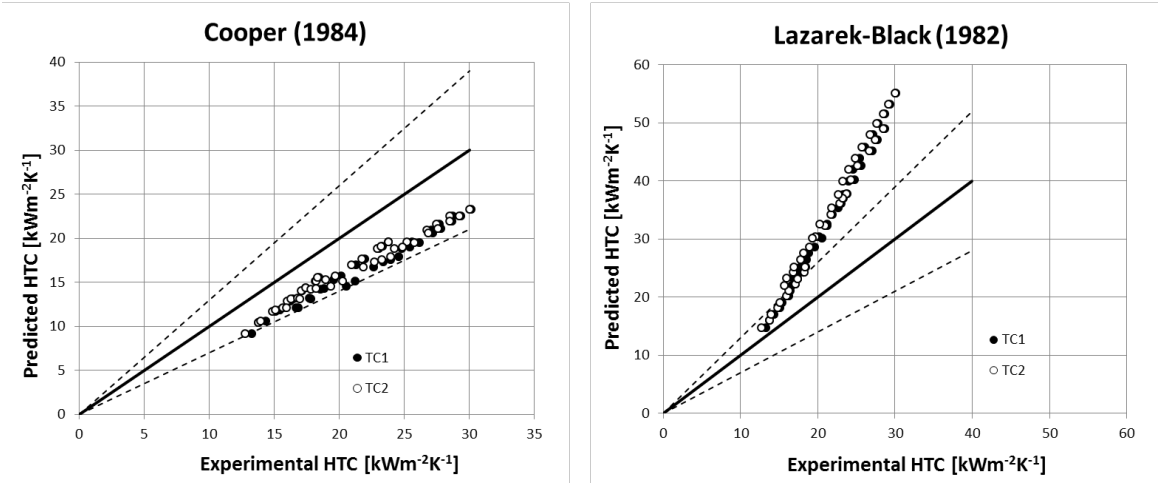


FIGURE 3.38: Comparison of experimental HTC data with different predictive correlations

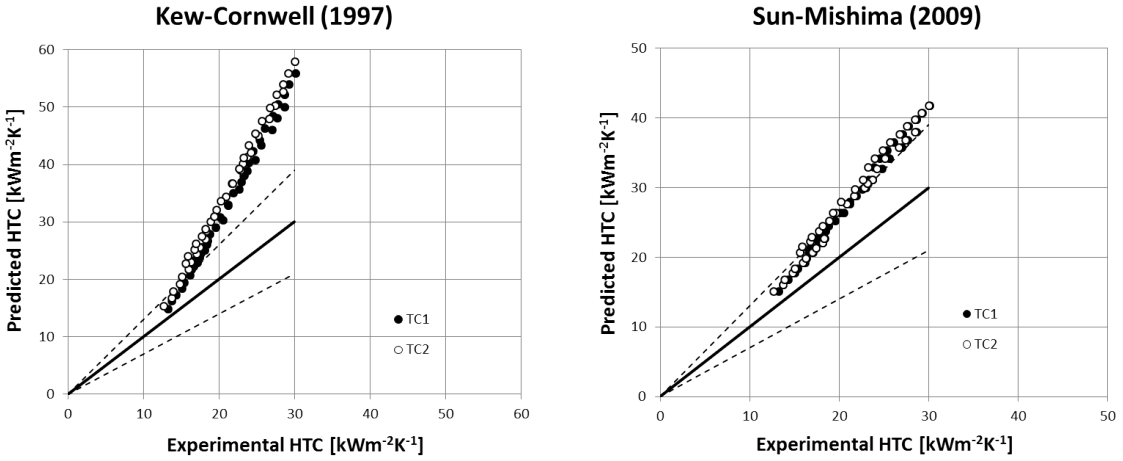


FIGURE 3.39: Comparison of experimental HTC data with different predictive correlations

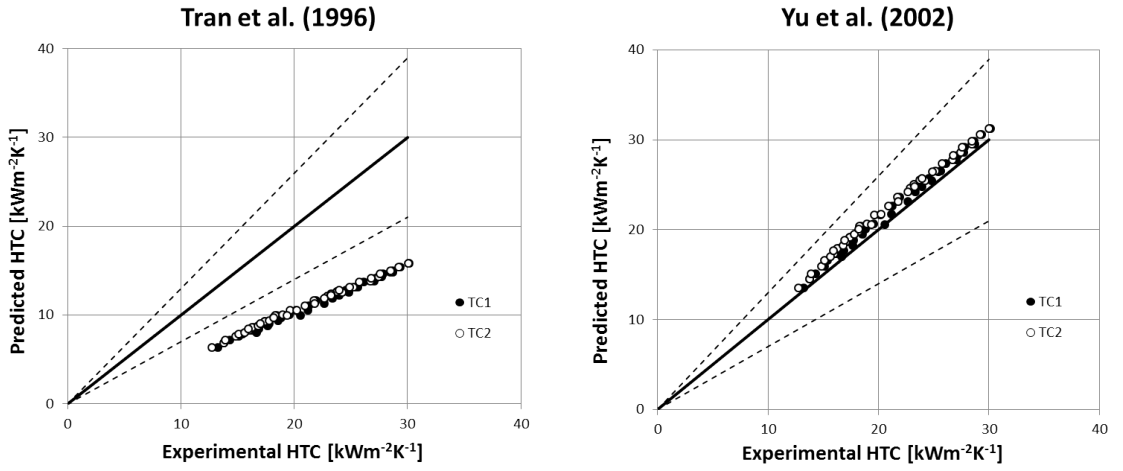


FIGURE 3.40: Comparison of experimental HTC data with different predictive correlations

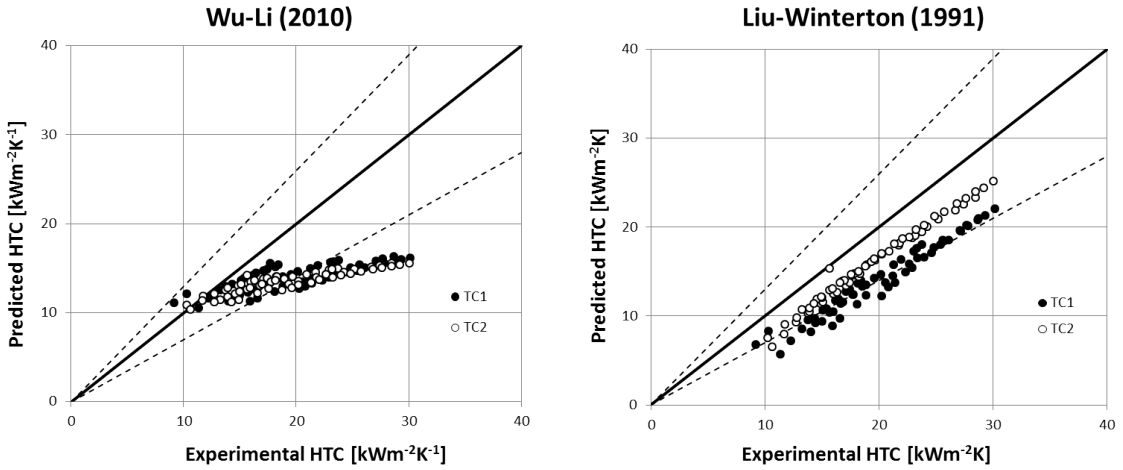


FIGURE 3.41: Comparison of experimental HTC data with different predictive correlations

## 3.9 Effect of tailored lateral roughness on flow boiling characteristics

The effect of surface roughness on flow boiling characteristics is a very important feature of the physics of microscale heat transfer phenomena and not enough investigated in experimental studies. For this reason, a dedicated test section was designed to address the effect of lateral tailored roughness on the microscale flow boiling heat transfer process. The test section is identical to the one used in the previous experiments, except for the presence of lateral roughness structures introduced during the fabrication process. In order to increase the repeatability of the process and to have a full control on the dimension of the roughness structures, these were included in the lithography mask thus assuring a perfect pattern transfer to the silicon substrate during the lithography process and the subsequent etching step. The roughness structures were designed with a precise pattern similar to real roughness structures within the microfabrication capabilities available at the processing site. The structures are designed like triangular cavities for the full height of the microchannels. The depth of the cavity is 10 $\mu$m, the width of the mouth is 20 $\mu$m and the interspace between two cavities is 100 $\mu$m and this pattern is repeated for the full length of the microchannel on both lateral walls.

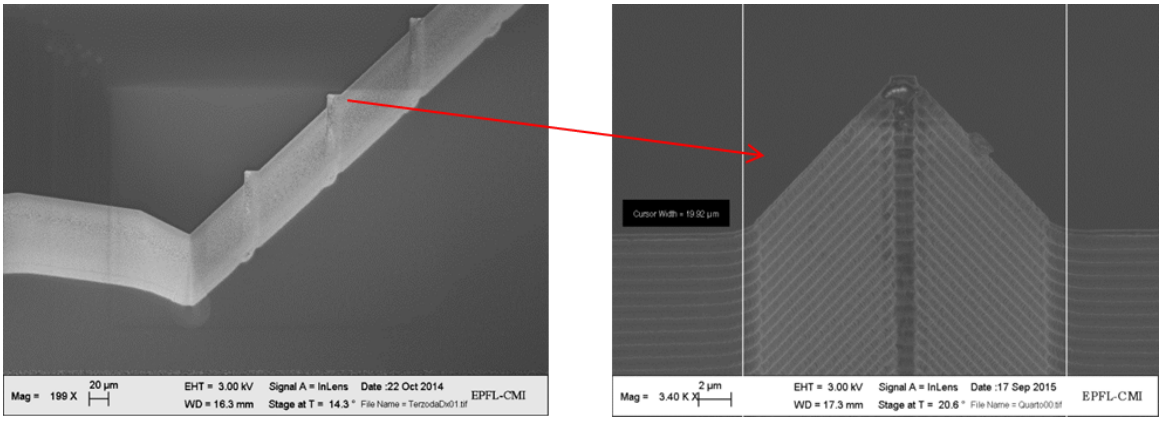


FIGURE 3.42: Scanning Electron Microscope images of the triangular roughness elements.

The characterization tests were performed for two mass velocities G=800 and G=1600 kg m−2s−1 at the same experimental condition set for the previous tests. The comparison of

the boiling curves obtained with the plain channel and with the microstructured channel is reported in Fig. 3.43-3.44.

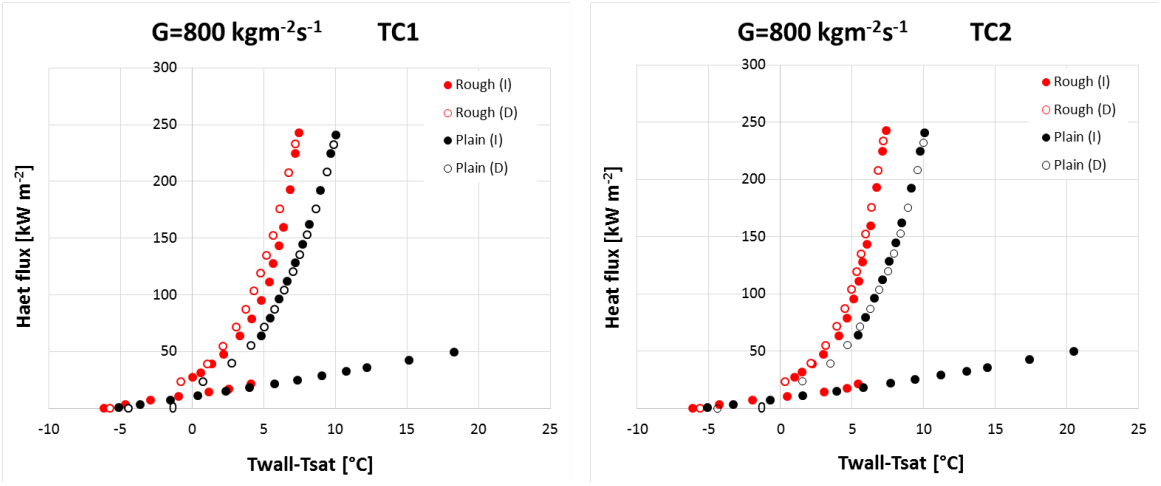


FIGURE 3.43: Comparison of boiling curves for the plain microchannel and the microstructured microchannel for G=800 kg $m^{-2}s^{-1}$

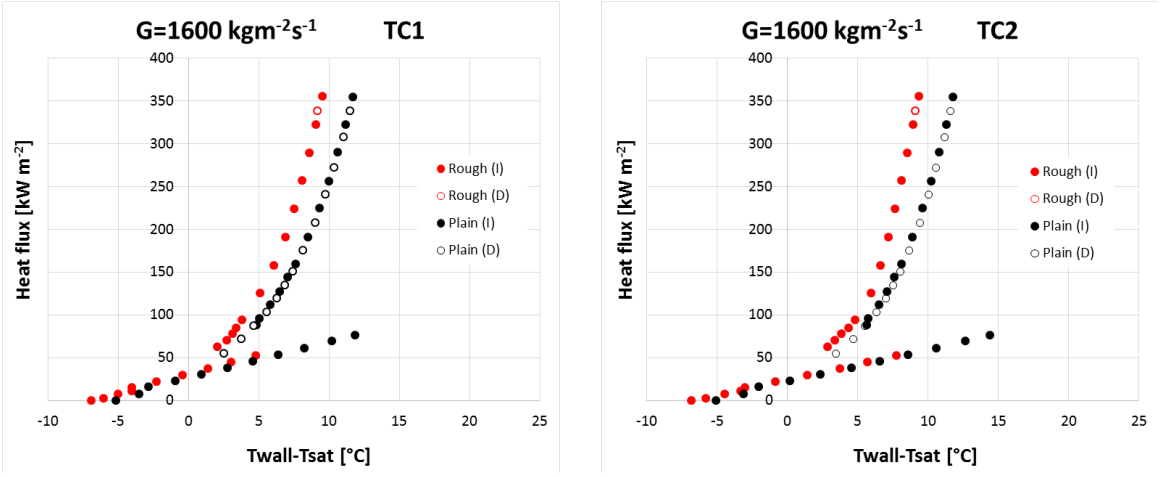


FIGURE 3.44: Comparison of boiling curves for the plain microchannel and the microstructured microchannel for G=1600 kg $m^{-2}s^{-1}$

As for the case of the plain microchannel, no hysteresis effects are observed between the boiling curve at increasing power and the curve at decreasing power. The comparison between the boiling curve for the plain microchannel and the boiling curve for the microstructured channel provides interesting insights. First, it is possible to see that for the case of the microstructured channel the temperature overshoot at the onset of nucleate boiling is much reduced compared with the plain channel. This is probably because the microstructures

introduced increases the availability of nucleation sites and thus decreases the temperature required to activate a specific nucleation site. Is then worth noting that the full boiling curve for the microstructured channel is shifted towards lower temperature differences. This means that in the structured microchannel the heat transfer process is enhanced compared to the plain channel. This is probably related to the increased heat transfer area by the microstructures, the increased turbulence at the wall improving heat transfer performance and the increased number of active nucleation sites. When comparing the heat transfer coefficient for the case of the plain channel and the structured channel the increase of the heat transfer performance become clear.

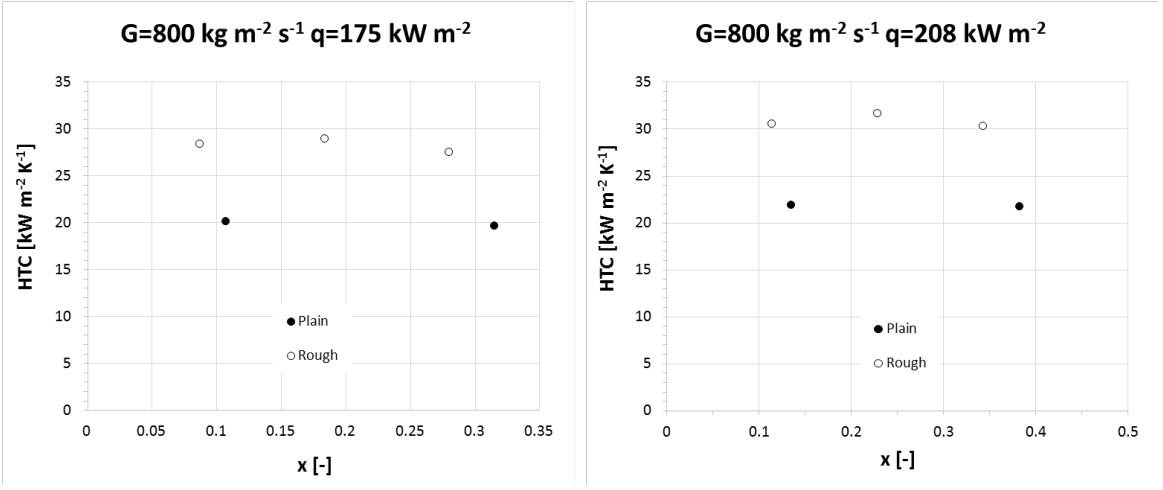


FIGURE 3.45: Figure 50 Comparison of experimental HTC for the plain microchannel and the structured microchannel at G=800 kg $m^{-2}s^{-1}$.

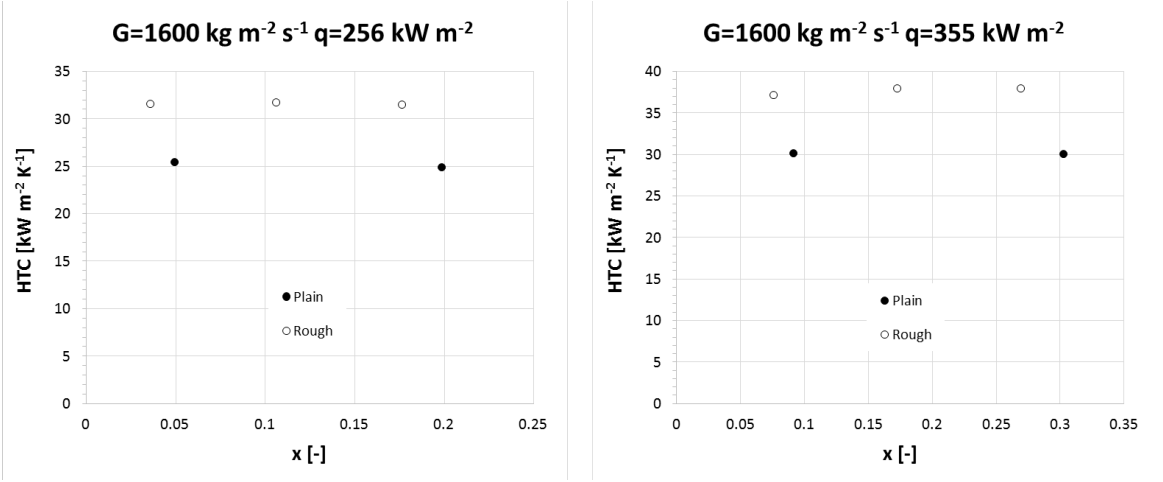


FIGURE 3.46: Comparison of experimental HTC for the plain microchannel and the structured microchannel at G=800 kg$m^{-2}s^{-1}$.

The increase of the heat transfer coefficient for the test conditions is around 40% at G=800 kg $m^{-2}s^{-1}$ and around 25% at G=1600 kg $m^{-2}s^{-1}$. The reduction of the heat transfer enhancement at higher mass fluxes could mean that the main heat transfer enhancement process in the microstructured channel is the increase of the number of active nucleation sites at a certain temperature. This process is related to the nucleate component of the flow boiling process and not to the convective component. This could explain the decrease of the heat transfer enhancement in the structured channel at higher mass fluxes where the convective term increases of importance. Further test will be necessary to confirm this theory and completely characterize the effect of the lateral wall roughness on the two-phase flow and flow boiling process.

## 3.10 Conclusions

In this study, a dedicated test section was designed and fabricated to perform flow boiling experiments at the microscale. The design of the test section was optimized to increase heat flux uniformity at the channel walls improving the reliability of flow boiling heat transfer measurements. A detailed investigation of thermal losses to the environment allowed precisely quantifying the different sources of losses as confirmed by energy balance measurements. Single-phase characterization shows an early departure from laminar conditions around Re=1000. Full laminar friction factor data are well described by the Shah-London equation, while turbulent flow correlations represent the experimental data with MAE around 20%. Single-phase heat transfer data are well described by turbulent flow correlations with a MAE=7.6% provided by the Dittus-Boelter correlation. Flow boiling tests allowed measuring the full boiling curves for increasing and decreasing heat fluxes. No hysteresis effects were detected between the two curves for the four different mass fluxes tested. The Onset of Nucleate Boiling was clearly detected by the increase of the pressure drop in the channel and the fall of the surface temperature. Experimental ONB data are described with success by the correlation of Celata et al. and Thom et al. Flow boiling Heat Transfer Coefficient (HTC) data don't exhibit effect of the vapor quality neither of the mass flux. The comparison of HTC data with predictive correlations show that the experimental

set is well predicted by the Yu et al. correlation, but only modifying the coefficient from $6.4x10^6$ to $6.4x10^5$, as previously suggested by other researchers. Some correlations give fair results with MAE around 20% while other correlations completely fail the description of the experimental data set. The effect of the wall surface roughness on flow boiling characteristics was also investigated with a dedicated single microchannel test section featuring tailored microstructure at the vertical walls of the channel. Compared with the data obtained for the case of the plain microchannel, this test section shows a lower surface temperature at ONB, sign that nucleation sites activate at lower temperatures. Much higher HTC were also measured with this test section, mainly because of the increased number of active nucleation sites for a certain value of heat flux.

# Chapter 4

# High Energy Physics experiments

## 4.1 Introduction

Physics research at the Large Hadron Collider (LHC), the world largest and most powerful particle accelerator currently operating at the at European Organization for Nuclear Research (CERN), has always been pushing technological frontiers to the limit trying to reach unprecedented accuracy in the understanding of the fundamental laws of Nature. The LHC, with a circumference of 27 km and a design energy of 14 TeV at the centre of mass, was designed to test the predictions of different theories of particle physics, and particularly to verify the predictions of the Standard Model and to put bounds to the large family of new particles expected by supersymmetric theories. The existence of the Standard Model Higgs boson was confirmed in 2013 thanks to the LHC data, while evidence of supersymmetric particles has still to be observed. The LHC is expected to address in the next years some of the unsolved questions of physics, advancing human understanding of physical laws. To achieve these results, several experiments were designed and built to study high-energy particle collisions generated at the LHC (Fig. 4.1) Advancements in particle physics research are strictly connected to technological improvements. The unique characteristics of particle detectors for High Energy Physics (HEP) experiments can explain the cutting edge technology developed for their realization. Most of the detectors for High Energy Physics applications have similar underlying principles and thus similar design characteristics. The

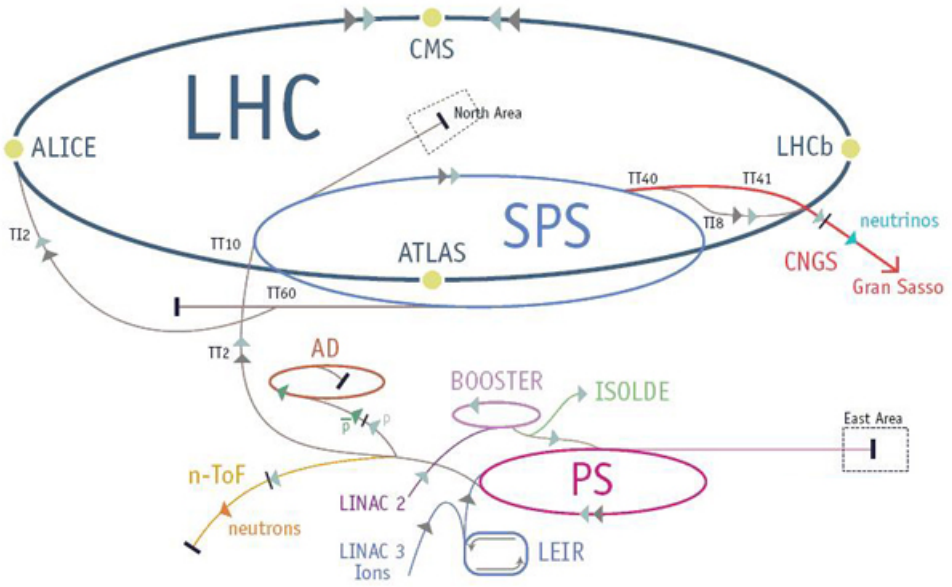


FIGURE 4.1: Layout of the CERN accelerator complex with the location of the main LHC experiments

knowledge of particle detector principles and their design guidelines are fundamental for the full comprehension of the technical choices adopted for the realization of the prototypes presented in this work. For this reason, the next sections briefly introduce the high energy physics experiments with particular emphasis on ALICE (A Large Ion Collider Experiment) and the ALICE Inner Tracking System (ITS) upgrade project.

## 4.2 The Standard Model of Particle physics

The Standard Model is the most accurate theory describing the elementary particles and the way they interact with each other through four fundamental forces: the electromagnetic force, the strong force, the weak force and the gravitational force. The exertion of the fundamental forces among particles is mediated by fields: in the Standard Model this process results from the exchange of force-carrying particles called gauge bosons. These force mediators carry discrete amounts of energy, or quanta, from one particle to another. Each force has its own characteristic boson:

- The strong interaction, the short-range force ($10^{-15}$ m) which holds quarks together to form hadrons and holds hadrons to from nuclei, is mediated by the gauge boson called "gluon".
- The electromagnetic force, the infinite range force acting on charged particles, is exerted through the exchange of a photon, the quantum unit of the electromagnetic force.
- The weak interaction, the short-range force ($10^{-18}$ m) involved in many nuclear decay processes, is mediated by the Z and W bosons.
- The gravitational force is an infinite range interaction acting on all particles. This force is predicted by the Standard Model to be mediated by the exchange of a gauge boson called graviton; however, this particle has never been observed experimentally so far.

According to the Standard Model, fundamental particles are subdivided in fermions, the building blocks of matter, and bosons, which mediates fundamental forces between fermions. The fermions of the Standard Model are classified according to the way they interact (or equivalently, by what charges they carry). They can be distinguished between six quarks (up, down, charm, strange, top, bottom), and six leptons (electron, electron neutrino, muon, muon neutrino, tau, tau neutrino). Quarks carry color charge, i.e. they interact via the strong force [116]. Because of a Quantum Chromo Dynamics (QCD) process called "color confinement", quarks are always confined in composite particles (hadrons) composed either by a quark and an antiquark (mesons) or three quarks (baryons) held together by the strong force through the exchange of gluons. Proton and neutron are examples of baryonic particles. Quantum Chromo Dynamics, the theory that describe the strong interaction, predicts the existence of a novel phase of elementary hadronic matter, consisting of non-confined quarks and gluons, if sufficiently high temperature and density values are reached. At these conditions, the strong interaction weakens (asymptotic freedom), and quarks and gluons are expected to behave like a plasma. This state is called Quark-Gluon Plasma (QGP) [117]. This particular condition of deconfinament is thaught to be the state of

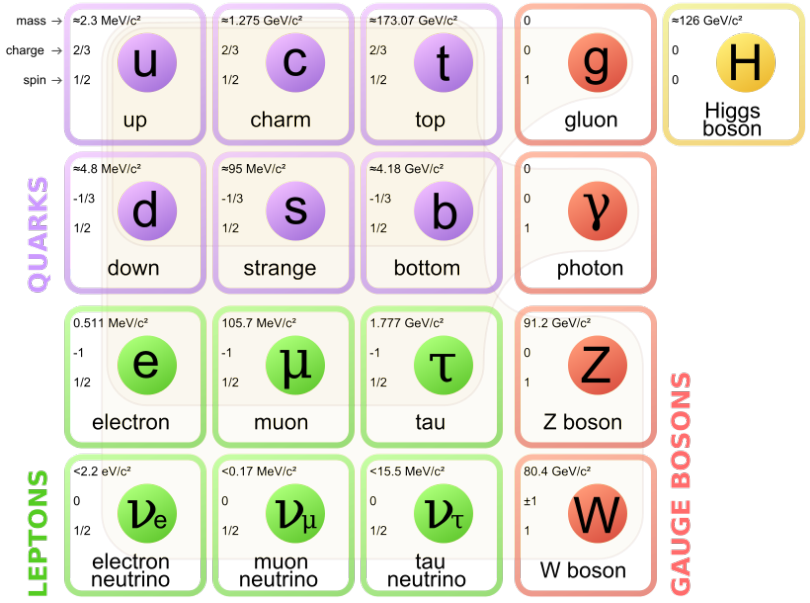


FIGURE 4.2: The elementary particles described in the Standard Model.

the universe few microseconds after the Big Bang, before the hadronization process led to ordinary baryonic matter. Quarks also carry electric charge and weak isospin. Hence they interact with other fermions both electromagnetically and via the weak interaction. The remaining six fermions (electron, muon, tau and the corresponding neutrinos) do not carry colour charge and are called leptons. The three neutrinos do not carry electric charge either, so their motion is directly influenced only by the weak nuclear force, which makes them difficult to detect. However, by virtue of carrying an electric charge, the electron, muon, and tau all interact electromagnetically.

## 4.3 Particle detection in modern High Energy Physics experiments

From the hundreds of particles that generate in terascale hadron-hadron collisions, like those generated by the LHC, most of them are so unstable (i.e their life-time is so short) that they cannot leave a track in the detector. They decay before the first detection layer, forming a so-called secondary vertex which originates secondary particles [118]. Among the particles that leave a track in the detector, the most common by far are electrons, muons, photons,

charged pions, charged kaons, neutral kaons, protons and neutrons:

$$e^{\ddagger}\ \mu^{\ddagger}\ \gamma\ \pi^{\ddagger}\ K^{\ddagger}\ K^{O}\ p^{\ddagger}\ n$$

Neutrinos have very limited interactions with matter and for this reason they can pass through the entire detector without leaving any detectable sign. Because of this, they are usually detected indirectly with a momentum balance on all the collision products. The detector must therefore guarantee a high degree of "hermeticity", i.e. being able to detect and measure all the particle types generated by the collision, with the exception of neutrinos. In modern HEP experiments, the check of the Standard Model predictions at the terascale energy level requires a full reconstruction of the collision's products and the precise measurements of their properties, including momentum, energy, spin, mass, charge, lifetime and identity [119]. To achieve these tasks, HEP experiments exploit particle detectors based on different technologies, usually assembled around the interaction point of the colliding beams. At the LHC energy scale, these detectors are exposed to extremely high particle fluxes and thus must be fast, radiation-hard and finely segmented [120]. The generic detector for HEP experiments is usually design in a barrel geometry surrounding the interaction point, in order to have a large coverage of the particle shower (Fig. 4.3). It consists of several subsystems with specific roles in particle detection and identification. The technology, size and location of the detector subsystems follow from the physics requirements. These sensitive elements are stacked in layers from the collision point outwards so that the particles generated in the collisions traverse one or more of them depending on their type and energy, leaving detectable signs. Depending on the design, all or part of the sensitive volume is immersed in a solenoidal magnetic field in order to bend the tracks of charged particles for momentum and charge sign determination. The generic apparatus for HEP experiments usually includes (Fig. 4.4):

- a Vertex detector, to determine the position of the primary interaction point and secondary vertices from fast decaying particles, such as heavy quarks and leptons. It is typically made of cylindrical layers, positioned at radii at a few centimetres from the interaction point. In order to increase the spatial resolution, the vertex detector must

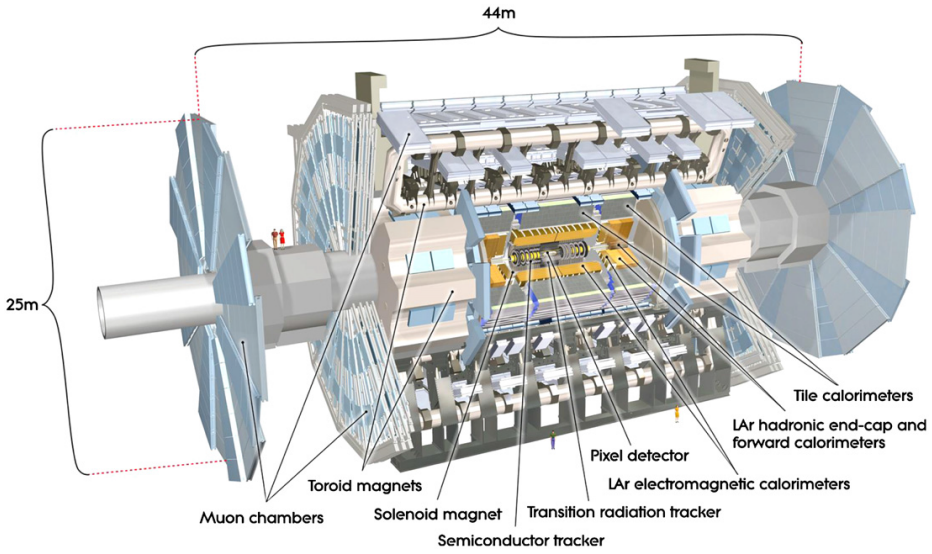


FIGURE 4.3: Layout of the ATLAS (A Toroidal LHC ApparatuS) detector at LHC

be as close as possible to the collision point. Since the colliding beams are contained in a UHV (Ultra-High Vacuum) system, this means that the vertex subsystem will be as close as possible to the vacuum beam pipe containing the two beams. Modern vertex detectors are made of silicon pixel detectors, but precise drift chambers have also been used successfully.

- a Tracker detector in combination with a strong solenoidal magnetic field to measure the trajectory of particles produced in the collisions, thus allowing the measurement of charge, position and momentum of all the different charged particles. Photons may convert into electron–positron pairs and can in that case be detected in the tracking system. Charged kaons decays may also be detected in a high-resolution tracking system [121].

- a calorimeter, massive block of instrumented material in which particles are fully absorbed and their energy transformed into a measurable quantity. The interaction of the incident particle with the detector (through electromagnetic or strong processes) produces a shower of secondary particles with progressively degraded energy. The energy deposited by the particles of the shower in the active part of the calorimeter, serves as a measurement of the energy of the incident particle. Two different kind

of calorimeter are necessary for charged or neutral particles and they are called Electromagnetic calorimeter (ECAL) and Hadron calorimeter (HCAL). The ECAL is the first calorimeter struck by outgoing particles in a generic detector design. It has the role of measuring the energy and position of photons and electrons created in the LHC collisions through their electromagnetic interactions (e.g. bremsstrahlung, pair production). After the ECAL there is the HCAL, used to measure mainly hadrons through their strong and electromagnetic interactions. They can be further classified according to their construction technique into sampling calorimeters and homogeneous calorimeters. Sampling calorimeters consist of alternating layers of an absorber, a dense material used to degrade the energy of the incident particle, and an active medium that provides the detectable signal. Homogeneous calorimeters, on the other hand, use only one type of material that performs both tasks, energy degradation and signal generation [122].

- muon detectors: muons are identified with high accuracy due to the fact that they can penetrate through large amounts of material without any strong interaction, since they have long lifetime. For this reason, muon detectors are usually placed outward the detectors chain in the experiments and in particular outside the magnet containing the tracking detectors.

- Particle Identification Detectors: the identification of particles at different transverse momenta is usually improved by the help of many subsystems based on different detection technologies such as: measurement of the energy deposit by ionization, time-of-flight (TOF) measurements, detection of Cherenkov radiation or detection of transition radiation.

Photons, electrons and positrons deposit all their energy in the EM calorimeter (Fig. 4.5). Their showers are indistinguishable, but they can be identified by the existence of a track in the tracking system that is associated to the shower. In this case the energy deposit must match the momentum measured in the tracking system. Hadrons on the other hand deposit most of their energy in the hadron calorimeter (part of it is also deposited in the EM calorimeter). However, the individual members of the families of charged and neutral

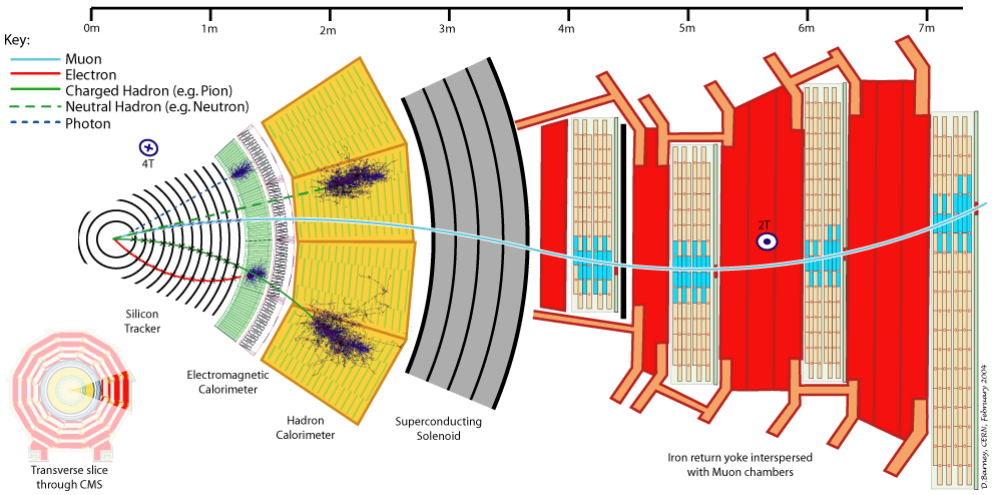


FIGURE 4.4: Particle detection in a slice of the CMS experiment: the basic subsystems and their interactions with particles is shown.

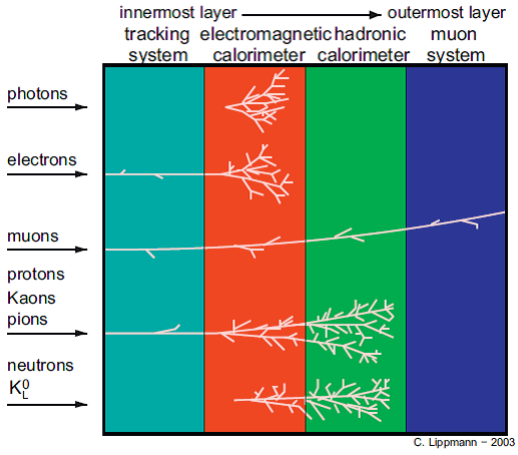


FIGURE 4.5: Detection techniques for the main particles traversing a generic HEP experiment

hadrons cannot be distinguished in a calorimeter and additional information from the tracker is used to at this end [121].

## 4.4 The ALICE experiment at the CERN LHC

ALICE (A Large Ion Collider Experiment) is a major experiment at the CERN Large Hadron Collider. It is designed to address the physics of strongly interacting matter in ion-ion collisions and in particular the properties of the Quark-Gluon Plasma [123]. In order

to reconstruct with sufficient accuracy the interaction of ultra-relativistic ion beams, the ALICE experiment was conceived comprising several sub-detectors specifically tailored for a comprehensive study of hadrons, electrons, muons, photons and jets produced in heavy-ion collisions. Its overall dimensions are 16x16x26 $m^3$ with a total weight of approximately 10 000 t (Fig. 4.6). Each subsystem is designed with specific technology solutions to meet

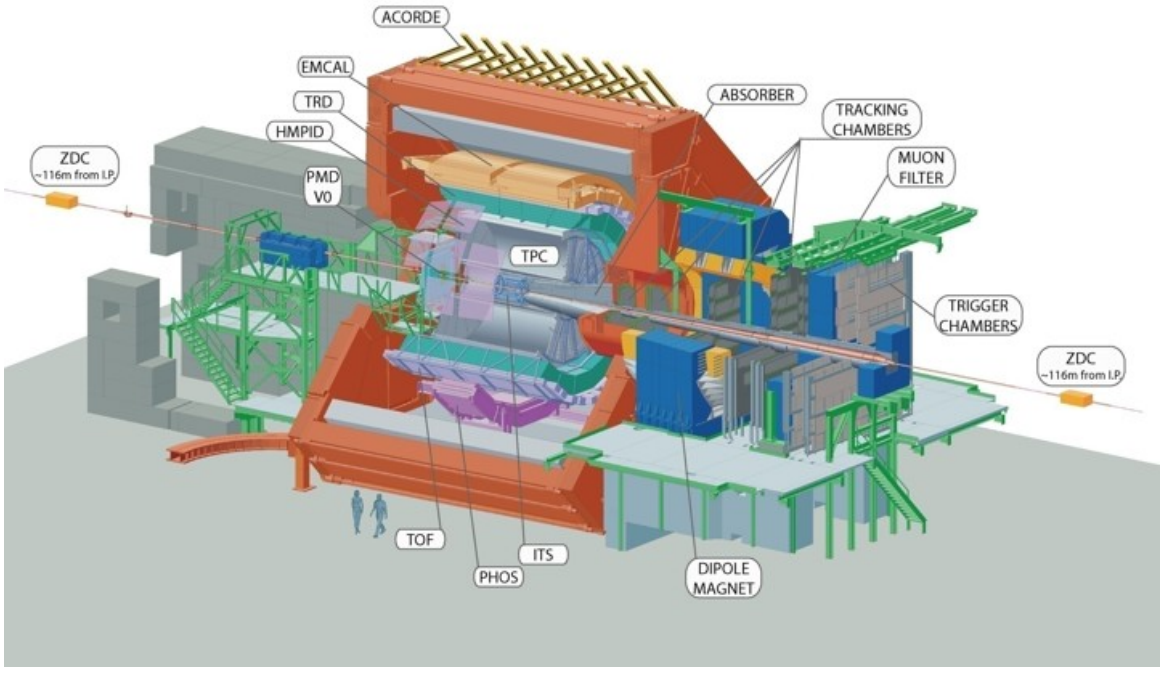


FIGURE 4.6: The layout of the ALICE experiment installed at the LHC Point2

demanding physics requirements at extreme experimental conditions. The most stringent design constraint is the extremely high particle multiplicity in central Pb-Pb collisions (up to 10000 tracks per collision). The different subsystems are conceived to provide high-momentum resolution as well as excellent Particle Identification up to high multiplicities. ALICE consists of a central barrel part located inside a large solenoidal magnet measuring hadrons, electrons and photons, and a forward muon spectrometer. From the inside out, the barrel contains an Inner Tracking System (ITS) composed by six planes of silicon detectors, a cylindrical Time-Projection Chamber (TPC), three particle identification arrays of Time-of-Flight (TOF), Ring Imaging Cherenkov (HMPID) and Transition Radiation (TRD) detectors, and two electromagnetic calorimeters (PHOS and EMCal). All detectors except

HMPID, PHOS, and EMCal cover the full azimuth. The forward muon arm consists of a complex arrangement of absorbers, a large dipole magnet, and fourteen planes of tracking and triggering chambers. Several smaller detectors (ZDC, PMD, FMD, T0, V0) for global event characterization and triggering are located at small angles. An array of scintillators (ACORDE) on top of the magnet is used to trigger on cosmic rays.

**Vertexing and Tracking detectors**

Vertexing and tracking in ALICE is performed by the Inner Tracking System (ITS) and the Time-Projection Chamber (TPC). The Transition Radiation Detector (TRD) is also used for tracking in the central region improving the $p_t$ resolution at high momenta. The inner detectors provide primary and secondary vertices reconstruction of heavy flavour and strange particle decays, particle identification and tracking of low-momentum particles, and improvement of the impact parameter and momentum resolution. The ITS consists of six cylindrical layers of silicon detectors, located at radii between 4 and 43 cm (Fig. 4.6). The number, position and segmentation of the layers are optimized to increase physics performance. In particular, the outer radius is determined by the necessity to match tracks with those from the TPC, and the inner radius is the minimum allowed by the radius of the beam pipe. The ITS surrounds the beam pipe and it also provides mechanical support reducing relative movements during operation. The detectors and front-end electronics are held by lightweight carbon-fibre structures. The main tasks of the Inner Tracking System (ITS) are:

- Localization of the primary vertex with a resolution better than 100 $\mu$m
- reconstruction the secondary vertices from the decays of hyperons and D and B mesons
- tracking and identification of particles with momentum below 200 MeV/c
- improvement of the momentum and angle resolution for particles reconstructed by the Time-Projection Chamber (TPC)
- reconstruction of particles traversing dead regions of the TPC.

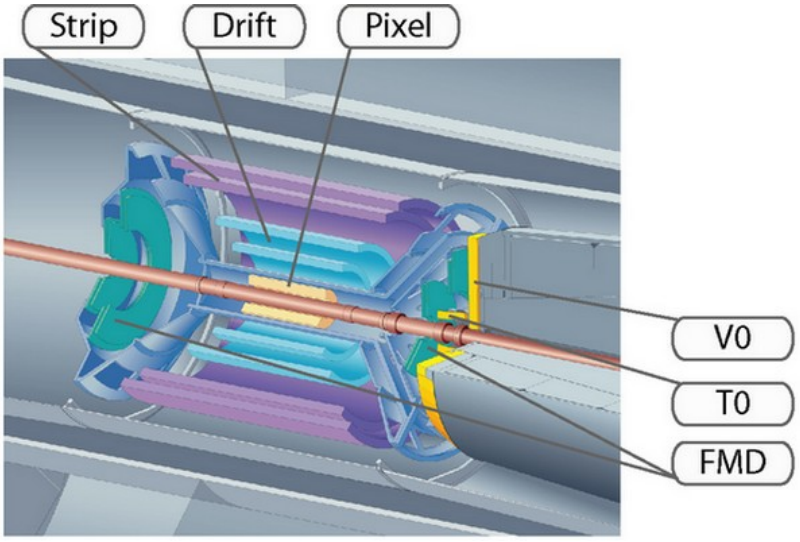


FIGURE 4.7: The six silicon planes composing the ITS detector around the ALICE beam pipe

Because of the high particle density expected in heavy-ion collisions at LHC, (around 50 particles per $cm^2$ per collision for the inner layer), and in order to achieve the required impact parameter resolution, hybrid silicon pixel detectors have been chosen for the two innermost layers. The four outer layers are equipped with Drift and Strip silicon detectors which allow for particle identification via dE/dx measurement in the non-relativistic region.

## 4.5 The upgrade of the ALICE Inner Tracking System

With the aim of improving the resolution and the physics capabilities of the current detector, the ALICE collaboration is preparing a major upgrade of its apparatus [124], planned for installation during the second long LHC shutdown (LS2) in the years 2019-2020. This upgrade will enable the study of rare physics channels by improving low-momentum vertexing and tracking and increasing read-out speed to cope with the increased LHC interaction rate to 50 kHz in Pb-Pb during Run 3. The upgrade plan includes:

- A new beampipe with smaller diameter (in order to reduce the distance between the first detection layer and the interaction point);

- A new, high-resolution, low-material Inner Tracking System (ITS) (for increasing the impact parameter resolution and the standalone tracking efficiency);
- Upgrade of the TPC consisting in the replacement of the wire chambers with GEM detectors and new pipelined readout electronics;
- Upgrade of the readout electronics of TRD, TOF, PHOS and Muon Spectrometer for high rate operation;
- Upgrade of the forward trigger detectors;
- Upgrade of the online systems and offline reconstruction and analysis framework.

In the frame of the upgrade of the ALICE experiment, a major topic is the development of a new high resolution, high speed and low mass Inner Tracking System [125]. The main features of this new detector will be:

**First detection layer closer to the interaction point**

The reduction of the beam pipe diameter in the centre of the ALICE detector is one of the main ingredients to improve the measurement of the impact parameter resolution. The beam pipe inner radius will be reduced to 19.2 mm from the present value of 29 mm. The wall thickness of the central Beryllium beam pipe section is assumed to be 0.8 mm. A smaller value of 0.5 mm is challenging due to possible issues with gas tightness and mechanical stability. Thanks to the reduced beam pipe diameter the first detection layer will get closer to the interaction point reducing its distance from 39 mm to 22 mm, improving vertexing and stand-alone tracking performance.

**Reduction of material budget**

Reducing the material budget of the first detection layers is particularly important for improving the impact parameter resolution. In general, reducing the overall material budget significantly improves both the tracking performance and the momentum resolution. The use of Monolithic Active Pixel Sensors (MAPS) allows reducing the silicon material budget per layer by a factor seven when compared to the present ITS (50 $\mu$m instead of 350 $\mu$m). A proprietary analogue front-end with optimized timing specifications and a custom made

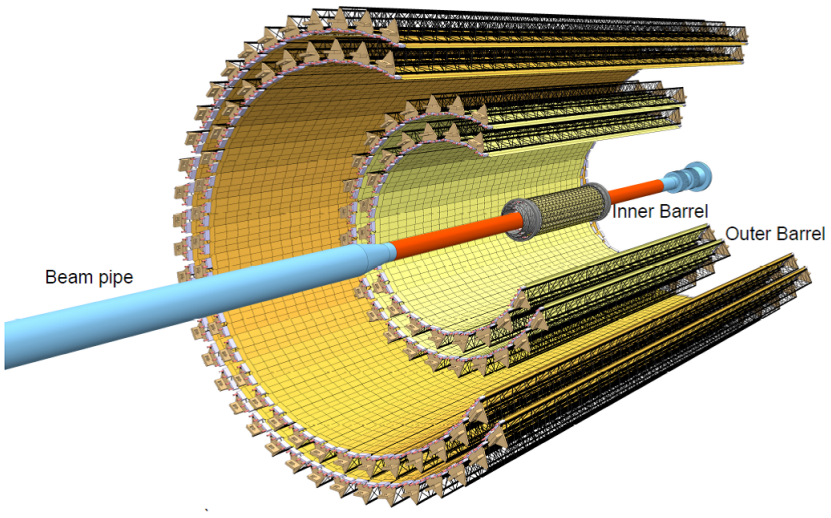


FIGURE 4.8: Layout of the future ITS detector

read-out architecture also permits to reduce the power by more than a factor two, which will also translate in a substantial reduction of material budget due to the reduced cooling requirements. At the same time, the pixel density will increase by a factor of 50, further improving the tracking performance. The lower power consumption and a highly optimised scheme for the distribution of the electrical power and signals will also reduce by a factor five the material budget of the electrical power and signal cables. Mechanics, cooling and other detector elements will be also improved with respect to the present ITS design. Combining all these new elements together, it should be possible to build a detector with a radiation length of 0.3% $X_0$ per layer or better for the three innermost layers.

**Improving the detector intrinsic spatial resolution**

The detector will be composed by seven concentric cylindrical layers covering a radial extension from 22 mm to 430 mm with respect to the beam line (Fig. 4.8). The radial positions of the layers was optimised in order to achieve the best combined performance in terms of pointing resolution and transverse-momentum resolution and tracking efficiency in Pb-Pb collisions at hit densities of about 19cm$^{-2}$/event on average for minimum-bias events in the innermost layer. The reduction of the pixel size from 50x425 $\mu$m$^2$ to 30x30 $\mu$m$^2$ will increase the detector intrinsic spatial resolution. The detector will cover a total surface of 10.3 m$^2$ containing about 12.5·10$^9$ pixels with binary readout.

## 4.6 Silicon Pixel Detectors for vertexing and tracking applications in HEP experiments

Tracking detectors are of paramount importance for many experiments in high energy and nuclear physics, being used to determine the charge, momentum and energy of traversing particles and to allow quark flavour identification through reconstruction of secondary vertices. The main two families of tracking detectors are gaseous and semiconductor detectors, while more exotic ones are fibre or transition radiation tracking (TRT) devices [126]. Advances in particle tracking have always been closely related to advances in technology and improvements in experimental methods [127]. Taking advantage of the rapid growth of silicon microfabrication technologies in the early eighties, silicon microstrip detectors were introduced, dramatically increasing the resolution in the identification of secondary vertices and hence particles life time measurements. Pixel detectors are the last step in this technological development and represent the instrument of choice for the tracking of charged particles close to the interaction point in modern HEP experiments. At the LHC, with a centre of mass energy of 14 TeV, on average 22 interactions with ∼1200 tracks occur during one bunch crossing every 25 ns, no other detector at the moment can cope with this high density and rate of particle tracks in a strong radiation environment. The most widely used technologies of pixel detectors for vertexing and tracking application in nowadays HEP experiments comprise hybrid pixel detectors and monolithic pixel detectors, while CCDs have been successfully employed mostly in the past and the so-called 3D detectors are still under development, and represent a very interesting solution for future experiments. Hybrid pixel detectors consist of a pixelated sensor chip (the sensitive element) interconnected by bump-bonding to a CMOS readout chip (Fig. 4.9). The sensitive element is usually depleted by an electric field to maximize the charge collection efficiency and speed. The charge collected in the sensing chip is read by the corresponding read-out cell in the read-out chip via the bump-bond interconnection. Since every sensor pixel has its own readout electronic cell, all channels can operate in parallel, dramatically increasing the readout speed. Furthermore, being the sensor and the readout chip realized on different wafers, it is possible to adopt

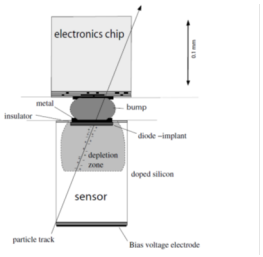


FIGURE 4.9: Cross-section of one pixel cell, the basic block of a hybrid pixel detector. The ionizing particle crosses the sensor and generates charges that, moving in the depletion region under the effect of an electric field, produce signals which are amplified and analysed by the electronics

specifically optimized sensing materials to maximize the signal-to-noise ratio and the radiation tolerance of the detector, at the same time exploiting commercially available sub-micron CMOS processing to implement the readout circuitry. A draw back of hybrid detectors is that the minimum pixel size is limited by the footprint of the per-pixel readout electronics and the interconnection technology with the sensor, thus limiting the spatial resolution. Furthermore, hybrid sensors are highly mechanical sensitive because of the bump-bonding technique. The high production and assembly costs (mostly driven by the alignment and bonding procedure) limit this technology to small area coverage.

**Monolithic active pixel sensors**

While an extremely effective and well-proven technology, the hybrid pixel sensors can not meet the specific requirements of the ALICE ITS upgrade, in particular in term of granularity, material budget and cost. Monolithic Active Pixel Sensors have been instead chosen as the sensor technology which better meets the ITS upgrade requirements. The use of CMOS Monolithic Active Pixel Sensors (MAPS) for charged particle tracking in subatomic physics gained considerable attention in the last years. They in fact integrate the sensing volume and the readout electronic within the same silicon die, avoiding the limitations and costs of the interconnection required in hydrid sensors. MAPS can be fast, reasonably radiation tolerant (when compared to CCDs) up to few hundreds kGray, and can integrate complex electronic functions within a few micron thick silicon die, allowing the integration of large detecting systems at an affordable cost. MAPS basic structure consists of a matrix of reverse biased p-n diodes (formed by N-well/P-epi junctions in CMOS technology) acting as sensing element and coupled to an in-pixel readout circuitry, which can greatly vary in

complexity depending on the application. The outputs from the readout circuitry embedded in every pixel are gathered into a so-called periphery, where further signal processing can be performed. The concept of periphery adopted here is mostly figurative, as these additional functional blocks can be either grouped at the physical chip periphery, spread across the pixel matrix, or both. The charge generated by a particle passing across the sensitive element (the depleted p-n diode junction) is collected and transformed into an electrical signal by the integrated read-out electronics, then delivered to the next functional block. Being the connection between the sensing element and the readout circuitry few microns long, it is possible to realize an ultr-fine segmentation (down to 1 $\mu$m or less), as well as low parasitic capacitance. The intrinsic low capacitance at the readout node makes it possible to realize extremely power-efficient sensors, when compared to the hybrid technology, which in turn allows lesser cooling requirements and a correspondent lower material budget. Material budget can be further improved by thinning the device down to its active thickness, which usually varies, depending on many technological flavours, from 5 um to 50um. From a functional point of view, the use of CMOS VLSI process with multiple wells technology makes straightforward to implement advanced logic functions (memories, logic, etc.) within both the pixel matrix and the periphery, widening the operational capabilities of the sensor. A Monolithic Active Pixel Sensor with deep p-well shield has been chosen for the future Inner Tracking System in the ALICE experiment. While not as radiation tolerant as hybrid pixels, which uses a much thicker (usually few hundreds microns) charge collection volume, nevertheless modern, well designed MAPS sensors can withstand up to 100 kGray equivalent dose of ionizing radiation without losing functionality and/or detection efficiency. For the specific requirements of the ALICE ITS upgrade, the TowerJazz 180 nm CMOS imaging sensor process with a deep pwell has been chosen, and implemented on different combination of epitaxial layer resistivity and thickness [128]. The focus of the ITS R&D has been on investigating the radiation hardness and on balancing the power efficiency respect to the readout speed. It has been successfully verified that the transitors radiation tolerance is well beyond the ALICE requirements and a fully custom-made architecture made it possible to achieve low power densities across the chip respect to the readout rate. However, mechanical and integration requirements for the ITS detector design make the thermal managment

of the sensors a critical task in the design of the system.

## 4.7 Mechanics and cooling for vertex detectors

The development of ultra-light mechanical support structures and efficient thermal management systems for the on-detector electronics in pixel vertex detectors is a key element in the design of future HEP experiments which are requested to exhibit extremely high resolution while working in very harsh environments. The requirements set by physics performance optimization in the design of HEP experiments can be resumed as follows [129]:

- **Hermeticity within a given coverage range**. This is required for the complete reconstruction of all the collision products.
- **High transparency to particles**. The detector has to minimize his influence on the particle flux, and this is obtained by minimizing the mass introduced in the detector that could affect the particle trajectories by multiple scattering, bremsstrahlung, photon conversions and nuclear interactions. The material budget is a parameter for evaluating the effect of different materials on the interaction with particles and it is usually expressed as fraction of the radiation length Xo that is the length of material (in cm) necessary to reduce the energy of an electron by a factor 1/e.
- **High stability to a few microns**. Because of the extreme spatial resolution expected in vertex detectors, the stability of the system is crucial. Gravitational deflections, thermal distortions, displacements by external loads and cabling must be minimized by an accurate design of the system and proper materials selection. The stability could be influenced by long term effects (such as swelling due to moisture release from resin-based structures and/or coolant absorption, creep of plastics due to loading conditions and irradiation) and short term effects (temperature transients during operations, pressure variations in the cooling system), vibrations from services.

The design of vertex detectors is further complicated by the harsh environment where they are expected to work:

- **High radiation**: important radiation damage to materials and induced radiations on the detector components. This limits the material selection for the design.
- **Humidity**: if the detector is working out of vacuum, particular attention must be kept in order to avoid condensation on the detector surface during operation.
- **Low maintenance**: access to the system is usually very reduced because of its position at the centre of the experiment and the radioactive environment during the operation.
- **integration**: challenging space constraints and cabling requirements.

All these requirements could be translated in the following specifications for the design of the mechanical support and the thermal management systems:

- **Lightweight**: low mass materials with high radiation length $X_o$
- **stiff**: small natural deflections, minimum mass, high natural frequencies;
- **stable**: materials with small coefficients of thermal (CTE) and moisture (CME) expansion;
- **radiation hard**: reduced radiation induced damages;
- **reliable**: intrinsic robust design.

The pixel chips are usually positioned in a module called "stave", which includes:

- the on-detector electronics, composed by the pixel chips, the read-out electronics usually bump-bonded on the pixel sensor and a hybrid circuit wire-bonded to the read-out chips providing interface to the optical, signal and power cables;
- the mechanical support structure that support the sensors in place with the necessary stability and guarantee the optimum integration inside the detector;

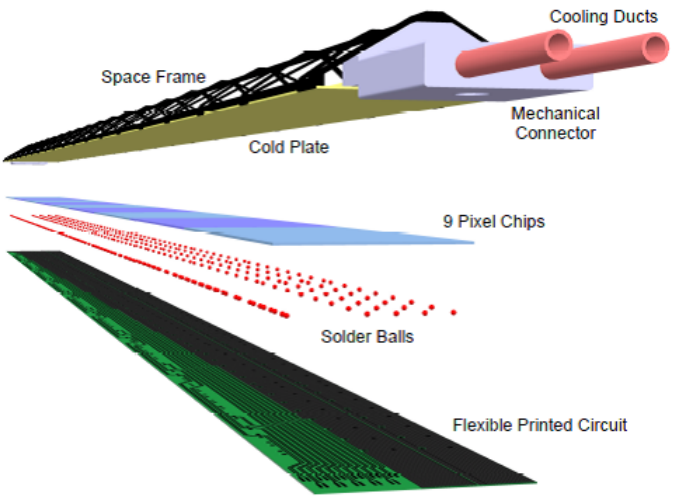


FIGURE 4.10: Schematic view of the ITS Inner Barrel stave components

- the on-detector cooling system that remove the power dissipated by the on-detector electronics keeping the sensor within operational constraints set by physics performance optimization.

For the upgrade of the ITS detector, the stave is composed by the following components (Fig. 4.10):

- **Hybrid Integrated Circuit (HIC)**: an assembly of a polyimide Flexible Printed Circuit (FPC) on which a nine pixel chips and some passive components, are bonded by means of solder balls laser soldering.
- **Space Frame**: a carbon fibre support structure providing the mechanical support and the necessary stiffness; the specific stiffness and the low Z are the parameters driving the design. Therefore, the choice is oriented to the use of high modulus carbon fibre with high Young's modulus like the M60J 3K (588GPa). The space frame is manufactured using a manual winding process.
- **Cold Plate**: a plate with an active on-detector cooling system, which is integrated within the Space Frame; the Cold Plate is in thermal contact with the Pixel Chips or with the Module carbon plate to remove the generated heat.

## 4.8 Silicon microchannel cooling for vertex detectors

Several different solutions are available for the design of the stave cooling plate and thus for the thermal management system of the on-detector electronics. Silicon microchannels have gained a huge attention over the last years in the microelectronics industry for the cooling of computer CPUs and other high heat flux electronic components because of the following three main reasons [130]:

- Heat transfer enhancement at the microscale;
- Increasing heat flux dissipation in microelectronic devices, in accordance with the Moore's law;
- Increase of microscale devices that require small and portable cooling systems.

In particle detector applications, the heat flux dissipation is usually quite law if compared with computer CPUs, but the volumetric power density starts to be important. Furthermore, challenging requirements of extremely low mass and severe space constraints for integration, together with the above mentioned critical environmental conditions and reliability expectations, pose several issues in the design of these systems. The first application of silicon microchannel cooling in a HEP experiment is at CERN in the NA62 Gigatracker [131]. This detector consists of three silicon pixel planes installed along the beam line providing measurement of time, direction, and momentum of all the beam tracks ($\sim$109/sec). For cooling the GTK on-detector electronics a silicon plate with microchannels was developed for single-phase operation with $C_6F_{14}$ fluid. A similar concept was later adopted for the Vertex Locator (VELO) detector, under development in the LHCb experiment at CERN [132]. The VELO detector is composed of 88 silicon planes arranged along the beam providing the hit information on R-f coordinates. Also in this case, silicon microchannel cooling was selected for cooling the on-detector electronics. In this case, the layout of the channel has been optimized with respect to the final power dissipation map. For fulfilling the design requirement set for the detector design, a two-phase cooling system was adopted

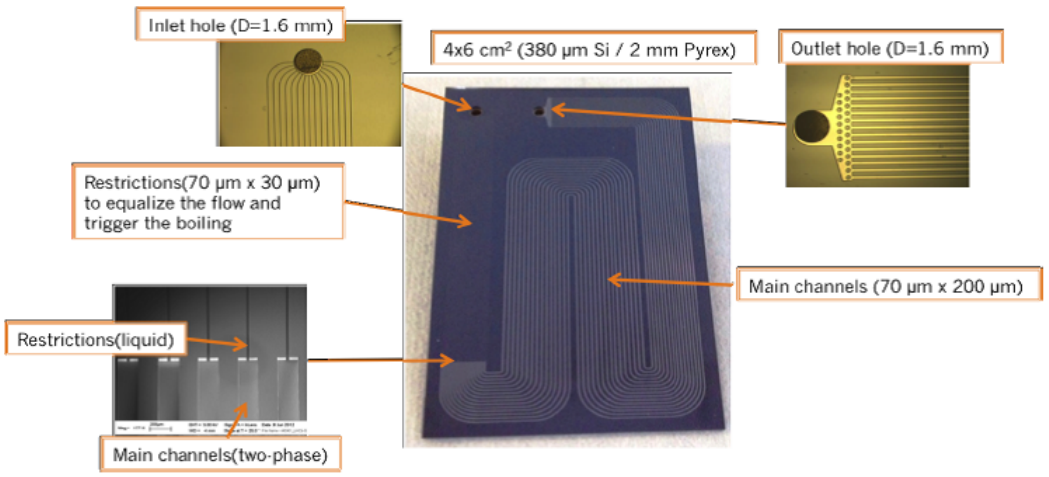


FIGURE 4.11: Schematic view of the ITS Inner Barrel stave components

with $CO_2$ as refrigerant fluid (Fig. **??**). Silicon microchannel cooling was also proposed for the thermal management of the future ITS detector. Thanks to the rapid advancement in microfabrication techniques for electronics and MEMS applications, it is now possible to fabricate very thin and small devices with micrometric precision. This opens a wide range of possibilities in the design of the system, allowing tailoring the layout to the specific application. While single-phase cooling is the most used cooling system in microchannel applications, it has some limitations in the heat transfer process and in the temperature uniformity along the channels. Since severe temperature constraints are set for the optimal operation of the ITS detector, a flow boiling cooling system is investigated for the electronics thermal management. The main advantages of flow boiling over single-phase cooling are the ability of the fluid to remove large amounts of thermal energy through the latent heat of vaporization with minimal temperature gradients over the chips surface: this feature is especially important for vertex detectors thermal management, where small temperature gradient constraints have to be guaranteed over very large active surfaces ($m^2$). In addition, flow boiling exhibit much larger heat transfer coefficients, thus reducing the temperature difference between the chip surface and the fluid, another important feature because of the temperature limitations set for the detector operation, and higher heat removal capability for a given mass flow rate of the coolant. This solution has also drawbacks and issues, which are resumed below:

- High pressure drop: the reduction of the hydraulic diameter drastically increase the pressure drop of the device, requiring a careful design of the system, especially in very long devices as those investigated for this application. In addition, large pressure drop can cause temperature gradients related to the change of saturation pressure that can affect the chip's surface temperature;

- Instability: two-phase flow in parallel multi-microchannel devices could be affected by oscillations of the refrigerant flow rate, the saturation pressure and temperature, flow instabilities, vapour back flow, early critical heat flux and dryout;

- knowledge: as confirmed by recent results on microscale flows, single-phase fluid flow and heat transfer characteristics can be predicted using convectional macroscale correlation, provided that surface roughness and entrance effects, axial conduction and viscous heating are taken into account. This is not true for two-phase flows, where macroscale models are not realistic for predicting fluid dynamics and heat transfer characteristics in microchannels, as shown in Chapter 1. For this reason, the design of microscale two-phase cooling system is usually more complicated and requires extensive testing and modelling.

In this study, an innovative on-detector cooling system for next generation HEP vertex detector is proposed. This solution is based on low material budget silicon frames with embedded microchannels.

# Chapter 5

# Development of interconnected low mass silicon frames with embedded microchannels

## 5.1 Introduction

Silicon detectors for the High Energy Physics are requested to exhibit good spatial resolution, precise energy loss measurements, limited material budget and high radiation hardness. The design of vertex detectors for HEP experiments requires very low mass of the detector in order to enhance the physics reconstruction capabilities of the system by reducing multiple scattering and photon conversions phenomena. For the upgrade of the ALICE Inner Tracking System, the minimization of the materials introduced in the detector design is paramount. The influence of the materials composing the detector on the reconstruction of the trajectories of the particles generated by the collisions is evaluated by a parameter called material budget. The material budget of a certain material is defined as the ratio between the thickness of the material x and its radiation length $X_0$ and it is usually expressed in percent:

$$Materialbudget = \frac{x}{X_o}\% \tag{5.1}$$

The radiation length of a material is the mean thickness of the material (in cm) required to reduce the energy of an electron by the factor 1/e. For improving the overall detector resolution, the reduction of the material budget is of particular importance for the three innermost layers of the ALICE experiment, composing the ITS Inner Barrel (IB). In order to minimize the material budget contribution, the detector cooling system and mechanical support structure has to be as light as possible, without affecting thermal performances and mechanical stability. In order to guarantee the optimum operation of the detector, the chip surface must be kept between 15°C (minimum allowed temperature to avoid condensation on the detector electronics) and 30°C (maximum temperature for the optimum operation of the MAPS chip) and a maximum temperature difference of 5°C over the surface of the whole detector is requested. From the thermal point of view, the chip is characterized by two distinct zones with different power dissipation (Fig. 5.1): on the pixel area the power dissipation is low, because of the simple in-pixel electronics. The periphery of the chip, where most of the in-chip electronics is located, shows higher power dissipation, representing 80% of the total power dissipated by the chip.

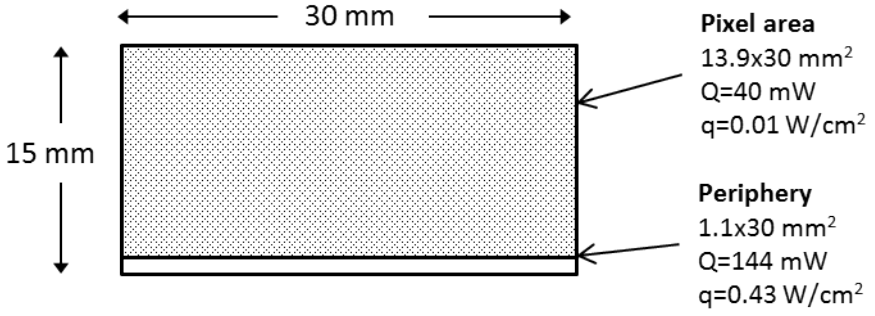


FIGURE 5.1: Detail of the ITS chip size with the two distinct power dissipation zones: the pixel area and the periphery.

For what concern the geometrical and mechanical requirements, the system must guarantee initial position accuracy within 200 $\mu$m and exceptional stability in time below 5 $\mu$m. Space constraints are very demanding as it is possible to see in Fig. 5.2, where the position of the three layers with respect to the ALICE beam pipe is reported.

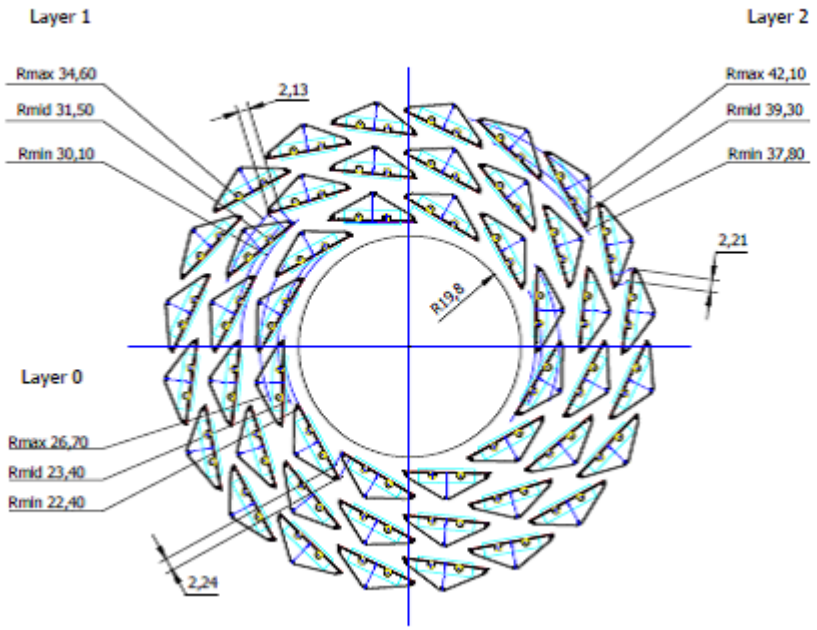


FIGURE 5.2: Cross section of the three laytes composing the ITS Inner Barrel surrounding the beam pipe (mm).

Another fundamental requirement for the system design is to allow fast extraction of the detector from the ALICE experiment for inspection and maintenance. This condition requires the routing of all services and cooling lines only on one side of the detector for the extraction of detector from the central barrel. This constraint strongly affects the design of the cooling system, requiring having inlet and outlet fluidic connections on the same side of the stave.

## 5.2 Performance of a thin silicon frame with embedded microchannels

The design of an integrated cooling system meeting the thermal and mechanical requirements set for the upgrade of the ALICE Inner Tracking System requires a careful optimization of the layout. The minimization of the material budget asks for a complete removal of any unnecessary material. For the on-detector cooling system, this translates in the removal

of material in low power dissipation regions (pixel reticule) concentrating the material in high dissipation zones (periphery). A frame design would allow meeting this requirement by avoiding any additional material in the pixel region and concentrating the material at the edges in order to house an active cooling system for the chip on-detector readout. At the periphery, a high performance cooling system is required to remove the power dissipated by the on-detector electronics with minimum junction temperature between the fluid and the chip surface and reduced temperature gradient along the stave. The ideal candidate for the thermal management of the chip periphery with reduced space contribution and optimized layout is microchannel cooling. Thanks to recent advancements in silicon microfabrication techniques, devices with very low thickness and high dimensional precision can be fabricated. The boom of MEMS devices has also introduced new fabrication techniques increasing the potential of microfabrication processes. On the other side, microchannel cooling exhibit high heat transfer rates enabling thermal management of high power dissipation components at reasonable temperatures with minimum material and space demands. The decision between single-phase liquid cooling and flow boiling heat transfer is based on several aspects: single-phase cooling is much simpler to control and to predict and it is usually very stable. On the other hand, it suffers from significant temperature gradients along the channel when absorbing sensible heat. Flow boiling heat transfer usually features nearly constant temperatures, only affected by the decrease of the saturation temperature associated with the pressure drop along the channel. Two-phase fluid dynamics, however, is much more complex and difficult to predict. Flow boiling exhibits very high heat transfer coefficients but also significant pressure drops. The design of microscale evaporators is complicated by the lack of a comprehensive knowledge of the fluid dynamics involved, thus requiring extensive experimental testing. If not correctly designed, these devices could suffer from instable operating conditions, oscillations and unequal flow distribution leading to degraded performances. Because of the demanding requirement expected from the system, a two-phase solution was adopted with the aim of enhancing the heat transfer performance and improving temperature uniformity over the detector surface.

### 5.2.1 Design and fabrication of the prototype

A first prototype of silicon frame with embedded microchannels was designed and it is presented in Fig.5.3. To cope with the integration constraints, the total width of the device is the same of the chip, 15 mm. This pilot prototype is designed to cool two ITS chips.

FIGURE 5.3: First prototype of silicon frame with embedded microchannels

The prototype is fabricated in the class 100 MEMS clean room at the EPFL (École Polytechnique Fédérale de Lausanne) Centre of MicroNanoTechnology (CMi) in Lausanne. The micro-fabrication process flow is shown in Fig. 5.5. It starts with a 380 µm thick p-type 4" ¡100¿ silicon wafer double side polished. A first photolithography performed on the backside of the wafer with 4 um of AZ9260 photosensitive resin transfers the layout of the Layer 1 with alignment marks, dicing crosses and the central pool for the removal of the inner region silicon bulk. With this design the backside is patterned with dry etching of the oxide layer (Fig. 5.4) and the photoresist is then stripped in oxygen plasma. A second photolithography is used to pattern the wafer frontside with the Layer 2 where the fluidic layout is reported. Another step of dry etching is used to transfer the design removing the oxide layer. At this point, after stripping the frontside resist, the microchannels are etched for 200 $\mu$m in a plasma etcher using the oxide layer as hard mask. After stripping the

resist, the frontside is treated for the subsequent anodic bonding. Surface treatment include removal of the oxide layer: this is done first etching the full surface with plasma leaving only some tens of nm of oxide. The remaining oxide is removed with a Buffered HF bath that provides a much smoother surface than dry etching, increasing the bonding reliability. The cleaning of the surface is composed by a sequence of Piranha cleaning, oxygen plasma and Piranha cleaning, performed on both silicon and Pyrex wafers. This procedure guarantees a good condition of the surface avoiding residual from the previous steps. The choice of a 525 µm thick Pyrex cover is only limited to the fabrication of these first prototypes since it allows for optical access to the boiling process inside the channels and provides sealing of the microchannels through Si-Pyrex anodic bonding, a technique not particularly demanding in terms of surface quality and process control. However, the final production of the thermal management devices will rely on a direct bonded silicon device allowing the suppression of all material in the central region and a cover thickness reduced to only few tens of microns of Silicon. The two wafers are joined with an anodic bonding procedure, ensuring perfect sealing of the channels. A thin layer of aluminium is deposited by sputtering on the Pyrex side: this is required by the plasma etcher that has an electrostatic chuck to hold the wafer. The inner part of the frame is then removed from the backside using the Layer 1 patterned oxide as hard mask. This step also opens the inlet and outlet ports to the manifolds. At this point, after removing the aluminium layer with a Ion Beam Etching, the wafer is diced providing three distinct frames.

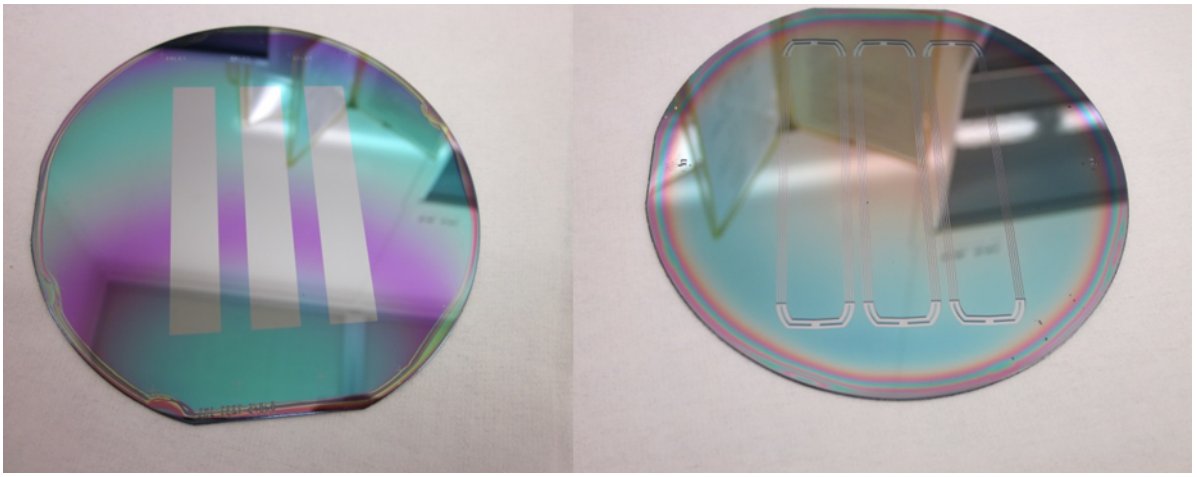

FIGURE 5.4: Backside of the wafer patterned with the pools design (left) and frontside of the wafer after etching the channels (right).

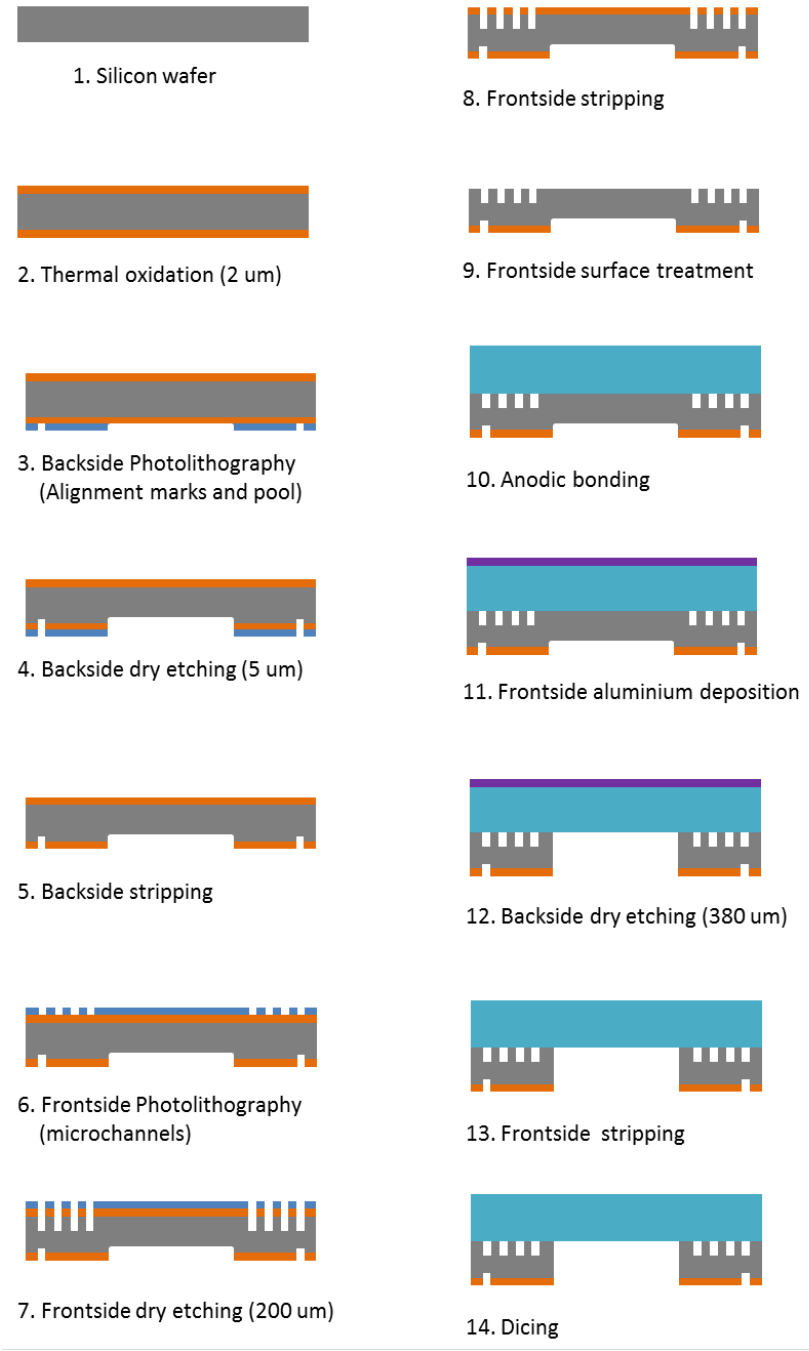


FIGURE 5.5: Microfabrication process flow of the silicon frame with embedded microchannels.

Inlet and outlet of the fluid to the device is obtained through square ports etched on the silicon backside wafer providing access to the manifolds (Fig. 5.6 left). After the entrance the fluid is split into two branches that feed the two sides of microchannels. 4 microchannels with a cross section of 200x200 $\mu m^2$ and a 300 $\mu$m wall in between (Fig. 5.6 right) are present on each side for a total length of 61 mm. Restriction were included at the inlet of each channel for the minimization of backflow and instability effects.

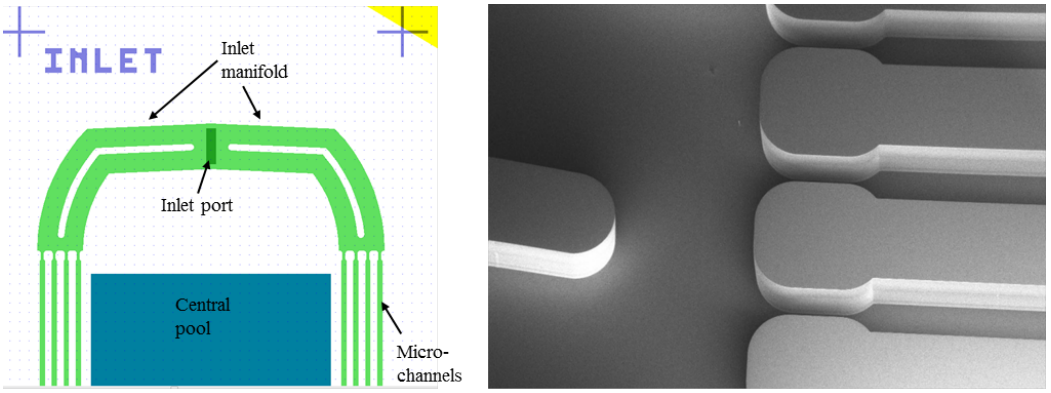


FIGURE 5.6: Layout of the microchannel circuit (left) and detail of the inlet restrictions (right).

Because of the reduced thickness of the device, the inlet and outlet connections must stand out-of-the plane. For this first prototype, a commercial connector was adopted for interfacing the silicon microchannel system with the external piping. This is a Peek connector from Nanoport, which can be easily connected to a standard stainless steel pipe (Fig. 5.7 ).

FIGURE 5.7: The silicon frame prototype equipped with Peek connectors and two silicon dummy chips.

Dedicated silicon dummy chips were produced to simulate the mechanical and thermal behavior of the detector chips. The dummy chip has the same size of the pixel chip (15x30 $mm^2$) and it is 100 $\mu$m thick. The chip is coated with a 200 nm Platinum film by sputtering

with a 20 $\mu$m Titanium layer for adhesion enhancement. The platinum layer on the chip is then electrically connected to a power supply through two electrodes. By applying a voltage difference at the electrodes, the current flowing in the thin metal layer produces a heat flux by Joule effect that simulates the power dissipation generated in the silicon pixels. A stabilized DC power supply has been used in the present experimental apparatus. The electrical power provided to the prototype is obtained from the voltage measurement at the outlet of the power supply and the current measurement is performed using a calibrated shunt resistor. The Platinum film has a uniform thickness over the chip surface, therefore the power dissipation can be assumed to be uniformly distributed. By focusing on a cross section of the device (Fig. 5.8), it is possible to see that only at its edges the chip is in direct contact with the micro-channels while in the inner region no active cooling is present: this means that the power generated in the inner region must move by conduction along part of the silicon dummy chip before reaching the micro-channels.

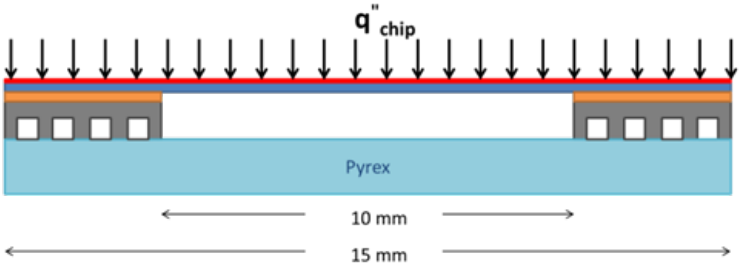


FIGURE 5.8: Cross sectional view of the prototype (not to scale).

In order to estimate the real heat flux on the walls of each channel for a certain power dissipation of the chip, a 2D numerical simulation of the prototype cross section was performed. In the numerical model, heat flux is applied on the chip surface and single-phase heat transfer coefficient is imposed at the three silicon walls of the channels, while the pyrex side is considered adiabatic. The heat transfer coefficient is calculated for fully developed laminar flow in a three sided heated microchannel as suggested by Kandlikar [130] . The 2D temperature profile in a cross section at the middle of the first chip is shown in Fig. 5.9. The case considers 0.3 $Wcm^{-2}$ power dissipation on the chip surface and R134a mass flux G=880 $kgm^{-2}s^{-1}$.

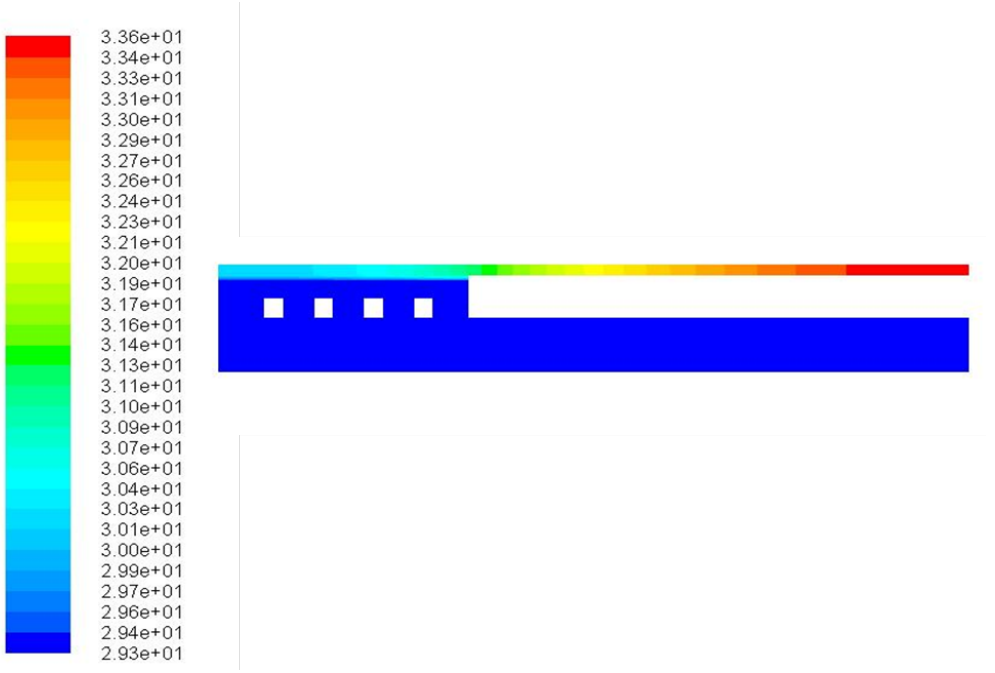


FIGURE 5.9: Temperature map obtained from the simulation of the device cross section [°C].

The simulation reveals that the main temperature gradient is enclosed in the chip. The thermal resistance of the glue layer and the high conductivity of the silicon bulk assure a uniform temperature and uniform heat flux distribution at the channel walls (5.10). The maximum deviation of the wall heat flux from the ideal value of perfectly uniform distribution is within 2%. For the experimental characterization, the same setup used for the tests on the single microchannel and described in chapter 3 was used.

### 5.2.2 Thermal losses assessment

Prior to the experiments, the thermal losses of the prototype to the surrounding environment were evaluated. This was done in two steps: first, vacuum was created inside the prototype and power was applied to the dummy chips with the prototype in its final testing configuration. After the stabilization of the thermal conditions, the chip surface temperature for the applied power was recorded for different power dissipations. A correlation between the chip surface temperature and the power dissipated to the environment is reported in Fig. 5.11.

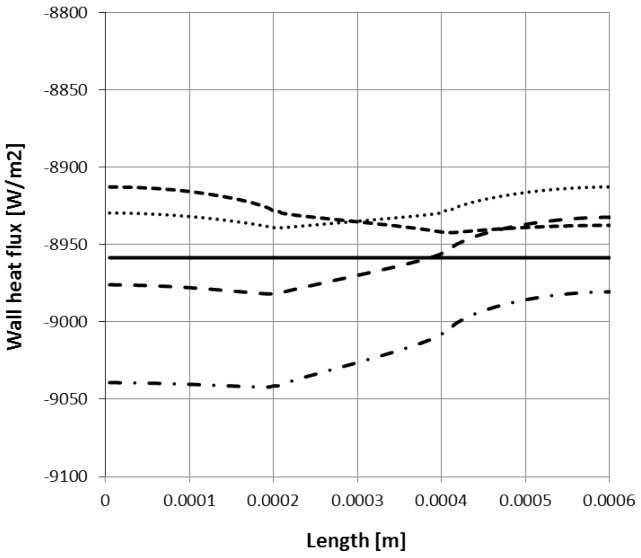


FIGURE 5.10: Wall heat flux for the four channels obtained from numerical simulations compared with the ideal value (straight line).

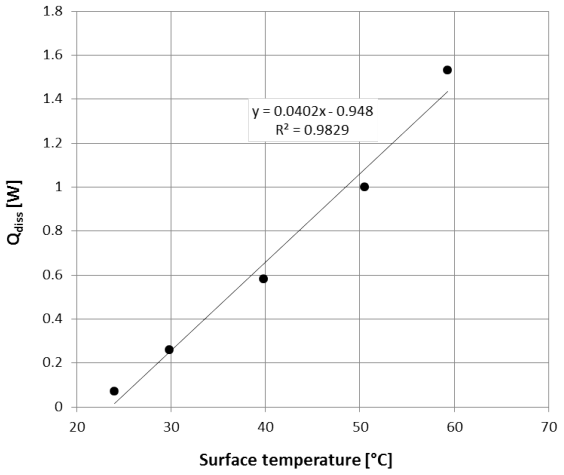


FIGURE 5.11: Power dissipated to the environment for different chip surface temperatures.

Secondly, thermal balance check on the fluid side was performed by comparing the electrical input power and the thermal power absorbed by the fluid based on the inlet and outlet fluid temperature values at different flow rates and different power dissipation rates, including the corrections obtained with the vacuum test. The results are reported in Fig. 5.12. It is possible to see that already at 2 W the error in the thermal balance is below 10%.

Since the heat transfer coefficient in two phase flow is generally much higher than that of single phase flow, the error is expected to be much lower during flow boiling tests.

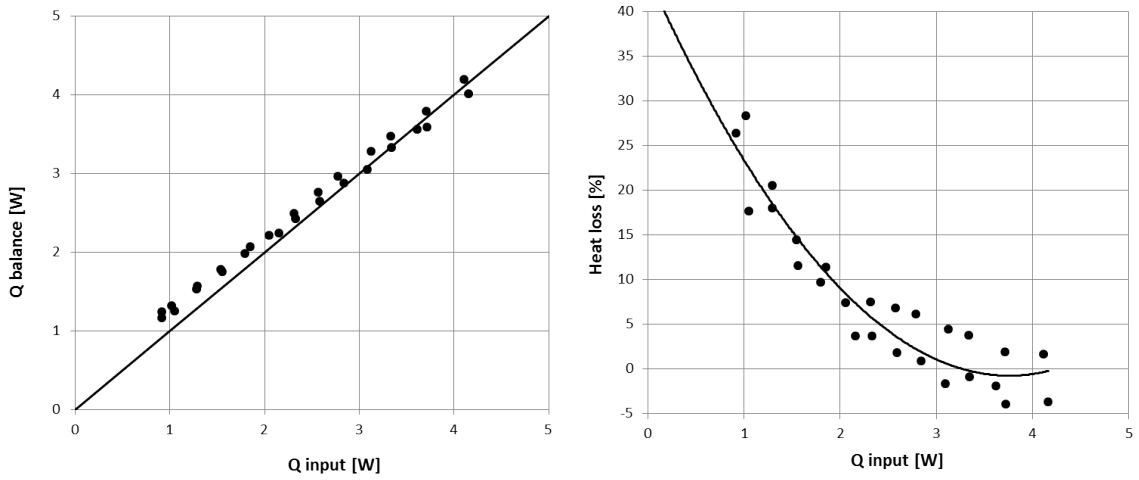


FIGURE 5.12: Thermal balance check during single-phase R134a flow.

### 5.2.3 Single-phase characterization

Before the flow boiling tests, the prototype was characterized in term of single-phase liquid pressure drop and heat transfer. Single-phase pressure drop tests were performed with subcooled liquid R134a at P=10 bar and T=20°C with mass fluxes ranging from G=100 to G=3500 $kgm^{-2}s^{-1}$ and Reynolds number ranging from 100 to 3200. Local pressure drops in the inlet and outlet ducts are calculated with appropriate correlations from [133] and the pressure drop in channels is obtained by subtracting these contributions to the total pressure drop measured by the differential pressure transducer. The pressure drop in the channel is shown in Fig. 5.13 compared with single phase pressure drop correlations from the literature. A close-up to the laminar region of the pressure drop characteristics shows an early departure from laminar conditions: this is probably caused by the inlet and outlet manifolds and restrictions, where the fluid undergoes several changes of directions and cross section that could introduce instabilities in the flow. The experimental data are well predicted by standard correlations also in the transition regions.

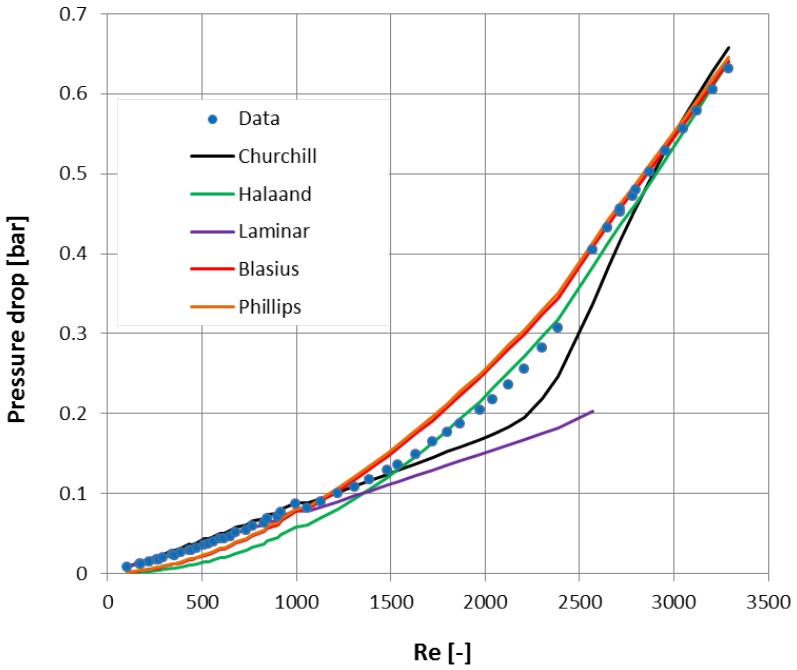


FIGURE 5.13: Experimental single-phase liquid pressure drop data compared with predictive correlations

Thermal performance of the prototype during single-phase flow is evaluated measuring the chip surface temperature with an IR camera. Longitudinal temperature profiles at the chip centreline for different chip heat fluxes are presented in Fig.5.14 and Fig.5.15 for two different mass fluxes, G=880 $kgm^{-2}s^{-1}$ and G=1750 $kgm^{-2}s^{-1}$.

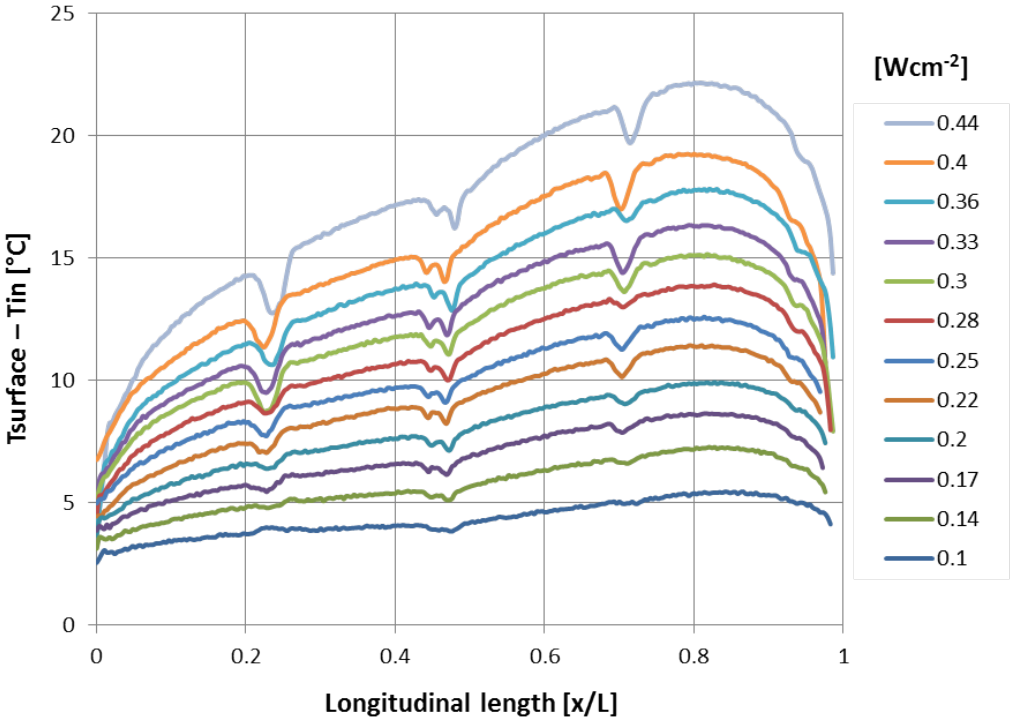


FIGURE 5.14: Chip surface temperature profile obtained from Infrared imaging at different base heat fluxes during R134a single-phase flow at G=880 $kgm^{-2}s^{-1}$ and $T_{in}$=22°C.

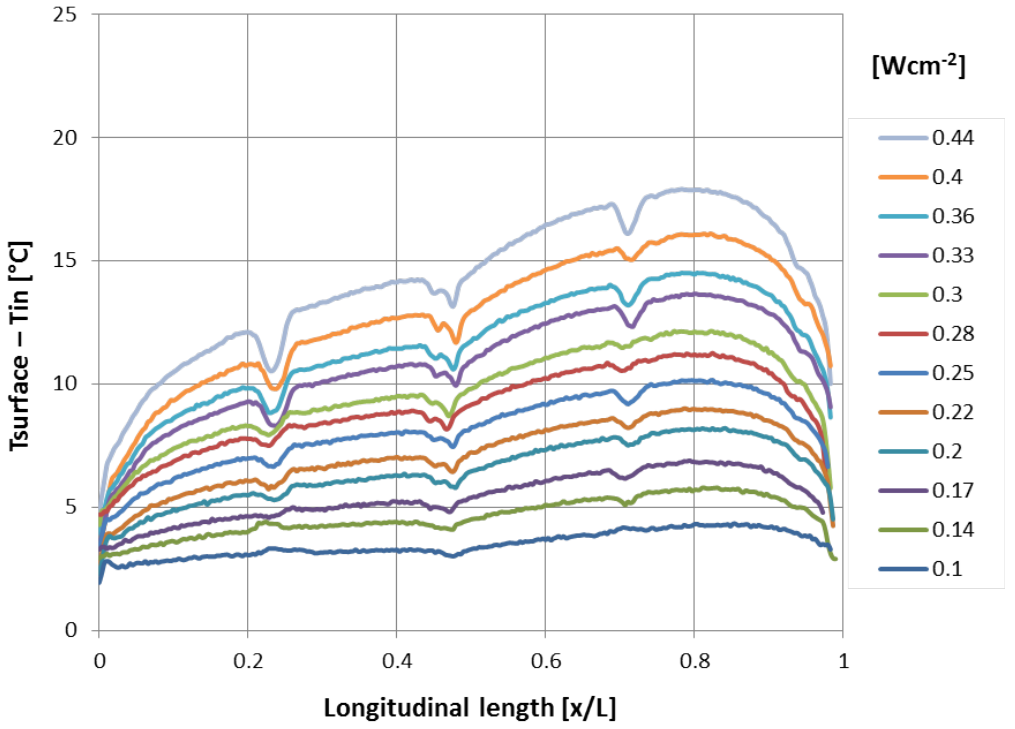


FIGURE 5.15: Chip surface temperature profile obtained from Infrared imaging at different base heat fluxes during R134a single-phase flow at G=1750kg $m^{-2}s^{-1}$ and Tin=22°C.

Because of the particular design of this device, the transversal temperature gradient is critical, since the chips are cooled only at the two edges and no active cooling is provided in the inner region. In 5.16 and 5.17, transversal temperature profiles obtained from the Infrared survey at the centre of the prototype, are shown for different power dissipation for the two mass fluxes tested.

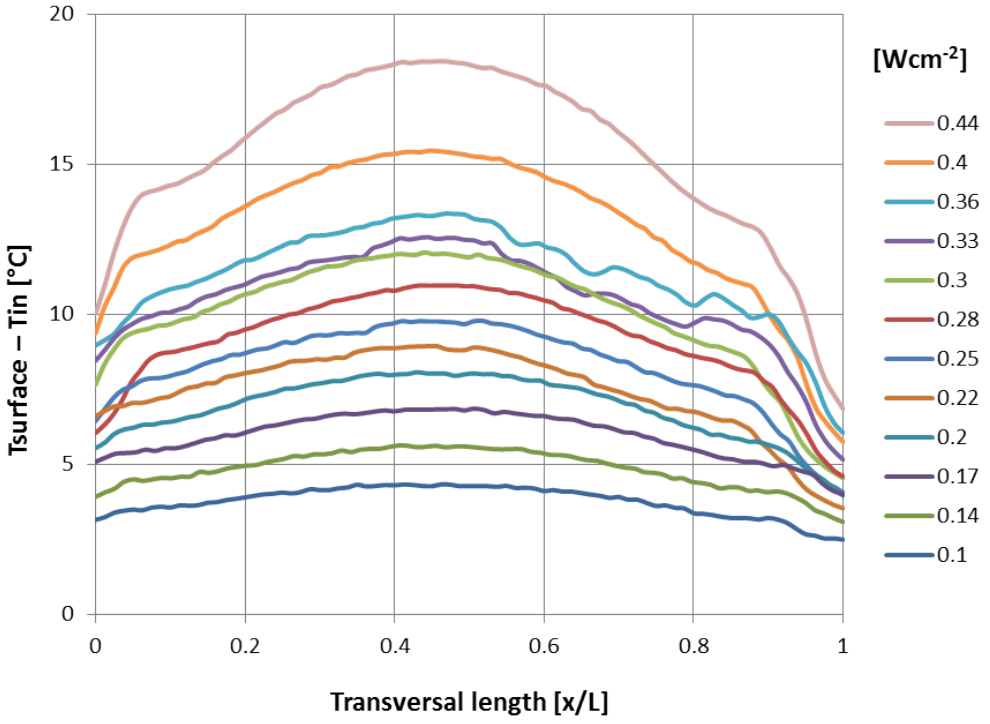


FIGURE 5.16: Transversal temperature profiles obtained from Infrared imaging at different base heat fluxes during R134a single-phase flow at G=880 kg $m^{-2}s^{-1}$ and Tin=22°C.

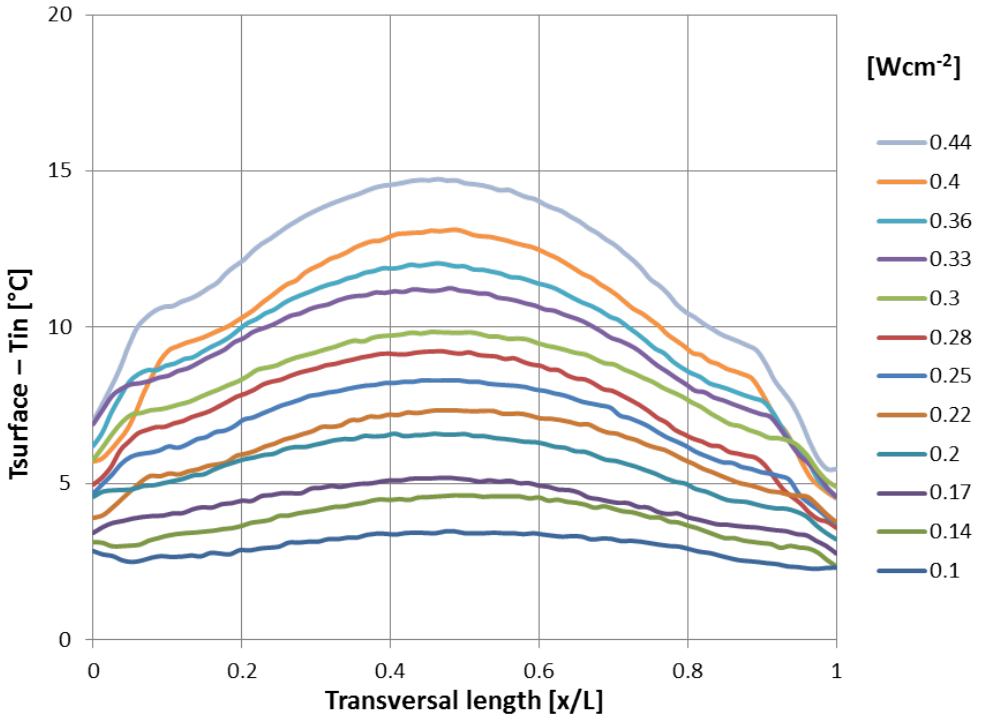


FIGURE 5.17: Transversal temperature profiles obtained from Infrared imaging at different base heat fluxes during R134a single-phase flow at G=1750 kg $m^{-2}s^{-1}$ and Tin=22°C.

Experimental data of the transversal temperature profile on the surface of the chip were compared with numerical results obtained with the model presented in section 5.2.1. The temperature profile over the chip surface for different power dissipation is obtained imposing the heat flux over the chip surface and imposing the single-phase heat transfer coefficient obtained from standard correlation at the three silicon walls of the channels, while the glass wall is assumed to be adiabatic. The comparison shows a quite good agreement between experimental and numerical results for chip surface heat fluxes ranging from 0.2 $Wcm^{-2}$ to 0.5 $Wcm^{-2}$.

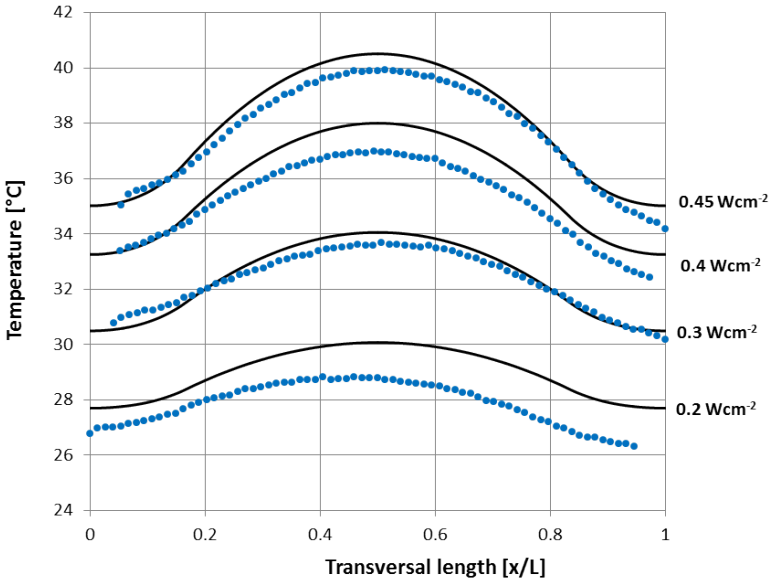


FIGURE 5.18: Transversal temperature profile on the chip surface in the middle of the prototype obtained from the numerical model for three different power dissipations during R134a single-phase liquid flow at G=880 kg $m^{-2}s^{-1}$ (continuous lines) compared with experimental profiles obtained from the infrared survey for the same conditions.

### 5.2.4 Flow boiling experiments

Flow boiling experiments were carried out using HFO-R1234ze as working fluid. Two tests cases resumed in Table 1 were investigated.

| **Case** | **G** | **m** | **Tsat** | **Tin** | **Δ Tsubc** |
|---|---|---|---|---|---|
| | **[kg $m^{-2}s^{-1}$]** | **[kg $h^{-1}$]** | **[C]** | **[C]** | **[C]** |
| a | 300 | 0.35 | 22.5 | 21 | 1.5 |
| b | 750 | 0.87 | 21 | 19.5 | 1.5 |

TABLE 5.1: Experimental test cases.

The surface temperature distribution captured by the IR camera in the two cases is shown in Fig. Fig.5.19 the surface temperature profiles above the channels are reported for the two cases. As it can be seen, the temperature variation along the channel is within 1°C and the difference between the surface and the saturation temperature is 2°C. This is a key point for

limiting the maximum surface temperature without decreasing the saturation temperature below the dew point, where condensation on the detector surface could appear.

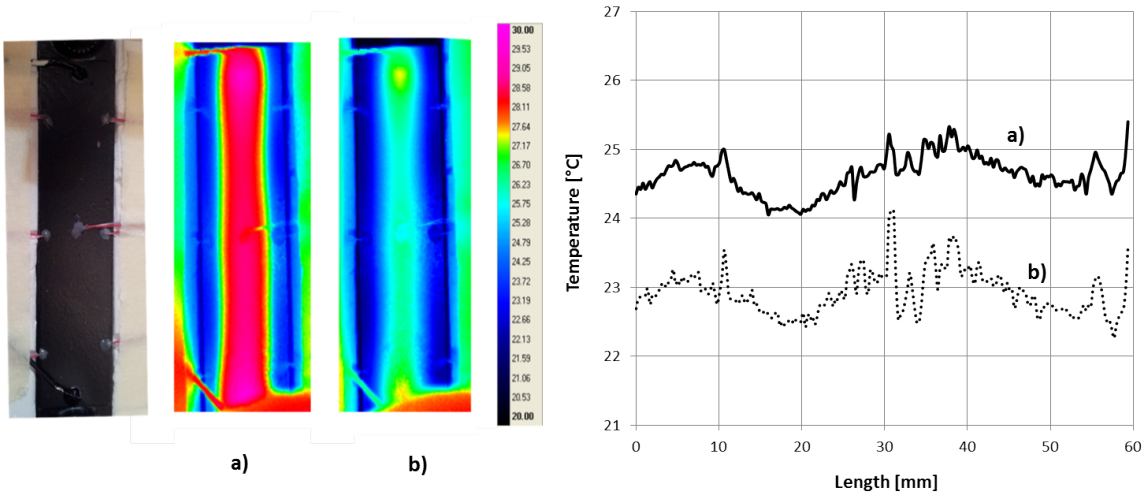


FIGURE 5.19: Infrared image of the surface of the chips for the two test cases (left) and longitudinal temperature profiles along the frame (right).

Based on the frame design, where no active cooling is provided in the inner region, the transversal temperature profile represents a critical parameter for evaluating the thermal performance of the device. This value has to be kept lower than 5 °C for an efficient operation of the detector. The transverse temperature profiles extracted from the IR images of Fig. 5.19 at the same axial location where the thermocouples are installed are reported for case a) and case b) in Fig. Fig.5.20

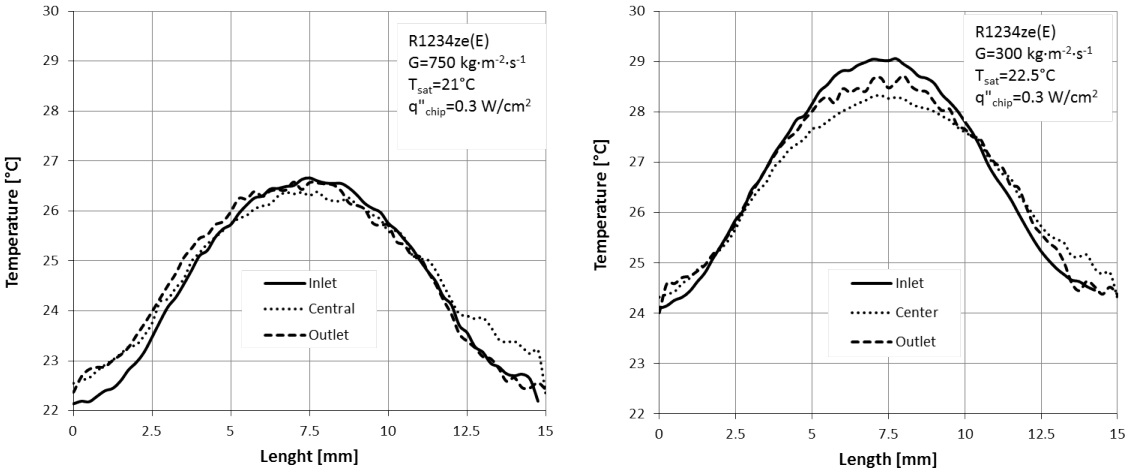


FIGURE 5.20: Infrared image of the surface of the chips for the two test cases (left) and longitudinal temperature profiles along the frame (right).

The transverse temperature gradient observed in this case ranges from 4 to 5°C, and so within the design constraint. Above the channels a mean temperature difference of 2°C between the surface and the fluid was observed. Decreasing the saturation temperature from 22.5 to 21 for case b), allows decreasing the maximum surface temperature below 27°C shifting down the temperature profiles while no differences in the transverse temperature distribution are observed. The same analysis was then performed at the maximum power dissipation expected for the ITS pixels, that is 0.5 Wcm−2. This was performed at G=700 $\mathrm{kgm^{-2}s^{-1}}$ (m=0.8 $\mathrm{kgh^{-1}}$) with a saturation temperature of 21°C, the liquid entering the test section at 19°C and $\Delta t_{sub}$=2°C. The temperature distribution over the chip area for this case is shown in Fig. 5.21 together with the transverse temperature profiles at the three thermocouples position and the longitudinal temperature along the channels.

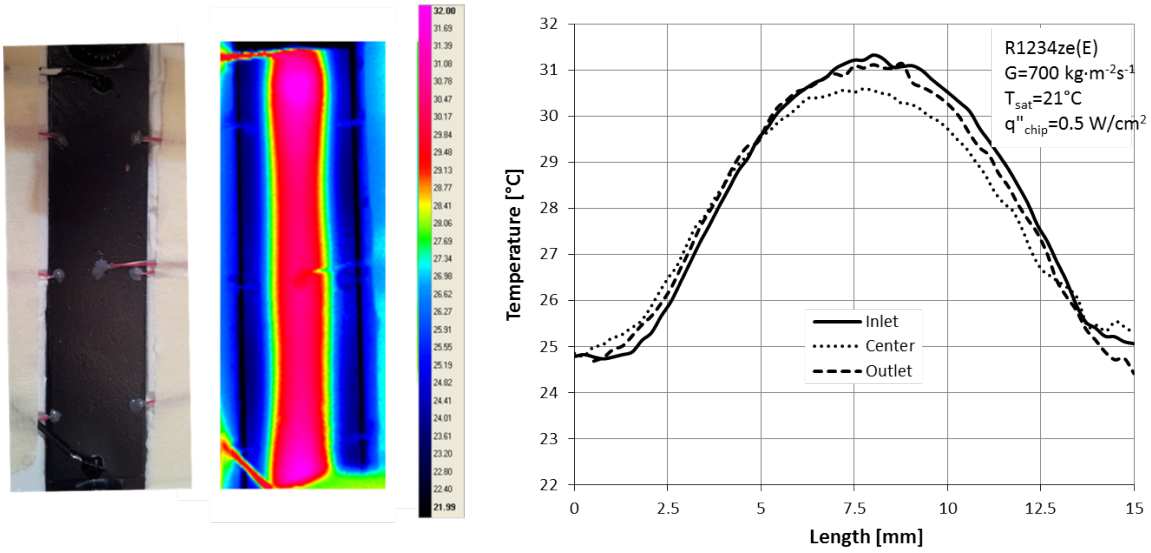


FIGURE 5.21: Chip surface temperature and transversal temperaure gradient for the power dissipation q=0.5Wcm$^{-}$2

In this case the maximum temperature detected in the dummy chip surface is slightly above the maximum temperature recommended from the design specifications (30°C). However, as shown in the previous case, the saturation temperature can be lowered, decreasing in this way the surface temperature. The lower limit on the saturation temperature is set by the dew point of the ALICE experimental hall environment to 15°C: below this value condensation can occur on the detector surface damaging the on-detector electronics. Although outside the expected operating range for the future ITS pixel sensors, some tests were also performed at higher heat fluxes. The results show a change from the parabolic shape of the transverse temperature profile presented above: at higher heat fluxes a plateau appears in the central region and a very high temperature gradient was recorded in the channels region (Fig. 5.22). A higher temperature gradient in the channels region implies a different heat flux for each channel and therefore different heat transfer coefficients. At the highest power dissipation the maximum temperature is the same, because for these cases heat exchange with the surrounding air is the dominant heat exchange mechanism for the power dissipated by the chips.

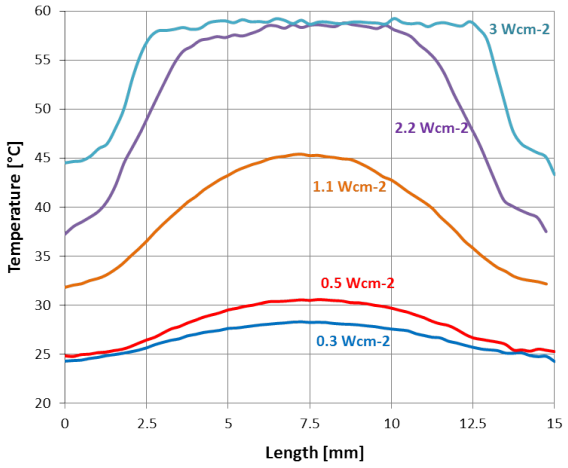


FIGURE 5.22: Progress of the transversal temperature profiles at increasing chip power dissipation rates.

In order to have more insights about the thermal performance of the system, further flow boiling tests were performed at different mass fluxes ranging from G=200 kg $m^{-2}s^{-1}$ to G=1200 kg $m^{-2}s^{-1}$ and for different power dissipations. During these tests the prototype was completely insulated since no infrared survey was performed. The heat losses to the surroundings in this configuration were evaluated from a dedicated test and subtracted to the electrical input power. The global performance of the system at different electrical power and for different mass fluxes under flow boiling conditions was then evaluated and the results are resumed in Fig. 5.23 in terms of temperature difference between the sensor surface and saturation temperature.

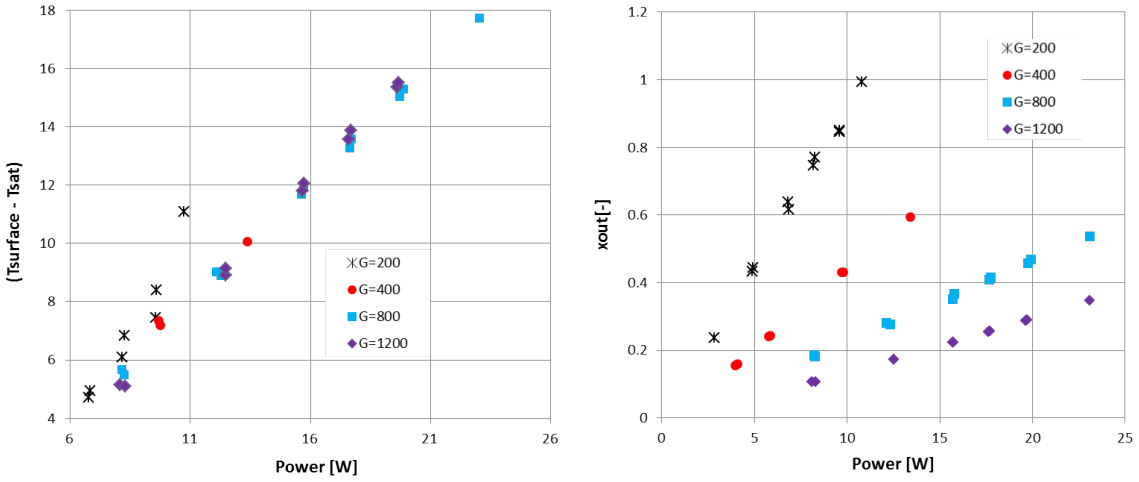


FIGURE 5.23: Progress of the transversal temperature profiles at increasing chip power dissipation rates.

No influence of the mass flux is observed except for the lowest value tested. This is very important for this application since several of these prototype will have to run in parallel in their final setup inside the ITS barrel. During the detector operation the power dissipation could change from module to module and also with time in the same module. The change in power dissipation could affect the pressure drop inside the micro-channels and therefore the mass flow rate inside each module. The above results show that also for a mass flux variation from G=400 to G=1200 $\mathrm{kgm^{-2}s^{-1}}$ no significant effects are appreciated in term of detector surface mean temperature. Only at G=200 $\mathrm{kgm^{-2}s^{-1}}$ the effect of the mass flux become visible and a deviation from the general trend is observed. This can be correlated to the flow vapour quality increase for the same power dissipation at low mass flux. In Fig. 5.23 the outlet vapor quality as obtained from a heat balance in the measuring sector for the previous data set is plotted versus the power dissipation. As it can be seen, the data points diverging from the general trend in Fig. 5.23 present an outlet vapour quality above 0.8 and therefore these data are affected by dry-out conditions. High-speed visualization from the Pyrex side, allowed getting some hints on the fluid dynamics involved in the flow boiling process. The flow patterns observed are mainly bubbly flow, intermittent flow (slug-plug flow and elongating bubble flow) and annular flow at higher vapor qualities towards the exit of the channels. It was possible to identify the nucleation sites for each channel (Fig. 5.24) and for the tests performed in this study, the nucleation sites for each channel were located

at approximately the same longitudinal location from the inlet manifold for a certain test condition.

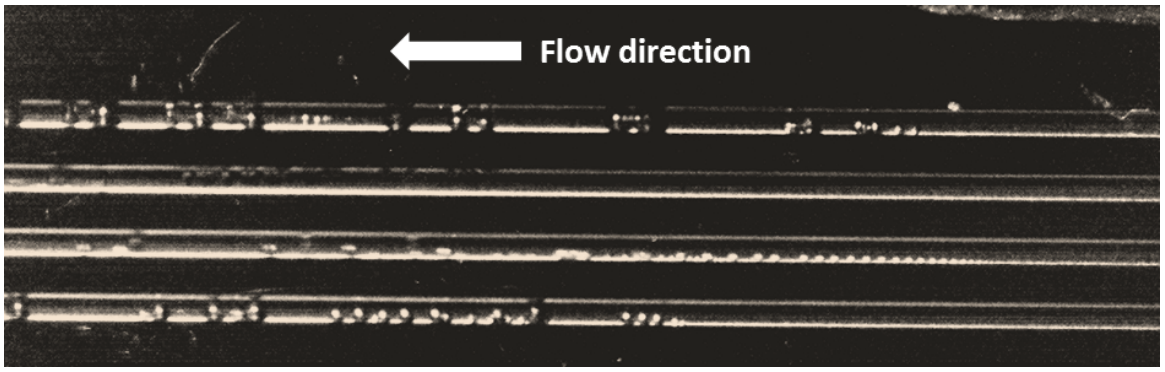


FIGURE 5.24: Active nucleation sites generating trains of bubbles.

For this particular condition, bubbles are observed to be unconfined for an important length before reaching the channel diameter and starting increasing in length. Bubble departure frequency for different nucleation sites has been recorded and it is presented in Fig. 5.25. As it can be seen, the frequency is very similar for the different sites and this is compatible with the prevision of the uniform heat flux and the assumption of equally distributed flow. However, the nucleation is neither continuous nor simultaneous in all channels. Each channel undergoes a sequence including the generation of a train on bubbles. When the bubbles downstream get confined by the channel wall, they start to increase in length both forward and backwards. The increase of pressure generated by this step suppresses the nucleation sites active in that channel. Once the slugs are evacuated in the outlet manifold, the site becomes active again and starts generating bubbles.

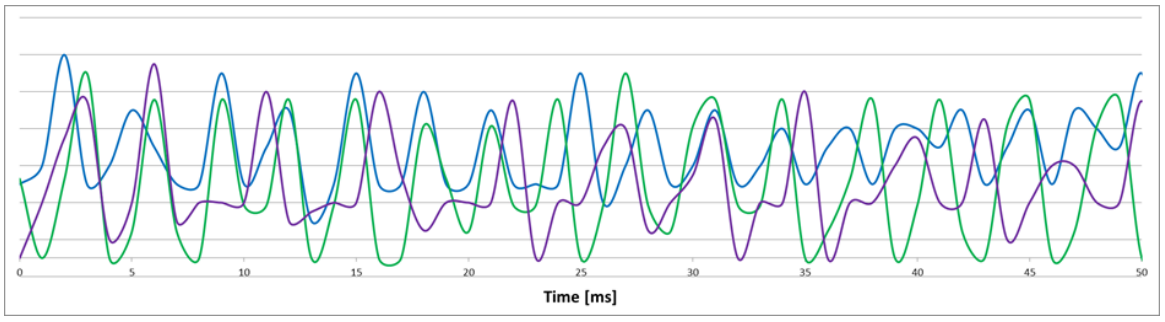


FIGURE 5.25: Nucleation frequency of three different nucleation sites in different channels for the same test condition (P=12 W, m=0.8 kg/h).

The observation of the inlet header outlined backflow problems (Fig.5.26). When the nucleation process is strong at high heat fluxes, the increase of the bubble volume during evaporation proceed in the longitudinal direction once the bubble reach the diameter of the channel and the flow is thus confined. For high nucleation rates the expansion process is so strong that the vapor slugs can reach the inlet manifold. We observed that the restrictions placed at the inlet of the microchannels were not able to avoid vapor backflow into the inlet header. The expansion process seemed to reach a peek and after that the flow was reversed again and the bubbles evacuated towards the outlet manifolds. This process is not simultaneous in all channels: while one channel is experiencing strong vapor expansion and revers flow into the inlet header usually the nucleation process is reduced because of the higher local pressure and because of the passages of the slugs that reduces the local wall temperature. In the meanwhile, an adjacent channel could be expelling vapor slugs towards the outlet manifolds, so the vapor slugs moving backwards to the inlet header could enter the adjacent channel since the pressure is lower. Once the channel has expelled the slugs the local pressure decreases and the local temperature increases so the nucleation rate rises again and the process start again. For a same heat flux, we observed that reverse flow reduces at increasing mass flow rate. This because the Onset of Nucleate Boiling is postponed along the channel and thus the vapor expansion process is not able to reach the inlet header, but also because the higher velocity promotes the expulsion of the vapor slugs towards the outlet manifold. For two chip power dissipation tested (9 W and 12 W) the same mass flow rate of 0.8 $kgh^{-1}$ marked the transition between reversed flow and no reverse flow conditions.

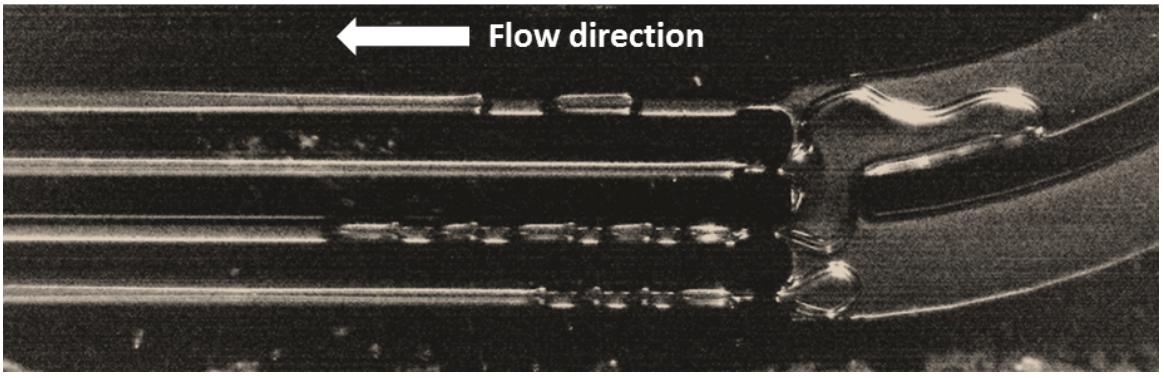


FIGURE 5.26: Reverse flow into the inlet header caused bu rapid vapor expansion inside the microchannels.

## 5.3 Interconnection of multiple silicon microchannel frames

The coverage of the total active area of one ITS stave (15x270 $mm^2$, corresponding to 9 chips 15mmx30mm) with an integrated silicon microchannel cooling frame would require fabrication on very large wafers. For the ITS Inner Barrel staves, a 12" wafer would be required for the fabrication of one single frame. This solution has several major drawbacks:

- The percentage of the used wafer area is very low, strongly increasing production costs
- MEMS facilities with 12" capabilities are quite limited
- Because of tthe reduced thickness of the frame, fragility of the final device would complivate the handling during the assembly phase
- Very long microchannels would have limitatios in the control of the exit vapor quality

In order to overcome these issues, a different solution was investigated. The idea is to have some silicon microchannel frames with embedded microchannels in a row, hydraulically interconnected. This solution allows fabrication on small wafers, improve handling of the components during the assembly phase and optimize the fabrication process. However, this solution introduces new challenges: the efficient distribution of the refrigerant fluid to multiple devices, the hydraulic interconnection of multiple microchannel evaporators with effective sealing and the efficient operation of two-phase flows in very complex networks. A pilot prototype composed by two frames and covering half of the ITS Inner Barrel stave has been produced and characterized.

### 5.3.1 Design and fabrication of the prototype

In this concept, the distribution of the fluid to the different devices is obtained with the introduction of a distribution line running in the frame thickness alongside the microchannels (Fig. 5.27). The fluid entering the first frame from the inlet port in part fills the inlet manifold feeding the microchannels of the first frame, in part runs along the distribution

line towards the second frame. From the inlet manifolds, the fluid is distributed to the microchannels running at the two edges of each frame. From the outlet manifolds, the fluid is recollected and led outlet port of the stave through the return line. Based on design requirements inlet and outlet ports for the fluid must stay on the same side of the stave, i.e. the distribution line and the return line will run on opposite direction on the silicon frames: while in the distribution line the fluid runs concurrent with the microchannels, in the return line the fluid runs in the opposite direction.

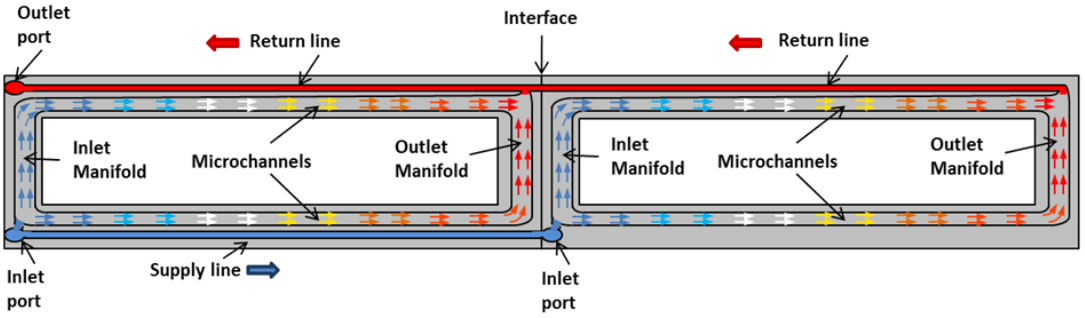


FIGURE 5.27: Sketch of two interconnected silicon microchannel frames. In blue is represented the supply distribution line connecting the inlet ports of the two frames while in red the return line that lead the fluid to the outlet port.

This layout, where the microchannels are completely enclosed within each frame, requires the interconnection of only two channels: the supply and the return distribution lines. An innovative concept called "microbridge" (Fig. 5.28) has been developed to achieve this interconnection. The microbridge is a short microchannel acting like a bridge for moving the fluid from one frame to the following, with minimum mass contribution and space occupancy. At the end of each frame the two distribution lines stop and the fluid is forced to go out of the plane. At this point the fluid enters the microbridge that brings it to the inlet port of the following frame crossing the intersection. The microbridge is obtained in the same wafer of the frames, thus it undergoes the same fabrication process. The process flow is similar to the one developed for the previous single frame prototype, but it includes some major differences and improvements. In particular, the realization of the distribution lines requires etching at two different levels on the front side. This is obtained with a two steps etching. With a first photolithography, the layout of the full fluidic circuit including manifolds, microchannels and distribution lines, is transferred to the hard mask with a

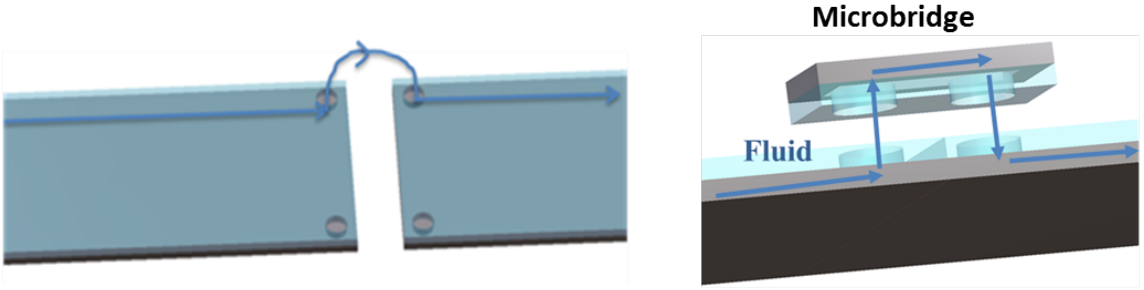


FIGURE 5.28: Interconnection of two silicon frames with the microbridge concept.

plasma etching. The second lithography transfers only the distribution lines, since their depth $L^{DL}$ is greater than the microchannels depth $L^{chann}$ ( $L^{DL}$=350 $\mu$m -$L^{chann}$=100 $\mu$m (Fig. 5.29). The photoresist is used as mask for the etching of the distribution lines until the intermediate depth $L^{int}$=$L^{DL}$-$L^{chann}$. At this point the photoresist is removed with a oxygen plasma and the hard mask is used for etching the manifolds and microchannels while reaching the nominal depth of the distribution lines $L^{DL}$. The silicon microfabrication process flow is presented in Fig 5.30.

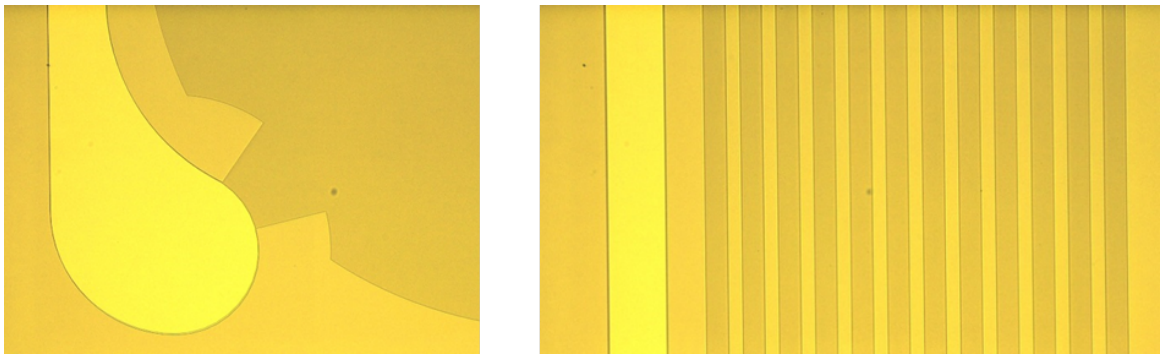

FIGURE 5.29: Details of the double lithography for the realization of different depth channels.

Another major difference is the in/out connection. In the previous prototype, the in/out connections were etched in the silicon wafer backside in correspondence of the manifold. In this new prototype in/out ports are provided on the opposite side by means of holes realized in the Pyrex plate by sandblasting. This choice is the result of the fact that at this stage of the development, a glass cover wafer is used temporarily to seal the channel. The bridge and in/out ports must stay on the glass side of the frame to allow positioning of the chips on the silicon side. This new solution for the in/out ports requires a step of

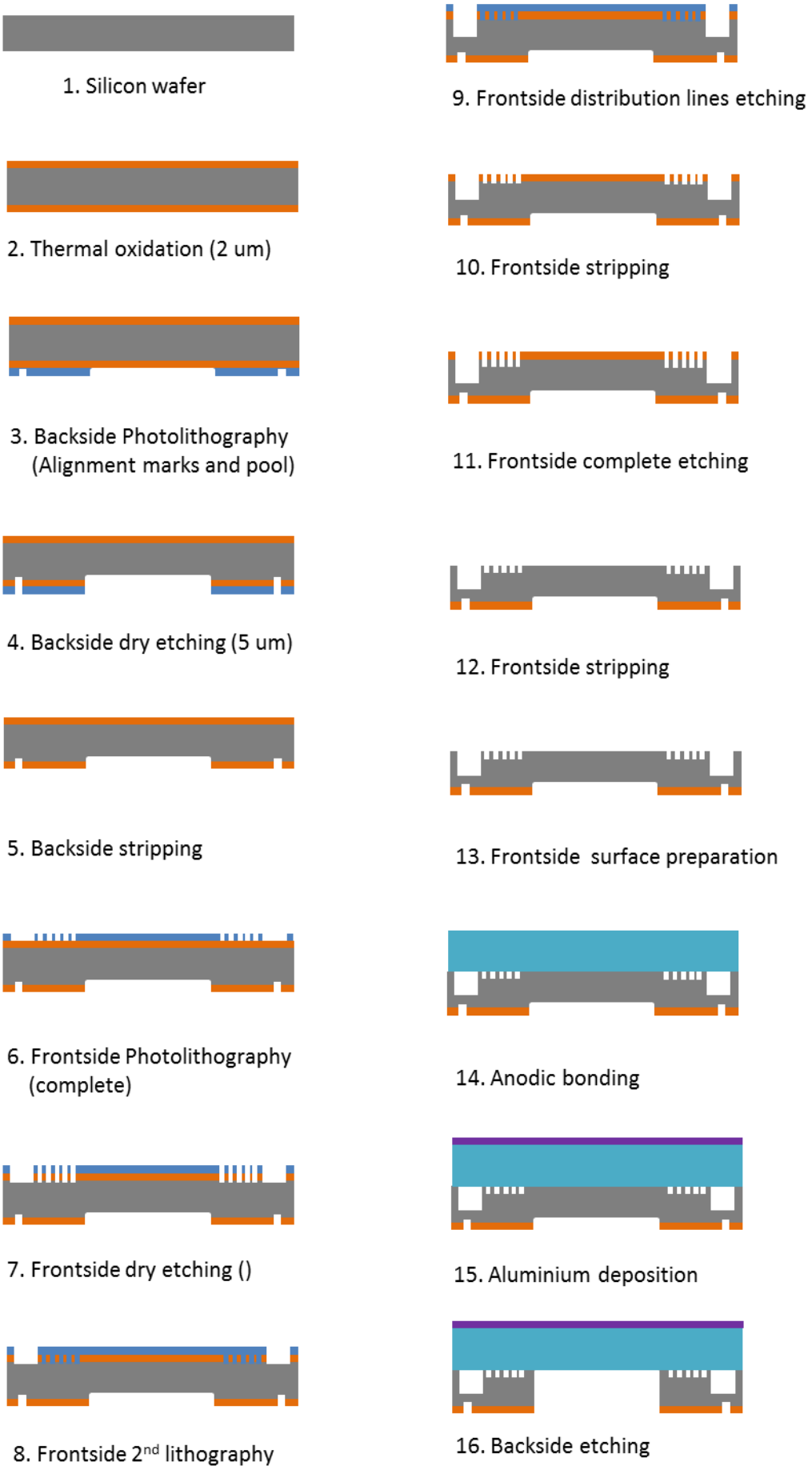


FIGURE 5.30: Process flow of the interconnected silicon frames with embedded microchan-

alignment of the Pyrex wafer and the silicon wafer before the anodic bonding. The presence of alignment marks and the silicon wafer and the Pyrex cover provides very good results during the alignment step preceding the anodic bonding (Fig. 5.31).

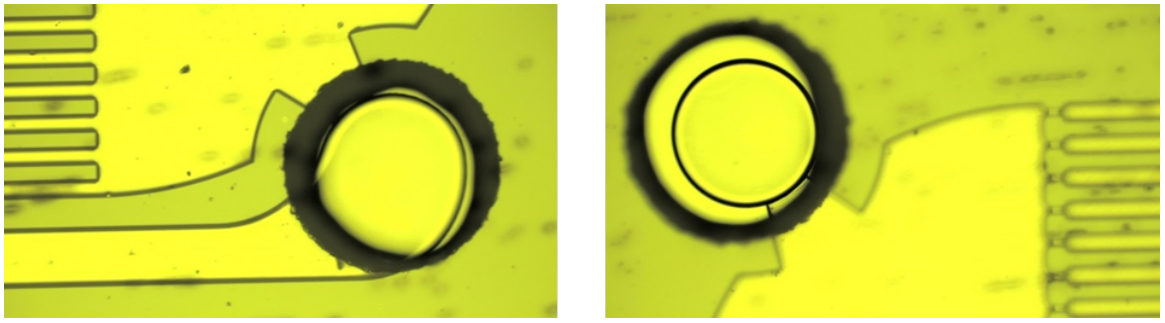

FIGURE 5.31: Alignment of the in/out holes in the glass cover wafer with respect to the fluidic circuitry etched on the silicon wafer.

The full wafer during processing is shown in Fig. 5.32. The wafer includes 4 frames and several microbridges. The length of the frame is 67.5 mm.

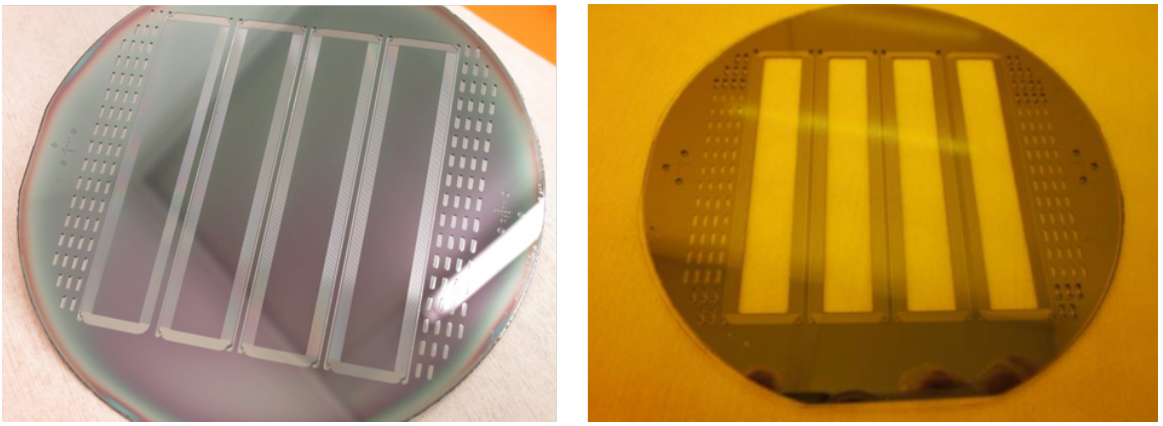

FIGURE 5.32: The wafer during the processing: after the frontside etching (left) and after the removal of the central pools (right).

Once the individual frames are diced out of the wafer, they are assembled into the final prototype. First, two frames are glued head-to-head with epoxy glue. Then, with a precise positioning tool (Fig. 5.33), the micro-bridge is aligned at the interface between the two frames with respect to the inlet/outlet holes of the devices. The interface is then sealed using epoxy glue.

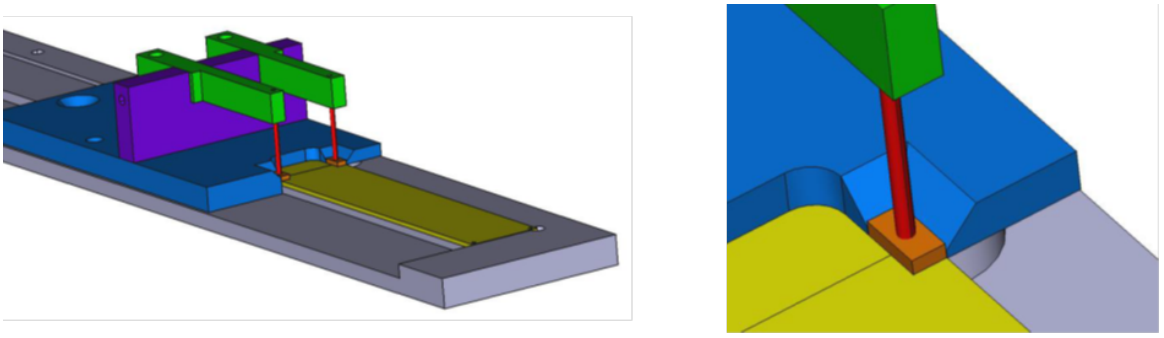

FIGURE 5.33: Jig for the installation of the microbridge. The jig provides a precise position of the microbridge with respect of the frames and special tips guarantee the position during the gluing process.

The tool is based on the exact dimensions of the frame and thus providing a precise positioning of the bridge with respect of the two frames. After the positioning, a tip keeps the bridge in position for the gluing step. This tool gives excellent results in terms of alignment as it can be seen in Fig.5.34.

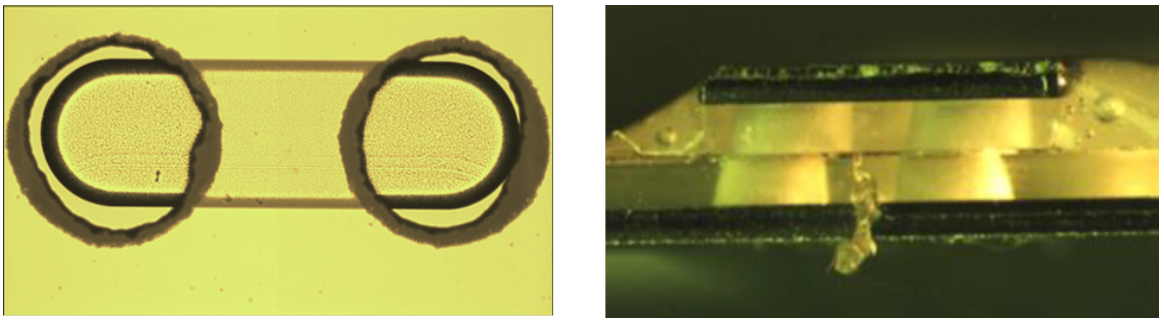

FIGURE 5.34: The machined Pyrex wafer aligned with respect of the channel forming the bridge (left) and installation of the micro-bridge at the interface between two frames (right).

For simulating the detector power dissipation, silicon dummy chips are used. Since the prototype covers half Inner Barrel stave, four and half chips are installed. Tin lines guarantee electrical interconnection of the Platinum film on different chips and two thin electrodes soldered at the two extremities are used for the power input (Fig.5.35).

FIGURE 5.35: The final prototype equipped with silicon dummy chips. The tin soldering lines for the electrical interconnection of the Platinum film and the two electrodes at the extremities are also visible.

### 5.3.2 Experimental test setup

The prototype has been characterized at CERN using a replica of the cooling facility used for the thermal management of the Silicon Pixel Detector installed in the ALICE experiment. The layout of experimental rig is reported in Fig. 5.36. The test fluid is perfluorobutane ($C^4F^{10}$).

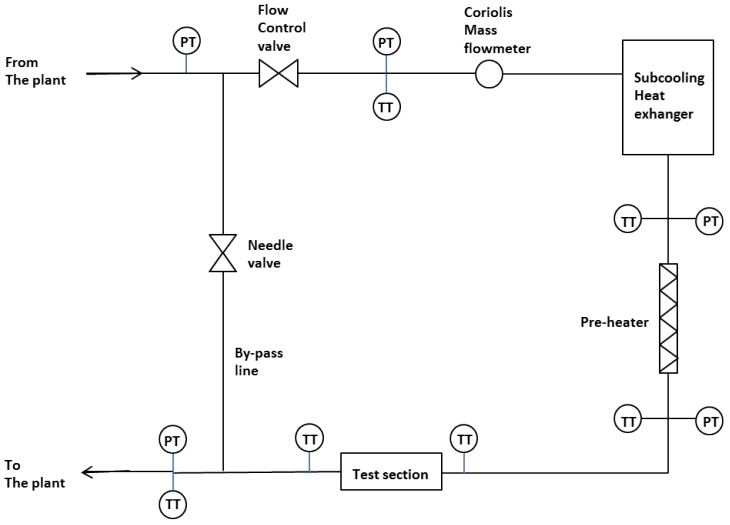


FIGURE 5.36: Layout of the experimental loop (PT=pressure transducer, TT=temperature transducer).

### 5.3.3 Heat loss estimation

Before the experimental characterization, heat loss estimation was performed. Since interested in the temperature of the whole surface of the chips, it was not possible to insulate the test section. In order to assess these thermal losses to the environment by free convection and radiation, a preliminary test without flow was performed. After creating vacuum

inside the test section, chips were powered with a certain power and the temperature of the surface after stabilization was recorded. In this way it was possible to correlate the surface temperature of the chips with the heat losses to the environment by free convection. A thermal balance during single-phase flow was performed to evaluate the power loss to the environment. The results are reported in Fig. 5.37 left. The line represents the input power for different heat fluxes at the chips surface:

$$\mathrm{Q_{chip}} = q_{\mathrm{chip}} \cdot A_{\mathrm{chip}} \cdot n_{\mathrm{chip}} \tag{5.2}$$

where $\mathrm{q}_{chip}$ is the heat flux applied on the surface of the chip, $\mathrm{A}_{chip}$ is the area of one chip and $\mathrm{n}_{chip}$ the number of chips. The dots represent the power measured from the thermal balance on the fluid corrected with the expected power losses predicted with the results obtained with the test without flow and resumed in Fig.5.37 right:

$$\mathrm{Q_{bal}} = \dot{m} \cdot c_p \cdot (T_{out} - T_{in}) + \mathrm{Q}_{loss} \tag{5.3}$$

where $\mathrm{T}_{out}$ and $\mathrm{T}_{in}$ are measured close to the inlet and outlet of the prototype by means of pt100 probes glued outside the supply and return tubes glued to the silicon frame. As it can be seen, power losses are well predicted for low heat fluxes, while are slightly underestimated at higher heat fluxes: this could be attributed to the measurement of the inlet and outlet fluid temperatures, which could be affected by the environment since being measured at the wall of the tube.

### 5.3.4 Single-phase characterization

Single-phase pressure drop characterization of the full prototype in the range of mass flow rate of interest for the application is shown in Fig. 5.38. Experimental data are compared with analytical calculations assuming equal distribution of the fluid within the two frames. Contraction and expansion loss coefficients $\mathrm{K}_c$ and $\mathrm{K}_e$ are derived from Kays and London [134] while for the 90 degree bends it was assumed $\mathrm{K}_{90}$=1.2 as suggested by Phillips [135]. A

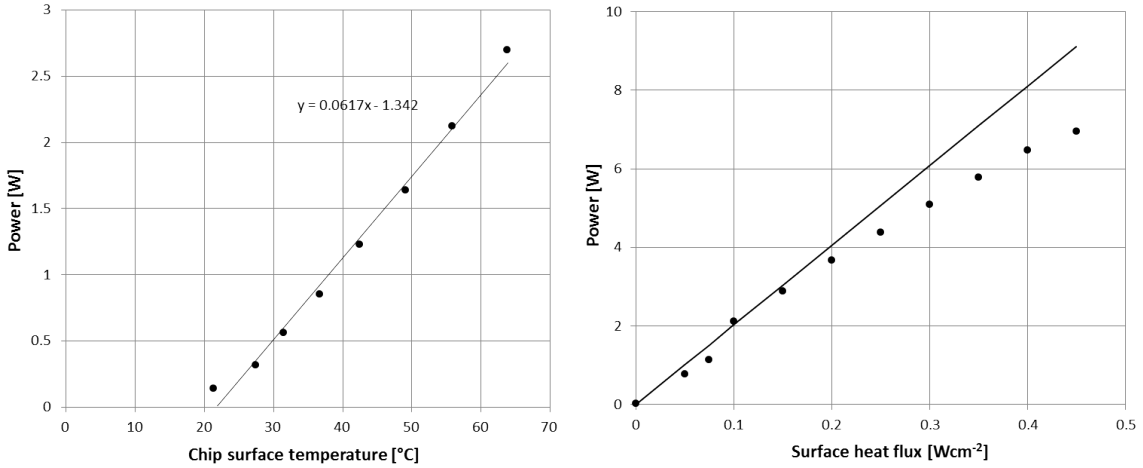


FIGURE 5.37: Power losses to the environment at different temperature of the chips surface (left) and thermal balance during single-phase flow (right).

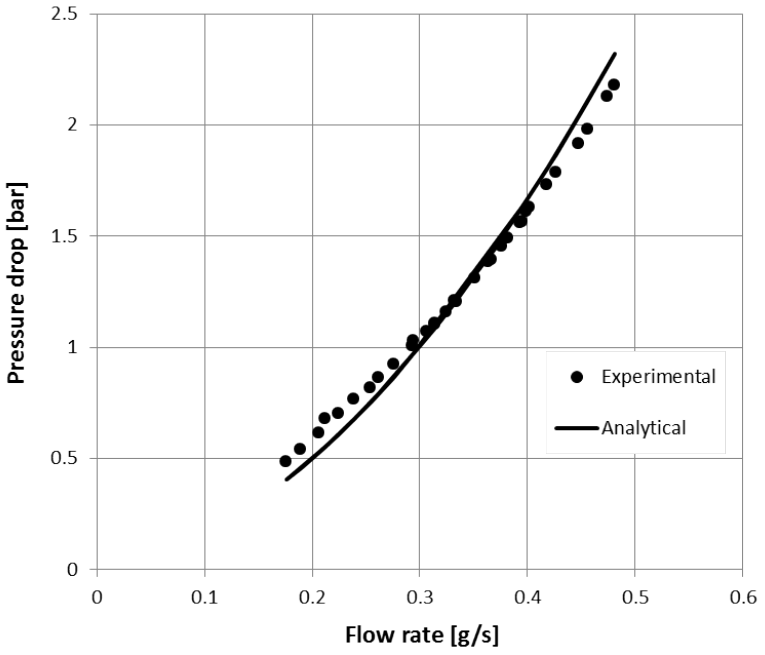


FIGURE 5.38: Single-phase pressure drop characteristics of the prototype.

good agreement between experiments and analytical prediction was found. Single-phase heat transfer performance is evaluated by looking at the chip surface temperature once a certain uniform heat flux is applied on the chips. The IR map of the chip surface during single-phase flow is shown in Fig. 5.39 for a uniform power dissipation qchip=0.1 $Wcm^{-2}$ and a mass flow rate m=0.4 $gs^{-1}$. The fluid enters the test section from the bottom left corner in subcooled condition: therefore at the left side of the prototype the surface temperature is dominated by the inlet manifold where the fluid is distributed to the microchannels. The fluid running inside the microchannels warms up because of the high HTC while the remaining fluid flows inside the supply line to reach the inlet manifold of the second frame: at the interface between the two frames, the surface temperature drops because of the cold liquid filling the inlet manifold of the second prototype.

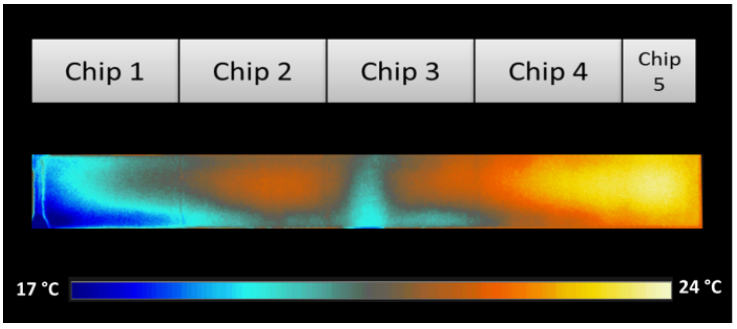


FIGURE 5.39: Infrared temperature map of the chips surface for a power dissipation of $q_{chip}$=0.1 $Wcm^{-2}$ and a mass flow rate m=0.4 $gs^{-1}$ of $C_4F_{10}$ single-phase liquid flow.

The longitudinal temperature profiles along three different lines (supply line, centre of the prototype and return line) are shown in Fig. 5.40 where the temperature drop at the inlet manifold of the second frame is visible for x/L=0.5.

Transversal temperature profiles in Chip 2 for different heat fluxes are presented in Fig.5.41. The experimental results obtain from the IR image of the chip surface temperature (dotted lines) are compared with numerical results (solid line). Steady state conduction simulations were performed on a cross section of the prototype (Fig. 5.41). Heat flux was imposed at the chip surface and analytical heat transfer coefficients for fully developed single-phase laminar flow and three side heating condition were imposed at the walls of the channels.

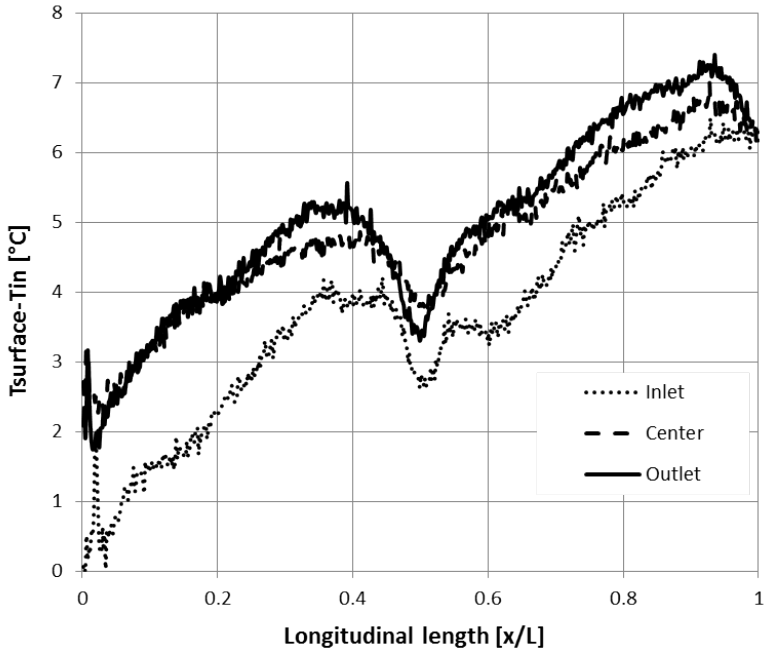


FIGURE 5.40: Longitudinal temperature profiles on the chips surface along three different lines.

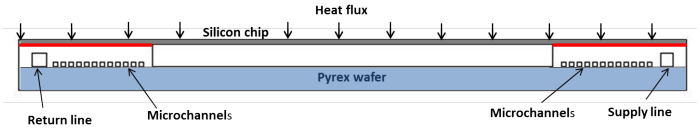


FIGURE 5.41: Cross section of the prototype used for the numerical calculations of the chip surface temperature.

The effect of the refrigerant mass flow rate on the temperature gradient over the surface of the chips for$q_{chip}$= 0.1 Wcm$^{-2}$ is reported in Fig. 5.43. The test was performed at inlet fluid temperature Tin=18°C and inlet pressure pin=3.9 bar. The mass flow rates tested range from 0.2 gs$^{-1}$ to 0.5 gs$^{-1}$. As expected, the surface temperature of the chips is rather affected by the refrigerant mass flow rate. The minimization of the temperature gradient would require higher flow rates but increase the total pressure drop of the device, that for this complex geometry becomes important.

### 5.3.5 Flow boiling characterization

The microfluidic circuit was designed to have single-phase liquid in the inlet headers and in the distribution line. Restrictions where introduced at the inlet of each channel to trigger

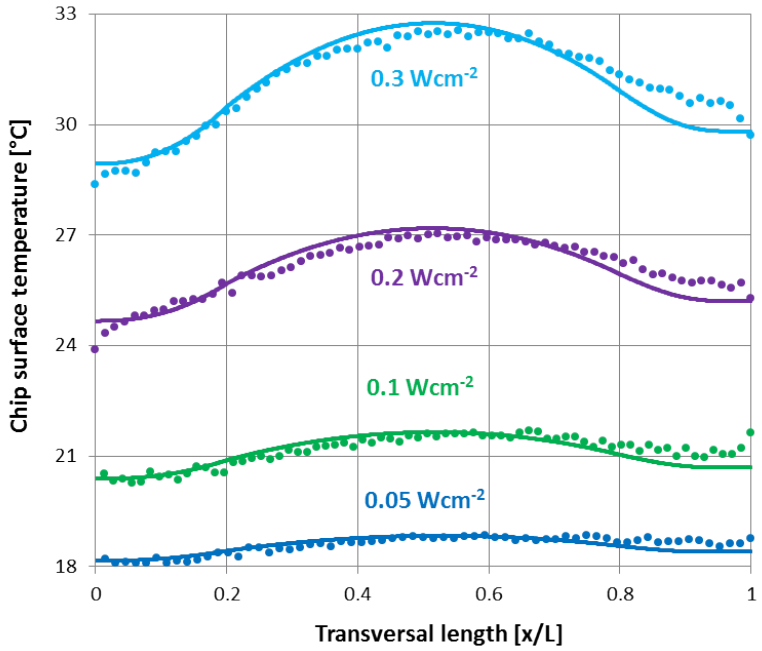


FIGURE 5.42: Transversal temperature profile obtained from the IR measurements at different power dissipations (dotted lines) compares with numerical results (bold lines).

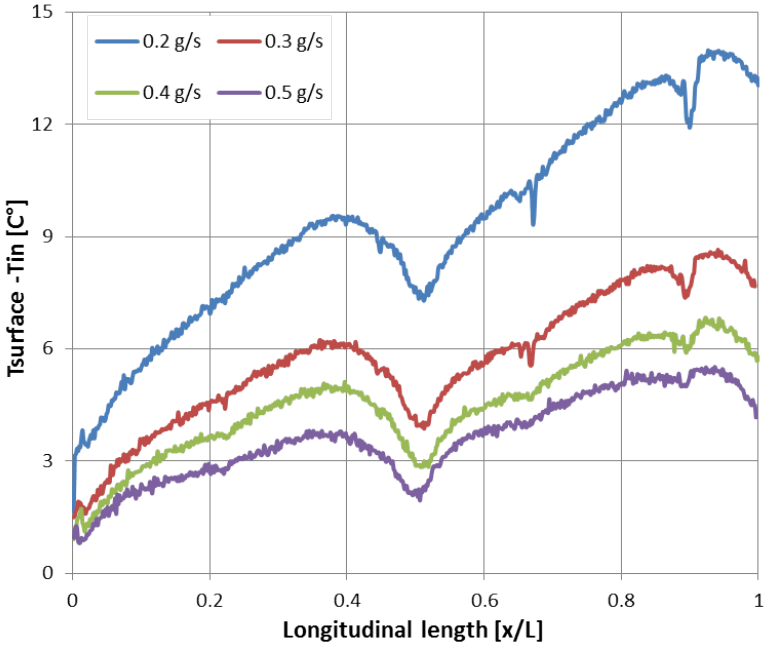


FIGURE 5.43: The effect of the refrigerant flow rate on the surface temperature of the chip.

the boiling process and avoid backflow and instabilities [16]. However, the following issues prevented the operation of the device in the design conditions. First, the very high pressure drop of the whole device during two-phase flow drastically limited the flow rate range of operation. Secondly, the low heat flux from the chips (0.1-0.3 $Wcm^{-2}$) was not sufficient to obtain the Onset of Nucleate Boiling at the beginning of the microchannels. When entering the prototype close to saturation conditions, heat exchange with the surroundings and axial conduction into the inlet header was sufficient to initiate boiling, creating a two-phase entrance of the fluid rather than the desired liquid only flow at the inlet. Increasing the inlet sub-cooling rate resulted in single-phase liquid flow in the whole device, since the chip's power was not enough to start boiling. For these reasons, the tests were carried out with two-phase conditions at the entrance of the prototype. Two-phase flow in such a complex fluidic circuit suffered from instabilities and oscillations of the mass flow rate measured by a Coriolis Mass Flow Meter, ranging from 0.03 to 0.07 gs−1 for a nominal mass flow rate of 0.05 gs−1. These instabilities cause rapid variations of the local conditions resulting in oscillations of the wall surface temperature. These effects are then dumped by materials composing the prototype so that at the surface of the chip, the amplitude of the temperature oscillations is within 0.5°C (Fig. 5.44), thus compatible with the detector operation.

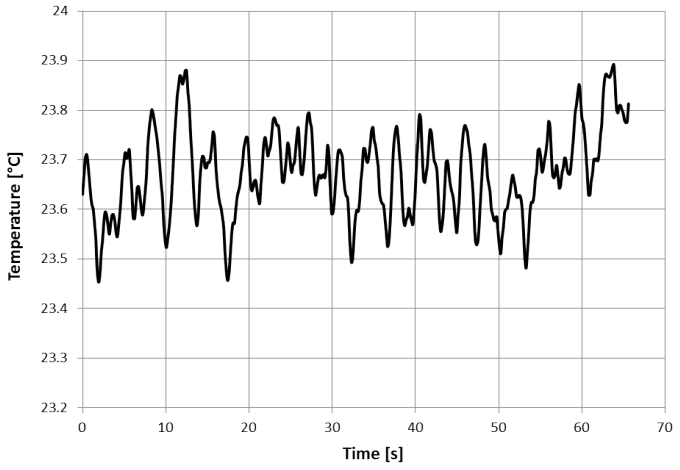


FIGURE 5.44: Temperature oscillations on the surface of the chip.

The temperature map for $C_4F_{10}$ flow boiling (m=0.05 $gs^{-1}$) in the test section for a uniform power dissipation $q_{chip}$=0.1 $Wcm^{-2}$ on the chip surface is reported in Fig.5.45. The longitudinal temperature profiles along three different lines (supply line, centre of the prototype

and return line) are shown in Fig. 5.46. The total temperature difference in the prototype is $\Delta T_{tp}$=3 °C, while a $\Delta T_{tp}$=7 °C was recorded in single-phase flow for the same heat flux on the chip surface but with a higher flow rate (m=0.4 $gs^{-1}$). The high pressure drop measured in the whole prototype during two-phase flow causes an important decrease of the fluid's temperature. This is visible on the top left corner of the Infrared map of the chip surface in Fig. 5.45. This effect is maximum on the left frame where the fluid from both evaporators runs in the return line.

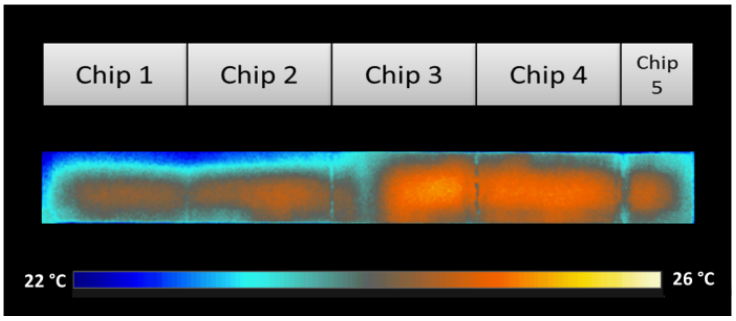


FIGURE 5.45: Infrared image of the surface of the chips during flow boiling $C_4F_{10}$ (m=0.05 $gs^{-1}$) at a uniform power dissipation $q_{chip}$=0.1 $Wcm^{-2}$ on the chip surface.

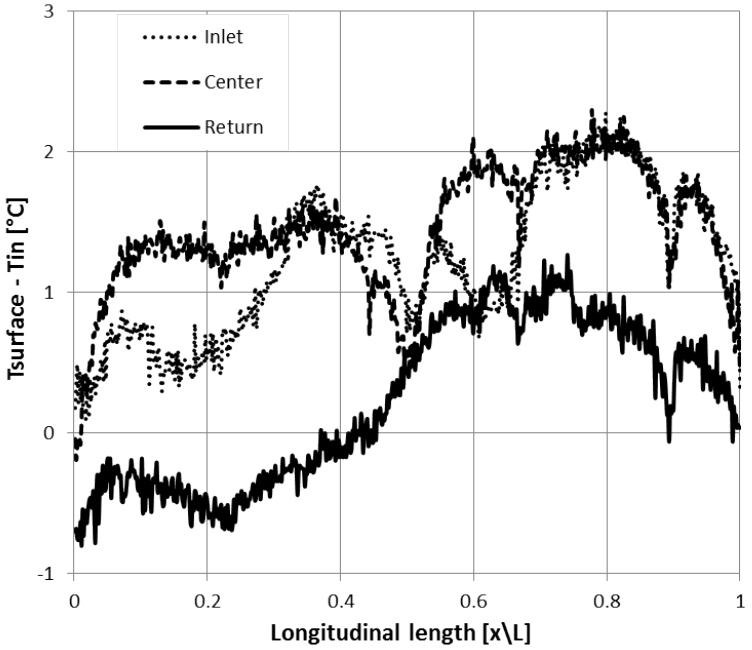


FIGURE 5.46: Longitudinal temperature gradients with respect of the inlet temperature ($T_{in}$=23.2 °C) for flow boiling (m=0.05 $gs^{-1}$) with $q_{chip}$=0.1 $Wcm^{-2}$ uniform heat flux on the chip surface.

For certain operating conditions unequal distribution of the refrigerant within the two frames

was observed. This caused only a small fraction of the total mass flow to reach the second frame. In this case, a dryout condition is observed starting from the middle of the second frame (Fig. 5.47) while stable two-phase flow is established on the rest of the prototype.

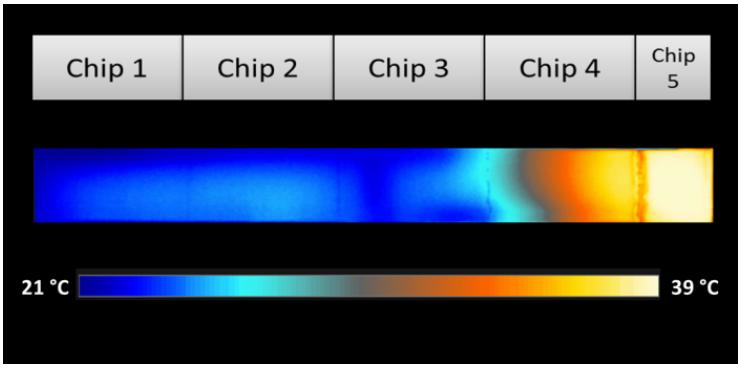


FIGURE 5.47: Infrared image of the surface of the chips with dryout conditions from the middle of the second frame.

This is an indication that optimum performance of two-phase flow heat transfer in complex geometries and interconnected evaporators requires a careful design of the fluidic circuit. In particular, an optimization of the design should address the following three main topics:

- Reduction of the total pressure drop of the device by optimizing the geometrical characteristics of channels and manifolds and identifying possible sources of localized instabilities.
- Improvement of the bridge design reducing concentrated pressure drops from sudden area variations and flow direction changes. Development of a new interconnection concept embedded in the frame thickness for an improved integration.
- Optimization of the inlet restriction for a better control on the Onset of Nucleate Boiling. This can be achieved following different ways: Modification of the geometrical characteristics, tailoring the superficial properties and introducing localized heat generators.

In order to overcome these issues a complete redesign of the inlet manifold was performed. With the aim of reducing the maximum fluid velocity at the bridge exit, the bridge-manifold

connection was redesigned increasing the cross section of the interconnection. In order to reduce the instabilities inside the manifold and the recirculation areas, the profile of the manifold was changes to better follow the fluid lines. For this, a low-drag five-digit symmetric NACA profile 23021 was adopted. Further efforts were dedicated to an ulterior reduction of the material budget. This is achieved by thinning the device to the minimum thickness. The adoption of 30 $\mu$m top and bottom wall was considered as the minimum thickness achievable for a safe operation of the device.

## 5.4 Towards a full stave cooling prototype

With all the information obtained in the previous tests, the development of a microchannel based cooling system covering the full length of the ITS Inner Barrel stave was started. For this prototype a full silicon body is envisaged, requiring silicon-silicon fusion bonding. Compared to silicon-glass anodic bonding, this bonding technique is much more demanding in terms of smoothness, flatness and cleanliness of the surfaces to be bonded. The fabrication process flow has thus to include these additional requirements. In order to accommodate all the innovations introduced in this new prototype, a special fabrication process flow was developed, which is shown in Fig. 5.48. Because of the complexity of the new Process flow, the fabrication of the devices was outsourced to an external company, in this case the Thai Micro Electronic Centre (TMEC) based in Bangkok. The first production batch suffered from problems to the bonding, the most critical step of the Process Flow. The wafer with the microchannels experienced explosion of the membranes (Fig. 5.49) resulting from the etching of the central pool. This was caused by mechanical stresses from pressure difference between the air trapped inside the pools and the vacuum in the bonding chamber and thermal deformations during the rise up to 1150 °C for the fusion bonding.

In order to overcome this problem, a Plasma Activated direct bonding allowing for fusion bonding at low temperature (350 °C) and ambient pressure was investigated. This technique, however, resulted in poor adhesion at the bonding interface, as it is possible to see in Fig.5.50.

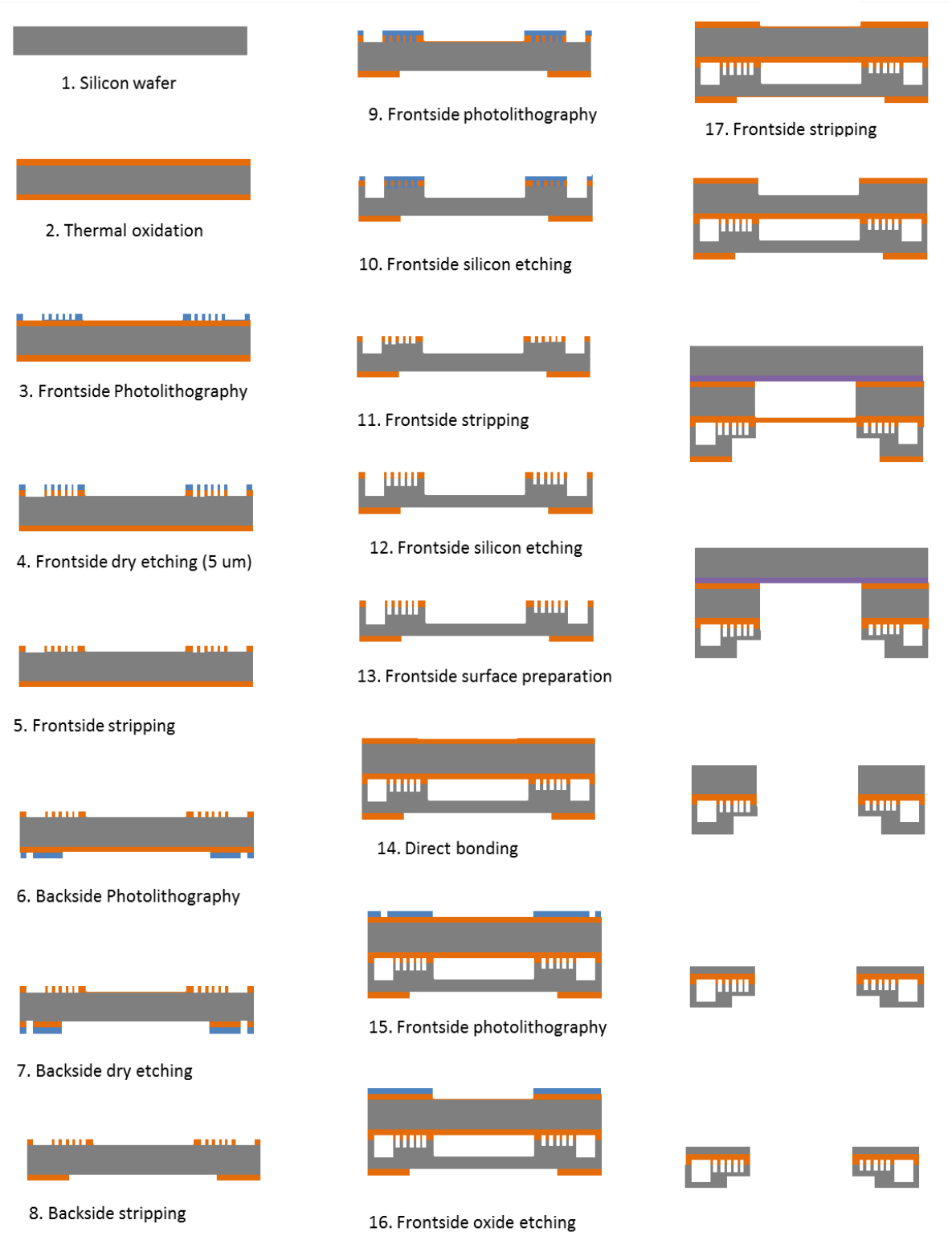


FIGURE 5.48: Fabrication process flow of full silicon interconnected frames for the ITS stave thermal management.

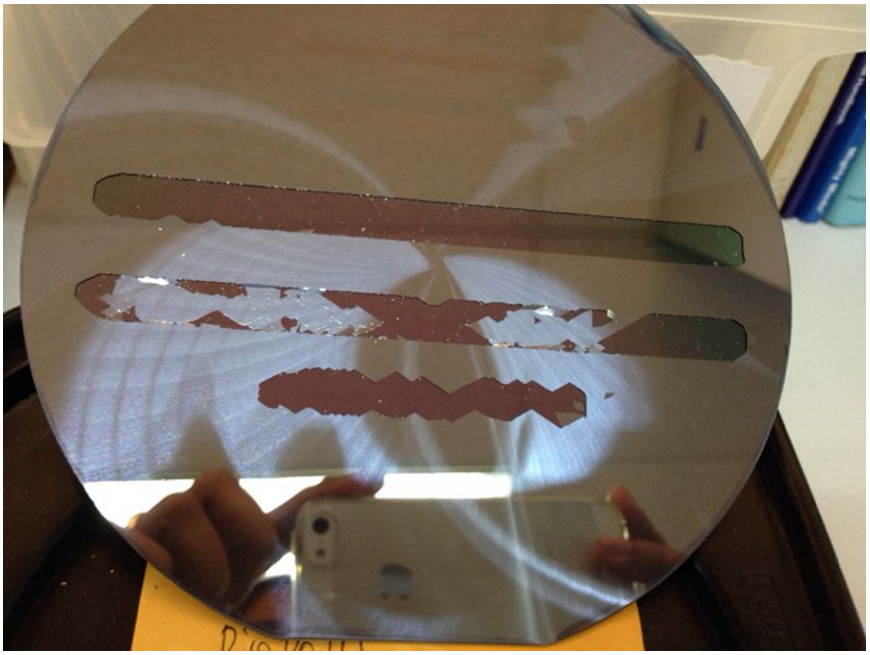

FIGURE 5.49: Rupture of the thin membranes at the bottom of the pools.

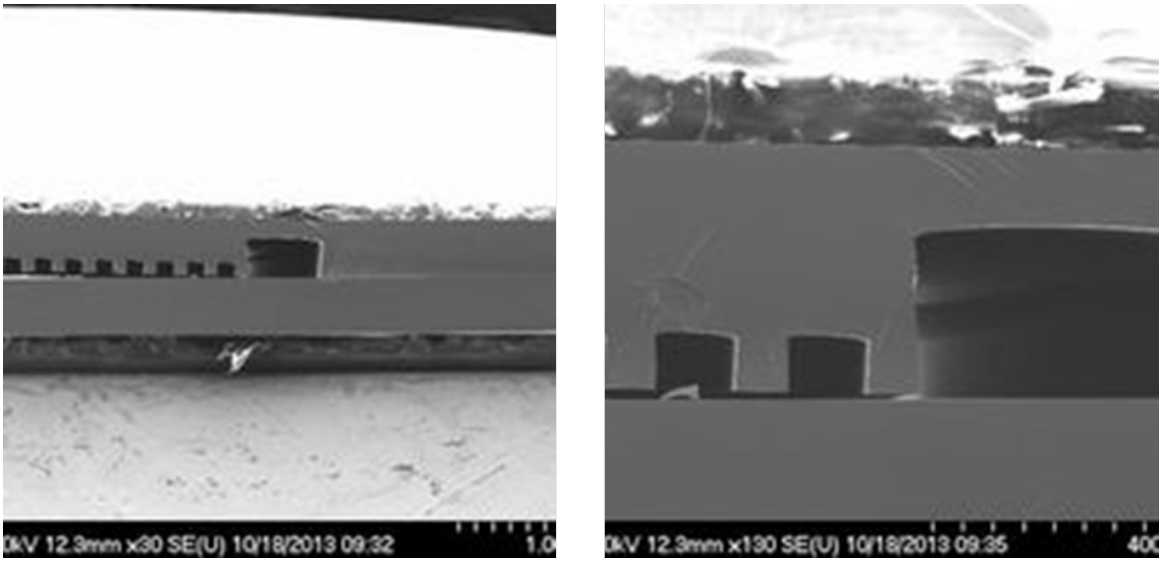


FIGURE 5.50: Rupture of the thin membranes at the bottom of the pools.

Because of these issues, an improved Process flow was developed. The problem of the pool burst during bonding was solved opening some holes before the bonding allowing for pressure equalization at the membrane surface during the bonding process. Because of the high complexity of the direct bonding process, this step was outsourced to Philips in the Netherlands, who has a large experience with this technique.

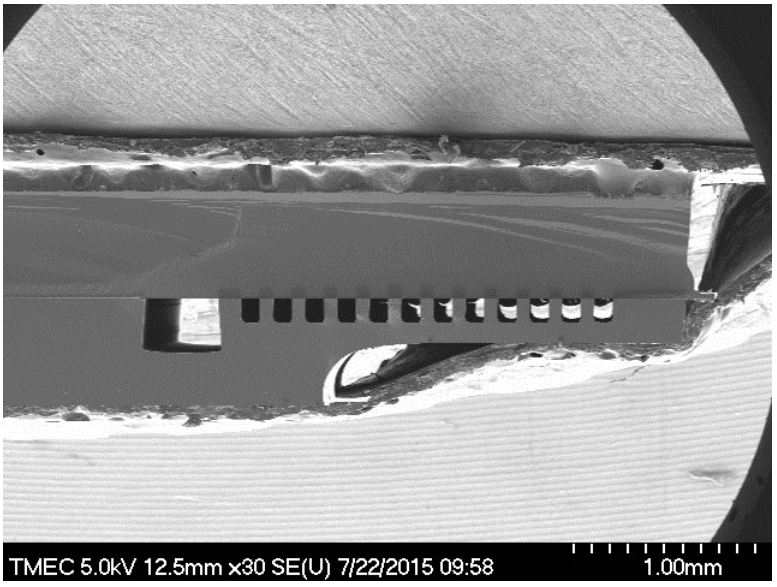


FIGURE 5.51: SEM image of the cross section of the optimized full silicon frame before final thinning.

The modifications introduced in the fabrication process flow were correct and first wafers fabricated with this process were succesfully delivered (Fig.5.52). Final steps including dicing of the frames and thinning were perfromed at EPFL with success.

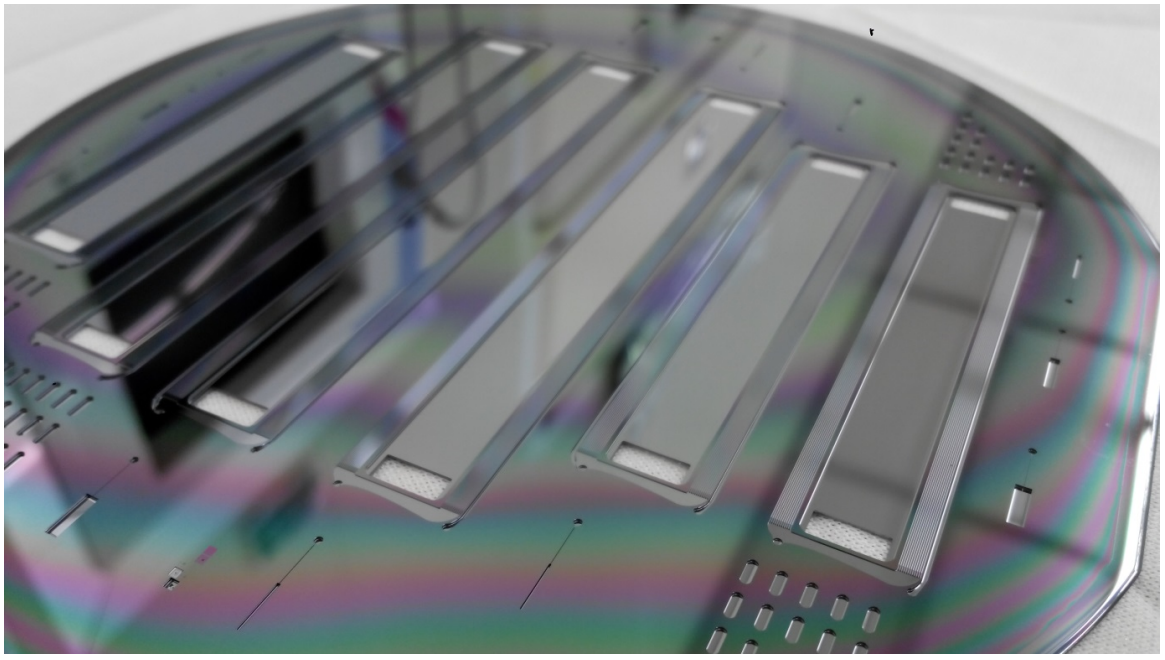

FIGURE 5.52: Image of the processed wafer before the bonding with the silicon cover plate.

## 5.5 Integration of the silicon microchannel devices in the detector system

In the development of low mass integrated cooling systems for vertex detectors in HEP experiments, a fundamental step concern the integration of these devices into the final detector layout by means of lightweight mechanical support structures and also the interface with the detector services and the refrigerant external piping system. These issues are here solved with the development of ultra-lightweight support structures based on high-performance composite materials and the fabrication of 3D printed connectors for the precise installation of the stave inside the detector layout and for interfacing the stave with services. Both these studies are described in this chapter.

### 5.5.1 An ultra-light composite support structure

Design constraints for the ITS detector includes demanding requirements in terms of position accuracy, stability in time with minimum mass contribution. In particular, a precision better than 200 $\mu$m is required during the construction of the detector and a stability of position resolution better than 5 $\mu$m has to be guarantee during the operation of the detector. In order to improve the stave mechanical stability for matching these requirements, the silicon frame assembly is stiffened by a light filament wound carbon structure with a triangular cross section, or Space Frame. The obvious choice of material with high specific stiffness, low specific mass and high radiation length is carbon Fibre reinforced Plastics (CFRP) with a cyanate ester resin system, which is preferable over epoxy for its low humidity absorption and better dimensional stability in time. For this component, the specific stiffness and the low Z are the main parameters driving the design. For this reason, high modulus carbon fibre systems with Young's modulus larger than 300 GPa were considered in the design. In particular, the M60J 3k (588 GPa) was selected as the best candidate matching the design requirements. The Space Frame is manufactured using a standard process for composite materials called filament winding. The process involves winding a band of resin-impregnated filaments under tension over a rotating mandrel. The mandrel rotates around the spindle

while a delivery eye traverses horizontally in line with the axis of the rotating mandrel, laying down fibres in the desired pattern or angle. The structure obtained with this process is shown in Fig. 5.53. The mandrel is in two parts and the silicon microchannel frames are housed in between. The frames periphery slightly protruding from the edge of the mandrel is glued to the carbon filament during the winding process.

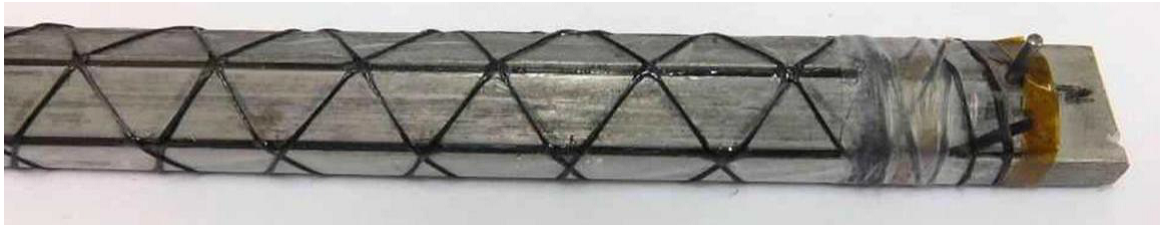

FIGURE 5.53: Mould for the winding process.

After the winding process, the CFRP structure undergoes a curing process obtained by a heating cycle, needed for the resin polymerisation, along with a pressure load which provides the force needed to squeeze the excess of resin. After the polymerisation, the structure is cut along the axis (Fig. 5.54) releasing the final structure composed by the silicon frame assembly with the carbon filament wound Space Frame (Fig. 5.55).

FIGURE 5.54: Release of the silicon frame from the mould by lateral cutting.

The two key structural parameters that define the achievable accuracy and stability in the position of the chips are the Stave sagging under its own weight and the first natural frequency of the Stave. The sag provides the information on the deviation of the chips final position respect to the nominal one while the first natural frequency indicates the frequency at which an external impulse can induce resonance phenomena in the structure resulting in oscillations of the chip positions. The sag and the natural frequency for a given Stave mass depend on the Stave stiffness that is provided by the Space Frame. As a conservative assumption, in both analysis and tests the contribution of the FPC to the overall stiffness has been neglected. A three-point bending test was performed to characterise the structure. Tests were carried out by applying a lumped mass to the centre of the Space Frame,

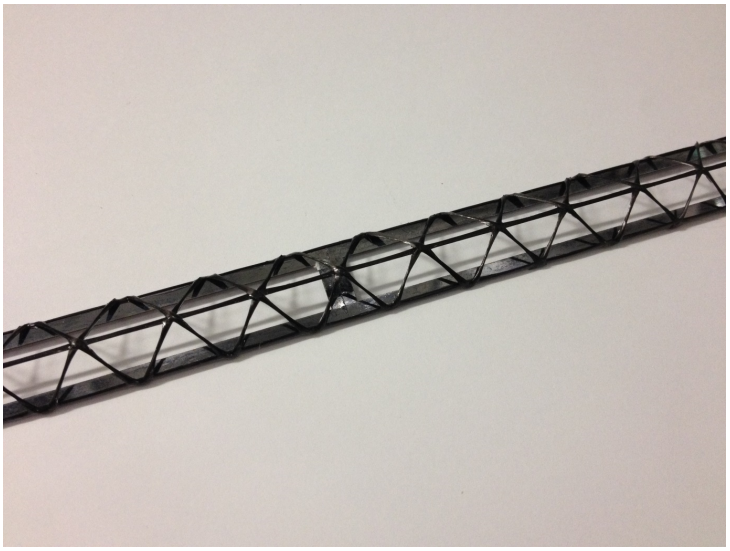

FIGURE 5.55: Detail of the composite space frame on the silicon microchannel frames.

simply supported (free rotations) at the two extremities (Fig. 5.56). From the test results (Fig. 5.57), the stave behaviour under real working conditions (distributed mass and fixed extremities) could be extrapolated. The measured sag could also be used to predict the first natural frequency of the structure.

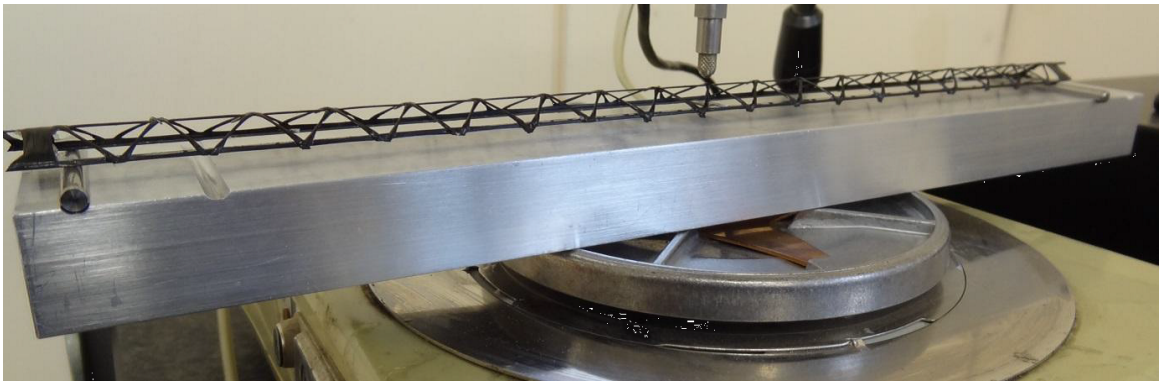

FIGURE 5.56: Test setup for the three point bending test.

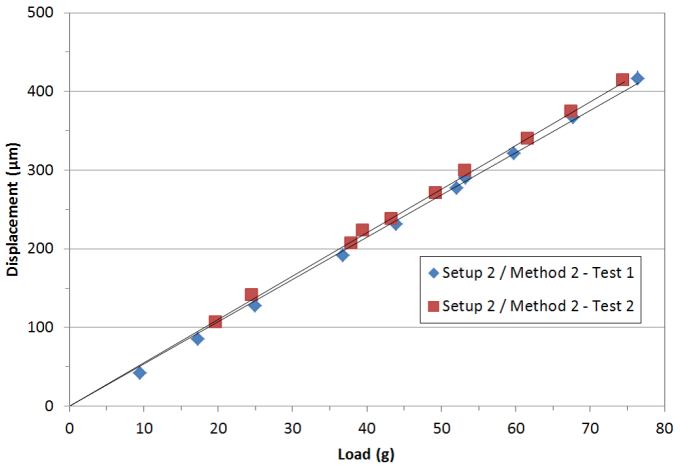


FIGURE 5.57: Results of the three point bending test.

### 5.5.2 High-precision positioning connectors with fluidic features

The ITS Inner Barrel staves are assembled in layers forming the Barrel geometry surrounding the beam pipe. The three layers composing the Inner barrel are positioned at the two extremities in two end-wheels, which are light composite end-rings ensuring the precise positioning of the stave in layers. The two end-wheels are provided with reference planes for the positioning of the two extremities of each stave. Staves are positioned on the reference plane by two connectors that engage a locating ruby ball fixed in the end-wheels at both ends (Fig. 5.58).

While the C side connector provides only mechanical support to the stave and reference for the positioning, the A side connector is also used to interface the microchannel device with the external piping system. This connector is provided with two distinct fluidic circuits: one is the main circuit for exchange of the cooling fluid with the silicon microchannel frame while the other is the glue dispensing system. The main circuit is characterized by two distinct pipes, one for the supply of the refrigerant to the microchannel device and one for the returning fluid (Fig. 5.59). The connectors are fabricated by 3D printing using stereolithography, a process based on the selective laser-solidification of a liquid resin (i.e. a photopolymer) in successive layers. Three different polymers were investigated for this purpose, Accura Bluestone, Accura 48HTR and Accura 25. This last was then selected

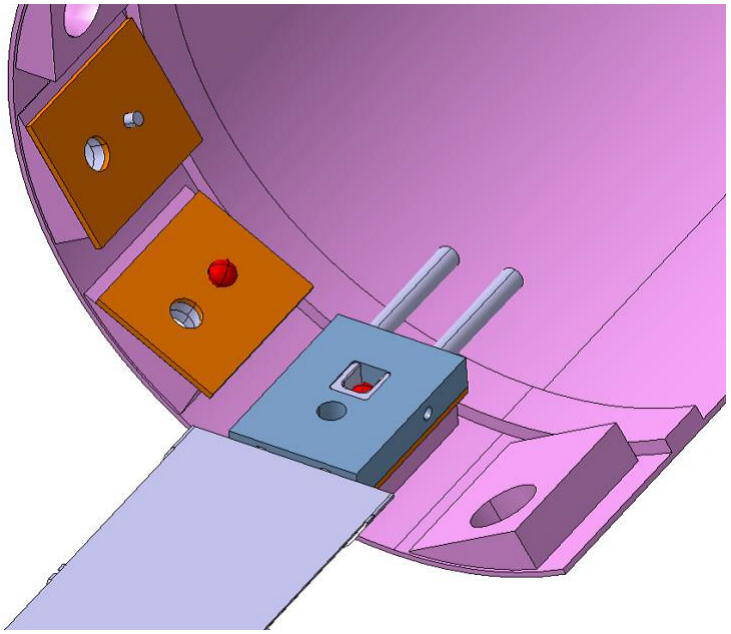

FIGURE 5.58: Positioning of the ITS stave on the End-wheel by means of a precise ruby ball.

for the fabrication of the connectors mainly due to its low viscosity (250 cps) which allows obtaining a very controlled thickness and flatness for each layer allowing realization of very small features. On the silicon frames the inlet/outlet ports are simply holes open to the inlet manifold and the return line respectively. Because of the very tight space constraints between the inner layers, the external pipes must be in the same plane of the silicon frames. For this reason, the connector is designed to provide the change of direction of the fluid from the out-of-plane direction at the inlet/outlet ports on the frame to the in-plane direction of the external piping. The connector also is provided with holes where standard 1/16" Stainless steel pipes can be glued.

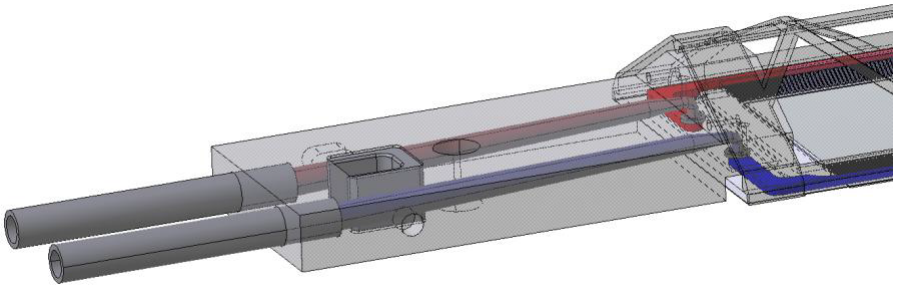

FIGURE 5.59: Refrigerant supply and return lines in the inlet connector.

In order to improve the accuracy in the installation of the connector with respect to the microchannel system, a self-centering feature is included in the design: this is provided by protrusion in the connectors at the end of the supply and return lines, entering the in-out holes in the silicon cover plate. The two protrusions are equipped with o-rings used to avoid glue from entering in the inlet and outlet of the microchannels frame (Fig 5.60). The diameter of the o-rings is smaller than the protrusion diameter to be slightly extended when positioned, ensuring the hermeticity of the assembly. In addition, the o-rings are thicker than the cavity (respectively 0.2 mm and 0.16 mm), resulting in the O-rings being squeezed when assembled, enhancing the tightness of the seal according to the guidelines given by the supplier.

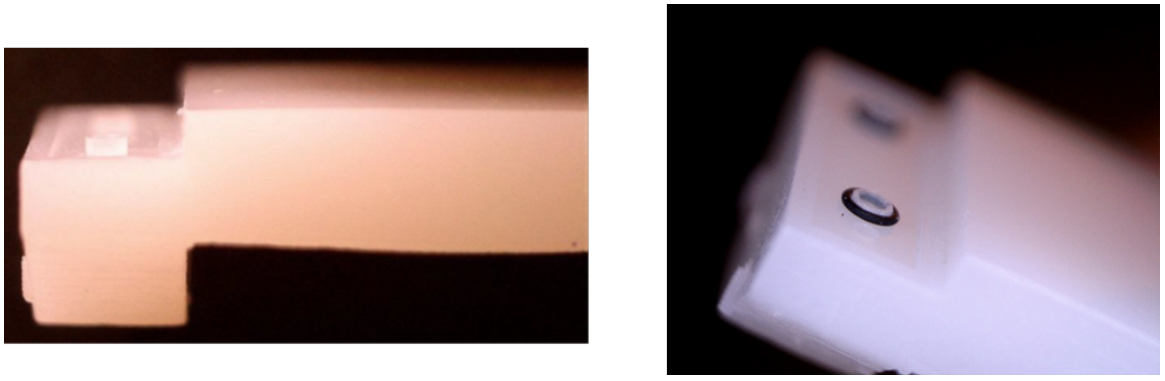

FIGURE 5.60: Details of the protrusions for the alignment of the connector.

The connector is glued to the silicon frame. The glue dispensing system, realized with a devoted fluidic circuit embedded in the connector, is used for this purpose (Fig. 5.61) . The circuit is composed by a small reservoir in contact with the silicon frame and inlet and outlet ducts. The glue is injected through the inlet duct by means of a syringe. The glue fills the reservoir and the excess glue exit from the outlet duct. Air initially in the cavity is gradually forced out through the outlet in the process. When glue comes out of the outlet, injection is maintained for a few moments to allow residual bubbles to be ejected out of the cavity.

In order to characterize the strength of the adhesive interface, traction tests were performed in a UTS 200 testing machine. To allow clamping of the connector for traction, dedicated test samples were designed. They feature the same gluing interface and dispensing system

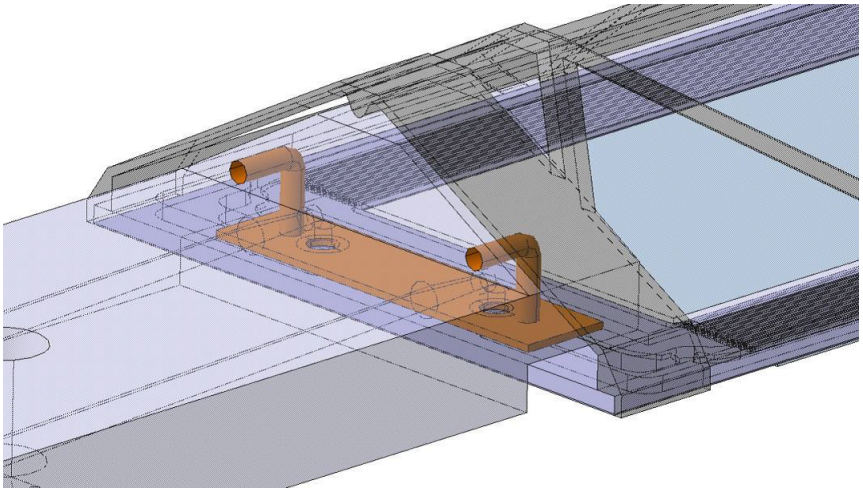

FIGURE 5.61: The glue dispensing system lines in the connector.

with a long protruding structure to be clamped by the testing setup. During the tests great attention was taken to avoid deflection of the silicon substrate during the tension. Results of the displacements for different loads are reported in Fig.5.62 for 5 test samples. As it can be seen, the curves are very different from each other, a characteristic of interfacial failures. A maximum load of 11 N was recorded in the worst case, corresponding to a weight of more than 1 kg. Since the weight of the complete stave is in the order of 5 g, the tests qualify the mechanical performance of the gluing process.

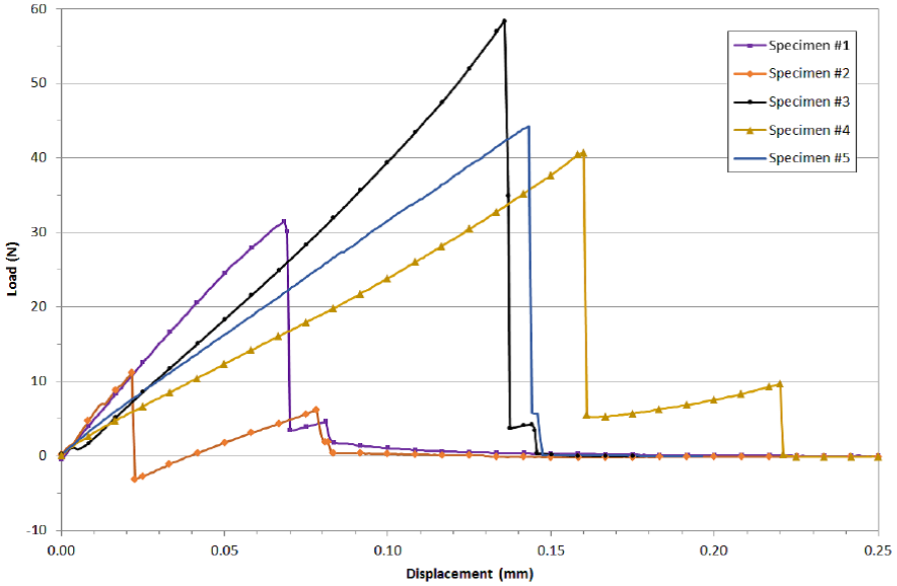


FIGURE 5.62: Results of the traction tests on five connector samples.

# Conclusions

This thesis has addressed microscale flow boiling heat transfer for the thermal management of high heat flux electronics devices. The physics of the process has been experimentally investigated thanks to the development of a dedicated test section, consisting of a single silicon microchannel with a 0.4x0.4 $mm^2$ cross section fabricated using standard silicon microfabrication techniques. Preliminary single-phase characterization validated the design of the test section by comparison of the experimental friction factor and heat transfer coefficient results with appropriate predictive correlations. Flow boiling tests allowed measuring boiling curves, properties at the onset of nucleate boiling and flow boiling heat transfer coefficients. No hysteresis effects were observed between boiling curves at increasing heat flux and decreasing heat flux. The onset of nucleate boiling was seen decreasing at higher mass fluxes except for the lowest mass flux value tested. Heat flux values at ONB are accurately predicted by the correlations of Celata and Thom. Heat transfer coefficient shows negligible sensitivity to the mass flux for the range of conditions tested in this work. The effect of vapor quality is also reduced at constant heat flux for vapor quality values up to 0.6. Flow boiling heat transfer coefficient data were compared with several predictive correlations available in the literature. Some of them are able to predict the data with mean absolute errors within 30% while other correlations completely fail in describing the experimental data set. The effect of surface roughness on flow boiling heat transfer characteristics has been investigated with a dedicated test section featuring tailored microstructured roughness on the two sidewalls of the channel. This new test section show an increase of active nucleation sites and improved thermal performance as deduced by the decrease of the temperature overshoot at ONB and the heat transfer coefficient increase by 20% to 40% according to

the operating conditions. Further experiments are required for a full characterization of the thermal performance of the test section at different operating conditions and for a clear explanation of the effect of the microstructured roughness in the flow boiling process. In the second part of the work, the development of a low mass cooling system based on flow boiling in silicon microchannels for the thermal management of vertex detectors for High Energy Physics experiments is described. In order to reduce the interference of the systems in the reconstruction of particle trajectories, the mass of the system had to be minimized. For this reason, a silicon frame design was adopted with microchannels running along the two sides of the frame. Special techniques were developed for the interconnection of multiple frame evaporators required to cover the full length of the detector. This technique paves the way for the application of silicon microchannel cooling to large active areas. Several prototypes have been fabricated and fully characterized. The tests show that this technique is able to cool the on-detector electronics in future vertex detectors with good performance. First prototypes of a cooling system for the ALICE Inner Tracking System detector are currently under production based on the design developed in this work. The results obtained in this work have a wide applications in all the sectors where high heat flux components needs to be cooled with compact and efficient devices.

# Bibliography


[1] G. E. Moore, "Cramming more components onto intergrated circuits," *Electronics*, vol. 38, no. 8, pp. 114–117, 1965.

[2] D. B. Tuckerman and R. F. W. Pease, "High-performance heat sinking for vlsi," *Electron Device Letters, IEEE2*, no. 5, pp. 126–129, 1981.

[3] A. Francescon *et al.*, "Application of micro-channel cooling to the local thermal management of detectors electronics for particle physics," *Microelectronics J.*, vol. 44, pp. 612–618, 2013.

[4] B. Agostini, M. Fabbri, J. E. Park, L. Wojtan, J. R. Thome, and B. Michel, "State of the art of high heat flux cooling technologies," *Heat Transfer Engineering*, vol. 28, no. 4, pp. 258–281, 2007.

[5] G. L. Morini, "Viscous heating in liquid flows in microchannels," *Int. J. Heat Mass Transfer*, vol. 48, pp. 3637–3647, 2005.

[6] J. R. Thome, "Wolverine heat trnasfer engineering data book iii,"

[7] B. Agostini and J. R. Thome, "Comparison of an extended database for flow boiling heat transfer coefficients in multi-microchannels elements with the three-zone model," *ECI heat trensfer and fluid flow in microscale Conference.*

[8] Y. Katto and H. Ohno, "An improved version of the generalized correlation of critical heat flux for the forced convective boiling in uniformly heated vertical tubes," *Int. J. Heat and Mass Transfer*, vol. 27, no. 9, pp. 1641–1648.

[9] W. Qu and I. Mudawar, "Measurement and correlation of critical heat flux in two-phased micro-channel heat sinks," *Int. J. Heat and Mass Transfer*, vol. 47, pp. 2045–2059, 2004.

[10] C. L. Ong and J. R. Thome, "Marco-to microchannel transition in two-phase flow: Part 2 - flow boiling heat transfer and critical heat flux," *Exp. Thermal Fliud Science*, vol. 35, pp. 873–886, 2011.

[11] G. Ribatski, L. Wojtan, and J. R. Thome, "An analysis of experimental data and prediction methods for two-phase frictional pressure drop and flow boiling heat transfer in micro-scale channels," *Exp. Thermal Fliud Science*, vol. 31, no. 1, pp. 1–19, 2006.

[12] W. L. Owens, "Two-phase pressu gradient," *Int. Dev. In Heat Transfer*, no. Pt. II ASME, 1961.

[13] W. H. McAdams, "Heat transmission," vol. Third ed., 1954.

[14] A. Cicchitti, C. Lombardi, M. Silvestri, G. Soldaini, and R. Zavalluilli, "Two-phase cooling experiments - pressure drop, heat transfer and burnout measurement," *Energia Nucl.*, vol. 7, no. 6, pp. 407–425, 1960.

[15] A. E. Dukler, W. Moye, and R. G. Cleveland, "Frictional pressure drop in two-phase flow, part a: a comparison of existing correlations for pressure loss and hold-up, and part b: an approach through similarity analysis," *AIChE J.*, vol. 10, no. 1, pp. 38–51, 1964.

[16] D. R. K. Beattie and P. B. Whalley, "Simple two-phase frictional pressure drop calculation method," *Int. J. Multiphase Flow*, vol. 8, no. 1, pp. 83–87, 1982.

[17] M. M. Awad and Y. S. Muzychka, "Effective property models for homogeneous two-phase flows," *Exp. Thermal Fluid Sciene*, vol. 33, no. 1, pp. 106–113, 2008.

[18] S. Lin, C. C. K. Kwok, R. Y. Li, Z. H. Chen, and Z. Y. Chen, "Local frictional pressure drop during vaporization for r-12 through capillary tubes," *Int. J. Multiphase Flow*, vol. 17, pp. 95–102, 1991.

[19] W. W. Akers, H. A. Deans, and O. K. Crosser, "Condensing heat transfer within horizontal tubes," *Chem. Eng, Prog.*, vol. 54, pp. 89–90, 1985.

[20] D. Steiner, "Vdi waermeatlas (vdi heat atlas)," *VDI-Gesellscaft Verfahsenstechnik und Chemieingenieurwesen (GCV)*, vol. Chapter Hbb.

[21] Z. Rouhani and E. Axelsson, "Calculation of volume of fraction in the subcooled and quality region," *In. J. Heat Mass Transfer*, vol. 107, pp. 383–393, 1970.

[22] R. W. Lockhart and R. C. Martinelli, "Proposed correlation of data for isothermal two-phase, two-component flow in pipes," *Chem. Eng. Prog.*, vol. 45, pp. 39–48, 1949.

[23] D. Chisholm, "A theoretical basic for the lockhart-martinelli correlation for two-phase flow," *Int. J. of heat Mass Transfer*, vol. 10, pp. 1767–1778, 1967.

[24] C. J. Baroczy, "A systematic correlation for two-phase pressure drop," *Chem. Eng. Prog.*, pp. 232–249, 1965.

[25] D. Chisholm and L. A. Sutherland, "Prediction of pressure gradients in pipeline system during two-phase flow," *Proc. Inst. Mech. Engineers*, vol. 184, pp. 24–32, 1969.

[26] R. Groennerud, "Investigation in liquid holdup, flow resistance and heat transfer in circular type evaporators, part iv: Two-phase resistance in boiling refrigerants," *Bulletin de l'inst. du Froid*, pp. –, 1972.

[27] D. Chisholm, "Pressure gradients due to friction during the flow of evaporating two-phase mixtures in smooth tubes and channels," *Int. J. Heat Mass Transfer*, vol. 16, pp. 347–358, 1973.

[28] L. Friedel, "Improwed friction pressure drop correlations for horizontal and vertical two-phase pipe flow," *European Two-Phase Flow Group Meeting*, vol. Paper E2, pp. –, 1979.

[29] H. Mueller-Steinhagen and K. Heck, "A simple friction pressure drop correlation for two-phase flow in pipes," *Chem. Eng, Process*, vol. 20, pp. 297–308, 1986.

[30] G. M. Lazarek and S. H. Black, "Evaporative heat transfer pressure drop and critical heat flux in a small vertical tube with r-113," *Int. J. Heat Mass Transfer*, vol. 25, pp. 945–960, 1982.

[31] K. Moriyama, A. Inoue, and H. Ohira, "The thermohydraulic characteristics of two-phase flow in extremely narrow channels (the frictional pressure drop and heat transfer of boiling two-phase flow, analytical model)," *Heat Transfer Japanese Research*, 1992.

[32] K. Mishima and T. Hibiki, "Some characteristics of air-water two-phase flow in small diameter vertcal tubes," *Int. J. Multiphase Flow*, vol. 22, pp. 703–712, 1996.

[33] Y. Y. Yan and T. F. Lin, "Evaporation heat transfer and pressure drop of refrigerant r134a in a small pipe," *Int. J. Heat Mass Transfer*, vol. 41, pp. 4183–4194, 1998.

[34] H. J. Lee and S. Y. Lee, "Pressure drop correlations for two-phase flow within horizontal rectangular channels with small heights," *Int. J. Multiphase Flow*, vol. 27, pp. 783–796, 2001.

[35] T. N. Tran, M. C. Chyu, M. W. Wambsganss, and D. M. France, "Two-phase pressure drop of refrigerants during flow boiling in small channels: an experimental investigation and correlation development," *Int. J. Multiphase Flow*, vol. 26, no. 11, pp. 1739–1754, 2000.

[36] P. A. Kew and K. Conrwell, "Correlations for the prediction of boiling heat transfer in small-diameter channels," *Appl. Thermal Eng.*, vol. 17, pp. 705–715, 1997.

[37] M. Zang and R. L. Webb, "Correlation of two-phase friction for refrigerants in small-diameter tubes," *Exp. therm. Fluid Sci.*, vol. 25, pp. 131–139, 2001.

[38] A. Kawahara, P. Y. Chung, and M. Kawaji, "Investigation of two-phase flow pattern, void fraction and pressure drop in a microchannel," *Int. J. Multiphase Flow*, vol. 28, no. 9, pp. 1411–1435, 2002.

[39] W. Yu, D. M. France, M. W. Wambsganss, and J. R. Hull, "Two-phase pressure drop, boiling heat transfer, and critical heat flux to water in a small-diameter horizontal tube," *Int. J. Multiphase Flow*, vol. 28, no. 9, pp. 927–941, 2002.

[40] G. R. Warrier, V. K. Dhir, and L. A. Momoda, "Heat transfer and pressure drop in narrow rectangular channels," *Exp. Therm. Fluid Sci.*, vol. 26, pp. 53–64, 2002.

[41] W. Qu and I. Mudawar, "Measurement and prediction of pressure drop in two-phase microchannel heat sinks," *Int. J. Heat Mass Transfer*, vol. 46, pp. 2737–2753, 2003.

[42] J. Lee and I. Mudawar, "Two-phase flow in high-heat-flux micro-channel heat sink for refrigeration cooling applications: Part i - pressure drop characteristics," *Int. J. Heat Mass Transfer*, vol. 48, pp. 928–940, 2005.

[43] Y. W. Hwang and M. S. Kim, "The pressure drop in microtubes and the correlation development," *Int. J. Heat Mass Transfer*, vol. 49, pp. 1804–1812, 2006.

[44] L. Sun and K. Mishima, "Evalutation analysis of prediction methods for two-phase flow pressure drop in mini-channels," *Int. J. Multiphase Flow*, vol. 35, pp. 47–54, 2009.

[45] W. Zhang, T. Hibiki, and K. Mishima, "Correlations of two-phase frictional pressure drop and void fraction in mini-channel," *Int. J. Heat Mass Transfer*, vol. 53, pp. 453–465, 2010.

[46] W. Li and Z. Wu, "A general correlation for adiabatic two-phase pressure drop in mini/micro channels," *Int. J. Heat Mass Transfer*, vol. 53, pp. 2732–2739, 2010.

[47] S. Kim and I. Mudawar, "Universal approach to predicting two-phase frictional pressure drop for adiabatic and condensing mini/micro-channel flows," *Int. J. Heat Mass Transfer*, vol. 55, pp. 3246–3261, 2012.

[48] P. Lee and S. V. Garimella, "Saturayed flow boiling heat transfer and pressure drop in silicon microchannel arrayas," *Int. J. Heat Mass Transfer*, vol. 51, pp. 789–806, 2008.

[49] K. I. Choi, A. S. Pamitran, J. T. Oh, and K. Saito, "Pressure drop and heat transfer during two-phase flow vaporization of propane in horizontal smooth minichannels," *Int. J. Refrigeration*, vol. 32, pp. 837–845, 2009.

[50] A. Cioncolini, J. R. Thome, and C. Lombardi, "Unified marco-to-microscale method to predict two-phase frictional pressure drops of annular flows," vol. 35, pp. 1138–1148, 2009.

[51] A. Cavallini, D. D. Col, M. Matkowic, and L. Rossetto, "Pressure drop during two-phase flow of r134a and r32 in a single minichannels," *J. Heat Transfer*, vol. 131, 2009.

[52] D. D. Col, A. Bisetto, M. Bortolato, D. Torresin, and L. Rossetto, "Experiments and updated model for two-phase frictional pressure drop inside minichannels," *Int. J. Heat Mass Transfer*, vol. 67, pp. 326–337, 2013.

[53] B. Agostini and J. R. Thome, "Comparison of an extended database for flow boiling heat transfer coefficients in multi-microchannels elements with the three-zone model.," *CI heat transfer and fluid flow in microscale*, vol. E. Castelvecchio Pascoli, Italy, 2005.

[54] J. C. Chen, "Correlation for boiling heat transfer to saturated fluids in convective flow," *IEC Process Des. Dev.*, vol. 5, no. 3, pp. 322–329, 1996.

[55] A. E. Bergles and W. M. Rohsenow, "The determination of forced-convection surface-boiling heat transfer," *J. Heat Transfer*, vol. 86, pp. 365–372, 3 1964.

[56] H. K. Foster and N. Zuber, "Dynamics of vapour bubbles and boiling heat transfer," *A.1.Ch.E. J*, vol. 11, pp. 531–535, 1955.

[57] F. W. Dittus and L. M. K. Boelter, "Heat transfer in automobile radiators of the tubural type," *University of California Publications in Engineering*, vol. 2, pp. 443–461, 1930.

[58] M. M. Shah, "Chart correlation for saturated boiling heat transfer: Equations and further study," *ASHRAE Trans.*, vol. 88, no. Part 1, pp. 185–196, 1982.

[59] K. E. Gungor and R. H. S. Winterton, "A general correlation for flow boiling in tubes and annuli," *Int. J. Heat Mass Transfer*, vol. 29, pp. 351–358, 1986.

[60] M. G. Cooper, "Heat flow rates in saturated nucleate pool boiling - a wide ranging examination using reduced properties," *"In "Advances in Heat Transfer"*, vol. 16, pp. 157–239, 1984.

[61] K. E. Gungor and R. H. S. Winterton, "Simplified general correlation for satured flow boiling and comparisons of correlations with data," *CHem. Eng. Res Des.*, vol. 65, pp. 148–156, 1987.

[62] D. B. R. Kenning and M. G. Cooper, "Saturated flow boiling of water in vertical tubes," *International Journal of Heat Mass Transfer*, vol. 32, no. 3, pp. 445–458, 1989.

[63] S. G. Kandlikar, "A general correlation of saturated two-phase flow boiling heat transfer inside horizontal and vertical tubes," *J. Heat Transfer*, vol. 112, pp. 219–228, 1990.

[64] S. G. Kandlikar, "An improved correlation for predicting two-phase flow boiling heat transfer coefficient in horizontal and vertical tubes," *Proceedings of 21. ASME/AIChE National Heat Transfer Conference*, pp. –, 1983.

[65] S. G. Kandlikar, "Flow boiling maps for water, r-22 and r-134a in the saturated region," *9th International Heat Transfer Conference*, 1990.

[66] B. S. Petukhov and V. N. Popov, "Theoretical calculation of heat exchange and frictional resistance in turbulent flow in tubes of an incompressible fluid variable physical properties," *Teplofiz. Vysok. Temperatur*, vol. 1, no. 1, 1963.

[67] V. Gnielinski *Int. Chem. Eng.*, vol. 6, pp. 359–368, 1976.

[68] S. G. Kandlikar, "A model for correlating flow boiling heat transfer in augmented and compact evaporators," *Journal Heat Transfer*, vol. 113, no. 4, pp. 966–972, 1991.

[69] S. G. Kandlikar and M. E. Steinke, "Flow boiling heat transfer coefficient in minichannels - correlation and trends," *12th International Heat Transfer Conference*, pp. –, 2002.

[70] S. G. Kandlikar and M. E. Steinke, "Predicting heat transfer during flow boiling in minichannels and microchannels," *ASHRAE Annual Meeting*, 2003.

[71] Z. Liu and R. H. S. Winterton, "A general correlation for saturated and subcooled flow boiling in tube and annuli, based on a nucleate pool boiling equation," *Int. J. Heat Mass Transfer*, vol. 34, no. 11, pp. 2759–2766, 1991.

[72] J. P. Wattelat, J. C. Chato, A. L. Souza, and B. R. Christoffersen, "Evaporative characteristics of r-12, r-134a, and a mixture at low mass fluxes," *ASHRAE Trans*, vol. 94-2, pp. 603–615, 1994.

[73] G. M. Lazarek and S. H. Black, "Evaporative heat transfer pressure drop and critical heat flux in a small vertical tube with r-113," *Int. J. Heat Mass Transfer*, vol. 25, pp. 945–960, 1982.

[74] P. A. Kew and K. Cornwell, "Correlations for the prediction of boiling heat transfer in small-diameter channels," *Appl. Thermal Eng.*, vol. 17, pp. 705–715, 1997.

[75] "Small circular- and rectangular- channel boiling with two refrigerants," *Int. J. Multiphase Flow*, vol. 22, pp. 485–498, 1996.

[76] K. Stephan and M. Abdelsalam, "Heat transfer correlations for natural convection boiling," *Int. J. Heat Mass Transfer*, vol. 23, pp. 73–87, 1980.

[77] Y. Y. Lin and T. F. Lin, "Evaporation heat transfer and pressure drop of refrigerant r-134a in a small pipe," *Int. J. Heat Mass Transfer*, vol. 41, pp. 4183–4194, 1998.

[78] W. Yu, D. M. France, M. W. Wanbsganss, and J. R. Hull, "Two-phase pressure drop, boiling heat transfer, and critical heat flux to water in a small-diameter horizontal tube," *Int. J. Multiphase Flow*, vol. 28, pp. 927–941, 2002.

[79] W. Zhang, T. Hibiki, and K. Mishima, "Correlation for flow boiling heat transfer in mini-channels," *Int. J. Heat Mass Transfer*, vol. 47, pp. 5749–5763, 2004.

[80] G. R. Warrier, V. K. Dhir, and L. A. Momoda, "Heat transfer and pressure drop in narrow rectangular channels," *Exp. Thermal Fluid Sci.*, vol. 26, pp. 53–64, 2002.

[81] S. G. Kandlikar and P. Balsubramanian, "An extension of the flow boiling correlation to transition, laminar, and deep laminar flows in minichannels and microchannels," *Heat Transfer Eng.*, vol. 25, no. 3, 2004.

[82] S. Saitoh, H. Daiguji, and E. Hihara, "Correlation for boiling heat transfer of r-134a in horizontal tubes including effect of tube diameter," *Int. J. Heat mass Transfer*, vol. 50, pp. 5215–5225, 2007.

[83] L. Sun and K. Mishima, "An evoluation of prediction methods for saturated flow boiling heat transfer in mini-channels," *Int. J. Heat Mass Transfer*, vol. 52, pp. 5323–5329, 2009.

[84] S. S. Bertsch, E. A. Groll, and S. V. Garimella, "A composite heat transfer correlation for saturated flow boiling in small channels," *Int. J. Heat Mass Transfer*, vol. 52, pp. 2110–2118, 2009.

[85] J. Kaew-On and S. Wongwises, "Experimental investigation of evaporation heat transfer coefficient and pressure drop of r-410a in a multiport mini-channel," *Int. J. Refrigeration*, vol. 32, pp. 124–137, 2009.

[86] S. E. Haaland, "Simple and explicit formulas for the friction factor in turbulent pipe flow," *J. Fluids Eng.*, vol. 105, pp. 89–90, 1983.

[87] J. Kaew-On, K. Sakamatapan, and S. Wongwises, "Flow boiling heat transfer of r134a in the multiport minichannels heat exchangers," *Exp. Thermal Fluid Sci.*, vol. 35, pp. 364–374, 2011.

[88] M. Jacobi and J. R. Thome, "Heat transfer model for evaporation of elongated bubble flows in microchannels," *J. Heat Transfer*, vol. 124, pp. 1131–1136, 2002.

[89] M. S. Plesset and S. A. Zwick, "The growth of vapor bubbles in superheated liquids," *Journal of Applied Physics*, vol. 25, no. 4, pp. 493–500, 1954.

[90] Z. Y. Bao, D. F. Fletcher, and B. S. Haynes, "Flow boiling heat transfer of freon r11 and hfcfc123 in narrow passages," *Int. J. Heat Mass Transfer*, vol. 43, pp. 3347–3358, 2000.

[91] J. R. Thome, V. Dupont, and M. A. Jacobi, "Heat transfer model for evaporation in microchannels: Part i. presentation of the model," *Int. J. Heat Mass Transfer*, vol. 47, pp. 3375–3385, 2004.

[92] K. Moriyama and A. Inoue, "Thickness of the liquid film formed by a growing bubble in a narrow gap between two horizontal plates," *J. Heat Transfer*, vol. 118, pp. 132–139, 1996.

[93] M. J. Madou, "Fundamentals of microfabrication and nanotechnology," *CRC Press, Taylor and Francis Group*, 2012.

[94] S. Franssila, "Introduction to microfabrication," *John Wiley and Sons Ltd, The Atrium*, pp. –, 2004.

[95] W. Kern and D. A. Puotinen, "Cleaning solutions based on hydrogen peroxide for use in silicon semiconductor technology," *RCA Rev.*, vol. 31, pp. 187–206, 1970.

[96]

[97] B. Mortini *C.R. Physique*, vol. 7, 2006.

[98] B. Scienes, "Spin coating theory,"

[99] P. J. Kelly and R. D. Arnell, "Magnetron sputtering: a review of recent developments and applications," *Vacuum*, vol. 56, pp. 159–172, 2000.

[100] I. V. Svadkovski, D. A. Golosov, and S. M. Zavatskiy, "Characterisation parameters for unbakanced magnetron sputtering systems," *Vacuum*, vol. 68, pp. 283–290, 2003.

[101] D. M. Mattox, "Fundamentals of ion plating," *J. Vac. Sci. Technology*, vol. 10, pp. –, 1973.

[102] B. E. Deal and A. S. Grove, "General relationship for the thermal oxidation of silicon," *J. Appl. Phys.*, vol. 36, no. 12, pp. 3370–3778, 1965.

[103] M. Yun, "Investigation of koh anisotropic etching for the fabrication of sharp tips in silicon-on-insulator (soi) material," *Journal of the Korean Physical Society*, vol. 37, no. 5, pp. 605–610, 2000.

[104] M. S. Kulkarni and H. F. Erk, "Acid-based etching of silicon wafers: mass-transfer and kinetic effects," *Journal of The Electrochemical Society*, vol. 147, no. 1, 2000.

[105] A. J. Perry and R. W. Boswell, "Fast anisotropic etching of silicon in an inductively coupled plasma reactor," *Applied Physics Letters*, vol. 55, no. 148, 1989.

[106] G. S. Oehrlein, "Reactive-ion etching," *Physics Today*, vol. 39, no. 10, 1986.

[107] F. Laermer and A. Schilp, "Method of anisotropically etching silicon," *Robert Bosch GmbH, US-Patent*, no. 5501893, pp. –.

[108] F. Karouta, "A practical approach to reactive ion etching," *J. Phys. D: Appl. Phys.*, vol. 47, pp. –, 2014.

[109] C. Gui, M. Elwenspoek, N. R. Tas, and J. G. E. Gardeniers, "The effect of surface roughness on direct wafer bonding," *J. Appl. Phys.*, vol. 85, no. 10, pp. 7448–7454, 1999.

[110] A. Plossl and G. Krauter, "Material science and engineering r25," pp. 1–88, 1999.

[111] T. M. H. Lee *et al.*, "Detailed characterization of anodic bonding process between glass and thin-film coated silicon substrates," *Sensors and actuators*, no. 86, 2000.

[112] J. Lee and I. Mudawar, "Two-phase flow in high heat-flux micro-channel heat sink for refrigeration cooling applications - part ii," *Int. J. Heat Mass Transfer*, vol. 48, pp. 941–955, 2005.

[113] D. D. Col, S. Bortolin, and L. Rossetto, "Convective boiling inside a cicrular microchannel," *Int. J. Heat Mass Transfer*, vol. 67, pp. 1231–1245, 2013.

[114] G. P. Celata, M. Cumo, and A. Mariani, "Experimental evaluation of the onset of sudcooled flow boiling at high liquid velocity and subcooling," *Int. J. Heat Mass Transfer*, vol. 40, pp. 2879–2885, 1997.

[115] J. R. S. Thom, W. M. Walker, T. A. Fallon, and G. F. S. Reising, "Boiling in subcooled water during flow up heated tubes or annuli," *Symposium on boiling heat transfer in steam generating units and heat exchangers*, 1965.

[116] "https://en.wikipedia.org/wiki/standard model," pp. –.

[117] S. Hamieh, J. Letessier, and J. Rafelski, "Quark-gluon plasma fireball," *Phys. Rev.*, vol. C6, no. 2, 2000.

[118] W. Riegler, "Particle physics instrumentation," *CERN Yellow Report*, vol. CERN-2014-001, pp. 241–251, 2014.

[119] F. Hartmann and A. Sharma, "Multipurpose detectors for high energy prhysics, and introduction," *Nuclear Instruments and Methods A*, pp. 1–9, 2012.

[120] D. Green, "At the leading edge, atlas and cms lhc experiments," *World Scientific Publishing*, 2010.

[121] C. Lippmann, "Particle indentification," *Nuclear instruments and Methods A*, pp. 148–172, 2012.

[122] C. W. Fabjan and F. Gianotti, "Calorimetry for particle physics," *Reviews of Modern Physics*, vol. 75, no. Issue 4, pp. 1243–1286.

[123] K. Aamodt *et al.*, "The alice experiment at the cern lhc," *JINST*, vol. 3, no. S08002, 2008.

[124] B. Abelev and others (The ALICE Collaboration), "Upgrade of the alice experiment. letter of intent," *Journal of Physics G: Nuclear and Particle Physics*, vol. 41, no. 8, pp. –, 2012.

[125] B. Abelev *et al.*, "Technical design report for upgrade of the alice inner tracking system," *J. Phys. G*, vol. 41, pp. –, 2014.

[126] F. Hartmann, "Advances in tracking detectors," *Annual Review of Nuclear and Particle Sciene*, pp. 197–221, 2011.

[127] N. Wermes, "Pixel vertex detectors," *34th SLAC Summer Institute on Particle Physics*, vol. SSI 2206, pp. –, 2006.

[128] G. A. Rinella *et al.*, "Monolithic active pixel sensor development for the upgrade for the alice inner tracking system," *TWEPP*, 2013.

[129] M. Olcese, "Mechanics and cooling of pixel detectors," *Nucl. Instr. and Meth. A*, vol. 465, pp. 51–59, 2001.

[130] S. G. Kandlikar, "Heat transfer and fluid flow in minichannels and microchannels," *Elsevier*, 2006.

[131] G. Romagnoli *et al.*, "Silicon micro-fluidic cooling for na62 gtk pixel detectors," *Microelectronic Eng.*, vol. 145, pp. –133–137, 2015.

[132] A. Nomerotski, J. Buytart, P. Collins, R. Dumps, E. Greening, M. John, A. Mapelli, A. Leflat, Y. Li, G. Romagnoli, and B. Verlaat, "Evaporative co2 cooling using microchannels etched in silicon for the future lhcb vertex detector," *Journal of Instrumentation*, vol. 8, no. 4, pp. –, 2013.

[133] I. E. Idelchik *Handbook of Hydraulic Resistance*, vol. 3rd Edition, pp. –, 1996.

[134] W. M. Kays and A. L. London, "Compact heat exchangers," *McGraw Hill*, no. 86, 1984.

[135] R. J. Phillips, "Forced convection, liquid cooled, microchannel heat sinks," *MS Thesis*, no. 86, 1987.

# *Acknowledgements*

I wish to thank all the people who contributed in many ways to the completion of this document.
First of all I would like to thank my supervisors Prof. Davide Del Col and Dr. Luciano Musa for their continuous support and help. Their guidance and suggestions have been fundamental in the accomplishment of this complex work.
Many thanks to my group at the University of Padova for creating a wonderful working environment and for their precious suggestions and help.
I also would like to acknowledge the help of the CERN PH-DT group for providing always solutions to the technical challenges encountered during the development of this work.
Non potro mai ringraziare abbastanza la mia famiglia per l'amore che mi ha dimostarto in tutti questi anni. A special thanks to Roby the Master of LaTeX for the inestimable help in typesetting this document.
And my complete gratitude to my beloved Edit, my half and life. Thank you for your patience and for your immense love.